

Testing of Conventional Construction W-shape brace members and their bolted end connections undergoing reversed cyclic loading

By

Alina Rudman



McGill

Department of Civil Engineering and Applied Mechanics

McGill University, Montreal, Quebec, Canada

December 2018

A thesis submitted to McGill University in partial fulfillment of the requirements of the degree of Masters of Engineering

© Alina Rudman 2018

ABSTRACT

In Canada, the seismic design of steel structures involves the principle of capacity based design, which takes advantage of the inelastic ductility of the Seismic Force Resisting System (SFRS). Specific to concentrically braced frames, the moderate ductility (MD) and limited ductility (LD) categories both require that the members and connections in the lateral load carrying path be designed for the probable capacity of the braces in tension and compression. However, there also exists the Conventional Construction (CC) category as outlined in Clause 27.11 of the CSA S16-14 Standard, for which the engineer is allowed to waive capacity based design principles and design a SFRS which is expected to behave principally elastically when subjected to design-level earthquakes. These Type CC systems are designed using low R-values ($R_o = 1.3$ & $R_d = 1.5$), and hence do not depend on the yielding and buckling of a fuse element (brace) to dissipate earthquake energy. Instead, the energy dissipation is assumed to occur due to localized yielding of connections and through friction within these joints. The CSA S16-14 Standard requires the engineer to increase the seismic forces by a factor of 1.5, if it cannot be demonstrated that the connections in the lateral load carrying path have an expected failure mode that is ductile. This has proven to be challenging to engineers because no guidelines or recommendations are provided to determine the ductility of connections. As a result, quantifying the level of ductility of these components becomes an important factor in designing Type CC systems under seismic loading.

While Type CC braced frames are used extensively throughout the country, there is very little research available to give insight on the ductility of these systems, particularly in the case of W-shaped braces with bolted end connections. As such, the objective of this research was to measure the response of full-scale W-shape braces and their bolted connections under reversed cyclic seismic loading. Six brace specimens were tested, including two common bolted connection types and two W-shape section sizes. These connections were designed following the provisions in CSA S16-14 without any capacity design rules. The 1.5 penalty from Clause 27.11 was not included. The loading protocol was developed using statistical data from a nonlinear

numerical study of five buildings designed with Type CC braces. Test measurements indicated that that Type CC brace specimens were able to achieve storey drift ratios of 1%-2%.

RÉSUMÉ

Au Canada, la conception sismique des structures en acier se base sur le principe de la conception basée sur la capacité, qui bénéficie de la ductilité inélastique des systèmes de résistance aux charges sismiques (SRCS). En particulier pour les contreventements en treillis concentriques, les catégories de conception de ductilité modérée (MD) et ductilité limitée (LD) exigent que les éléments structuraux et les connexions sur le trajet de la charge latérale soient conçus pour la capacité probable des diagonales en traction et en compression. Cependant, il existe également la catégorie Construction Conventiionnelle (CC) décrite à la clause 27.11 de la norme CSA S16-14 qui dit que l'ingénieur est autorisé à déroger aux principes de conception basés sur la capacité et à concevoir un SRCS dont le comportement devrait être principalement élastique. Ces systèmes de type CC sont conçus avec de faibles valeurs R ($R_o = 1,3$ et $R_d = 1,5$) et ne dépendent donc pas de la déformation et du flambement des diagonales pour dissiper l'énergie sismique. Au lieu de cela, la dissipation d'énergie peut se produire par des déformations localisées des connexions et du frottement dans ces jointures. La norme CSA S16-14 impose à l'ingénieur d'augmenter les forces sismiques par un facteur 1,5 s'il ne peut pas démontrer que les connexions sur le trajet de la charge latérale ont un mode de rupture ductile. Ceci s'avère difficile pour les ingénieurs car aucune directive ni recommandation n'est donnée pour déterminer la ductilité de ces connexions. En conséquence, la quantification du niveau de ductilité de ces composantes devient un facteur important dans la conception de ces systèmes.

Bien que les diagonales de type CC soient largement utilisés dans tout le pays, il existe très peu de recherche sur la ductilité de ces systèmes, en particulier dans le cas des diagonales en forme de I avec des connexions boulonnées. L'objectif de cette recherche était donc d'observer le comportement et la ductilité des diagonales en forme de I et de leurs connexions boulonnées sous une charge sismique cyclique inversée. Six spécimens, incluant deux types de connexions boulonnées et deux tailles de section en forme de I, ont été testés. Ces connexions ont été conçues conformément à la norme CSA S16-14. La pénalité de 1,5 de l'article 27.11 n'a pas été incluse. Le protocole de chargement a été développé à partir de données statistiques provenant d'une étude

numérique non linéaire de cinq bâtiments. Les résultats des essais ont montré que les spécimens type CC étaient capables d'atteindre des taux de dérive entre étages de 1% à 2%.

ACKNOWLEDGEMENTS

First and foremost, I would like to express my deepest gratitude to my two supervisors, Professors Colin Rogers and Robert Tremblay. Their expertise, insights, and mentorship were invaluable from the very first planning stages of this project to the final submission of this thesis. I have learnt so much from them and I will carry this knowledge with me through to my future endeavors.

Secondly, I would like to thank all the staff at the Polytechnique de Montréal structures laboratory for welcoming me into their laboratory and helping me along the way through the challenging testing phase of this project. The help and expertise of Martin Leclerc, Patrice Bélanger, Romain Siguier, David Ek, Benoît Marleau, and Xavier Willem allowed for the completion of the tests of six specimens in the months that I had spent at Polytechnique de Montréal. The testing phase would also not have been possible without the helping hands of many students whose hard work helped in the assembly and instrumentation of specimens. For their unwavering dedication to helping me complete my testing phase, endless jokes, and moral support throughout challenges, I would like to thank Charles Prot, Andrés González Ureña, Rosie Gonzales Carranza, Mohamed Afifi, Elizabeth Jolicœur, Keith Lee, Gaston Kasongo, and Maximilien Bernard.

Thirdly, I would like to thank NSERC, FRQNT, and Hydro Québec for providing the funding that allowed me to focus on this research without worrying about personal finances. I would also like to thank DPHV and ADF for their donation of the full-scale steel specimens for the laboratory testing phase of this study. Moreover, I must thank Martin Frappier from DPHV and Vincent Paschini from ADF for their guidance regarding the design, the fabrication, and the assembly of the test specimens.

I would also like to thank my friends and colleagues in the office at McGill. I could always rely on them for insights, second opinions, and a critical eye, but, and perhaps more importantly, I could rely on them for making my stay in graduate school more than just about the research. To Ghalia Baki, Chris Orcutt, David Pizzuto, Rico Massa, Ryan Tack, Nicholas Adomat, Andrea Iachetta, and everyone else: thank you for the memories.

Finally, I would like to thank my friends, family, and Christopher Grey. Thank you for supporting me in many ways throughout my Master's degree. Your belief in me helped me get through any challenges I had faced and achieve the goals that I had set for myself.

TABLE OF CONTENTS

ABSTRACT	i
RÉSUMÉ	iii
ACKNOWLEDGEMENTS	v
TABLE OF CONTENTS	vii
LIST OF FIGURES	xi
LIST OF TABLES	xvi
Chapter 1 : Introduction	1
1.1 Background.....	1
1.2 Research objectives.....	7
1.3 Methodology	7
1.4 Thesis organization.....	8
Chapter 2 : Literature Review	9
2.1 Brace behaviour	9
2.1.1 Effect of global and local slenderness, cross-section shape and brace inclination	9
2.1.2 Expected brace capacity	13
2.1.3 Behaviour of CBF systems	16
2.1.4 CBFs in the CC category	22
2.1.5 Numerical modelling	27
2.2 Bolted connections.....	29
2.2.1 Bolt shear	29
2.2.2 Impact of fillers.....	31

2.2.3 Bolt bearing	33
2.2.4 Tension failure modes: net section, plug shear, block shear, and shear lag.....	36
2.2.5 Effect of flexure in bolted connections	43
2.2.6 Impact of hole-making process	46
2.2.7 Bolted connections at W-shape ends.....	46
2.3 Summary	50
Chapter 3 : Pre-Testing Numerical Modelling	52
3.1 W-shape specimens and end connection design.....	52
3.2 Design of five buildings	56
3.3 Nonlinear modelling.....	59
3.3.1. Preliminary models.....	60
3.3.2. Final model	66
3.4 Displacement demand results from the numerical modelling	71
3.4.1. Design seismic displacement demand of the bearing connection.....	71
3.4.2. Loading protocol development	76
Chapter 4 : Laboratory Testing of Full-scale CC-type Braces.....	83
4.1 Testing program	83
4.1.1. Material properties.....	86
4.1.2. Calculation details	88
4.1.3. Specimen assembly details.....	96
4.1.4. Instrumentation.....	98
4.1.5. Loading protocol in testing.....	105
4.2 Test Results	106
4.2.1. J310-T and J310-C Results	106

4.2.1.1. Test observations.....	106
4.2.1.2. Test versus expected capacities	113
4.2.1.3. Overall brace displacements.....	115
4.2.2. J360-T and J360-C Results	116
4.2.2.1. Test observations.....	116
4.2.2.2. Test versus expected capacities	125
4.2.2.3. Overall brace displacements.....	127
4.2.3. C360-T and C360-C Results.....	128
4.2.3.1. Test observations.....	128
4.2.3.2. Test versus expected capacities	135
4.2.3.3. Overall brace displacements.....	137
4.2.4. Linear elastic slope	138
4.2.5. Bolt slip	139
4.2.6. Effective buckling length	141
4.2.7. Energy dissipation.....	141
4.2.8. Difference between capacities in tension and compression	143
4.2.9 Force distribution between the flanges and the web of the W-shape	144
4.2.10. Ductility.....	146
Chapter 5: Summary and Recommendations.....	154
5.1 Numerical modelling observations	154
5.2 Laboratory testing observations	155
5.3 Recommendations	158
BIBLIOGRAPHY.....	160
APPENDIX A: DETAILED DESIGN CALCULATIONS.....	172

APPENDIX B: SPECIMEN SHOP DRAWINGS..... 194

APPENDIX C: TABLES OF CALCULATED CAPACITIES..... 198

APPENDIX D: SHOP DRAWINGS OF MODIFIED BEARING PLATE SPECIMENS 205

APPENDIX E: FORCE-STRAIN HYSTERESIS OF STRAIN GAUGES IN CONNECTIONS..... 208

LIST OF FIGURES

Figure 1-1 Braced frame configurations	3
Figure 1-2 W-shape brace-to-gusset connections.....	5
Figure 1-3 $2t_g$ linear clearance	6
Figure 2-1 Failure modes in bolted angle brace connection (Wakabayashi et al., 1980)	11
Figure 2-2 Performance of HSS braced frame at -2.55% drift (Clark, 2009).....	18
Figure 2-3 Performance of W-shape braced frame at -2.55% drift (Clark, 2009)	18
Figure 2-4 Effect of load limiting mechanism on force vs. deformation curves: (a) tension and compression - gusset (YGT/BGC), (b) tension - gusset/compression - brace (YGT/BBC), (c) tension - brace/compression - gusset (YBT/BGC) (Walbridge et al., 2005)	21
Figure 2-5 Welded W-shape connection in tests by Richard (2009)	23
Figure 2-6 Force vs. deformation hysteresis of W360x134 brace (Richard, 2009)	24
Figure 2-7 Force vs. deformation hysteresis of W310x97 brace (Richard, 2009)	24
Figure 2-8 Local buckling modes of (a) W360x134 and (b) W310x97 braces (modified from Haddad, 2017)	25
Figure 2-9 Fillers (a) Undeveloped fillers (b) Developed fillers	31
Figure 2-10 Bolts slipping into bearing (Kulak et al., 1987)	33
Figure 2-11 Tension failures.....	36
Figure 2-12 Alternate block shear failure mode.....	39
Figure 2-13 Ratio of design strengths from new and old criteria versus ratio of net to gross shear area (Epstein, 1996a).....	40
Figure 2-14 Specimen connection configurations (Tanaka and Enomoto, 1989)	48
Figure 2-15 Force vs. deformation hystereses of test specimens (Tanaka and Enomoto, 1989)	49
Figure 3-1 Standard bolted W-shape connections (a) jaw plate connection (b) angle connection	54
Figure 3-2 Modified bolted W-shape connections (a) modified jaw plate connection (b) modified angle connection	55
Figure 3-3 Close-up of fuse-type bearing connection (a) bearing plate configuration (b) alternate counter boring configuration	55

Figure 3-4 Plan view, elevations, and simplified model of an example building in the numerical modelling study	56
Figure 3-5 Example of split X braced bay frame (VE_11x9.75).....	59
Figure 3-6 Generalized axial force vs. displacement backbone curve for modeled brace response	60
Figure 3-7 Force-displacement backbone of (a) Slip element, (b) Gap element, (c) Hook element, and (d) expected combined response	62
Figure 3-8 Link composition of example ETABS model	63
Figure 3-9 Link force response histories for (a) Connection and Buckling elements and (b) all elements excluding the Middle Gap and Middle Hook elements.....	65
Figure 3-10 Example force-displacement monotonic test results for the bearing failure mode serving as the basis of numerical models' backbone curves (modified from Castonguay (2010)).....	68
Figure 3-11 Final nonlinear numerical brace model.....	69
Figure 3-12 MC_17x14.5 model with jaw plate connection in ETABS.....	70
Figure 3-13 First storey left link force-displacement hysteresis for the ME_13x11.75 building model.....	74
Figure 3-14 First storey left link force-displacement hysteresis for the VE_11x10.25 building model.....	74
Figure 3-15 Third storey left link force-displacement hysteresis for the ME_13x11.75 building model.....	75
Figure 3-16 Third storey left link force-displacement hysteresis for the VC_13x11.75 building model.....	75
Figure 3-17 Loading protocols tested: (a) MRF (b) EBF (c) CBF (modified from Chen and Hu, 2016).....	77
Figure 3-18 Loading protocol developed from numerical data.....	82
Figure 4-1 Diagram and photo of brace specimen assembly in the 12 MN press.....	85
Figure 4-2 Brace length and buckling length (dimensions in mm)	85
Figure 4-3 Drawings of brace specimens' end connections within testing grips	86

Figure 4-4 Definition of web area	88
Figure 4-5 Hole edges of (a) punched holes in web plate (b) drilled holes in W-shape (c) punched holes in angle.....	91
Figure 4-6 Modified shim plates (left) and shim plates in assembled connection (right).....	97
Figure 4-7 Instrumented specimens (a) Strain gauges on W-shape flanges, (b) strain gauges on W-shape web and web plate, (c) linear pots on top connection, and (d) overall set-up ...	99
Figure 4-8 String pot and linear pot locations	101
Figure 4-9 Locations of strain gauges in connecting plates (dimensions in mm).....	102
Figure 4-10 Locations of strain gauges on W-shape sections.....	102
Figure 4-11 Speckle pattern on specimen J360-T.....	103
Figure 4-12 DIC camera set-up	104
Figure 4-13 DIC control setup showing views (on monitors) of the three camera angles.....	104
Figure 4-14 Loading protocol for specimen J310-T	105
Figure 4-15 Loading protocol for remaining five specimens	106
Figure 4-16 Force-displacement hystereses of (a) J310-T and (b) J310-C.....	108
Figure 4-17 Images captured of the bottom connection of specimen J310-T taken at selected load peaks and valleys.....	109
Figure 4-18 Buckling in specimens J310-T and J310-C (a) overall buckling in J310-T and (b) overall and local buckling in J310-C.....	110
Figure 4-19 Post-test photos of bottom connection of specimen J310-T (a) North flange, (b) close-up of North flange, and (c) W-shape web and gusset plate with web plates removed	111
Figure 4-20 Post-test photos of specimen J310-C (a) bottom connection, (b) close-up of North flange, and (c) W-shape web and gusset plate with web plates removed from top connection.....	111
Figure 4-21 Bolts from J310-C (a) bottom flange connection (b) top flange connection (sheared)	112
Figure 4-22 Deformed W-shape webs of J310-C on the left and J310-T on the right: (a) bottoms of W-shapes (b) tops of W-shapes	112

Figure 4-23 Local buckling in middle of W-shape of specimen J310-C.....	112
Figure 4-24 Out-of-plane displacements at midpoint of the brace for (a) J310-T and (b) J310-C	116
Figure 4-25 Force-displacement hystereses of (a) J360-T and (b) J360-C.....	118
Figure 4-26 Images captured of the bottom connection of specimen J360-C taken at selected load peaks and valleys.....	119
Figure 4-27 Bending of gusset plate in specimen J360-C	119
Figure 4-28 North jaw plate fracture in specimen J360-T (a) initial bending of plate, (b) complete fracture of plate, and (c) bottom fractured edge	120
Figure 4-29 Rotation at the top of the assembly at the end of the test for specimen J360-T...	121
Figure 4-30 Bottom connections of specimens (a) J360-T and (b) J360-C at the end of the tests	121
Figure 4-31 Locally buckled flanges and torn web in specimen J360-C	123
Figure 4-32 Torn gussets at the end of the welded jaw plates	123
Figure 4-33 W-shape webs in the bottom connections of (a) J360-T and (b) J360-C	124
Figure 4-34 Photos of deformed web plates	125
Figure 4-35 Out-of-plane displacements at the brace midpoint for (a) J360-T and (b) J360-C..	128
Figure 4-36 Force-displacement hystereses of (a) C360-T and (b) C360-C	130
Figure 4-37 Images captured of the bottom connection of specimen C360-C taken at selected load peaks and valleys.....	131
Figure 4-38 Set-up for specimens with claw angle connections (a) East of bottom connection, (b) North of bottom connection, (c) top connection, (d) overall brace assembly	131
Figure 4-39 Buckled W-shape flange in specimen C360-T.....	132
Figure 4-40 Global and local buckling of the W-shape brace of specimen C360-C.....	133
Figure 4-41 Block shear failure in angles of specimens: (a) C360-C and (b) C360-T	134
Figure 4-42 Block shear in the W-shape webs for specimens: (a) C360-T and (b) C360-C	134
Figure 4-43 Deformed W-shape web of top connection in specimen J360-T	135
Figure 4-44 Post-test bent bottom gusset plate from specimen C360-T.....	135
Figure 4-45 Block shear through net shear area in angle.....	136

Figure 4-46 Out-of-plane displacements at the brace midpoint for (a) C360-T and (b) C360-C	138
Figure 4-47 Dissipated energy of brace test specimens	142
Figure 4-48 Strains in the J310-T W-shape during the slow tension excursion at (a) 25 mm from the uppermost edge of the connection and (b) 305 mm above the uppermost edge of the connection	146
Figure 4-49 Deformation beyond the edge of the bottom gusset plate of specimen C360-C...	152
Figure 4-50 Block shear deformations in the bottom W-shape web of specimen J360-T	153

LIST OF TABLES

Table 2-1 Coefficients for post-buckling strength equation (Tremblay, 2002)	15
Table 3-1 Gravitational loads used in the gravity frame design of buildings in the numerical study	57
Table 3-2 Load combinations (from NBCC 2015, Table 4.1.3.1.2.-A) used for design of buildings in the numerical study.....	57
Table 3-3 Summary of seismic design for building models	58
Table 3-4 Summary of brace section sizes per floor.....	59
Table 3-5 Force-displacement definition in compression	66
Table 3-6 Force-displacement definition points for tensile failure modes	69
Table 3-7 Displacement demand data for W360x134 (mm)	73
Table 3-8 Displacement demand data for W310x97 (mm)	73
Table 3-9 Loading protocol parameters (modified from Chen and Hu, 2016)	77
Table 3-10 Statistical analysis results of displacement response histories	79
Table 3-11 Statistic analysis results of four-storey displacement response histories (from Bara, 2007).....	79
Table 3-12 Amplitudes and number of cycles in the developed loading protocol.....	81
Table 3-13 Elastic load amplitudes used in loading protocol	82
Table 4-1 Testing parameters of the full-scale specimens	84
Table 4-2 Average material properties measured from coupon tests	87
Table 4-3 Design load components for W-shape flanges and web	88
Table 4-4 Summary of design parameters.....	89
Table 4-5 Design and expected failure mode capacities based on CSA S16-14	92
Table 4-6 Design and expected failure mode capacities based on AISC 360-16	93
Table 4-7 Design and expected resistances of the specimens using CSA S16-14.....	94
Table 4-8 Design and expected resistances of the specimens using AISC 360-16	94
Table 4-9 Initial measured lengths of string potentiometers.....	100
Table 4-10 Observations for specimens J310-T and J310-C	107
Table 4-11 Comparison of predicted capacities to test results for J310-T and J310-C	114

Table 4-12 Observations for specimens J360-T and J360-C	117
Table 4-13 Comparison of predicted capacities to test results for J360-T and J360-C	126
Table 4-14 Observations for specimens C360-T and C360-C.....	129
Table 4-15 Comparison of predicted capacities to test results for C360-T and C360-C.....	137
Table 4-16 Calculated and experimental elastic stiffness	139
Table 4-17 Predicted slip resistances compared to estimated slip resistances from tests.....	140
Table 4-18 Total dissipated energy of brace test specimens	142
Table 4-19 Factored and probable capacities of W310x97 and W360x134 braces	143
Table 4-20 Measured capacities in tension and compression	144
Table 4-21 Average and minimum normalized strain values of W-shape strain gauges	145
Table 4-22 Elongations in tension at P_y , P_u , $0.8P_u$, and $0.5P_u$	148
Table 4-23 Calculated specimen ductility	149
Table 4-24 Average and maximum measured bolt deformations.....	150
Table 4-25 Measured bolthole elongations.....	151
Table 4-26 Measured deformations beyond the original edge of the steel.....	153

Chapter 1: Introduction

1.1 Background

Seismic events trigger ground accelerations that cause lateral forces to develop in buildings and other structures. These lateral forces are carried by a Seismic Force Resisting System (SFRS). In North American steel construction, there are three common types of SFRSs, characterised by their energy dissipating element: moment resisting frames (MRFs), braced frames, and plate walls. Braced frames can further be divided into concentrically braced frames (CBFs), eccentrically braced frames (EBFs), and buckling restrained braced frames (BRBFs).

Seismic events of magnitudes that cause severe and irreparable damage to structures are relatively rare. Due to the unlikelihood of such earthquakes (magnitudes six and greater on the Modified Mercalli intensity scale) and the challenge in determining the precise magnitude of loading, SFRSs are designed to take advantage of the ductility within the system to dissipate energy inelastically and reduce the risk of the collapse of the building. The National Building Code of Canada (NBCC) requires buildings to be designed for ground accelerations determined based on a 2% probability of exceedance in 50 years (NRCC, 2015). However, the lateral forces produced by these ground accelerations may be reduced by factors R_d and R_o to account for the ductility and the overstrength, respectively, available in the SFRS (Mitchell et al., 2003). The total lateral force to be resisted by the SFRS, or base shear, could therefore be calculated as per Eq. 1-1 using the Equivalent Static Force Procedure (ESFP) with certain maximum and minimum constraints based on the chosen SFRS:

$$V = \frac{S(T_a)M_v I_E W}{R_d R_o} \quad (1-1)$$

$S(T_a)$ is the design spectral acceleration value calculated for the first period of the structure, M_v is a factor that accounts for higher mode effects, I_E is the earthquake importance factor, and W is the seismic weight of the structure. The loads are distributed among the braced bays and storeys. Overturning and torsional effects are also taken into account.

In some cases, such as in high seismic hazard regions or for irregular buildings, use of the ESFP is not permitted. In these cases, the numerical modelling of the building's response to ground

motions must follow the Dynamic Analysis Procedure to obtain the lateral earthquake loads. The Dynamic Analysis Procedure can also be used for regular structures or for low seismic regions to reduce the lateral force calculated with the ESFP by a maximum of 20%.

Depending on the type and the detailing of the SFRS, different R_d and R_o values are prescribed by the NBCC. A ductile system will have the most stringent detailing requirements, but will be designed to carry lower forces. Moderate and limited ductility (MD and LD) systems will have less detailing requirements but will be designed to carry somewhat larger forces. Furthermore, these SFRSs are designed based on capacity design principles. This means that the dissipating element is designed to resist the reduced seismic force, while the other elements of the SFRS must be designed to allow this member to attain its full ductility. That is, the energy-dissipating element is the weakest point in the SFRS. Using this design method, the energy-dissipating element is allowed to yield before the other elements, such as the connections, diaphragm, or the adjoining frame members.

In Canada, another category of SFRSs exists called conventional construction (CC). Conventional construction SFRSs have very few detailing requirements, and capacity design principles need not be followed. Due to the lack of detailing, CC SFRSs are designed with lower R_d and R_o factors (1.5 and 1.3, respectively), therefore higher seismic forces. For this reason, more severe height limitations exist for CC SFRSs. Additionally, the ductility factor, R_d , may only be used to limit the seismic forces in elements of the SFRS other than the brace if the connections are designed to be ductile, because they are not protected by the capacity design principle. Otherwise, a penalty factor is applied which eliminates the effect of R_d on the seismic forces for the design of the structural elements adjacent to the brace (while the brace itself can still be selected and designed for the seismic forces reduced by R_d). Furthermore, this category of SFRS cannot be used for buildings of high and post-disaster importance categories. Nonetheless, the CC category is commonly chosen by engineers due to the ease of meeting the detailing requirements, the savings in terms of engineering hours required for design, and the smaller connections that are not capacity protected.

The focus of this research project will be concentrically braced frames in the conventional construction category. The use of CBFs gained popularity when inspections of structures after the 1994 earthquake in Northridge, California and the 1995 earthquake in Kobe, Japan revealed some concerns with the welded moment-resisting connections used in MRFs (e.g. Tremblay et al., 1995; Tremblay et al., 1996; Nakashima et al., 2000). In addition, CBFs are selected for their economic benefit, for ease of construction, and for their increased elastic stiffness as compared to a MRF. As previously mentioned, CC-type CBFs are often selected because the ductility detailing requirements for these SFRSs are less stringent. Most research to-date has been focused on the more ductile CBF systems, i.e. type LD and MD, where the connections are considered to be protected components in the lateral load path. In CC-type braces, the behaviour of the connection becomes of greater concern because they are not designed following capacity design principles; that is, they may enter into the inelastic range during a seismic event. As such, the overall ductility of the type CC SFRS may be dependent on the force versus deformation characteristics of a brace's connections, or other components of the lateral force resisting system.

In design, CBFs are treated as vertical trusses carrying axial loads to the foundations. Braces are built into the structure as diagonal members to resist the lateral loads. These can be arranged in a variety of configurations. Some of the most common configurations are shown in Figure 1-1. In the past, braces have been designed to carry either tension and compression or only tension. Different structural sections have been used as the bracing members in CBFs. Examples of such sections include angles, rods (in tension-only bracing), C-shapes, tees, rectangular or circular Hollow Structural Shapes (HSS), and W-shapes. The section of the brace will affect the force versus deformation hysteretic behaviour of the braced frame system (Tremblay et al., 2008).

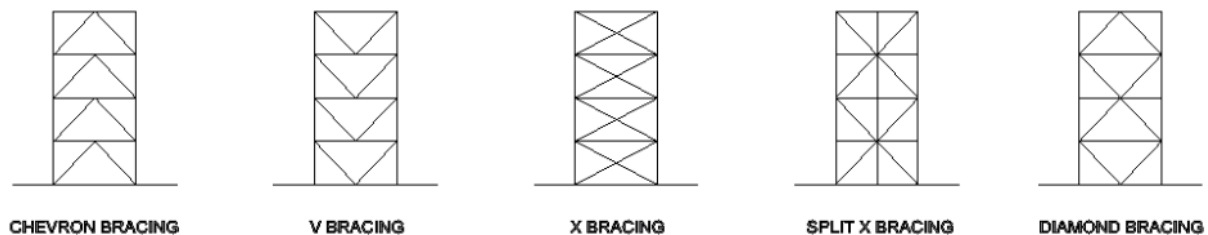


Figure 1-1 Braced frame configurations

In multiple testing programs, W-shape braces were found to have greater deformation ductility than HSS braces (Gugerli and Goel, 1980; Tremblay et al., 2008; Fell, 2008; Richard 2009; Tsai et al., 2010; Roeder et al., 2011a). Local buckling in W-shape and pipe braces was more gradual than in square HSS braces, thereby decreasing stress and strain concentrations at the locally buckled hinge point and decreasing the fracture potential (Fell, 2008). For this reason, the investigation of the cyclic behaviour of such sections and their CBFs becomes of interest for seismic application. However, HSS shapes have been found to show less degradation of compressive resistance in the post-buckling range (Lee and Bruneau, 2005). While many experimental studies have been conducted on HSS braces, comparatively few have been conducted on W-shape braces. Even fewer tests have been conducted for bolted W-shape braces under cyclic loading. This study therefore aims to expand the available data on this type of brace and its connections when designed for the CC category of SFRS.

In Clause 27.11 of the CSA S16-14 Standard (CSA, 2014), guidance is provided to the structural engineer on how to design CC CBFs. For the conventional construction category, the ductility factor, R_d , is given as 1.5 and the overstrength factor, R_o , is given as 1.3. Conventional construction CBFs are also subject to a 15 m height limit. This limit may be disregarded if the structure is not an assembly occupancy building and meets additional requirements as described in Clause 11.27.3 (CSA S16, 2014). No limitations on local or global brace slenderness are provided. While capacity design principles do not dictate the design of CC brace connections, the connections must be designed such that the expected failure mode is ductile if no penalty is to be applied on the design loads. For bolted brace connections, the Commentary to the CSA S16-14 Standard, which is found in the Canadian Institute of Steel Construction (CISC) Handbook of Steel Construction (CISC, 2016) recommends relying on plate yielding or bolt bearing as the connection failure mode. In lieu of designing for a ductile failure mode, the engineer can opt to design the connection for the gravity loads plus the seismic loads multiplied by an R_d of 1.5 up to the expected yield strength of the brace calculated using $R_y F_y$. As a 50% increase of the seismic load is significant, it is desirable for the engineer to know whether the connection has sufficient ductility for the expected seismic loading. Some examples of typical W-shape brace-to-gusset

connection designs used commonly in the industry, which were provided by the industry partner of this research program, are shown in Figure 1-2.

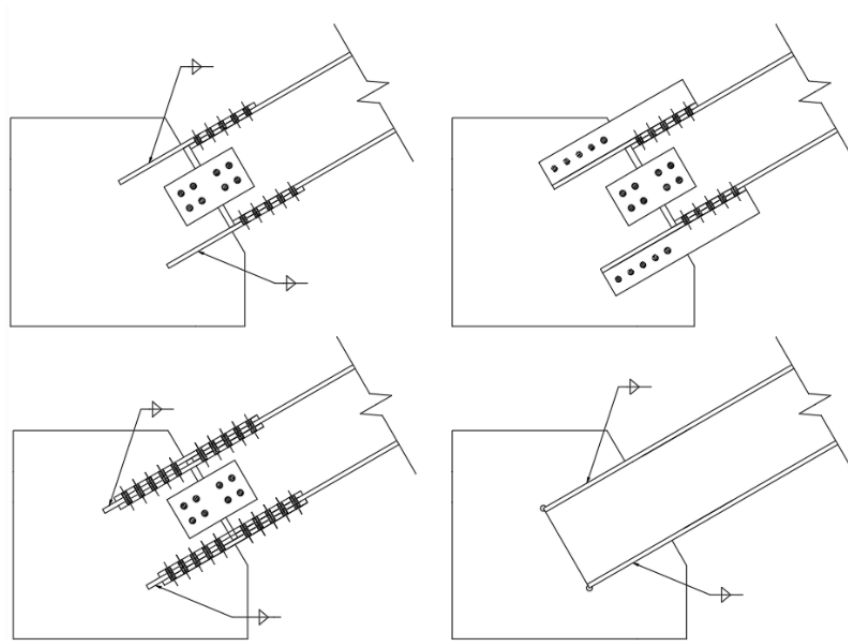


Figure 1-2 W-shape brace-to-gusset connections

Additionally, for the MD and LD categories of SFRSs, the gusset plates at the brace end connections are commonly designed with a clearance distance in the gusset plate equivalent to two times the gusset plate thickness ($2t_g$), as shown in Figure 1-3. This clearance distance allows for the creation of a hinge in the gusset plate to facilitate rotation at the connection during global buckling of the brace. For the CC category of braces, however, this is not a requirement. Some studies note a disadvantage of the $2t_g$ linear gusset plate clearance as being a loss in ductility due to the use of thicker gusset plates (for example: Lehman et al., 2008; Yoo and al., 2008). In general, the braces fractured earlier than the gussets.

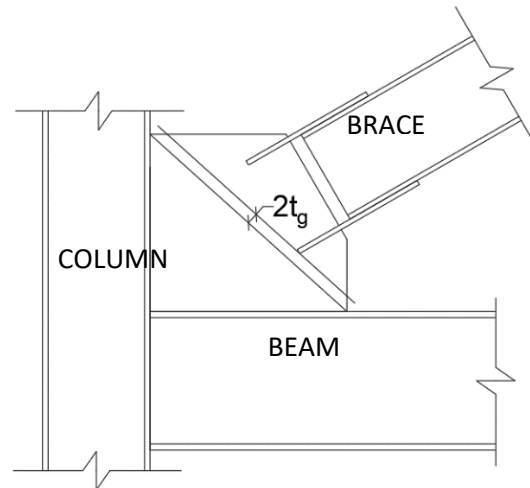


Figure 1-3 $2t_g$ linear clearance

In the AISC 341-16 Standard (2016), there are three types of concentrically braced frames: braced frames ($R = 3$ systems), Ordinary Concentrically Braced Frames (OCBFs), and Special Concentrically Braced Frames (SCBFs). SCBFs are expected to dissipate energy through the yielding and the buckling of the brace. Therefore, these systems use the principles of capacity based design to protect the connections from becoming damaged. The design of these systems has multiple requirements, much like the ductile systems in CSA S16-14. The OCBFs have less stringent design requirements than SCBFs. For buildings that do not use a seismic isolating system, the OCBFs are required to meet the width-to-thickness ratios of the moderate ductility category. That is, the width-to-thickness ratio of the flanges of W-shapes must not exceed $0.38\sqrt{E/F_y}$ and the height-to-thickness ratio of the web of W-shapes must not exceed $1.49\sqrt{E/F_y}$. Chevron and V bracing configurations must not exceed a global slenderness, KL/r , of $4\sqrt{E/F_y}$ and certain constraints are placed on the axial strength. The connections of OCBFs must be designed to withstand load effect based on the amplified seismic load, but do not need to be designed to resist a load exceeding the expected tensile and compressive resistances of the brace. The $R = 3$ systems are the most similar to CC-type CBFs. In design, these systems are not subject to the Seismic Provisions and, therefore, are not expected to achieve high ductility levels. These types of CBFs are therefore restricted to seismic category C or below.

1.2 Research objectives

As there is very little data available on CC-type braces and specifically their connections, the main objective of this research is to determine the ductility and behaviour of common bolted connections of W-shaped braces through physical testing of full-scale specimens under reversed cyclic loading. These results could then be used to help practicing engineers design conventional construction type bracing systems. All objectives are listed as follows:

- Observe the behaviours of the various specimens under reversed cyclic loading;
- Provide laboratory test data for bolted W-shape braces under reversed cyclic loading;
- Compare performance of different W-shape section sizes and two common bolted connections;
- Verify how capacity predictions of specimens' ultimate strengths with expected material properties and unfactored equations from both the CSA S16-14 and the AISC 360-16 standards compare to test results;
- Verify whether the direction of the first loading excursion has a significant effect on the behaviour and performance of W-shape braces with bolted end connections.

1.3 Methodology

The aforementioned objectives of this study were achieved through the following steps:

- A literature review on the topic of braces, and in particular W-shape braces, as well as bolted connections and their failure modes was conducted.
- Two sizes of W-shapes were selected.
- Five symmetric, regular, four-storey buildings were then designed to include these W-shapes as part of their SFRSs.
- Numerical analysis of the buildings were run in software available and computationally economical for practicing engineers to determine:
 1. Appropriate loading protocols for the laboratory testing
 2. Ductility demand on the connections under seismic loading

- The laboratory testing portion of this study included six full size brace specimens whose connection design was based on two common bolted W-shape connections found in the industry.
- The force vs. deformation hysteresees of the specimens were evaluated and compared.
- The ductility of each of the specimens was compared to the required ductility as determined by the numerical analysis.

1.4 Thesis organization

This thesis is divided into the following chapters. Chapter 2 includes a literature review on the topics of braces and bolted connections. The literature review focuses on tests conducted on W-shape braces. Tests on braces alone and CBF systems are included. The literature review on bolted connections includes the various failure modes encountered in tension and compression, as well as the effects of flexure. Chapter 3 contains the numerical phase of the project. The building design, non-linear modelling, and numerical results are discussed. Chapter 4 comprises the laboratory testing phase of this study. The design of the connections is presented for the different configurations, as well as the testing procedure and loading protocols. The resulting brace and connection behaviours are then presented for each of the different connection types. Finally, Chapter 5 includes the summary of the observations and recommendations resulting from this study.

Chapter 2: Literature Review

Braces resist common and recurring lateral forces (service level loads), such as wind loading, through linear elastic axial deformations. In the case of much larger lateral forces, such as rare earthquakes, braces enter the inelastic range and exhibit yielding of the steel in tension and buckling of the brace in compression. However, once buckling occurs, the compressive resistance of the brace decreases gradually with additional cycles. In seismic design, it is therefore necessary to understand how the various parameters of brace selection affect inelastic behaviour under reversed cyclic loading. In CC-type CBFs, the behaviour of the connection is equally important. For this reason, a literature review on the topics of brace behaviour and bolted connections is presented in this chapter.

2.1 Brace behaviour

Due to the popularity of CBFs, many laboratory and numerical studies were conducted to improve our knowledge of braces and braced frame systems. Lignos et al. (2012) have developed a database including 295 brace experiments, which can be used for the calibration of numerical models and for design purposes. Of these tests, fifty were conducted on W-shape braces, five of which were made of ASTM A992 steel. On average in W-shapes, overall buckling occurred at a 0.28% drift ratio, local buckling occurred at a 0.87% drift ratio, and brace fracture occurred at a 3.10% drift ratio. W-shapes achieved the greatest drift ratios prior to brace fracture (Karamanci, 2013). The studies in the database that included tests on W-shapes, as well as other studies found in the literature, will be discussed in the following sections.

2.1.1 Effect of global and local slenderness, cross-section shape and brace inclination

In the inelastic force versus deformation hysteretic behaviour of a typical brace, there are four major occurrences leading up to failure: global buckling, brace yielding, local buckling, and fracture initiation.

Fell (2008) determined that global buckling occurred at a 0.3% drift ratio for most specimens of varying slenderness and cross-sections. This result was slightly lower (0.2%) for slender W-shape braces and slightly higher (0.4%) for grout-filled HSS.

After global buckling, the brace enters the post-buckling range, where there is typically a degradation of the compressive resistance with successive cycles. Lee and Bruneau (2005) investigated brace behaviour in the post-buckling range. The global slenderness of the brace, KL/r , and the section shape will influence the level of degradation in the post-buckling range. The compression resistance can reduce to 20% of its original strength for braces with slenderness over 80 at displacement levels greater than five times the theoretical buckling displacement calculated as in Eq. 2-1.

$$\delta_b = \frac{C_r L}{EA} \quad (2-1)$$

Among other cross-sections, W-shapes have the most severe degradation of post-buckling compression strength (Lee and Bruneau, 2005).

After global buckling, a plastic hinge forms near the centre of the brace. The drift-level at the onset of plastic local buckling (between 2% and 5%) is more variable between braces, showing a greater dependence on brace shape and slenderness variables (Fell, 2008). Local width-to-thickness ratios of the cross-section's elements have the greatest influence on local buckling (Karamanci, 2013) depending on the loading protocol (Lignos and Karamanci, 2013). Brace fracture follows soon after at a drift level between 2% and 8% (Fell, 2008).

This inelastic behaviour can only be achieved if the connection has enough strength to carry the brace forces at yielding and overall buckling, and can allow the required rotation to form a hinge in the brace. The following test programs were conducted to observe the effects of varying global and local slenderness and cross-section shapes of braces on their inelastic behaviour.

W-shaped braces in CBFs were tested in Japan by Wakabayashi et al. (1977). These specimens were made with welded SS 41-grade steel plates. In total, 24 braced frames were tested. Slenderness ratios ranged from 40 to 120 for singular braces and from 22 to 84 for double-brace configurations. The energy dissipation of a braced frame decreased with successive cycles regardless of the slenderness of the brace. Local buckling was not found to have a significant effect on the force versus deformation hysteresis curve; however, its occurrence was closely followed by crack initiation and loss of carrying capacity. It was also found that some braces with small global slenderness ratios initially buckled about the major axis. With continued cyclical

loading however, these braces buckled about the minor axis. In the second part of the study, flat bars, round bars, and angles were tested (Wakabayashi et al., 1980). This was one of few papers, which included a bolted brace connection tested under cyclic loading. The only observation made regarding the performance of the bolted connection of the angles to the gusset plate was that cracking appeared around the boltholes or at the edge of the net section. The failures observed by Wakabayashi et al. are shown in Figure 2-1.

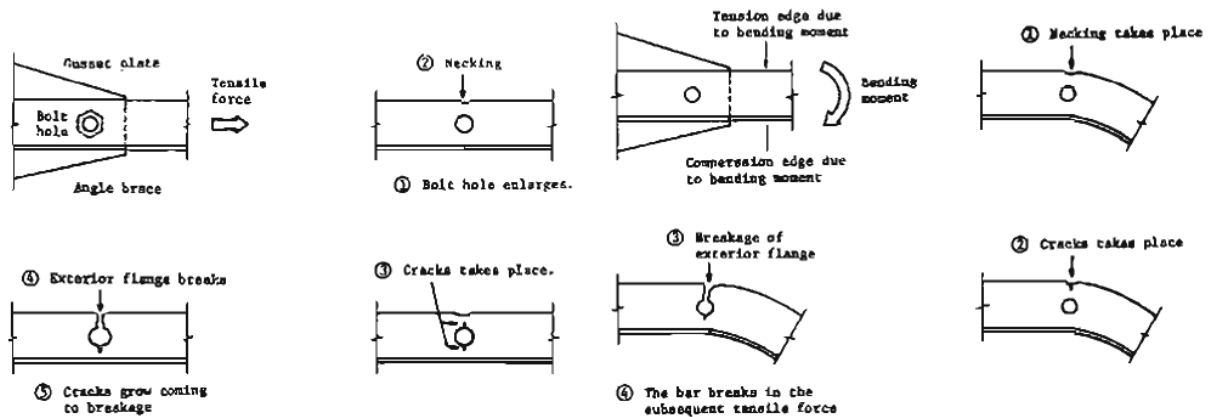


Figure 2-1 Failure modes in bolted angle brace connection (Wakabayashi et al., 1980)

Cross section types including W-shapes (A36 steel), tees, HSS shapes and single and double angles with varying slenderness ratios were later tested by Black et al. (1980). Global slenderness ratios varied between 40, 80 and 120. Due to brace length elongation, members which were first loaded in tension attained a lower initial buckling load on the subsequent compression loading cycle than those that were first loaded in compression. Smaller global slenderness ratios resulted in better energy dissipation. Furthermore, members with increased global slenderness showed a greater difference between tensile and compressive resistances because the braces with greater slenderness are expected to buckle at lower loads. The magnitude of this difference increased with successive cycles of loading. Black et al. concluded that the global slenderness ratio of a brace was the most important factor in determining its behaviour under reversed cyclic loading (1980). The effective length factor, K , of a brace provided a certain set of boundary conditions (fixed-pinned and pinned-pinned boundary conditions) was found to be the same for elastic and inelastic buckling of the members. Overall, the compressive capacity of all members decreased with the progression of the loading cycles. Black et al. suggested that the reasons for this effect

were: (1) a decrease in capacity due to the Bauschinger effect and (2) a decrease in capacity due to residual curvature as a result of each cycle of loading under inelastic behaviour. For the prediction of the reduction in compressive strength, Black et al. proposed the use of two reduction factors: R_B to account for the Bauschinger effect and R_E to account for the residual curvature.

Three British Universal Columns (UC shapes), which are wide-flange members, were tested by Leowardi and Walpole (1996). One section, 150 UC 30.0, was selected because it was deemed most representative of all UC sections based on parameters of flange width, flange thickness, web width, and web thickness, while having a capacity below that of the testing equipment. Global slenderness was varied by varying the lengths of the specimens 1 and 2 or by varying the end constraints of specimen 3 (from pinned-pinned to fixed-fixed) to achieve slenderness ratios of 40, 60, and 80. The end connections were welded to end plates using 50 mm fillet welds. The specimens were then subjected to reversed cyclic loading. It was found that the specimen with the lowest slenderness ratio produced wider force versus axial displacement hysteresis loops, while the specimens with larger slenderness ratios exhibited more pinching. The plastic moment capacity is therefore attained at a lower load for specimens with a higher global slenderness ratio. It was also found that in the post-elastic buckling cycles, buckling loads decreased more uniformly with each subsequent cycle when the global slenderness was lower. However, an increase in slenderness delayed the local buckling of the member. Consequently, the specimen with the highest slenderness experienced the greatest amount of cycles before fracture.

In a numerical study by Tremblay (2000), the effect of brace slenderness on seismic performance was compared for buildings of one, two, four, six, and eight storeys. It was found that a non-dimensional slenderness parameter, λ , of up to 2.65 could be permitted for both tension-compression and tension-only braces (with a height limit imposed on the tension-only braced buildings to avoid instability). However, for tension-compression braces, the inelastic demand and peak bending moment in braced frame columns increased for braces with lower global slenderness. The study confirmed that stockier braces dissipated more energy as compared to more slender braces but impose greater loading on adjacent frame members.

Fell et al. (2009) studied HSS, pipe and W-shape braces with varying cross section geometry, global slenderness, and element width-to-thickness ratios. The loading protocol took one of three forms: symmetrical seismic loading, tension cyclic loading, or compression cyclic loading. The authors found that the width-to-thickness ratios had the greatest effect on brace behaviour. The greater the width-to-thickness ratio, the more prone the member is to local buckling and thus the poorer the response to load. The plastic local buckling effects were more pertinent in the HSS member as the buckled shapes of the pipe and W-shape had more gradual deformations causing lower strains in the locally buckled area. The behaviour of HSS braces was improved when filled with mortar. However, Fell et al. suggested that the benefits of this construction method should be further investigated to verify if this advantage outweighs the increased cost and effort in fabrication. Increased local slenderness ratios seemed to decrease the strains in the locally buckled areas as well. The normalized amount of energy dissipated by each brace were also compared. W-shape braces dissipated the most energy.

Further tests were performed on built-up W-shapes to investigate the effect of width-to-thickness ratios (Ballio and Castiglioni, 1994). Two types of loading protocols were used: (1) a symmetric, constant amplitude loading protocol with the amplitude varied between tests, and (2) a random amplitude loading protocol. The specimens with greater width-to-thickness ratios exhibited less strain hardening and had greater and earlier degradation of strength, stiffness and energy dissipation. However, braces with the lower width-to-thickness ratios displayed more brittle failure modes such as tearing at the gusset plate welds.

The inclination of the brace member did not have a large impact on the force versus deformation hysteretic performance of a brace as seen in the performance of axial members tested in the horizontal or vertical directions (Gugerli and Goel, 1980).

2.1.2 Expected brace capacity

In design, the engineer must estimate the probable inelastic compression and tension capacities, C_u and T_u , of the brace. In MD and LD CBFs, these probable resistances are needed for the completion of a capacity based design. In CC braced frames, these values can be calculated to determine whether the brace properties or the connection properties will govern the ultimate

behaviour. In the CSA S16-14 Standard (2014), the probable yield strength is calculated as the probable yield stress multiplied by the area of the brace. The probable yield stress is calculated by multiplying the nominal yield stress of the steel grade by a factor, R_y . For W-shapes, R_y is 1.1. However, the expected yield stress of a W-shape section cannot be below 385 MPa according to the CSA S16-14 Standard provisions. A study by Fell and Kanvinde (2010) showed that this methodology of calculating the expected tension forces in the connections underestimated measured forces by 9%-11% on average across the specimens that were tested. In this study, 17 2:3 scale HSS, pipe, and W-shape braces were tested under cyclic loading (both near-fault and far-field loading protocols). Fell and Kanvinde concluded that the calculated estimates did not account for the strain hardening of the braces, which depends on the material and fabrication processes of the braces. They therefore suggested a different calculation method that provided more accurate predictions of the forces. In the proposed method, the average of the yield stress and the ultimate stress of the brace member is used. Fell and Kanvinde proposed using the measured values of yield stress and ultimate stress, when possible, or otherwise multiplying the nominal values by R_y and R_t , respectively.

In a review of tests on braces, the ratio of the maximum tensile force in hot-rolled structural steel braces to their $F_y A_g$ varied between 1.01 and 1.13 with a calculated average of 1.05 and a 0.04 COV (Tremblay, 2002). According to this data, the use of an R_y value of 1.1 as prescribed by CSA S16-14 would capture the maximum tensile strength of the majority of the specimens. It should be noted however, that the tests covered in this review spanned a significant period in time and included braces made of a variety of steel grades.

In elastic compression, the design buckling strength of a brace is calculated as shown in Eq. 2-2 in accordance with the CSA S16-14 Standard where ϕ is 0.9, A is the cross-sectional area of the brace, F_y is the yield strength of the brace, n is a parameter that accounts for the effect of residual stresses and out-of-straightness, and λ is the non-dimensional global slenderness.

$$C_r = \phi A F_y (1 + \lambda^{2n})^{-1/n} \quad (2-2)$$

In comparing the measured ultimate strength in compression of 76 brace members to those calculated using the using both Canadian and US design curves, the design predictions were lower

than the measured values (Tremblay, 2002). The average ratio of predicted values to measured values was 1.16 with a COV of 0.17. Thus, an equation, as shown in Eq. 2-3, to predict the expected ultimate buckling capacity of a brace, C_u , was developed. The lesser value between $R_y F_y A_g$ and $1.2C_r/\phi$ equation corresponds well to these findings.

$$C_u = \text{minimum}(R_y F_y A_g, 1.2C_r/\phi) \quad (2-3)$$

For seismic design, a prediction of the post-buckling strength of the brace, C_u' , is also required. In the CSA S16-14 Standard, C_u' is calculated as $0.2A_g F_y$. This simplified equation aims to be conservative for design purposes. However, it was found that this equation does not correspond well to experimental data (Tremblay, 2002). After reviewing the post-buckling strengths of 76 tested brace members and conducting a regression analysis, Tremblay (2002) suggested that Eq. 2-4 be used to calculate the post-buckling compression strength based on the required ductility of the brace, where coefficients a , b , and c depend on the desired ductility. The suggested coefficients are shown in Table 2-1. However, this method has yet to be included in CSA S16-14.

$$C_u' = A_g F_y (a + b\lambda^{-c}) \leq C_u \quad (2-4)$$

Table 2-1 Coefficients for post-buckling strength equation (Tremblay, 2002)

Ductility	A	B	C
2	0.058	0.23	1.40
3	0.084	0.12	1.61
5	0.095	0.046	2.22

The tensile resistance of a steel brace is typically greater than the compressive resistance due to buckling of the brace in compression. As a result, the selection of a brace for seismic design is often based on its compression resistance (C_r). In MD and LD CBFs, this presents a problem for the connection design, which according to capacity design principles, must resist the greatest anticipated force based on the probable resistance of the brace. A large difference in the compression and tension resistances of the member implies that the connections must be designed for much greater forces than the braces themselves. Two different methods exist to decrease the difference between the tensile and compressive resistances. The first is by using

buckling restrained braces; compressive resistance is increased because overall buckling is restrained. A second method, which can be used for W-shapes and other shapes, relies on the introduction of a fuse to reduce the tensile capacity. For example, the net tension area of the brace is reduced at a specific position along the member, without affecting the brace's compression resistance; this is achieved by means of additional reinforcement details at the fuse. Such fuses have been studied and modelled in previous research and have shown good results (Egloff et al., 2012; Egloff, 2013).

2.1.3 Behaviour of CBF systems

In buildings, braces do not act in isolation. Therefore, brace behaviour on its own cannot determine the performance of a building under seismic loading. The lateral resistance of a building is also affected by the performance of the brace member's connections including its gusset plate design, and by the adjacent members in the braced frame (columns, beams, anchors to the foundation, etc.). Multiple researchers have investigated the system effect of the braced frames and the connections. Some of these studies are discussed in this section.

Powell (2010) ran tests on single diagonally braced frames to determine braced frame system behaviour; including the column, beam, shear connections, gusset plate, brace connection and brace element. The braced frame gusset plate connections were designed using the balanced approach, which aims to force yielding in multiple elements in a predefined order before the ultimate fracture of the brace to enhance the ductility of the system (Roeder et al., 2005; Lehman et al., 2008). As part of this approach, an elliptical clearance is provided at the end of the brace, as opposed to the $2t_g$ linear clearance usually used in design. This method encourages the brace member to yield first, followed by the yielding of the gusset plate, while discouraging more sudden failure modes such as net section fracture of the brace, weld fracture in the connection, and block shear and buckling of the gusset plate (Roeder et al., 2011b). This approach has a similar effect to capacity design but additionally ranks failure modes from most favourable to least favorable, while effectively protecting the connection. Out of nine specimens, one of the studied specimens was a wide flange of size W150x37, which was selected to have a similar tension capacity to the HSS shapes that were tested. The wide flange showed the largest drift

ratio range of 5.56% (3.21% in compression and 2.35% in tension). It was the only specimen whose fracture did not occur within the brace. This specimen fractured at the weld interface (in the brace to beam and column connection) after completing 41 cycles. Therefore, the welded connection had the lowest ultimate capacity and could not resist the large rotational demand. This failure had occurred prior to local buckling of the brace.

This was also the case in a three-storey chevron braced frame with wide flange members tested in Taiwan, where the connections were also designed using the balanced design approach (Lumpkin, 2009). The wide flange brace had also exhibited a faster degradation of post-buckling compressive strength than the HSS braces. The energy dissipation of the wide flange braces was smaller than the HSS braces at corresponding drift levels due to more pinching in the wide flange brace force vs. deformation hysteresis (Lumpkin et al., 2012). Included in this study, was a comparison of brace behaviour due to the difference in gusset plate stiffness. As expected, braces with more slender or more flexible gusset plates buckled in the standard shape of a pin-pin ended member, while braces restrained by more a rigid gusset plate buckled in a slight double curvature closer to the behaviour of fix-fix ended braces. The latter limits the preferred brace behaviour and drift capacity. In this study, the wide flange braces dissipated more energy than the HSS braces by at least 19.6%. Additionally, the distribution of energy dissipation of the brace element as compared to the energy dissipation of the frame members (beams and columns) was also quantified. For the wide flange braced frame, 63% of the energy was dissipated by the brace, while 36% was dissipated by the frame. Lumpkin (2009) stated that the participation of the frame in energy dissipation increases as the drift ratio increases. Lumpkin also stated that one of the drawbacks to using wide flange braces is the increased complexity of their connection as compared to the slotted connection of HSS braces.

More full-frame system tests were carried out by Clark (2009) on two 2-storey chevron frames with connections designed using the balanced design approach. Figure 2-2 and Figure 2-3 depict the damage states of the frame with HSS braces and the frame with W-shape braces, respectively, at the same drift level. Again, the W-shape braces proved to be more ductile and exhibited delayed fracture. It is clear that at the same drift level, the frame with the W-shape braces has sustained less damage than the comparable frame with HSS braces. The yielding in the columns

and beams was less severe in the frame with the W-shape braces. However, the behaviour of the HSS braces improved with a tapered gusset plate in a third test. This frame attained a larger drift ratio as compared to the first HSS braced frame. For all three tested frames, the ductility demand was approximately evenly distributed between the first and second storeys, which corresponds to the results of numerical analyses for short buildings as performed by Castonguay (2010). The W-shape braced frames also had the largest crack develop in the gusset plate welds due to an increased rotational demand at high drift ratios. However, these cracks never attained the critical crack fracture length. The W-shape braced frame had a higher initial stiffness prior to buckling than the other specimens; however, its stiffness quickly degraded after buckling.

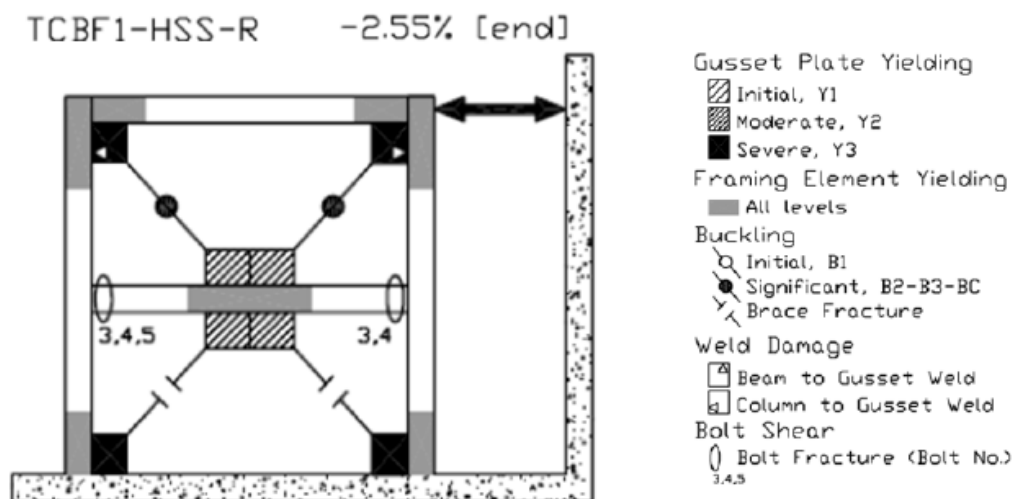


Figure 2-2 Performance of HSS braced frame at -2.55% drift (Clark, 2009)

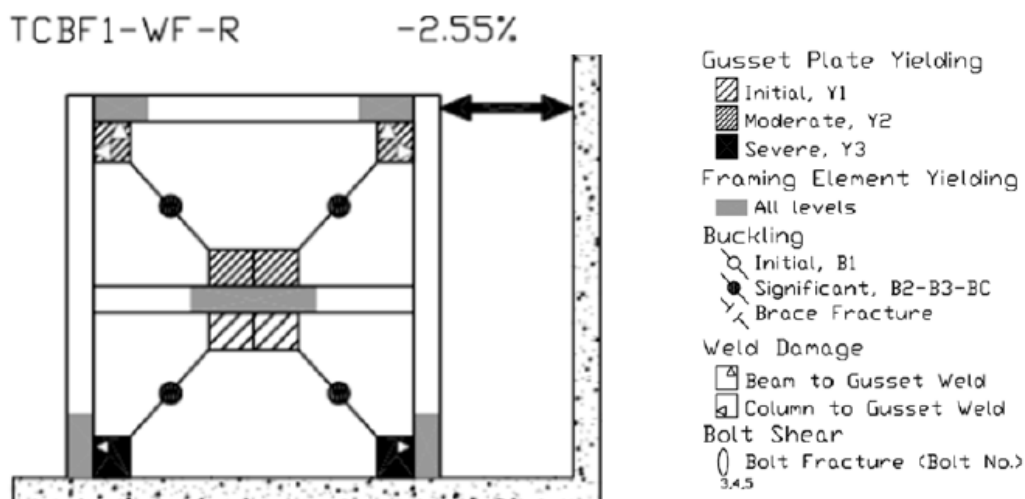


Figure 2-3 Performance of W-shape braced frame at -2.55% drift (Clark, 2009)

The results of full-frame tests were used to verify and calibrate numerical finite element models, which were then used to conduct parametric studies on braced frames and their gusset plate connections (Yoo et al., 2008; Alipour and Aghakouchak, 2013). These numerical models were used to study aspects such as gusset plate thickness, gusset plate taper, gusset plate clearance, gusset plate geometry, and brace angle. The results showed that all these parameters had an influence on storey drift and number of cycles before fracture, as well as the location of the fracture. Alipour and Aghakouchak (2013) had also investigated the performance of OCBFs with limited special detailing versus SCBFs. While the SCBF had improved performance over the OCBF, the OCBF displayed satisfactory performance. In increasing the clearance in the gusset plate, strain concentration moves from the gusset plate welds to the middle of the brace. Additionally, to mitigate buckling in the gusset plate, the thickness of the gusset plate must increase with increased clearance. This causes even more pronounced strain in the middle of the brace. Since, it is more desirable to have the failure occur in the brace as opposed to the connection, the $2t_g$ linear clearance is prescribed in the CSA S16-14 Standard for MD and LD CBFs.

A similar study was done by Zhang et al. (2011) on W-shape braces in the chevron frame configurations. Nine full-frame specimens were tested under symmetric cyclic loading with the same welded W-shape. The connections of all the tested specimens were designed according to the capacity design principle. The size, thickness, and clearance of the gusset plates were varied, as well as the eccentricity of the force lines to the centerline of the beam of the frame. This frame was modelled in ANSYS and the numerical analysis results were in agreement with the experimental results. The chevron brace configuration designed with protected connections showed a good level of ductility and dissipation of energy. Regarding gusset plate clearance, while the $2.5t_g$ linear gusset plate clearance showed the best results, braced frames design with zero and negative clearances were also able to achieve the required ductility levels.

The relationship between the gusset plate and brace behaviour was also studied numerically by Walbridge et al. (2005) using finite element modelling. The gusset plate model created using the ABAQUS software was first calibrated using the results from tests run by Rabinovitch and Cheng (1993) for gusset plate behaviour under both monotonic and cyclic loading. This model included considerations for the effects of material nonlinearity, initial imperfections, presence of framing

members, and bolt slip. The behaviour of the modelled gusset plate was in agreement with the test results. This model was subsequently used to observe the effect of certain parameters on the reversed cyclic behaviour of a brace and gusset system. Three parameters were studied: the relative compressive and tensile strengths of the brace and the gussets, the impact of the loading protocol, and the gusset plate thickness. The behaviour of each system was evaluated based on the force vs. deformation hysteresis and energy dissipation.

Three gusset plate thicknesses were tested. An improvement of the hysteretic behaviour accompanied the increase in gusset plate thickness when the gusset plate strength governed the response both in tension and in compression.

Lastly, the governing failure modes in tension and compression were varied for comparison. This resulted in four permutations: (1) brace yielding in tension and brace buckling in compression, (2) brace yielding in tension and gusset buckling in compression, (3) gusset yielding in tension and brace buckling in compression, and (4) gusset yielding in tension and gusset buckling in compression. The different combinations were achieved by varying the W-shape brace sizes and slenderness. The numerical study revealed that the strength ratios of the brace and gusset had a very important effect on the system behaviour. When gusset plate buckling governed in compression, the overall force vs. deformation hysteretic response was significantly improved. The force vs. deformation hysteresis exhibited less pinching in the compression range, and therefore the dissipation of energy was improved. Additionally, these specimens had no degradation of their tensile capacity after the braces had buckled. The governing failure mode in tension had no significant impact on the force vs. deformation hysteresis of the specimen. The resulting force vs. deformation hystereses are shown in Figure 2-4. Based on these results, Walbridge et al. recommended that the gussets of brace members be designed to be the weaker member of the system. In this recommendation, the gusset plate yielding and buckling would govern over the buckling and yielding of the brace thereby opposing the principles of capacity design. This approach would therefore be more suitable for CC-type CBFs.

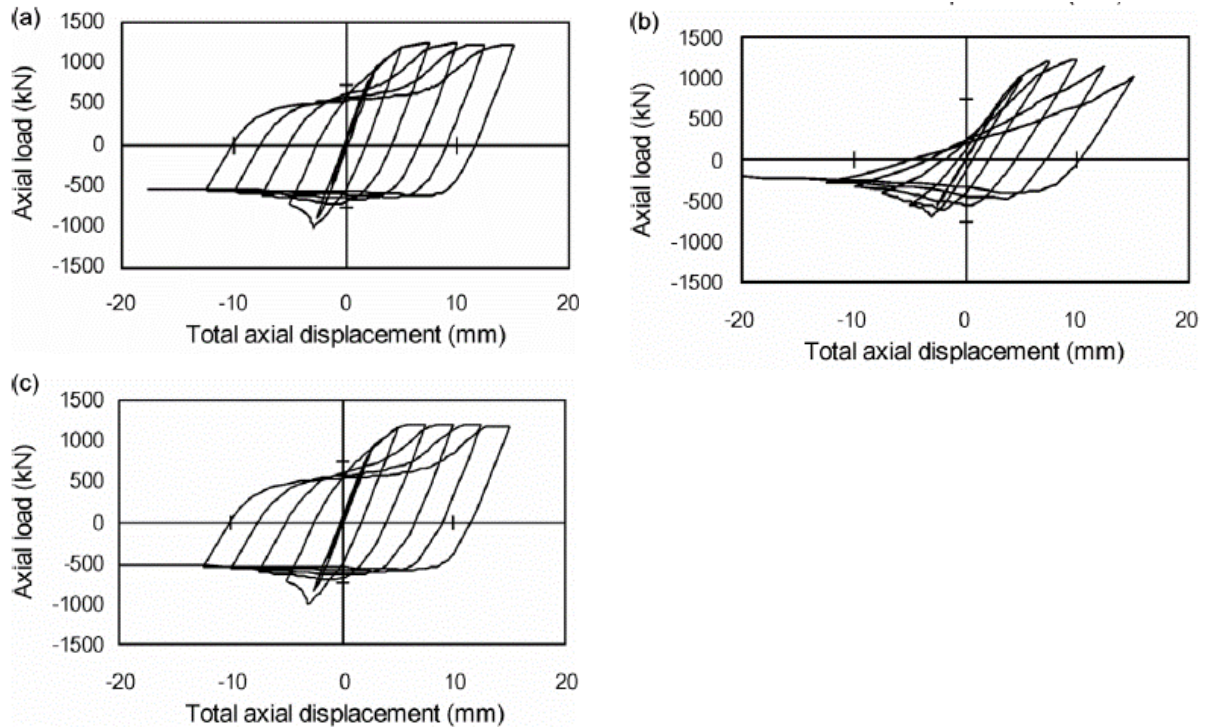


Figure 2-4 Effect of load limiting mechanism on force vs. deformation curves: (a) tension and compression - gusset (YGT/BGC), (b) tension - gusset/compression - brace (YGT/BBC), (c) tension - brace/compression - gusset (YBT/BGC) (Walbridge et al., 2005)

Another set of full braced bay systems was tested under cyclical loading at the University of California, Berkeley (Lai, 2012). Four tests were conducted on two-storey, one-bay specimens. The diamond brace configuration was chosen for study, as shown in Figure 1-1. For the first three tests, the cross-section shapes of the four braces, as well as the connection details, were varied. The cross-sections were square HSS, round HSS, and W-shapes. The last test was a hybrid test conducted with square HSS braces. The HSS braces had fully welded connections, while the W-shapes were only connected at the web to allow rotation as a pinned connection. This difference in the connection rigidity between specimens affected their performance (decreased drift range in the pin-connected specimen) and the damage of the surrounding frame. In all cases, the design of the specimens included a $2t_g$ linear clearance at the gusset plate. The round HSS braces attained the highest drift level before fracture, while the square HSS braces attained the lowest drift level before fracture. All braces buckled at low level drifts. The out-of-plane deformations were up to ten times greater than the axial deformations, which prompted Lai to warn of possible

significant damage to surrounding non-structural components (Lai, 2012). The degradation of the force versus displacement hysteresis was more gradual for the W-shape braces than for the other cross-section shapes. Furthermore, the storey drifts were more uniform between the first and second storeys for the round HSS and the W-shape brace as compared to the square HSS braces. Additionally, finite element models were created to attempt to replicate the test results. It was found that while shell element models had better capabilities in reproducing local behaviors such as local buckling and fracture, fibre based modelling was significantly more economic in terms of computational effort, and therefore better suited for full-scale modelling.

More recently, CBF systems were tested at UC Berkley to compare the performance of the Strongback CBF system (this system uses an inelastic vertical truss in combination with an elastic vertical truss to reduce the risk of weak storey formation) to more traditional CBF systems in terms of the formation of weak storeys (Simpson and Mahin, 2018). The CBFs tested were two-storey chevron-braced frames with square HSS braces. One of these specimens was designed without adhering to current seismic design requirements such as slenderness limits, the gusset plate linear clearance requirement, and capacity protection of the connection. While the referenced paper was more focused on the performance of the Strongback CBF system, the authors did indicate that this specimen exhibited significant local buckling in the braces resulting in earlier brace fracture, and weak-storey performance of the second storey. In comparison, the Strongback system was shown to allow for the mitigation of the formation of weak-storeys as hypothesized.

2.1.4 CBFs in the CC category

Relatively little research has been conducted for CBFs in the CC category. The three studies found on this subject are discussed in this section.

Richard (2009) conducted a study to evaluate the design practices in CSA S16-01 (CSA, 2001) of CC-type industrial buildings under earthquake loading. The project was divided into multiple phases. In one phase, large-sized braces common to industrial buildings were tested. The braces were chosen such that the global slenderness coefficients did not meet the requirements of MD- and LD-type structures. This was done to observe the impact of this parameter in conventional

construction on the behaviour and performance of such braces. The connections were therefore not the focus of these tests. Out of the six test specimens, two were wide flange braces of size W360x134 (KL/r of 40) and W310x97 (KL/r of 60). The connection assemblies of these specimens were welded, as shown in Figure 2-5. In both these cases, the final fracture occurred in the W-shapes because the connections themselves were stronger than the brace members were. These specimens were subjected to a cyclic axial quasi-static symmetric loading protocol characteristic of far-field earthquakes. The first cycle started with compression loading. During testing, the sections first exhibited global buckling followed by local buckling of the flanges and plastification. Fracture propagation started near the centre of the braces at the flanges; it then progressed inwards to the web until total loss of brace resistance. The W360x134 had an ultimate compressive capacity of 6000 kN and an ultimate tensile capacity of 6430 kN. The force vs. deformation hysteresis for the W360x134 brace is shown in Figure 2-6. The W310x97 brace had an ultimate compressive capacity of 3900 kN and an ultimate tensile capacity of 4760 kN. The force vs. deformation hysteresis for this section size is shown in Figure 2-7.

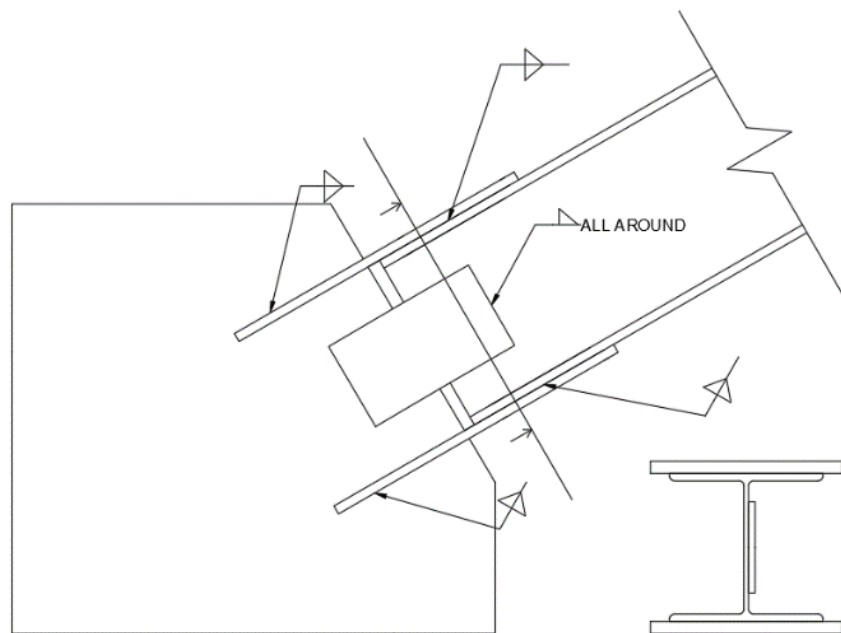


Figure 2-5 Welded W-shape connection in tests by Richard (2009)

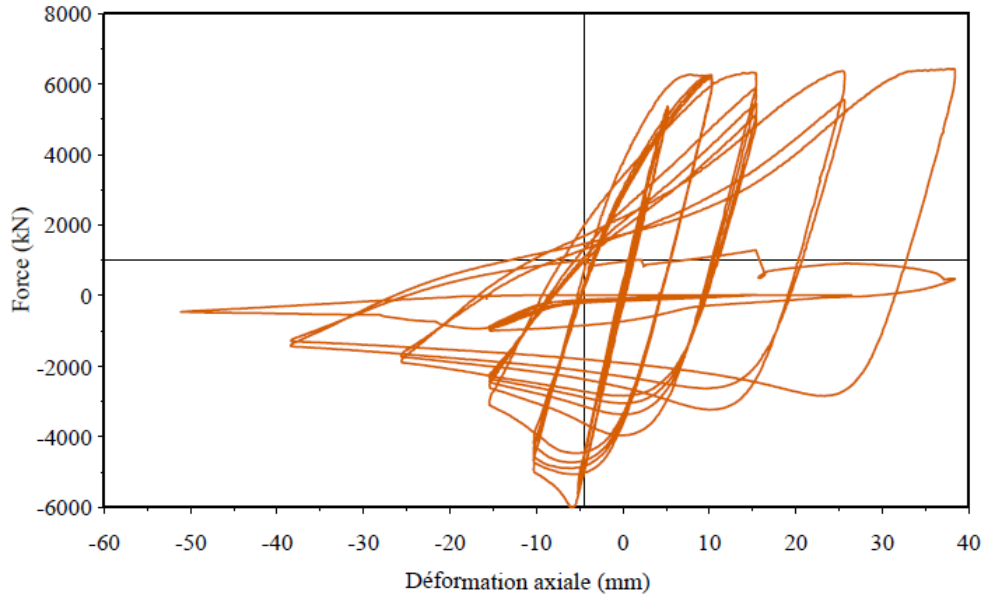


Figure 2-6 Force vs. deformation hysteresis of W360x134 brace (Richard, 2009)

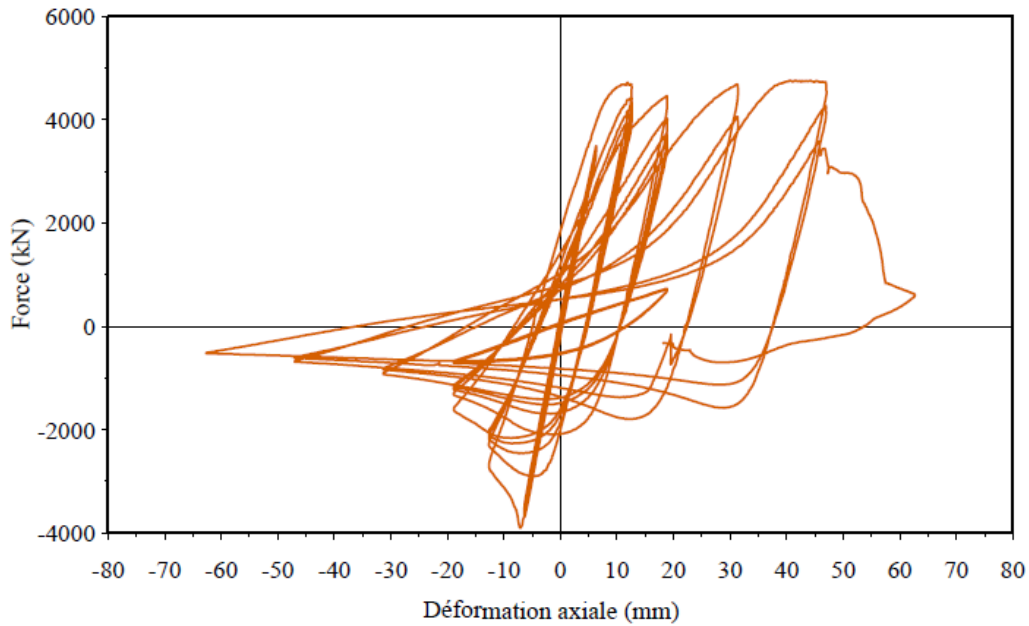


Figure 2-7 Force vs. deformation hysteresis of W310x97 brace (Richard, 2009)

The initiation of cracks occurred earlier in specimens with greater local slenderness. However, the local buckling and crack initiation occurred later in specimens with higher global slenderness ratios. Overall, the W-shape braces demonstrated a better force vs. deformation cyclic behaviour

than the HSS members, as measured by the ability to carry loads for more load cycles. This was attributed to their increased resistance to local buckling.

These W-shapes, which did not meet LD and MD requirements in terms of local slenderness, were subsequently modeled in ABAQUS to verify if finite element modelling could be used to accurately predict both the force vs. deformation hysteretic behaviour and the brace fracture (Haddad, 2017). Overall, the model showed excellent agreement with the experimental results. The local buckling phenomenon was well modeled (Figure 2-8) when the stress-strain curves were defined separately for the material of the web, the flange, and the k area of the W-shapes. These curves were obtained from coupon testing of the respective areas (junction of the W-shapes for the k-area). Haddad recommended the use of an element mesh size equivalent to the thickness of the members and five or more integration points.

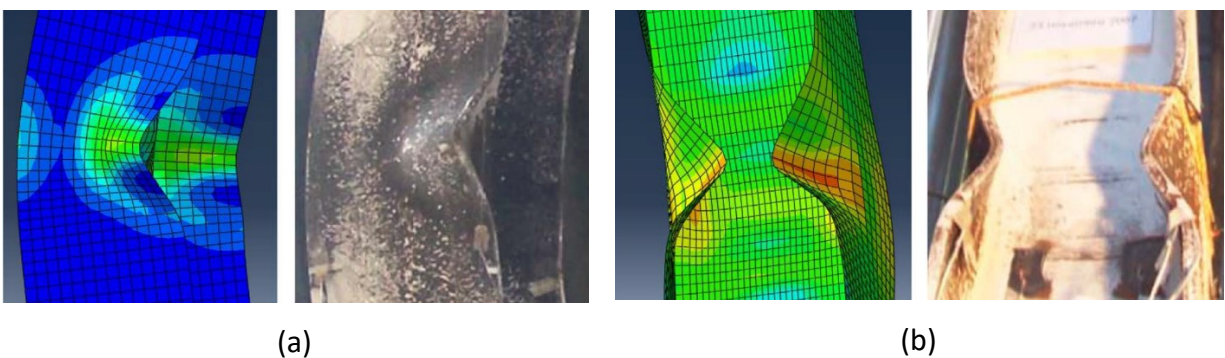


Figure 2-8 Local buckling modes of (a) W360x134 and (b) W310x97 braces (modified from Haddad, 2017)

Castonguay (2010) investigated the ductility properties of bolted angle connections for concentrically braced members designed for the CC category. The research program was separated into three phases. In the first phase, the goal was to determine the ductility of different failure modes of a double angle connection loaded under monotonically increasing tension. The following failure modes were studied: yielding of brace members, weld rupture, bolt bearing on the gusset plate, net section fracture of brace members, bolt shear rupture, and shear and tension block failure. The measured deformation of the connection at ultimate load was used to compare the ductility of the connections. The bearing failure of the bolts on the gusset plate was determined to be the most ductile failure mode. In the second phase of this research, the impact

of design parameters on the ductility of the angles-to-gusset plate connection with an expected failure mode in bearing was studied. The following parameters were evaluated: the end distance, bolt spacing (pitch), slotted holes, hole forming method, and thickness of gusset plates. These specimens were tested under monotonic loading and cyclic loading. The ductility of the connection increased with greater end distance, un-slotted holes (the difference between the two was only perceptible after ultimate loading), and with drilled holes (the difference was not very significant and is only seen in the deformation). The last phase of this research project included the numerical modelling in OpenSees of standard structures of different heights in Montreal and Vancouver for soil classes C and E. One goal of this phase was to evaluate the 15 m height limit for CC construction under different circumstances. Linear, non-linear, and incremental non-linear dynamic analyses were conducted. Some of the buildings were modelled with non-ductile connections to observe the forces in this component of a CC SFRS (Split-X and Chevron configurations). Forces in buildings with heights greater than 15 m were found to be significant. The author provided suggestions for the R_dR_o values to be used in design based on the findings.

Hsiao et al. (2014) conducted both experimental work and numerical modelling to investigate differences in behaviour and ductility between Special Concentrically Braced Frames (SCBFs) and concentrically braced frames, named nonseismic concentrically braced frames (NCBFs), due to lack of detailing as required by modern codes. In this sense, these braces were similar in design to the current CC design of braces. In the United States, before 1988, no requirements were placed on the slenderness and the connection capacities of braced frame systems to develop their full ductility. As such, buildings designed before this period were expected to be more vulnerable to seismic action. Tests on a braced frame designed with respect to the Uniform Building Codes predating the 1988 revision led to the following conclusions. The behaviour of these braces is heavily dependent on the design of their connections because they are not capacity-protected as they would be in the modern AISC 341-16 Standard or in the CSA S16-14 MD and LD design provisions. This means that results from a given test on this type of braced frame system could only be used insofar as the connection strength and ductility remain similar to those tested. Additionally, numerical predictions of the strength of these systems are made

more complex by their brittle failure modes. Further numerical modelling showed that the NCBF systems were more like to collapse than the SCBF systems demonstrating the need to design for higher forces when designing a CC-type SFRS.

2.1.5 Numerical modelling

It is not economically viable to physically test all possible variations of braces and braced frame systems. However, once some test results have been obtained, they can be used to calibrate a numerical model, which can be used to conduct parametric studies. In modelling braced frame systems, the inclusion of the effect of the brace-to-gusset and gusset-to-beam and column connections influences the accuracy of the model. While continuum based models produce accurate results including local behaviours, they are both time-consuming and computationally expensive. These models allow for the observation of local buckling and connection failures and have been shown to reasonably predict experimental behaviour. Various strain models are commonly used to predict failure modes due to fatigue (e.g. Yoo et al., 2008).

Phenomenological models are slightly simpler than fibre-based models. They require the input of force vs. deformation hysteretic data from testing. Ikeda et al. (1984) made many recommendations through their work with phenomenological models regarding the input parameters required in the development of these models for braces. These models show satisfactory agreement with experimental results for global behaviour and are not as expensive as continuum element models in terms of computational effort. However, they are unable to account for local strain effects such as local buckling. To increase the accuracy of such models, the impact of the brace connections should be integrated into the model. One such model has been developed for HSS and W-shape braces with tapered and rectangular gusset plates welded directly to the brace and the frame elements (Hsiao et al., 2012). Bara (2007) had conducted a parametric study on the influence of various input parameters on brace and braced frame behaviour predictions. The braces were composed of rectangular HSS members found in multistorey steel structures designed for the MD or LD categories. The parameters analyzed with respect to the brace model were the number of integration points, the number of elements and fibres, force-based analysis versus displacement-based, and the force vs. deformation hysteretic

model. While increasing the number of integration points did not yield additional accuracy, the increase of fibre elements within a brace showed an improvement in accuracy. Bara recommended using eight elements along the length of each brace with 16 fibres in the cross-section. The force-based analysis showed better predictive results than the displacement-based analysis. However, the latter option allows for shorter computational time. Lastly, the Giuffrè-Menegotto-Pinto model (Menegotto and Pinto, 1973) was preferred to the bi-linear model in representing the force vs. deformation hysteretic behaviour of the brace. Bara also developed a database for loading protocols for CBFs including statistical information on the number and magnitude of excursions experienced by different storeys in full building models. Data was collected for the median, 84th percentile, and maximum level observations. In a paper by Uriz et al. (2008), the authors developed a fibre-based phenomenological model for the inelastic buckling of steel braces. The authors suggested the use of two inelastic beam-column elements, an initial offset at the midspan of the brace of 0.5-0.1%, three integration points, and ten to 15 fibres along the full depth of the brace for future models. Finally, Karamanci and Lignos (2014) developed another fibre-based model for steel braces, including considerations for different sections of braces such as W-shape sections, particularly for the collapse assessment of buildings. The implication of damping simulation was also discussed.

The third type of model is a physical-theory model. Like phenomenological models, they lack the ability to model local effects but are computationally less expensive than continuum based modelling. The advantage that these models have over phenomenological models is that they do not require the input of force vs. deformation hysteretic data from physical testing. Ikeda and Mahin (1984) developed physical-theory models of concentric steel braces under dynamic loading that combined both analytical properties of steel brace behaviour with empirical data and equations. These models included the nonlinear behaviour of steel braces under reverse cyclic loading as well as plastic hinge properties at the midspan of the braces. D'Aniello et al. (2013) conducted a parametric study on physical-theory models of concentric braces in a modelling software called Seismostruct. The authors gave several recommendations for creating physical-theory models of CBFs. To maintain an acceptable level of accuracy while minimizing computational time, force-based elements with distributed plasticity, a bilinear shape for the

initial deflection, and a mesh with 100 fibres with at least two fibres over the thickness of the cross-section were recommended. The Menegotto and Pinto (1973) model should be used over the bilinear kinematic model because it includes Bauschinger effects. Lastly, the authors recommend using Eq. 2-5, proposed by Dicleli and Calik (2008), to calculate the length of the initial deflection, Δ_0 , to better predict buckling performance (where N_b is the buckling load and M_{pb} is the corresponding bending moment):

$$\Delta_0 = \frac{M_{pb}}{N_b \left(1 + \frac{N_b L^2}{8EI \left(\frac{N_b L^2}{\pi^2 EI} \right)} \right)} \quad (2-5)$$

2.2 Bolted connections

In early cyclic tests of brace members by Gugerli and Goel (1980), while HSS specimens all failed by fracture at the mid-points of the braces, the only wide flange member failed at its welded connection, showing that the connection strength capacity must be thoughtfully considered in the design of a brace member. This is particularly true for CC-type braces. For this reason, a literature review of failure modes in bolted connections is presented in this section.

2.2.1 Bolt shear

Bolt shear is a localized failure at each bolt rather than the failure of the connecting member. Bolt shear can occur on one or two shear planes per bolt depending on the number of connecting members. Bolt shear can also occur whether the connecting plate is in tension or compression. Since bolts are characterized by their strength in tension, F_u , a factor is used to convert the tensile strength to a shear strength. In bolt shear tests, the shear strength of bolts was approximately 62% (in tension tests) and 68% (in compression tests) of their tensile strength (Kulak et al., 1987). In CSA S16-14, the shear to tensile bolt strength factor is taken conservatively to be 0.60. A bolt's shear strength depends on the bolt grade and shear area. The shear area is reduced by 30% if the shear plane passes through the threads of the bolt. Bolt shear resistance in the CSA S16-14 Standard is given by Eq. 2-6, where ϕ_b is the resistance factor of 0.8, n is the number of bolts, m is the number of shear planes and A_b is the bolt shear area:

$$V_r = 0.60\phi_b n m A_b F_u \quad (2-6)$$

For lap splice connections that are longer than 760 mm, the bolt shear is reduced. In such connections, the shear resistance of the bolted connection, V_r , is calculated using Eq. 2-7.

$$V_r = 0.50\phi_b nmA_b F_u \quad (2-7)$$

The connection length is measured centerline-to-centerline of the extreme bolts in a lap splice connection and centerline-to-centerline of one extreme bolt and the bolt closest to the centre of the connection in a butt splice.

In the AISC 360-16 Standard (AISC, 2016), the bolt shear resistance calculation for LRFD is quite similar, as shown in Eq. 2-8.

$$\phi R_n = \phi F_{nv} A_b \quad (2-8)$$

In this case, the resistance factor, ϕ , is given as 0.75. F_{nv} is the shear strength of the bolt and accounts for the reduced shear area when the threads are included within the shear plane. When the connection length is 38 in (950 mm) or greater, the bolt shear is reduced to 83.3% of its full capacity.

The accuracy of these equations was evaluated in a review of 119 test specimens that failed in bolt shear (Tide, 2010). A statistical analysis was conducted for 79 of these specimens for which there was sufficiently detailed information. The test data was normalized with respect to the predicted single bolt strength with a double shear plane in a ratio labelled P_{TEST}/P_{PRED} . The resulting data pool was then used to measure the reliability of the AISC LRFD (2005) and CSA S16 (2001, 2005)/Eurocode (CEN, 1993) design equations. It was found that the reduction factors for the length of the connection were overly conservative in the case of the LRFD and unnecessarily complex in the case of CSA S16 (2001, 2005)/Eurocode (CEN, 1993). Tide recommended the application of a 0.9 reduction factor for connection lengths of less than 38 in. and a reduction factor of 0.75 for connection lengths greater than 38 in. Additionally, the shear resistance of the bolts was strongly affected by the net and gross areas of the plates. The two criteria shown in Equations 2-9 and 2-10 were developed for the assessment of the connections:

$$A_n \geq 0.56A_s F_u / F_{up} \quad (2-9)$$

$$A_g \geq 0.56A_s F_u / F_{yp} \quad (2-10)$$

A_n is the net cross-section area, A_g is the gross cross-section area, A_s is the total bolt shear area, F_u is the bolt shear strength, and F_{up} and F_{yp} are the plate tensile and yield strengths, respectively. For connections in which both criteria were satisfied, a length reduction factor of 0.9 was deemed satisfactory regardless of the connection length.

2.2.2 Impact of fillers

Fillers can affect the shear strength of bolts in a connection. Filler plates are added within a connection when the connected plates or members vary in thickness. The fillers are then inserted between the member of smaller thickness and the splice plates. There exist two types of fillers: developed fillers and undeveloped fillers (Figure 2-9). Developed fillers extend beyond the splice plate over the main connected member and additional bolts beyond those needed to transfer the load are added to bolt the filler to the main connected member. This allows the stress to be uniformly distributed between the connected member and the filler plate. Undeveloped fillers usually do not extend past the splice plates and are not considered to carry any axial loads.

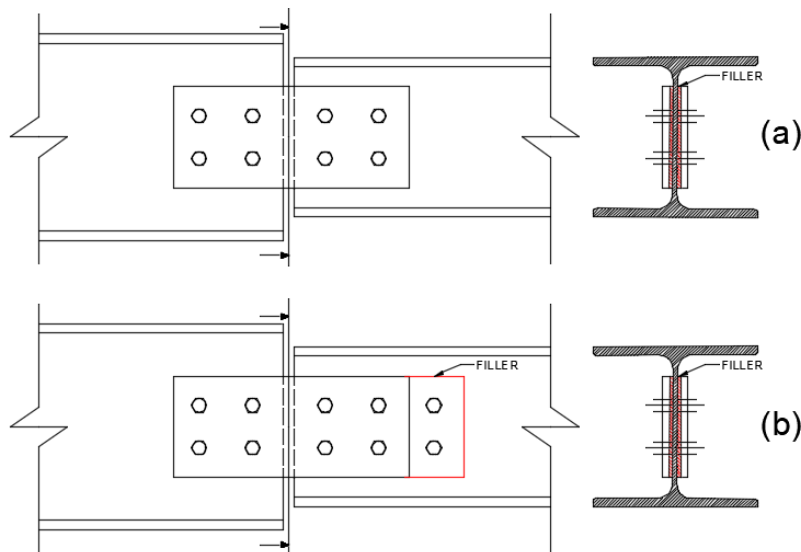


Figure 2-9 Fillers (a) Undeveloped fillers (b) Developed fillers

Experiments have shown that the addition of undeveloped fillers increases the flexibility of the joint, as well as the connection's displacement (Yura et al., 1982). This is due to the increased bending in the bolts. Fillers with plate thickness up to 19.05 mm did not significantly decrease the ultimate shear strength of the bolts. In fact, all specimens were stated to be within the

required level of safety. The connection strengths were recorded at a 6.35 mm deformation because this was believed to be the useful deformation limit of the connection. Using this criterion, the effect of the fillers was more detrimental to the strength of the connection. The authors suggested that fillers below 6.35 mm in thickness should not affect the design, while for a thickness greater than 6.35 mm, the bolt shear strength of connections should be reduced by a factor of $1 - 0.4t$ (where t is the thickness of the filler in inches).

In reviewing the results from Yura et al. (1982), Sheikh Ibrahim (2002) proposed a different bolt shear reduction factor based on a mechanistic model as opposed to a purely empirical model. This model takes into account the relative areas of the filler plate versus the areas of the connected plates. The reduction factor, R_b , is calculated as shown in Eq. 2-11.

$$R_b = \frac{1+\alpha}{1+2\alpha} \quad (2-11)$$

Where α is the ratio of the filler area, A_f , calculated as the sum of the areas on either side of the main connection plate and, A_p , is the smaller of either the main connected plate area or the sum of the areas of the splice plates on either side of the main plate. In comparing the results of the model to the experimental results from the tests by Yura et al., the new reduction factor yielded a bolt shear resistance nearer to the useful strength of the bolts than the previous reduction factor that gave results closer to the ultimate bolt shear resistance.

In the CSA S16-14 Standard, fillers of 19 mm or greater in thickness must be developed. For fillers between 6.4 mm and 19 mm, the bolt shear resistance is multiplied by a factor R_v , calculated as shown in Eq. 2-12 (where t is the thickness of the filler in mm):

$$R_v = 1.1 - 0.0158t \quad (2-12)$$

In the AISC 360-16 Standard, the reduction factor is given as $1 - 0.4(t-0.25)$ for t in inches or $1 - 0.0154(t - 6)$ for t in mm, but not smaller than 0.85. Furthermore, in the AISC 360-16 Standard, no upper limit is given on the thickness of the filler plates, but no reduction factor needs to be applied when filler plates are developed. For fillers of 6.4 mm or less in thickness for the CSA S16-14 Standard, or 6 mm or less in the AISC 360-16 Standard, no reduction is necessary. Thus, the

current standards reflect the findings of Yura et al. (1982) for the impact of fillers on bolt shear capacity.

2.2.3 Bolt bearing

Bolt bearing is a localized failure. Its occurrence at one bolt does not imply that it will occur at all bolts. If the end distance is too short, the bearing failure becomes a bolt tear-out failure also known as plug shear. If however, the cross-section is not great enough to sustain the bearing of the plate, net-section failure occurs. A combination of these two behaviours is block shear. Bolt bearing occurs after bolts overcome friction forces, slip, and come into contact with the connecting plates, as shown in Figure 2-10.

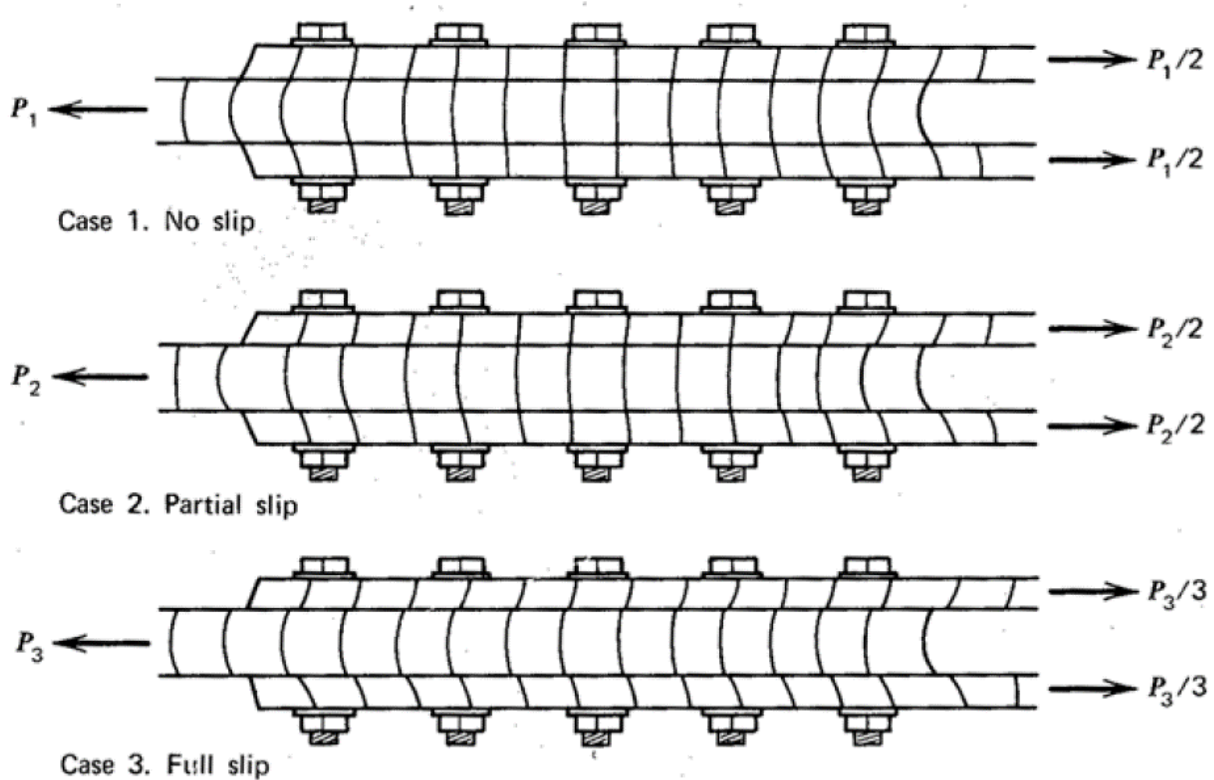


Figure 2-10 Bolts slipping into bearing (Kulak et al., 1987)

In tensile bearing tests of thirty bolted connections, Perry (1981) concluded that the elastic deformation of bolted connections was limited by a 6.4 mm (1/4") deformation at the most. This limit agreed with data from tests by Winter (1956), Chong and Matlock (1975), Gilchrist and Chong (1979), and Munse (1959). Lewis and Zwerneman (1996) further noted however that this

limit only applied to smaller bolts. For larger bolts, such as bolts with a 1" diameter or greater, more deformation is required to reach the strengths expected in design equations. For ultimate limit states design, Perry recommended that this displacement limit be used as a failure criterion because the connections lose most of their utility beyond this deformation. Plastification begins in the connection prior to this limit and connections reach 80% of their ultimate capacities. Failure occurred a greater deformation of 12.7 mm for thicker plates and 19.5 mm for thinner plates. The effect of pretensioned bolts versus snug-tight bolts was also observed at the 6.4 mm deformation limit. At this level of deformation, pretensioned bolts reached an ultimate load that was 10% greater than the hand-tightened bolted connections. Slotted holes attained even smaller ultimate loads (20% smaller than the pretensioned bolts). These differences were explained by the degree of restraint provided by the different bolting methods. A higher degree of restraint allowed the connections to attain greater ultimate loads.

In tests done by Kim and Yura (1999) on the bearing of 22 mm bolts onto a 5 mm plate, the ultimate strengths were reached in the plate at deformation magnitudes near $d/2$, in cases where there was sufficient end distance and bolt spacing to develop the bearing failure. Their tests also confirmed that the results were better predicted when calculated based on the ultimate strength of the bearing plate, rather than being based on the yield strength of the material. The authors reported that the ultimate-to-yield strength ratio does not have a significant effect on bearing strength. However, Može and Beg (2014) had determined that higher grades of steel bearing plates showed lower relative bearing capacity. Additionally, they had found that the pitch and edge distance of the bolts in the tensile connection do not have a significant effect on bearing capacity confirming this finding in the tests by Rex and Easterling (2003).

The degree of out-of-plane restriction of a deforming plate influences the ultimate capacity of the connection in bearing. For plates that are fully restricted in out-of-plane bending such as butt splices, bearing stresses can reach magnitudes of $3.0F_u$ to $3.5F_u$, while unrestricted plates which deform in bearing such as lap splices only reach stresses of magnitude of $2.0F_u$ to $2.8F_u$. For the same reason, connections with washers performed better than those without. This was particularly important in tests with light gauge steel where the plates were similar in thickness or thinner than the washers. These conclusions differed from conclusions in Winter (1959) and

Chong and Matlock (1975) both of which attributed negligible loss in capacity due to lack of out-of-plane restriction.

Perry (1981) concluded that the behaviour of bolted connections in tension can best be predicted through the bearing ratio. The bearing ratio (B.R.) is defined as shown in Eq. 2-13.

$$B. R. = \frac{g-d_h}{n \times d_b} \quad (2-13)$$

Where g is the plate width, d_h is the hole diameter, n is the number of bolts, and d_b is the diameter of the bolts. Perry summarized his findings with Equations 2-14 to 2-19 for the calculation of net section stress (f_{ns}) and bearing stress (f_b) at the 6.4 mm deformation limit based on the bearing ratio of the connection:

For round holes:

$$0.0 < B. R. \leq 2.0 : f_{ns} = 0.9F_u \quad (2-14)$$

$$2.0 < B. R. \leq 4.0 : f_b = 2.4 \times (0.5 + 0.125B. R.) \times F_u \quad (2-15)$$

$$4.0 < B. R. : f_b = 2.4F_u \quad (2-16)$$

For slotted holes (short slots perpendicular to the line of action):

$$0.0 < B. R. \leq 1.5 : f_{ns} = 0.9F_u \quad (2-17)$$

$$1.5 < B. R. \leq 4.0 : f_b = 2.0 \times (0.5 + 0.125B. R.) \times F_u \quad (2-18)$$

$$4.0 < B. R. : f_b = 2.0F_u \quad (2-19)$$

In the CSA S16-14 Standard, the bearing strength of a bolted connection is given by Eq. 2-20, where ϕ_b is the resistance factor of 0.8, n is the number of bolts, t is the thickness of the bearing plate, d is the diameter of the bolts, and F_u is the ultimate strength of the bearing plate:

$$B_r = 3\phi_{br}ntdF_u \quad (2-20)$$

For long slotted holes, the bearing resistance is calculated according to Eq. 2-21.

$$B_r = 2.4\phi_{br}ntdF_u \quad (2-21)$$

Considering that the connections developed 80% of their ultimate capacity at the 6.4 mm deformation limit, Perry's findings seem to agree with the current code-specified bearing stress of $3.0F_u$ for ultimate limit state design.

In the AISC 360-16 Standard, the bearing stress for LRFD in the situation where the deformation at service load is not a concern, such as in a SFRS, is given by Eq. 2-22 (where ϕ is the resistance factor of 0.75, l_c is the clear distance parallel to the applied force between the edge of the hole and the edge of the adjacent hole or the edge of the material, d is the bolt diameter, and t is the thickness of the connected material):

$$\phi R_n = 1.5l_c t F_u \leq 3.0dt F_u \quad (2-22)$$

2.2.4 Tension failure modes: net section, plug shear, block shear, and shear lag

When connections are loaded in tension, multiple additional failure modes exist for the fracture or yielding of the loaded steel section. The configuration of the bolts determines the governing failure mode. Important parameters include the ratio of gross cross-section area to net cross-section area, edge distance, end distance, and spacing. A discussion of these failure modes (see Figure 2-11) including net section fracture, plug shear and block shear, as well as the effects of shear lag will follow in this section.

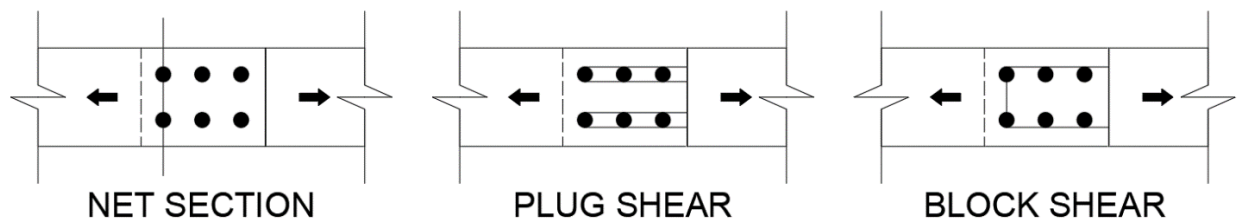


Figure 2-11 Tension failures

Net section fracture occurs when the net section area of the connecting plate is too small to sustain the load for other failure modes. In the CSA S16-14 Standard, the net-section fracture strength is calculated as shown in Eq. 2-23, where ϕ_u is the resistance factor of 0.75 and F_u is the ultimate strength of the connecting member:

$$T_r = \phi_u A_{ne} F_u \quad (2-23)$$

A_{ne} is the effective net area of the connecting member. The net area is determined by removing the area of the boltholes and can be increased by staggering the bolts. It is also affected by shear lag.

Shear lag affects eccentrically loaded connections and connections where only part of the steel member is connected. Most notable of these sections are angles connected by one leg, tees, C-shapes and W-shapes (connected by either only the flanges or only the web). The eccentricity of the connection decreases the uniformity of the stress distribution in the loaded member. Therefore, the connected portion of the section experiences an increased concentration of stresses, while the unconnected portion may experience lowered stress, no stress, or, in some cases, compression due to imposed bending. Shear lag therefore affects the member's capacity in net section fracture. To compensate for this effect in design, a factor to reduce the available net area A_n to an effective area A_{ne} is used to calculate the net section fracture capacity. Many studies have been conducted to help develop a reduction factor to account for shear lag effects.

Kulak and Wu (1997) and Abdelfattah and Soliman (2003) both used finite element models in ANSYS to study the impact of different parameters on shear lag in angles connected to a gusset plate by one leg. The results were similar in both studies. The effects of shear lag are present both under elastic and yielding conditions. The ratio of the length of the connected length and the unconnected leg had a very large impact on shear lag. The additional eccentricity of the longer unconnected leg counteracts the benefit that would have typically been gained from increase in net section area. In contrast, increasing the net area by increasing the thickness of the angles yielded a greater benefit in effective load carrying capacity. Bolt spacing and number of bolts (i.e. the length of the connection) also had an impact on the shear lag effect. By increasing the length of the connection by changing the spacing or the number of bolts, the impact of shear lag is diminished. There was no significant difference in shear lag impact between single and double angles. Lastly, the impact of shear lag was verified for C-shapes and W-shapes. W-shapes connected by the flanges were most resistant to shear lag effects as compared to other eccentric connections.

In the CSA S16-14 Standard, the inclusion of the effect of shear lag is simplified by the adoption of factors ranging from 0.60 to 0.90 depending on the cross-sectional shape of the connected member and the configuration of the bolts. The calculation of the net section rupture strength is almost identical in the AISC 360-16 Standard with some differences in shear lag factor values.

In addition to net section fracture, shear yielding and rupture can occur in the direction parallel to the sense of loading. When the loss of strength is due solely to yielding and rupture at the shear planes, this is called plug shear or bolt tear-out failure. Plug shear occurs when there is insufficient shear area to permit bearing to occur before the bolts rupture through the end of the connection such as in the case of a short end distance or insufficient spacing between bolts.

In CSA S16-14 the plug shear resistance is calculated as shown in Eq. 2-24, where ϕ_u is the resistance factor of 0.75, A_{gv} is the gross area in shear, and F_y and F_u are the yielding and ultimate strengths, respectively, of the connected member:

$$T_r = \phi_u \left(0.6A_{gv} \frac{(F_y + F_u)}{2} \right) \quad (2-24)$$

In the AISC 360-16 Standard, the rupture of the net shear area and the yield strength of the gross shear area are calculated separately and the lower value of the two governs the behaviour.

When the failure path of the connection in tension includes both a tensile and shear portion, it is called a block shear failure. In the CSA S16-14 Standard, the block shear equation is the sum of rupture at the tensile net section and gross shear area, as shown in Eq. 2-25.

$$T_r = \phi_u \left[U_t A_n F_u + 0.6A_{gv} \frac{(F_y + F_u)}{2} \right] \quad (2-25)$$

In the tensile rupture component, the shear lag is accounted for with the U_t factor, which is different from the factors used to calculate A_{ne} in net section fracture. The determination of the block shear path, which varies between cross-section shapes and bolt configurations, becomes critical to identifying the tension and shear areas. In tests where bolted Tee connections were tested in tension, a failure path other than the one expected was obtained (Epstein, 1996a). Instead of the expected fracture through the web, as the web length increased sufficiently, the failure plane started to go through a line parallel to the web just below the flanges (see Figure

2-12 for the geometry of the failure path). Omitting this path from calculations may lead to overestimating the capacity of the connection.

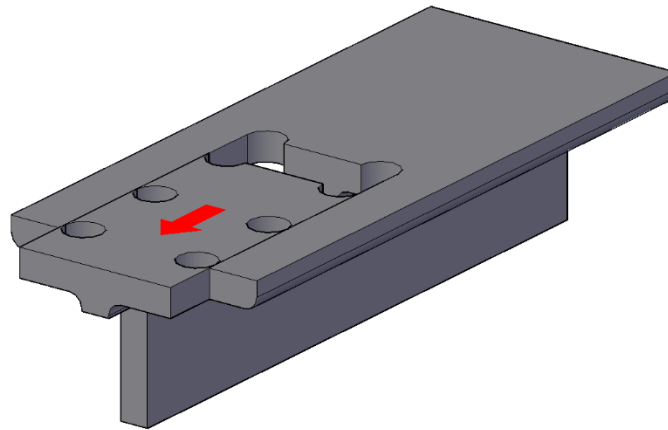


Figure 2-12 Alternate block shear failure mode

In the AISC standards, block shear resistance is calculated through a different approach. Since the 1986 edition of the AISC 360 Standard (AISC, 1986), two equations have been used to calculate block shear. One equation considers rupture at the net tension area (A_{nt}) and yielding at the gross shear area (A_{gv}) and the other considers yielding at the gross tension area (A_{gt}) and rupture at the net shear area (A_{nv}), as shown in Equations 2-26 and 2-27, respectively, where $\phi = 0.75$.

$$\phi[0.6F_yA_{gv} + F_uA_{nt}] \quad (2-26)$$

$$\phi[0.6F_uA_{nv} + F_yA_{gt}] \quad (2-27)$$

In this edition of the standard, the equation resulting in the larger resistance governs the behaviour. However, in the 1993 edition (AISC, 1993), a different criterion was provided for the selection of the governing equation for block shear. The selection criterion was the following:

If $F_uA_{nt} \geq 0.6F_uA_{nv}$ then Eq. 2-26 should be used and if $F_uA_{nt} < 0.6F_uA_{nv}$ then Eq. 2-27 should be used. Essentially, this criterion prescribes the selection of the equation with the larger rupture term (term containing F_u). That is, the rupture term should control the block shear failure.

In his paper, Epstein (1996b) analysed the consequence of these changes. By creating two variables, α and β (where $\alpha = \phi R_n(\text{Eq. 2-25})/\phi R_n(\text{Eq. 2-26})$ and $\beta = A_{nt}/0.6A_{nv}$), Epstein plotted a figure which identified the effects of this change to the calculations of block shear (see Figure

2-13). As a result, Epstein concluded that the new block shear calculations would either give the exact same result as the previous code or a more conservative result.

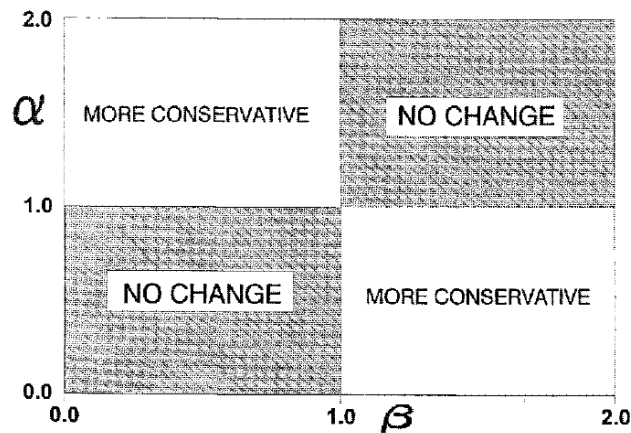


Figure 2-13 Ratio of design strengths from new and old criteria versus ratio of net to gross shear area (Epstein, 1996a)

Epstein and D’Aiuto (2002) and Epstein and Stamberg (2002) built on the testing of bolted tees and angles used in tension. The authors postulated that the equations for block shear in the 1999 version of the AISC Standard (AISC, 1999) as shown by Equations 2-28 and 2-29, do not account for shear lag in members with unconnected legs, thus overestimating the block shear capacity for these types of members.

$$\phi R_n = \phi[0.6F_y A_{gv} + F_u A_{nt}] \text{ if } F_u A_{nt} \geq 0.6F_u A_{nv} \quad (2-28)$$

$$\phi R_n = \phi[0.6F_u A_{nv} + F_y A_{gt}] \text{ if } F_u A_{nt} < 0.6F_u A_{nv} \quad (2-29)$$

The authors used equations that included the moment and the eccentricity effects of the connection in tees in tension. These equations provided satisfactory predictions of the block shear behaviour of tees. The authors concluded that shear lag in tension members failing in block shear is affected by the connection length, the overall length of the member, and the eccentricity of the connection to the centroid of the member’s section. The authors stated that it would not be practical to use such involved equations in design and further work would be needed to formulate specific recommendations for codes. Subject to further work, the authors recommend that a shear factor, $U = 1 - x/L$, should be used to account for the shear lag effect exhibited by these members.

For net section failure, the authors concluded that with a decrease in the connection length or with an increase in eccentricity of the connection the efficiency of the connection is decreased and more so than predicted by the current code's shear lag factor, $U = 1 - x/L$, and its current upper and lower bound limits. The authors recommended that the upper and lower bounds be amended to 0.9 and 0.65 and that the predefined tabulated values for specific connections should be lowered from their current values of 0.75 and 0.85.

In a discussion regarding the paper by Epstein and D'Aiuto (2002), Grondin (2005) argues that there is some confusion by the authors regarding shear lag and block shear. While shear lag occurs in tension due to the unconnected leg of the member, shear lag would not necessarily manifest itself in block shear in such members depending on the block shear path. Furthermore, the calculations in Epstein and D'Aiuto's paper would suggest that this effect would only be present in the case where the connection itself is eccentric. However, Grondin explains that symmetric connections may also be affected by shear lag.

A subsequent analytical study used ABAQUS finite element models of bolted gusset plates and coped beams to calibrate a ductile fracture model based on stress triaxiality, and subsequently to derive an equation to predict the capacity of block shear failures (Mahmoud and Wen, 2016). Following calibration, the two models had very good agreement with corresponding physical tests taken from Huns et al. (2002) and Franchuk et al. (2002). The proposed block shear equation, Eq. 2-30, for the connection resistance, R_n , was based on these findings.

$$R_n = U_{bs}F_uA_{nt} + \min\left\{\begin{array}{l} 0.75F_uA_{nv} \\ 0.6F_u(A_{nv} + A_{gv})/2 \end{array}\right\} \leq U_{bs}F_uA_{nt} + 0.6A_{gv}(F_u + F_y)/2 \quad (2-30)$$

The main change is to the shear plane portion of the equation, which may be calculated as the smaller of two possibilities. It was found that when fracture occurs only on the net shear area, the stresses are better predicted as $0.75F_u$, rather than the $0.6F_u$ used previously. However, the $0.6F_u$ stress is applicable when the fracture area is taken as the average of the gross and the net shear plane areas. The U_{bs} term in the tension area term accounts for possible shear lag in the connected member. For a symmetrically connected member with no eccentricity, this factor is taken as 1.0. When compared to a database of previous physical tests, this equation was found

to result in the closest predictions when compared to the AISC 2010 (AISC, 2010) specifications (too conservative) and the CSA S16-09 Standard (CSA, 2009) (some unconservative results).

In the current AISC 360-16 Standard block shear is calculated as shown in Eq. 2-31, where ϕ is a resistance factor of 0.75:

$$\phi R_n = \phi [0.60F_u A_{nv} + U_{bs}F_u A_{nt} \leq 0.6F_y A_{gv} + U_{bs}F_u A_{nt}] \quad (2-31)$$

The block shear resistance is therefore taken as the lesser of fracture at the net shear and tensile areas or yielding at the gross shear area and fracture at the net tensile area. The U_{bs} factor is added to the tensile fracture component and is taken as 1.0 when the distribution of stresses is expected to be uniform and 0.5 when it is expected to be non-uniform.

Driver et al. (2006) recognised that different codes had different approaches to calculating block shear capacity, and that the different methods had varying degrees of accuracy for different types of members in tension. Driver et al. collected the results from 205 block shear tests. These included results for the following: gusset plates, angles and tees, and coped beams. Angles and tees were grouped due to similarities in behaviours. The results of these block shear tests were compared to the capacities calculated using the methods in the following codes: AISC 360 (1999), AISC 360 (2005), CSA S16 (2001), and Eurocode 3 (1993). Furthermore, methods introduced in the following papers were also compared: Cunningham et al. (1995) and Topkaya (2004). Finally, an author-proposed unified equation given by Eq. 2-32, where R_t and R_v vary for different types of members, was also compared.

$$P_u = R_t A_{nt} F_u + R_v A_{gv} \left(\frac{F_y + F_u}{2\sqrt{3}} \right) \quad (2-32)$$

For different member types, the different methods had varying success of predicting the measured block shear failure resistance of test specimens. However, the proposed unified equation gave the most consistently accurate results. Furthermore, by using a resistance factor of $\phi = 0.70$ with the proposed unified equation, satisfactory levels of safety were achieved.

2.2.5 Effect of flexure in bolted connections

The effects of flexure in the end connections of braces are not accounted for directly in design according to CSA S16-14. The $2t_g$ linear gusset plate clearance is prescribed in MD and LD type CBFs to allow for the rotational demand. However, when this clearance distance is omitted, flexural stresses may be induced at the bolted connection as the brace end rotates out-of-plane. For this reason, the effects of flexure in bolted connections are discussed in this section.

Lilly and Carpenter (1939) conducted tests to determine the effect of rivets and holes in the tension flange of girders in bending. The standards at the time indicated that in designing such girders, the net section properties of the tension flange should be used in order to determine the bending capacity of the member. The authors postulated that due to the discrete number and placement of the rivet holes, this approach would be highly conservative. The authors performed tests to determine the effect of the holes in the tension flange of girders and compared the results to the predicted capacities using both the gross section properties and the net section properties.

Two types of girder specimens were tested in bending. Spacing between the holes or rivets of 5 inches and 2.5 inches were used. The specimens were loaded to service loads. Four cases were studied: no holes in the flanges, open holes in the flanges, machine bolts in the holes, and rivets in the holes. In addition, different cross-sectional areas were tested by the addition of cover plates to the flanges.

The location of the neutral axis in relation to the centerline and the effective moment of inertia obtained by specifying the deflection of the girders were determined and compared to the experimental data. For the girders tested, the experimental distance of the neutral axis from the centerline was smaller than the theoretical distance calculated with the net section properties. Likewise, the effective moment of inertia calculated using the gross section was closer to experimental effective moment of inertia than when calculated using the net section properties. However, as the pitch decreased, the experimental results approached those calculated using the net section properties. At the end of the paper, the authors state that it would be acceptable

for design purposes to use the gross section properties for girders in bending with holes in the tension flanges with a modification for girders with small pitch or cantilever girders.

Several authors expressed disagreement with the conclusions made by Lilly and Carpenter regarding their paper on the topic of net and gross section properties of girders in bending (Osgood et al., 1940). Most authors criticize the generalizations made in the conclusion, particularly that net section properties do not have to be used for the acceptable design of girders. Furthermore, most authors note that the calculations used to compute the effective moment of inertia from a known deflection would yield an average value from the entire length of the member. These properties would therefore not give the maximum stresses in the tension fibres. The stresses in the tension fibres near the net section holes would be greater than those at the gross section. Further testing was recommended by some authors including testing beyond service level loads.

The 15% rule in the CSA S16-14 Standard, which states that the gross section properties can be used if the net section area in tension is not less than 85% of gross section area in tension, was based on the findings of this paper by Lilly and Carpenter (1939).

In their paper, Dexter et al. (2002) observed the behaviour of tension flanges of different grades of steel (HPS70W high performance steel, HPS100W, and Grade 50 steel) with holes in bending with specific focus on the ductility of the HPS70W as compared to the other steel types. It was found that the ductile behaviour of the different sections could be characterized by the following ratio: $(A_n/A_g)/(Y/T)$ (where (Y/T) is the yield-to-tensile strength ratio). An adequate ductility resulted when this ratio was equal to 1.0 for all steel types. ABAQUS models were then used to predict the behaviour of the plates in tension. Using shell elements to model the member achieved sufficiently accurate results. The results were in accordance with the 15% rule. HPS70W displayed an adequate performance in both the tension and the flexural tests. It was further shown through the use of analytical models that the provisions of AISC 360-05 (AISC, 2005) with factors $\phi=0.5$ and $\Omega=1.67$ to calculate flexural resistances remained conservative in the case where holes were to be found in the tension flange of a W-shape Geschwindner (2010).

In subsequent tests (Dexter and Altstadt, 2003), girders of different material strengths (345 MPa and HPS-485) with splices were tested under bending loads. All specimens met the minimal design requirements for rotational ductility and achieved plastic behaviour. This paper builds on the previous research in plates (Dexter et al., 2002) by expanding the study to girders with splice connections. Compared to a plate, the tension flange of a girder in bending is somewhat restrained due to its connection to the web of the member. Dexter and Altstadt concluded that the higher strength steel, HPS-485, achieved the expected plastic moment and rotational ductility and no additional factors need to be considered. The member can fail at either the gross section plastic moment or at the net section fracture moment thus both should be checked. Unlike the results for the tests on tension members in Dexter et al. (2002), the ratio $(A_n/A_g)/(Y/T)$ did not seem to be a good indicator of ductile performance for girders: performance was adequate even in members whose ratio was 0.74. This study contributed to the validity of the 15% rule.

More recently, W-shape beams with holes in the tension flange were tested to measure the effect of yield-to-ultimate strength ratio on the behaviour of members (Sivakumaran et al., 2010). The authors estimated that the CSA S16-14 Standard, which is based on the 15% rule, is overly conservative for steel grades with yield-to-ultimate ratios less than 0.85 and inadequate for those with a ratio greater than 0.85 such as in the case of high strength steel. Four series of tests were conducted in this study. The first series had no hole in the flanges. The second series had holes in the tension flange with the net tension area percentages of the gross tension area varying between 50% and 90%. The third series had holes in both tension and compression flanges with net section area percentages of the gross section area varying between 60% and 85%. The last series had fasteners in all of the holes. The average yield-to-ultimate strength ratio was calculated to be 0.77 for the specimens. The specimens were loaded in four-point bending. For beams with holes in the tension flange, the failure mode changed progressively from compression flange buckling (with no holes) to net section fracture as the $(A_n/A_g)/(Y/T)$ decreased. If a strength variation of $\pm 5\%$ is deemed acceptable for design, then the net section of up to 71% of the gross area section could be used for beams of ASTM A992 grade steel. Based on these results, the CSA S16-14 15% rule appears to be overly conservative for this grade of steel. Specimens with holes in both tension and compression flanges were more likely to fail due to buckling as the

compression flange was weaker. However, including fasteners improved the performance of the specimens as compared to the specimens with holes in both flanges. These results agree with the findings of Arasaratnam (2008) from both experimental testing and finite element modelling.

2.2.6 Impact of hole-making process

Bar and tee specimens of different steels were tested in tension with holes of three diameters made by drilling, punching (using new and a worn equipment), grinding, and flame cutting to determine the effect of different hole-making procedures on the performance of tension members (Yuan, 2005). The quality for the drilled holes was visibly the best. The other holes were visibly less accurately cut. The holes fabricated with the worn punch equipment exhibited the worst quality in appearance. The drilled holes showed the most ductility followed by the flame cut holes. The cyclic tests for the different hole-types showed no difference between the steel grades and only a small change in ductility. Even though the punched holes displayed a decrease in ductility, enough ductility remained in the connection to develop the strain-hardened capacity of the members in tension.

In fabrication, 2 mm are added to the diameter of bolts for the diameter of the boltholes to allow for a certain tolerance in installation. In design calculations, the bolthole diameter is further increased to account for damage to the cross-sectional steel as a result of the hole-making process. In CSA S16-14, 2 mm are added to the bolthole diameter. However, this can be omitted for drilled holes corresponding to the greater performance as noted in Yuan (2005). In AISC 360-16, 1/16 in is added to the nominal diameter of the hole regardless of the hole-making process used.

2.2.7 Bolted connections at W-shape ends

In recognizing the use of W-shape braces for seismic resistance, Tanaka and Enomoto (1986) ran tests on the bolted splice connections of such members under tensile loading to quantify the tensile capacity of these connections subject to variations in bolted connection parameters such as end distance and bolt layout. Specimens included splice plates on only the flanges and splice plates on both the flanges and the web. They concluded that specimens with bolts in both the web and the flanges performed better in term of both slip resistance and ultimate tensile

resistance. Additionally, in the cases where the slip resistance was significantly greater than the gross section yield resistance of the W-shape, the connection details including the bolt layout and spacing were found to be inconsequential. In subsequent tests (Tanaka and Enomoto, 1989), the W-shaped specimens were connected to gusset plates by bolted plates or angles, and the specimens were subjected to cyclic loading. The connection designs and configurations were varied as shown in Figure 2-14, where each column represents a different type of connection (labelled J1-J4). The resulting force vs. deformation hysteretic curves of the specimens are shown in Figure 2-15. The connections were designed for three different strength levels, all of which were set to be higher than the yielding strength of the brace allowing the braces to yield prior to failure. The authors concluded that the connection design labelled J3 displayed better force vs. deformation hysteretic behaviour because it was connected directly to the gusset plate, while the connection design labelled J4 achieved the worst results.

Udagawa et al. (1998) ran similar tests on bolted W-shapes of section size H-250x150x7x10 made of steels with high ultimate strengths (590 and 780 MPa) and a more traditional SS400 steel (with an ultimate strength of 400 MPa). By testing specimens with only flanges connected, with only web connected, and with both connected, the assumption that the total connection capacity would be equal to the sum of the individual capacities of the flanges and the web was found to be true for the tested specimens. Failure modes included two types of block shear in the flanges and the web, plug shear in the web, and net section fracture.

Cai and Driver (2008) conducted monotonic tension tests on 50 full-scale wide flange bolted connections. The specimens were separated into three categories: (1) 12 W-shapes connected by the web only with an expected failure mode of bolt tear-out, (2) six W-shapes connected by both flanges and webs with combined failure modes of bolt tear-out and block shear, and (3) 32 W-shapes connected by the web-only designed with varying end distances. The bolt gauges, number of bolts, and end distances were varied between the specimens. The results most pertinent to the current work were those for the second category of tests showing the combined failure modes of the flanges and webs. The section sizes selected for the first two categories of tests were the following: W310x60, W310x39 and W250x49. 3/4" and 7/8" diameter bolts were used.

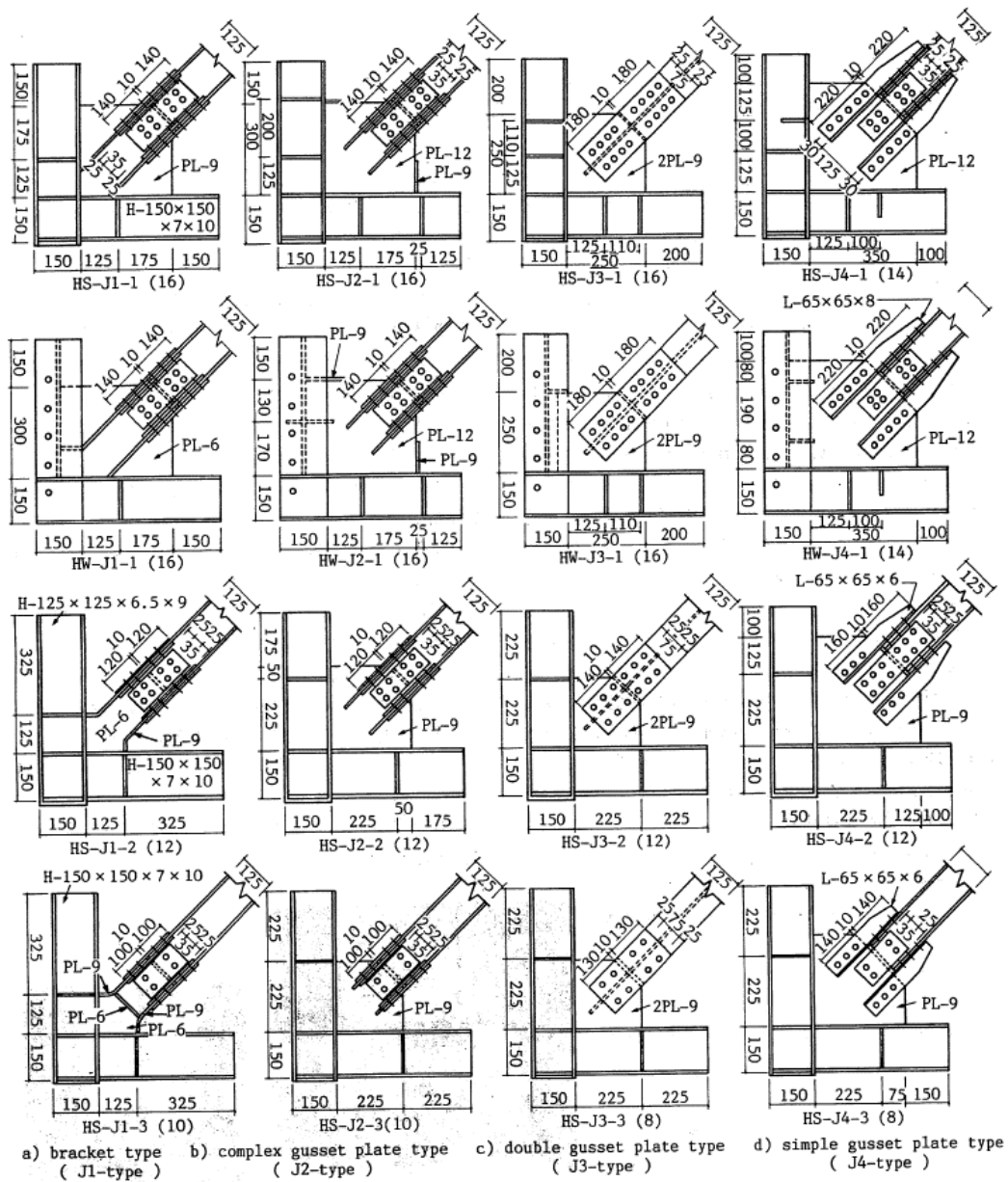


Figure 2-14 Specimen connection configurations (Tanaka and Enomoto, 1989)

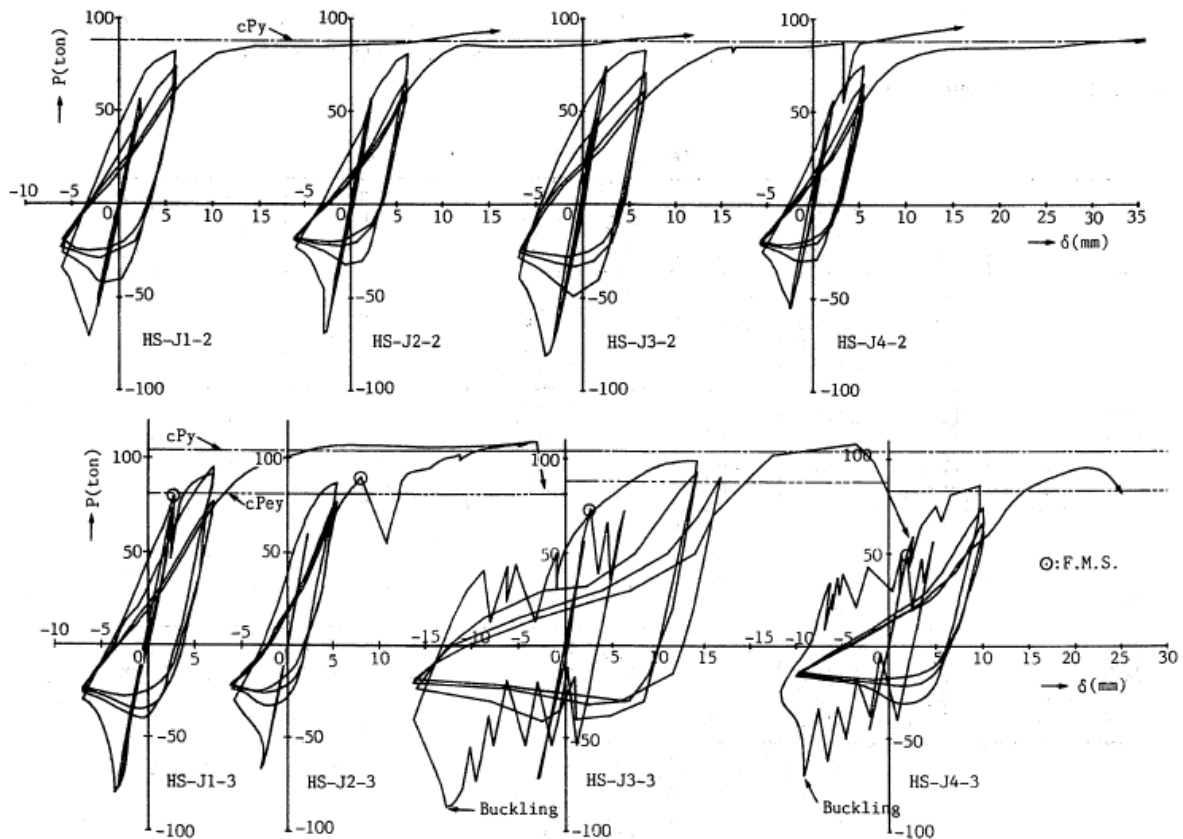


Figure 2-15 Force vs. deformation hysteretic curves of test specimens (Tanaka and Enomoto, 1989)

In the first category, the failure in the web was plug shear as expected. For the specimens in the second category, the predicted capacities were obtained by superposition of the individual capacities of the web and flange elements. The tests confirmed that the connection was ductile enough to develop forces in both the flanges and the web; however, the distribution of the forces in each element was not measured. The most common failure mode for the specimens in this category included plug shear failure in the web and block shear failure in the flanges.

The specimens with thicker webs, in the third category, were more likely to fail in a combination of bolt shear and bolt tear out or bearing. It was observed that the bolts in the row closest to the edge of the connection (outer bolts) were unable to develop their full capacities, as they were more flexible than the bolts further within the connection (inner bolts). As such, a common failure included the bolt shear of the four inner bolts and plug shear or bearing failure at the two outer bolts.

For the specimens with thinner webs in the third category, failure modes included bearing failure for the inner bolts and plug shear for the outer bolts. These failures occurred sequentially as opposed to simultaneously. The predicted bearing capacities calculated using the CSA S16-01 Standard (CSA, 2001) and the AISC 360-05 Standard (AISC, 2005) had underestimated the true bearing capacities of the specimens by a margin of 32%.

The authors recognized that capacities calculated using the unified equation gave a much closer prediction than either the equations in the CSA S16-01 Standard or those in the AISC 360-05 Standard, which were deemed overly conservative. Therefore, the block shear equation shown in Eq. 2-33 (similar to Eq. 2-32) was suggested for the calculation of capacities for block shear, plug shear, and net section rupture, where the factor ϕ is taken as 0.75.

$$P_r = \phi A_{nt} F_u + \phi A_{gv} \left(\frac{F_y + F_u}{2\sqrt{3}} \right) \quad (2-33)$$

In conclusion, there remain many aspects of this connection type that create complexity and complicate the accurate prediction of the ultimate failure capacities of the bolted W-shape connection. In particular, the distribution of forces between the web connection and the flange connection is not very well documented and the actual combination of failure modes is not always accurately predicted by design equations. However, this study shows that Eq. 2-33, the unified equations, most closely predicted the ultimate capacity of such connections.

2.3 Summary

The design of braces for CBF systems is affected by various parameters that directly influence performance under seismic loading. The global slenderness ratio will strongly affect the drift ratio at which the braces buckle. However, very stocky braces will result in larger concentrations of forces at the ends of the braces. Width-to-thickness ratios govern the local buckling response. More compact sections will tend to delay the onset of local buckling. Cross-section shapes also affect the brace response. While different sections have varying benefits and disadvantages when it comes to brace design, W-shapes have been shown to attain larger drifts than other cross-sections.

However, brace parameters are not the only elements of SFERS design. The braces act in a system including connections, gusset plates, braced frame members, diaphragms and foundations. In CC-type construction, the behaviour of these elements needs to be considered, because the principles of capacity design are not applied. Many research programs have been conducted on the influence of gusset plate design on the ductility of CBF systems. In capacity design, gusset plates are designed to allow out-of-plane deflections of the braces either by a $2t_g$ linear clearance or an elliptical clearance as suggested by some researchers. However, such provisions are not required for CC-type CBFs. Research has shown that while the additional clearance improves ductility, CBFs with no clearance may also attain satisfactory ductility levels. However, the design of the connections at the ends of CC-type braces becomes very important.

In bolted brace end connections, the designer must consider multiple failure modes both in tension and compression, such as bolt shear, bolt bearing, net section, plug shear, and block shear. Some of these failure modes have more desirable behaviour in terms of ductility. Particularly, yielding and bearing of the connected materials are preferred over net section fractures and bolt shear failure. Additionally, due to the out-of-plane bending induced in the brace, flexural effects are also encountered in the brace end connections.

There is very little available research regarding CC-type brace performance with bolted end connections. While some experimental data is available for CC-type bolted connections (Castonguay, 2010), these do not include testing of full-scale bolted brace assemblies, specifically with W-shape sections. However, this study aims to fill the gap in available research by providing test data for full-scale W-shape brace specimens with bolted connections. Furthermore, this study was designed to try to help clarify some of ambiguity regarding ductility in these types of connections to address the requirements of Clause 27.11.1 of the CSA S16-14 Standard (2014).

Chapter 3: Pre-Testing Numerical Modelling

Numerical modelling was not the primary objective of this study; however, some limited modelling was performed to gain insight into the ductility demands experienced by CC-type W-shape braces under seismic loading.

The objectives of the numerical modelling component of this study included the following:

- (1) Create a nonlinear dynamic model that can predict, reasonably well, the cyclic behaviour of a CC-type braced structure with a bolted connection subjected to a range of scaled ground motions on a software commonly used in industry (ETABS).
- (2) Determine the displacement demand on the brace connections of the specified braces under seismic loading.
- (3) Develop a loading protocol for the test specimens representative of the displacements they would be subject to under seismic loading.

3.1 W-shape specimens and end connection design

The maximum size of the selected W-shapes was limited by the capacity of the testing equipment. W-shapes of sizes W360x134 and W310x97 were selected for numerical modelling and testing. These sections are compact and are of common depths for diagonals in multistorey and industrial buildings. Compact W-shape sections are commonly preferred for the smaller difference between the tension and compression capacities. Unlike for the MD and LD seismic design cases, there is no class restriction on local slenderness or limitations on the global slenderness of CC braces. Both the W310x97 and the W360x134 sections have a class 1 web and class 3 flanges according to local slenderness limits as defined by the CSA S16-14 Standard (2014). The global slenderness values of the sections were 45 and 78 for the W310x97 sections and 64 and 38 for the W360x134 section, in the y- and x-axis, respectively.

Once the brace sizes were selected, the factored design buckling capacities were used as the strength requirement to design the brace end connections. This was done because the design buckling capacity was assumed to be the limiting selection factor for a brace in a typical CBF building. The design buckling capacities of the braces were calculated using Eq. 2-2. The

calculated design capacities were 2209 kN for the W310x97 braces and 3680 kN for the W360x134 braces assuming a buckling length of 6 m (using a corner-to-corner length of 6.67 m multiplied by a K factor of 0.9).

In reviewing connections currently used in the industry for bolted end connections of W-shape braces, two common bolted brace end connections were selected for testing in this study. The two connections, as shown in Figure 3-1, will be called the jaw plate connection (connected by a plate at each flange of the W-shape) and the claw angle connection (connected by two angles at each flange of the W-shape) for the remainder of this thesis. While the angles are bolted on both sides of the connection, the jaw plates are welded on the side of the gusset plate. All connections include two splice plates connecting the web of the W-shape to the gusset plate to minimise shear lag effects, which would have occurred in an unconnected web at the end connections. Two web plates were used as opposed to one to eliminate additional eccentricity at the connection. Rectangular gusset plates were selected as opposed to tapered gusset plates. In addition to being easier to design and manufacture, rectangular gusset plates have shown less tearing under cyclic loading as compared to tapered gusset plates due to lower stress concentrations (Roeder et al., 2011a). However, in a finite element parametric study, these have shown less ductility in a frame than tapered gusset plates (Alipour and Aghakouchak, 2013) but allow for the attainment of greater tensile and compressive resistances.

The connecting components were designed such that the limiting factored tensile resistance, as calculated using resistance equations from the CSA S16-14 Standard, was greater than the factored design buckling load of the brace. The 1.5 factor for non-ductile connections in CC-type braces, as prescribed in CSA S16-14 Clause 27.11.1 (2014), was not used in these calculations. This approach was taken to determine whether this factor is necessary to meet seismic ductility requirements.

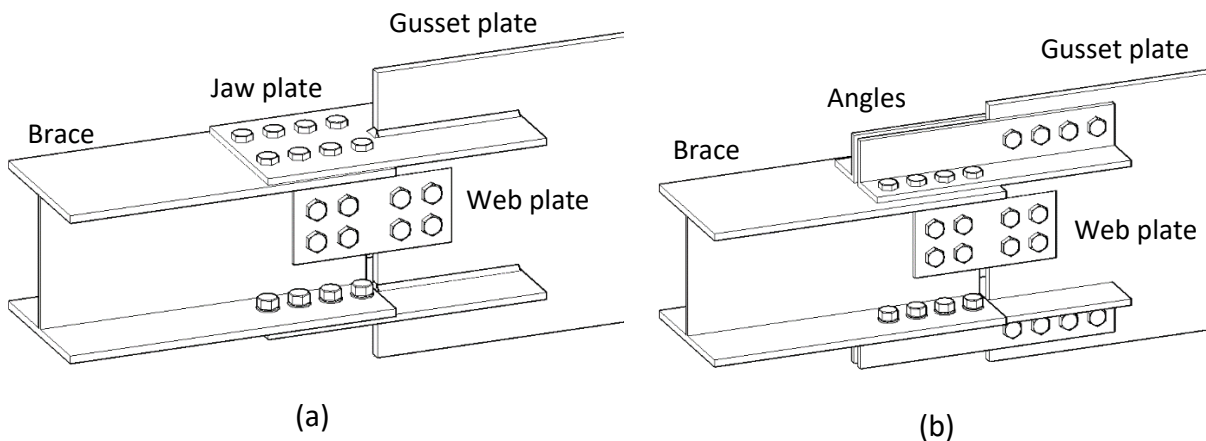


Figure 3-1 Standard bolted W-shape connections (a) jaw plate connection (b) angle connection

Two additional connections, as shown in Figure 3-2, were modified from the original connection designs in an attempt to improve the overall ductility. This was done by designing plates, thinner than the connecting plates at the flanges, to have a low bearing capacity allowing the bolts to bear onto this plate before attaining any other ultimate failure mechanism. As a result, these bearing plates would become a fuse during a design-level seismic event. To achieve a decreased bearing capacity, larger diameter bolts were chosen so that fewer bolts could be used. The connecting plates and angles, to which the bearing plates would be welded, would have slotted holes to allow the bolts to bear onto the bearing plates, which have standard holes sizes, for a predetermined bearing distance. A close-up of this bolt hole design is shown in Figure 3-3(a). The bearing plates would be welded onto the connecting plates or angles on both longitudinal sides.

An alternate design where there is no specially designed bearing plate is shown in Figure 3-3(b). In this design, the slotted hole is not punched through the entire connecting plate or angle to allow the bearing to occur directly in the connecting plate. While the alternate design is simpler, allows greater flexibility in the thickness of the bearing metal, and is more economical, it depends on the manufacturer's ability to create the intricate holes in the connecting plates. For this reason, only the design shown in Figure 3-3(a) will be discussed in this thesis.

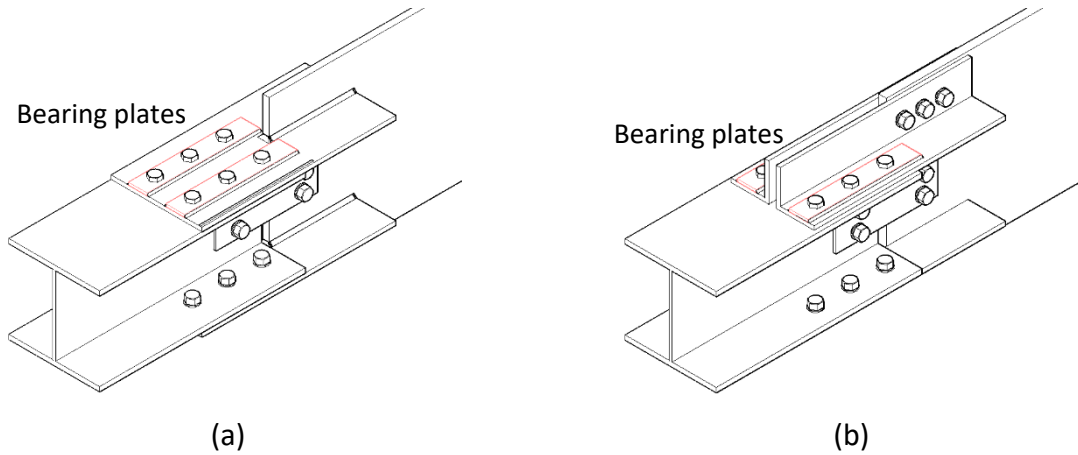


Figure 3-2 Modified bolted W-shape connections (a) modified jaw plate connection (b) modified angle connection

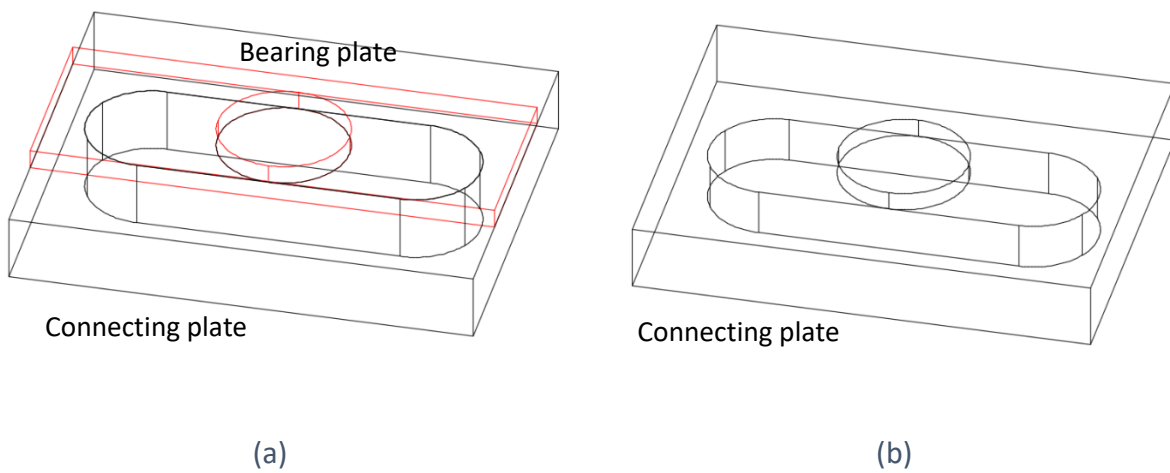


Figure 3-3 Close-up of fuse-type bearing connection (a) bearing plate configuration (b) alternate counter boring configuration

Overall, five different brace end connections were designed: a jaw plate connection for the W310x97 section, jaw plate and claw angle connections for the W360x134 section, and modified jaw plate and claw angle connections for the W360x134 section. A summary of the design elements and capacities can be found in Section 4.1.2. and detailed calculations for the common connections are shown in Appendix A.

3.2 Design of five buildings

Four-storey buildings (15 m in height in compliance with the CC building height restriction) were designed by varying the number of bays in each of the plan dimensions to obtain a seismic mass for which the SFRS design required the use of W310x97 and W360x134 brace sizes for two locations (Vancouver and Montreal) and two soil classes (E and C). The buildings in Vancouver were designed with four split-X braced frames in each direction, whereas the buildings in Montreal were designed with two split-X braced frames in each orthogonal direction. All braced bays were placed on the perimeter of the buildings. Bay widths were kept at 5.5 m and the bay heights at 3.75 m such that the corner-to-corner lengths of the braces were 6.66 m to match maximum brace length used for testing (see Chapter 4). In some cases, the last bay width was set to one quarter, half, or three quarters of the original bay width to obtain a more precise seismic weight for the building. Orthogonal views of an example building, as well as the 2D braced frame used in the SAP 2000 (2018) model, are shown in Figure 3-4. SAP 2000 v. 20.1.0. was used to do the preliminary brace design before switching to ETABS v. 17.0.1. for the nonlinear analysis of the models. The gravity frame design was carried out using the gravitational loads as presented in Table 3-1 and load combinations from the NBCC 2015 (NRCC, 2016) as presented in Table 3-2. The importance factor was set to 1.0 for normal type buildings.

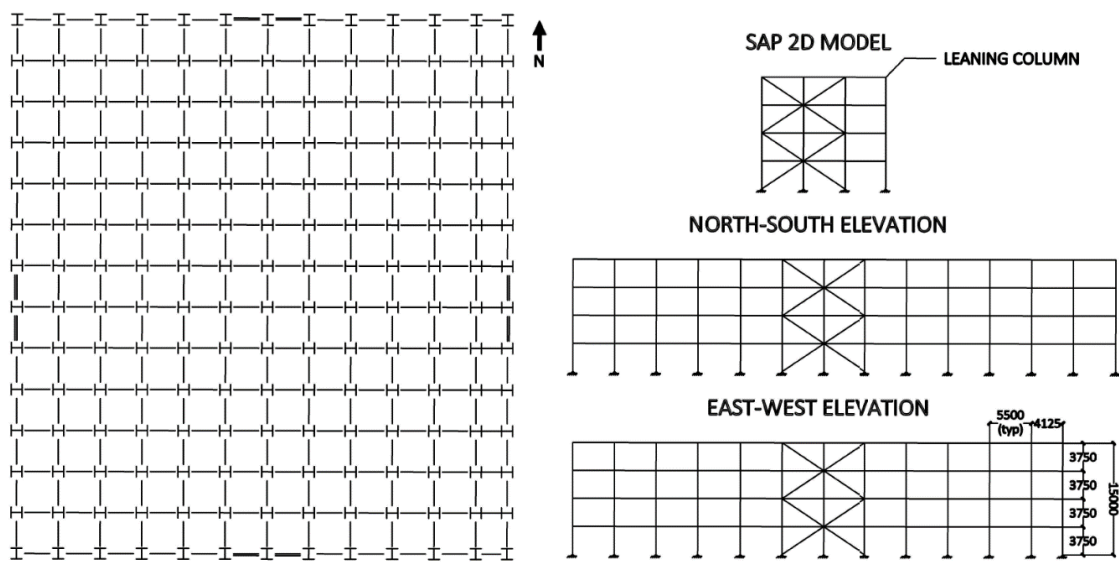


Figure 3-4 Plan view, elevations, and simplified model of an example building in the numerical modelling study

Table 3-1 Gravitational loads used in the gravity frame design of buildings in the numerical study

Roof snow load (kPa)	Montreal	2.48
	Vancouver	1.64
Roof dead load (kPa)		1.20
Roof live load (kPa)		1.00
Floor dead load (kPa)		3.70
Partitions (kPa)		1.00
Exterior walls (kPa)		1.20
Floor live load (kPa)		2.40
First floor live load (kPa)		4.80

Table 3-2 Load combinations (from NBCC 2015, Table 4.1.3.1.2.-A) used for design of buildings in the numerical study

Case	Load Combination	
	Principal Loads	Companion Loads
1	1.4D	
2	1.25D + 1.5L	1.0S or 0.4W
3	1.25D + 1.5S	1.0L or 0.4W
4	1.25D + 1.4W	0.5L or 0.5S
5	1.0D + 1.0E	0.5L + 0.25S

The Equivalent Static Force Procedure as described in the NBCC was used for the initial seismic design followed by an iterative dynamic analysis of the 2D braced bay frame using the SAP 2000 software. This 2D braced bay frame included a leaning column representing half of the building's seismic weight and stiffness in Montreal cases, and a quarter of the weight and stiffness in Vancouver cases to reflect two or four brace bays per direction, respectively. P-Delta effects on axial loads, as well as notional loads, were included in the numerical analysis. Accidental torsion effects were not considered, because they were assumed to have little effect on the four-storey, fairly symmetric, and regular buildings. A modal analysis was used to determine the building vibration modes. The seismic axial loads in the braces were extracted from a response spectrum

analysis with 5% constant modal damping. Design spectra from the NBCC 2015 for the four specific cases were used in the analysis.

The seismic weight was varied between iterations to obtain a design which included W310x97 and W360x134 members as braces in the braced frames with a resistance efficiency of 90% or greater, calculated as the factored axial load over the factored resistance of the brace. For the four given cases, it was found that the first-storey braces were W360x134 sections and the third-storey braces were W310x97 sections, with the remaining storeys in the buildings having braces of other section sizes. A fifth building (VE_11x10.25) was used to verify the effect of increasing the resistance efficiency of the first storey brace (W360x134) from 93.6% to 98.6%. A summary of the seismic information and design details for the five resulting buildings is provided in Table 3-3. The nomenclature for the names of the building models contains the following parts: the first letter indicates the location (M for Montreal and V for Vancouver), the second letter indicates the soil class (C or E), and the two following numbers indicate the number of bays in the North-South and the East-West directions, respectively, separated by an "X". The bolded base shear is the base shear used for design (seismic forces from SAP 2000 were scaled if they surpassed the 0.8V base shear limit as prescribed by the NBCC 2015).

Table 3-3 Summary of seismic design for building models

ID	VE_11x9.75		VC_13x11.75		ME_13x11.75		MC_17x14.5		VE_11x10.25	
BUILDING LOCATION	Vancouver		Vancouver		Montreal		Montreal		Vancouver	
SOIL CLASS	E		C		E		C		E	
NO. NS BAYS	11		13		13		17.00		11.00	
NS LENGTH (M)	60.5		71.50		71.50		93.50		60.50	
NO. EW BAYS	9.75		11.75		11.75		14.50		10.25	
EW LENGTH (M)	53.63		64.60		67.38		79.75		56.38	
AREA (M²)	3244		4621		4621		7457		3411	
SEISMIC MASS (KN)	50713		71155		72144		114714		53187	
C_F/C_R OF W360X134	0.936		0.942		0.955		0.995		0.986	
C_F/C_R OF W310X97	0.985		0.983		0.985		0.977		NA	
PERIOD AND MASS PARTICIPATION PERCENTAGE	0.467	78%	0.552	78%	0.795	78%	1.029	78%	0.473	78%
	0.176	16%	0.205	17%	0.292	17%	0.367	17%	0.177	16%
	0.122	5%	0.141	4%	0.197	4%	0.246	4%	0.121	4%
	0.086	1%	0.102	1%	0.145	2%	0.185	2%	0.086	1%
T_A (S)	0.47		0.55		0.75		0.75		0.47	
V (KN)	26480		26214		13227		13501		27772	
0.8V (KN)	21184		20971		10582		10801		22218	
V_E (KN)	41358		41411		20619		15986		43704	
V_D (KN)	21209		21236		10574		8198		22412	

A summary of brace sizes per floor for all the buildings is provided in Table 3-4.

Table 3-4 Summary of brace section sizes per floor

ID	VE_11x9.75	VC_13x11.75	ME_13x11.75	MC_17x14.5	VE_11x10.25
1	W360x134	W360x134	W360x134	W360x134	W360x134
2	W310x129	W310x129	W310x129	W310x117	W360x134
3	W310x97	W310x97	W310x97	W310x97	W310x107
4	W200x59	W250x67	W200x71	W250x73	W250x67

An example of a braced bay design (for VE_11x9.75) is shown in Figure 3-5.

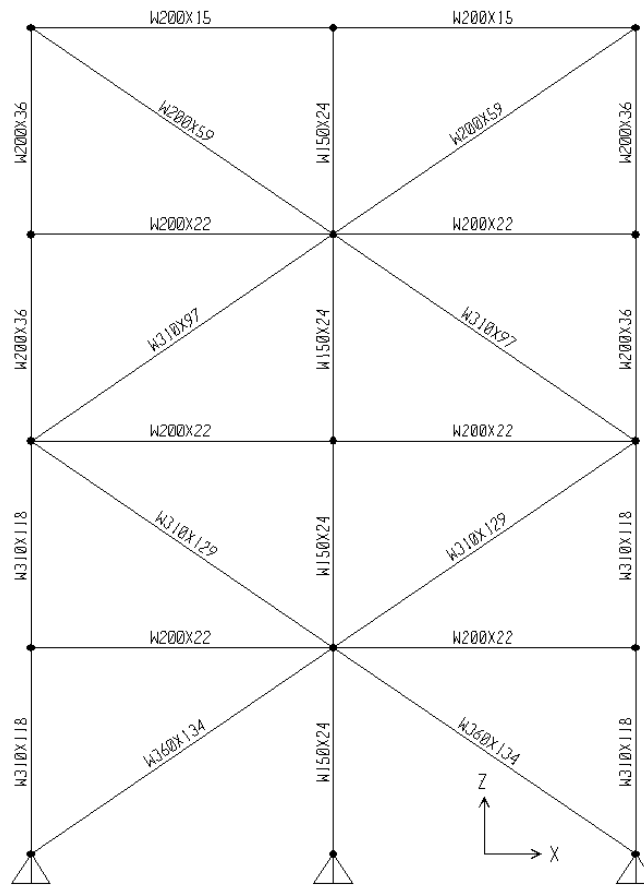


Figure 3-5 Example of split X braced bay frame (VE_11x9.75)

3.3 Nonlinear modelling

Models were created in ETABS v. 17.0.1 (2018) with the goal of capturing the nonlinear behaviour of the braces and the bolted connections under seismic loading, and observing the ductility

demands on the connections. ETABS was used for these numerical models as it presents better capabilities for nonlinear analysis, particularly in the application of P-Delta effects.

3.3.1. Preliminary models

Preliminary models aimed to include bolt slip, brace buckling, and the connection's tensile response at yield and ultimate failure, yet be simple enough that an industry-wide numerical modelling software such as ETABS could yield satisfactory results. Many model variations were evaluated that were not able to converge or show the expected behaviour under seismic loading. A short overview of these preliminary models is provided in this section for the purpose of posterity.

Each of the braces was created from a collection of links connected in parallel or in series. A link is a two-node frame element in ETABS to which a number of various behaviours and stiffness's can be attributed (similar to spring elements). The behaviour of the bolted braces was separated into four parts: the initial elastic response, the slip plateaus, the brace buckling in compression and the yielding and rupture response in tension (as shown schematically in Figure 3-6).

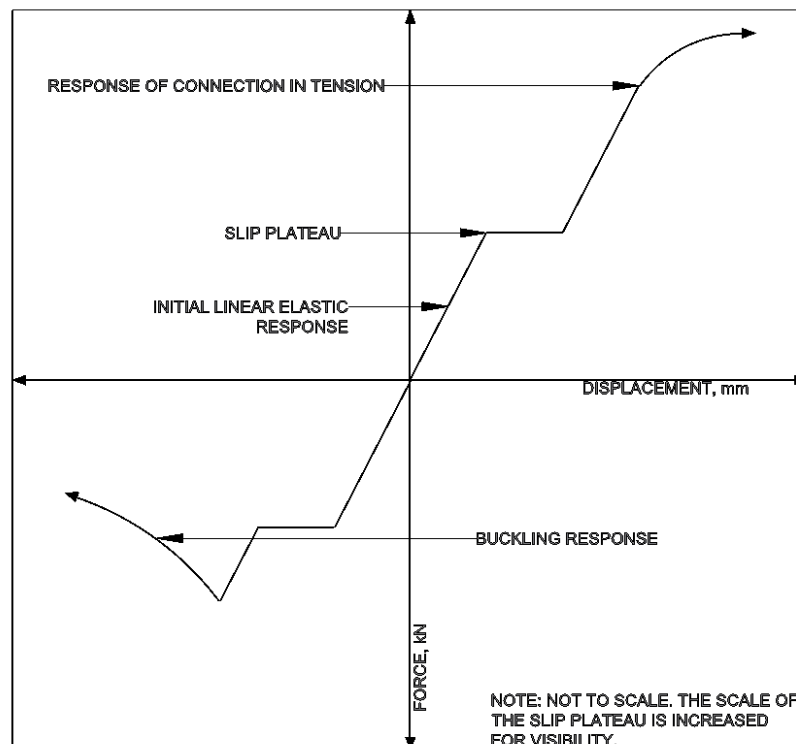


Figure 3-6 Generalized axial force vs. displacement backbone curve for modeled brace response

Different link elements were needed to characterize each behaviour. Five links with different behaviours were created and combined into a single brace to create the desired complex behaviour. The generalized characteristics of these links are described below, without going into detail because certain values and characteristics were varied between several trials and models.

The first three types of links were drawn in parallel (with each beginning and ending at the same nodes) to model the slip behaviour characteristic of bolted connections through the superposition of different behaviours. The first link labelled the “Slip” link modelled the initial linear elastic behaviour and slip plateau of a typical bolted connection. The behaviour of this link was governed by a kinematic multilinear plastic backbone curve, as shown in Figure 3-7(a). The linear elastic region extended to a displacement equivalent to the slip capacity divided by the stiffness of the link in both the negative and positive loading directions up to the slip capacity of the connection at which the force level was capped. The stiffness was assigned as three times the calculated brace stiffness so that the stiffness’s of the three parallel elements together gave the correct stiffness of the brace. The next two link elements, labelled “Gap” and “Hook” links, allowed the force to increase over the slip capacity once the displacement would be large enough for the bolts to make contact with the steel. Since the holes were made with a 2 mm allowance, this distance was approximated as 2 mm for the jaw plate connections and 4 mm for the claw angle connections, which had bolts on either side of the connection. The Hook element closes in tension, while the Gap element closes in compression. The force-displacement definitions for the gap and hook elements are shown in Figure 3-7(b and c). The overall behaviour of the superimposed links is shown in Figure 3-7(d).

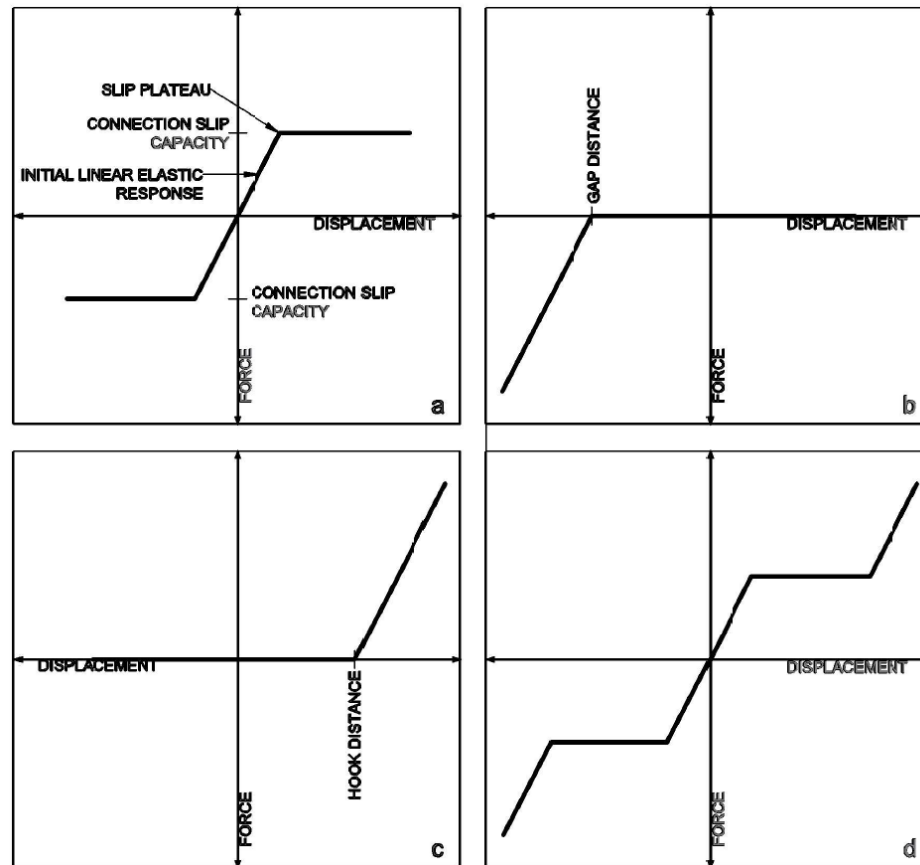


Figure 3-7 Force-displacement backbone of (a) Slip element, (b) Gap element, (c) Hook element, and (d) expected combined response

The next two links controlled the behaviour beyond the slip plateau in either tension or compression. The first element, which governed the compression side of the response, had a force-displacement definition following the expected backbone curve of typical brace buckling. These definitions depended on the section size of the modelled brace: W310x97 or W360x134. This link element was labelled the “Buckling” link in the models. The second element, which governed the tension side of the response, had a force-displacement definition modelled after results from previous tests on CC bolted connections (Castonguay, 2010). The definition depended on the expected tension mode of failure in the connection such as bolt shear, net section fracture, block shear, or steel bearing. This link element was labelled the “Connection” link in the models. Various force vs. deformation hysteresis types such as Kinematic, Takeda, and Pivot were used in different trials to characterize the force-displacement definition. Further details on the development of the force-displacement definitions of these links are provided for

the final model in Section 3.3.2. Frame elements were also added between the beginning and end nodes of the brace models to accurately model the flexural rigidity of the brace. The cross-sectional area of this superposed frame element was scaled down to be relatively negligible so as not to affect the axial response of the braces.

These links were then combined in different models to observe the full behaviour. Models varied in complexity for different trials from a simple brace, to a single-storey braced bay, to a four-storey braced bay. Fast Nonlinear Analysis (FNA) and Ritz modal analysis were used to analyze most of the models. However, certain trials were run with direct integration and the Eigen modal case sub type. In all cases, either the analysis was aborted before completion due to convergence issues or the combined behaviour of the links in the brace was non-realistic.

An example of a single brace model is discussed to exemplify what is meant by non-realistic behaviour. The single brace was oriented horizontally, as shown in Figure 3-8. Additional Gap and Hook elements with the same properties as discussed above were added such that the nodes of the buckling link and the connection link did not coincide. This was done in an attempt to separate the links involved in the response to compression loading (Gap elements and the Buckling element) and the links involved in the response to tension loading (Hook elements and the Connection element).

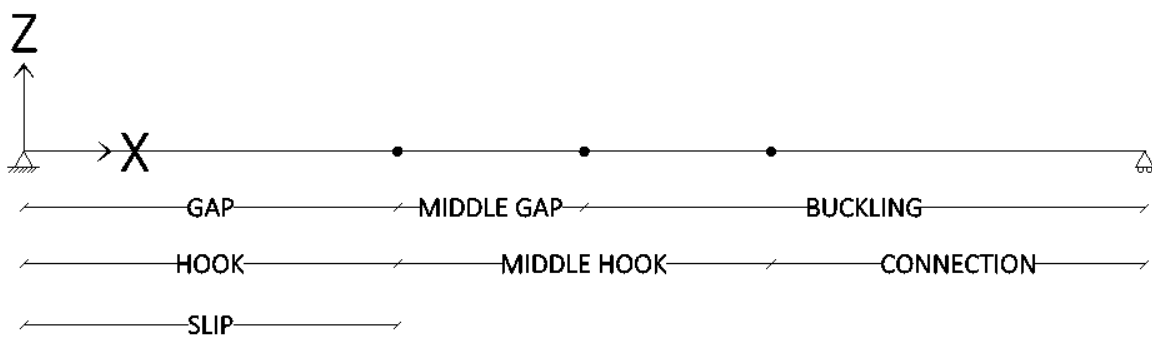


Figure 3-8 Link composition of example ETABS model

Figure 3-9 shows the response histories of the forces in the links when subjected to a sample earthquake loading (limited to the first 50 seconds). To comply with equilibrium, the total axial

force at every point on the brace (sum of the forces in the superimposed links at that point) should be equal for the full length of the brace throughout loading. Additionally, Gap and Buckling elements should not carry any tensile forces and Hook and Connection elements should not carry any compression forces, as shown in Figure 3-9(a), where the link force response histories of the Buckling and the Connection elements do not overlap.

The problematic behaviour arises after the brace goes beyond the slip deformation. Due to the stipulations made in the paragraph above, when the brace is in compression, the axial force in the Buckling element should be equal to the axial force in the Middle Gap element and the sum of the forces in the Gap element and the Slip element. However, this is not the case throughout the response history as illustrated in the magnified portion of Figure 3-9(b) (the Middle Gap and Middle Hook element response histories were not shown in this figure for clarity). In this magnified image, it is shown that the force in the Hook element is not zero when the brace is in compression. To comply with equilibrium, an increased compressive axial force in the Slip element balances this tension in the Hook element, while the force in the Gap element remains zero. However, this is not the desired behaviour. As this issue was not resolved throughout the trial models, the slip modelling was removed from the final model.

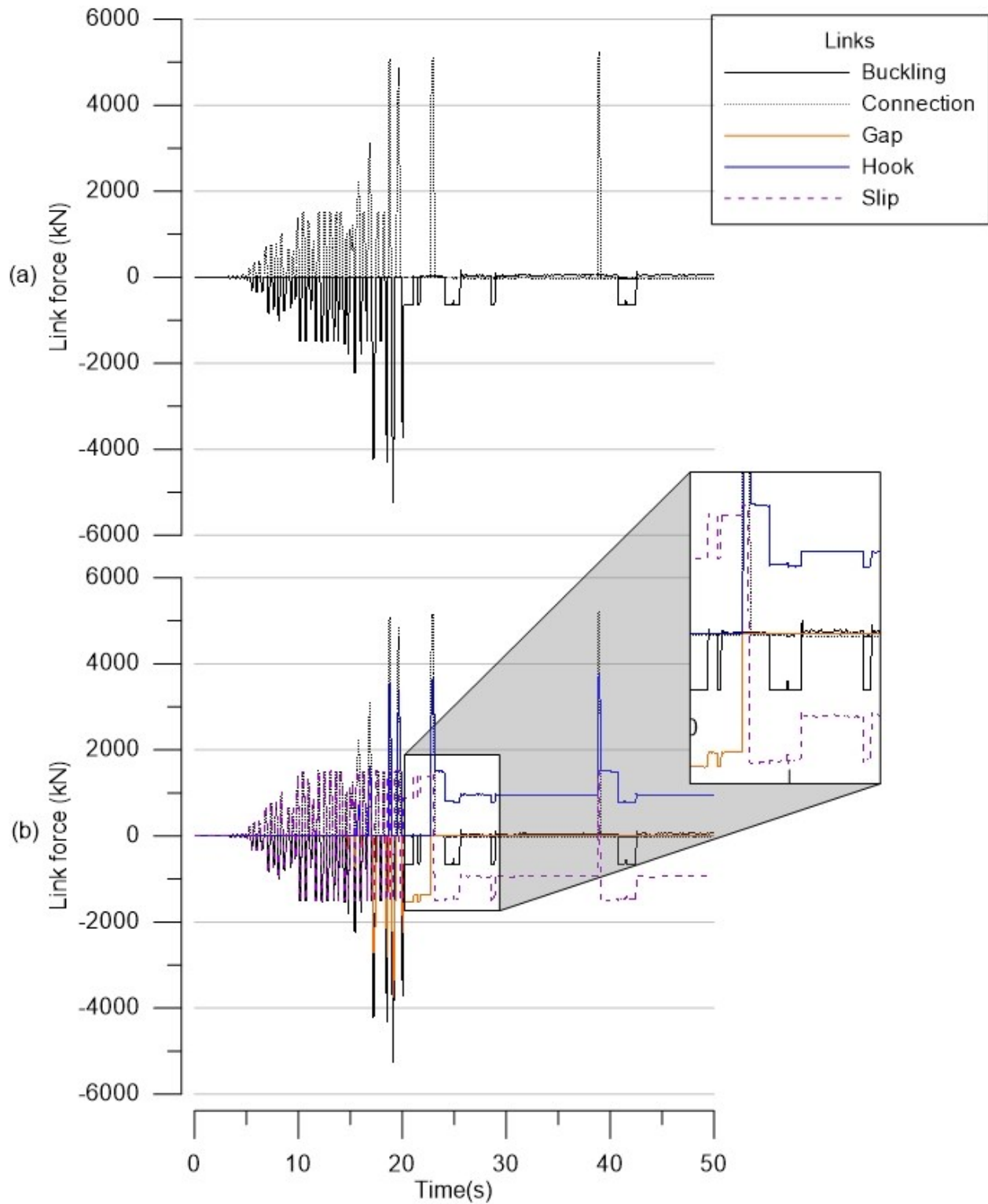


Figure 3-9 Link force response histories for (a) Connection and Buckling elements and (b) all elements excluding the Middle Gap and Middle Hook elements

3.3.2. Final model

The final model was created with one multilinear link element and two frame elements. The force-displacement definition of the multilinear link element was composed of the brace buckling response in compression and the tension response determined by the expected failure mode of the connection. The Pivot model was chosen for the force vs. deformation hysteresis type. While this model was initially developed for reinforced concrete members (Dowell et al., 1998), it has a pinched shape which coincides well with steel W-shape brace behaviour given certain specified parameters. The required parameters were set as follows as calibrated for W-shape braces by Brunet (2018): $\alpha_1 = 100000$, $\alpha_2 = 0.1$, $\beta_1 = 0.015$, $\beta_2 = 1$, and $\eta = 10$. The effective stiffness was entered as the nominal stiffness of the W-shape brace. No effective damping was applied to the link because this is not necessary for FNA.

The length of the link was defined as the length of the jaw plate connection assembly for the W360x134 brace without the bearing plate modification (443.8 mm). This length was not changed for other assemblies because the insignificant change to the length was not deemed to have a significant effect on the overall brace response.

For the buckling response of the link's force-displacement definition, the points used for the backbone curve are presented in Table 3-5. In this table, δ_u is the displacement at the ultimate compressive capacity, δ_y is the displacement at brace yield, C_u is the probable buckling capacity, C'_u is the probable post-buckling capacity, and K is the brace stiffness. The displacement, δ_u , is calculated using an empirical equation, as shown in Eq. 3-1 (Tremblay et al., 2003).

Table 3-5 Force-displacement definition in compression

Displacement (mm)	Force (kN)
$-\delta_u - 0.001$	0.0
$-\delta_u$	$-0.1C_u$
$-3\delta_y$	$-C'_u$
$-(C_u/K + 3\delta_y)/2$	$-C'_u + (C_u/K - 3\delta_y)$
$-C_u/K$	$-C_u$
0.0	0.0

$$\delta_u = \frac{(8.3\lambda + 2.4)\delta_y}{2} \quad (3-1)$$

For the tension side of the force-displacement definition, the backbone curve was derived from predicted ultimate capacities calculated using nominal material properties multiplied by R_y , unfactored design equations from CSA S16-14, and laboratory results from Castonguay's (2010) tests on bolted connections under monotonically increasing loading. The force-displacement curves from Castonguay's tests were simplified by a bilinear curve with one point at yield displacement (estimated from figures), one point at ultimate displacement (average ultimate displacement and average ultimate force were provided in the results), and one point at rupture (displacement at rupture was estimated from the figures). An example of Castonguay's force-displacement results for the bearing failure is provided in Figure 3-10. Once the force and displacement values at these points were obtained, the values of the forces were compared to the predictions given by unfactored equations from the CSA S16-14 Standard with probable material properties. From these comparisons, scaling factors were calculated for all potential failure modes in tension including bearing, net section, bolt shear, and block shear. The scaling factors are shown in Table 3-6. F_r and δ_r are the force (always zero) and the displacement at rupture, respectively. F_{exp} is the tensile connection capacity calculated with resistance equations from the CSA S16-14 Standard, unfactored and with material strength properties multiplied by the 1.1 R_y factor. Therefore, each nonlinear link represented the deformation of only one connection out of two. It was assumed that once the bottom or top connection started yielding, most of the deformation capacity would come from that end of the brace.

Additionally, the bearing connection models were further modified to increase the ductility for the specially designed connections. This was done to account for the bearing length allowance in the physical connections. The length in the physical connection was then modified based on the results obtained from the numerical models. This was done by extending a plateau at the ultimate force resistance to a displacement of 60 mm followed by a linear loss in capacity to zero at 70 mm. These displacements were found to be sufficient such that the nonlinear links did not rupture for any of the ground motions, and such that the models could reach the deformation length requirement of the bearing plate connections without numerical convergence problems.

The brace model also included two frame elements. The first frame element, which connected to a node shared with the non-linear link, was used to achieve the correct modal period for the building. The area of this frame element was multiplied by a factor of varying magnitudes depending on the link's force-displacement definition. For example, the VE_11x10.25 building with the jaw plate connections had frame elements with the areas multiplied by 30, whereas the same building with the bearing plate connection had frame elements with areas multiplied by 5.7.

The second frame element was assigned a length equivalent to the full length of the brace. Its purpose was to keep the non-linear link and the first frame element in line with each other throughout the duration of the applied ground motion excitation. The area of this frame was multiplied by zero such that it did not provide any additional axial stiffness. A diagram of the brace model is shown in Figure 3-11.

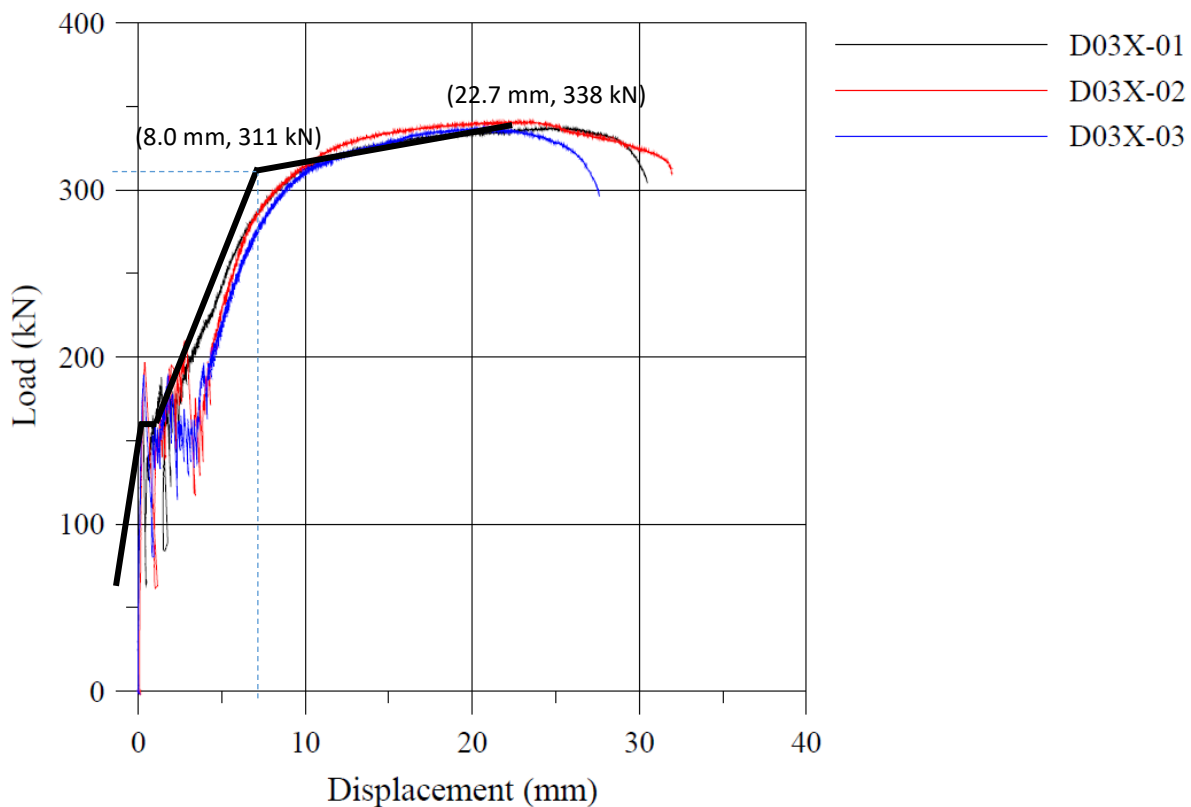


Figure 3-10 Example force-displacement monotonic test results for the bearing failure mode serving as the basis of numerical models' backbone curves (modified from Castonguay (2010))

Table 3-6 Force-displacement definition points for tensile failure modes

	δ_y	F_y	δ_u	F_u	δ_r	F_r
Net section (punched)	8.125	0.86 F_{exp}	16	1.03 F_{exp}	20	0
Net section (drilled)	10	0.9 F_{exp}	32.8	1.08 F_{exp}	37.5	0
Bearing	8	1.22 F_{exp}	22.7	1.34 F_{exp}	30	0
Bolt rupture	7	1.15 F_{exp}	15.7	1.28 F_{exp}	18	0
Block shear	7.8	1.06 F_{exp}	15.5	1.25 F_{exp}	20	0

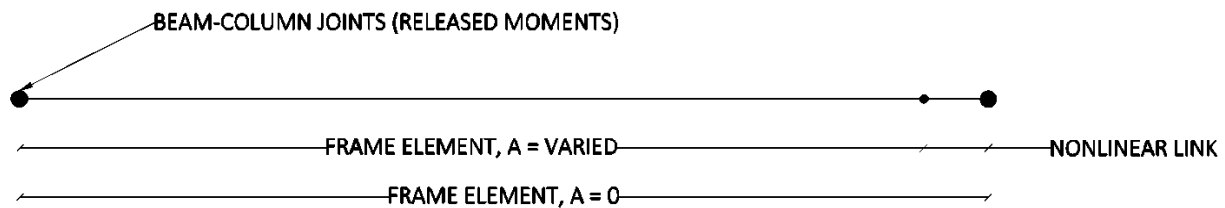


Figure 3-11 Final nonlinear numerical brace model

The rest of the braced frame was built with regular frame elements. The beams were pinned at both ends and the columns were continuous over two storeys. The masses were removed from the frame elements as it was assumed that structural masses were included in the point masses. Point masses were attributed to each storey at the corner(s) where the braces met the beam-column joint(s). The leaning column included the total stiffness of all columns for half (Montreal) or a quarter (Vancouver) of the building and was connected at each storey to the right side joints of the braced frame via rigid diaphragms. An example of the braced frame modeled in ETABS for MC_17x14.5 for the jaw plate connection is shown in Figure 3-12.

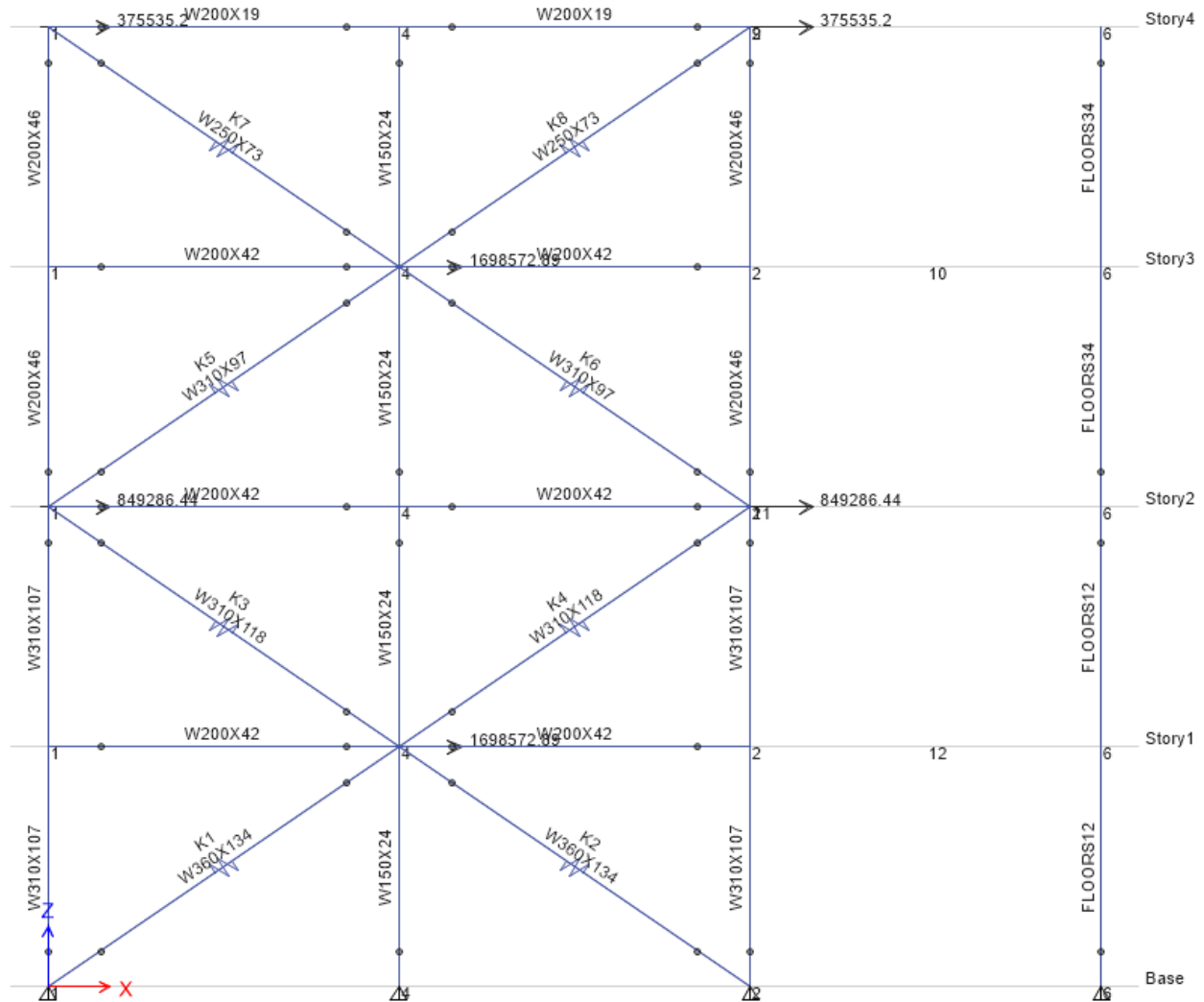


Figure 3-12 MC_17x14.5 model with jaw plate connection in ETABS

For the analysis, each model was subjected to a series of ground motions. Eleven scaled ground motions per site class were selected for Montreal and fifteen scaled ground motions per site class were selected for Vancouver. The Montreal ground motions were all simulated ground motions modelled after crustal-type earthquakes re-scaled for NBCC 2015 requirements from previously generated ground motions (Atkinson, 2009). Five of these were magnitude six earthquakes and seven were magnitude seven earthquakes. For Vancouver, the 15 ground motions were split into three suites depending on the type of earthquake: interface, in-slab, or crustal. Each suite included five ground motions. Some of these ground motions did not respect the NBCC 2015 criteria for selection and scaling below periods of 0.11 s. However, because the lowest second mode period was found to be 0.176 s and higher mode effects were expected to be negligible for

the stiff, four-storey buildings, this was considered acceptable, as it is challenging to scale this period range.

Gravity loads were first applied to achieve the initial state of the building before applying the ground motions. The buildings were loaded with the following load combination, $1D + 0.5L + 0.25S$, as prescribed by NBCC 2015 for seismic load cases. These gravity loads were ramped up gradually from 0% to 100% of the load in 4.7 seconds in the FNA. The P-Delta automation method was selected to be iterative based on these loads. The ground motion cases were then applied to the final state of the models at the end of this load case. All cases were run with FNA, the Ritz vector modal analysis, and constant 3% modal damping.

3.4 Displacement demand results from the numerical modelling

Once the models were created in ETABS, they were relied on to obtain the deformation demands in the end connections, which were used to create a reversed cyclic loading protocol based on the force-displacement behaviour of these braces under simulated seismic loading.

3.4.1. Design seismic displacement demand of the bearing connection

The design seismic displacement demands were considered to be the expected deformations in the connections of bolted CC-type braces under typical ground motions in the West and East of Canada. In the models, this translates to the axial extension in tension of the nonlinear links for the collection of simulated ground motions. These displacement demand results could then be used to design the slot length for the modified bearing plate connection allowing the bolts to bear on the bearing plate to achieve the full ductility demand.

The analysis was run in ETABS for the buildings with only the bearing failure mode force-displacement definition. The results obtained in all five building models for the W360x134 braces (first floor) and the W310x97 braces (third floor) for each ground motion are shown in Table 3-7 and Table 3-8, respectively. For buildings located in Montreal, the design seismic displacement demand was taken as the average of the maximum displacements for all the ground motions. For the buildings located in Vancouver, the design seismic displacement demand was taken as the average of the five largest values as required by the NBCC 2015. Each building model resulted in

two sets of data due to the symmetric nature of the split-X braced frames. The maximum values across all five buildings were 10.2 mm (0.3% SDR) for the W360x134 braces and 34.7 mm (1.1% SDR) for the W310x97 braces. These values will be used as preliminary estimates for displacement demands for the respective brace sizes.

The average connection displacement demand for the W310x97 braces was found to be 135% longer than the displacement demand for the W360x134 braces. This is true regardless of brace efficiency. For example, in the MC_17x14.5 building, the displacement demands for the W310x97 braces are higher than the demands for W360x134 braces, which have a greater efficiency. For the VE_11x10.25 building model, where the W360x134 braces have a higher efficiency than in the other Vancouver buildings, the displacement demand was 17% larger on average when compared to the VE_11x9.75 building model. This translates to approximately 1 mm of displacement demand. Displacement demands therefore seem to be concentrated to the two upper storeys of these buildings.

From the results for the W360x134 braces including the model where the efficiency of the W360x134 brace is increased to 98.6%, which attained somewhat larger displacement demands, it was determined that a standard long slot would be sufficient to accommodate the displacement demand. The total length of a 1 1/8" (28.6 mm) diameter standard long slot is 71.4 mm (2 13/16"), which allows for an additional 21.4 mm of displacement on either side of the 1 1/8" (28.6 mm) bolt (size of bolt for the bearing connection design). The standard long slot would simplify the fabrication process of this connection, while providing much more deformation capacity than the 10.2 mm requirement. Unfortunately, this is not the case for the W310x97 braces for which deformation demands exceed 21.4 mm for the Vancouver, soil class C building model. In this case, a standard long slot would not be adequate. However, if the buckling capacity of the brace is lower than the bearing capacity, the bolt can be moved to the complete end of the slot to increase the bearing length on the tension side of the connection. In this case, the standard long slot could also be used in the design of the W310x97 bearing connections. As an example, the force-displacement hystereses with the largest displacements in tension for

Montreal and Vancouver are shown for the W360x134 braces in Figure 3-13 and Figure 3-14 and for the W310x97 braces in Figure 3-15 and Figure 3-16.

Table 3-7 Displacement demand data for W360x134 (mm)

GM	VE_11x9.75		VC_13x11.75		ME_13x11.75		MC_17x14.5		VE_11x10.25	
	Left	Right	Left	Right	Left	Right	Left	Right	Left	Right
1	7.4	7	7.9	8.9	5.9	6.3	4.2	7.2	6.8	7.9
2	6.1	6.4	5.9	6.5	10.3	5.2	4.5	3.9	12.4	7.3
3	6.8	7.3	4.9	8.5	7.6	5.3	3.9	6.3	7.3	7.3
4	7.4	6.3	5.6	7.1	4.5	6.9	9.1	6.9	13.5	6.8
5	6	5	4.4	6.4	7.5	7.9	6.6	8	7.4	5.3
6	4.5	5	5	5.8	7	6	9.8	7.2	4.7	5.2
7	5.3	5.7	6.3	5.6	3.7	7.5	7.5	6.4	5.7	6.2
8	3.8	3.2	5.6	8.3	6.4	6.6	6	5.5	3.9	3.4
9	5.2	5.1	4.6	5.6	6.8	7	9.1	7.7	6.6	6.5
10	7.4	7	4.9	5.1	7.7	7.4	7.8	6.4	7.5	7.4
11	7	6.9	5.5	4.9	7	6.8	6.0	5.2	7.1	5.8
12	7	5.8	5.1	4.3	NA ¹	NA ¹	NA ¹	NA ¹	6.7	6.4
13	5.4	5.4	6.2	6.2	NA ¹	NA ¹	NA ¹	NA ¹	5.8	5.7
14	5.6	6.7	5	5.4	NA ¹	NA ¹	NA ¹	NA ¹	6.7	12.7
15	6.6	6.2	6.3	4.8	NA ¹	NA ¹	NA ¹	NA ¹	10	6.7
Design Seismic Demand	7.2	7.0	6.5	7.9	6.8	6.6	6.8	6.4	10.2	8.5

1. This data is not applicable because a suite of ten ground motions were used for Montreal buildings

Table 3-8 Displacement demand data for W310x97 (mm)

GM	Left	Right	Left	Right	Left	Right	Left	Right
1	11.9	6.6	42.2	10.3	56.3	5.7	8.0	6.7
2	7.6	12.6	19.9	8.7	20.2	7.2	4.8	4.3
3	10.2	11.5	9.8	10.3	9.8	16.6	8	5.4
4	11.3	37.5	23.9	37.6	21.1	6.8	7.5	7.9
5	7.1	5	22.2	33.6	5.6	23.6	6	6.2
6	4.3	4.7	29.9	8.5	8	16.5	6.5	6.4
7	7.3	5	5.9	44.4	14.9	6.1	5.2	12.2
8	3.7	3.4	5.3	18.2	8.8	20.9	7.4	7.1
9	6.3	6.8	6.9	7.6	20.2	9	7	10.8
10	13.9	14.3	5	5.2	9.6	22.4	7.8	16.2
11	6.3	5.1	3.9	6.4	7	17.8	8.4	12.5
12	14.5	25.7	7.7	7	NA ¹	NA ¹	NA ¹	NA ¹
13	4.5	5	23.3	6.4	NA ¹	NA ¹	NA ¹	NA ¹
14	32.6	11.1	8.9	6.7	NA ¹	NA ¹	NA ¹	NA ¹
15	6.2	7.6	6	39.5	NA ¹	NA ¹	NA ¹	NA ¹
Design Seismic Demand	16.8	20.3	28.3	34.7	16.5	13.9	7.0	8.7

1. This data is not applicable because a suite of ten ground motions were used for Montreal buildings

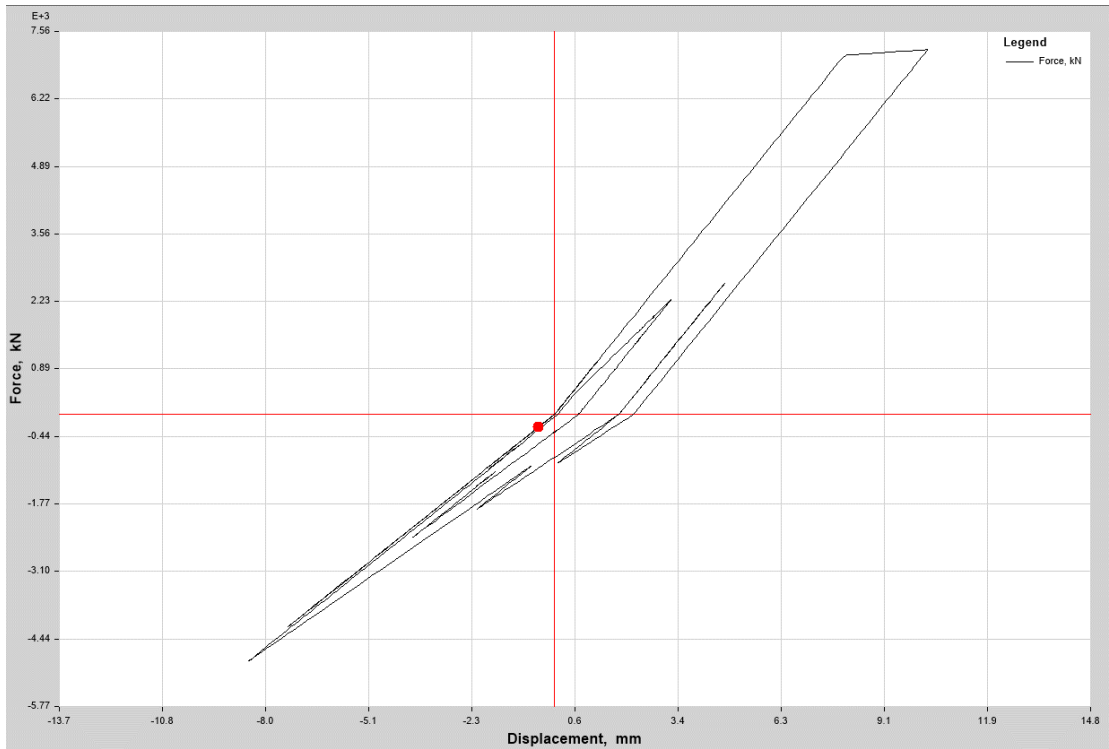


Figure 3-13 First storey left link force-displacement hysteresis for the ME_13x11.75 building model

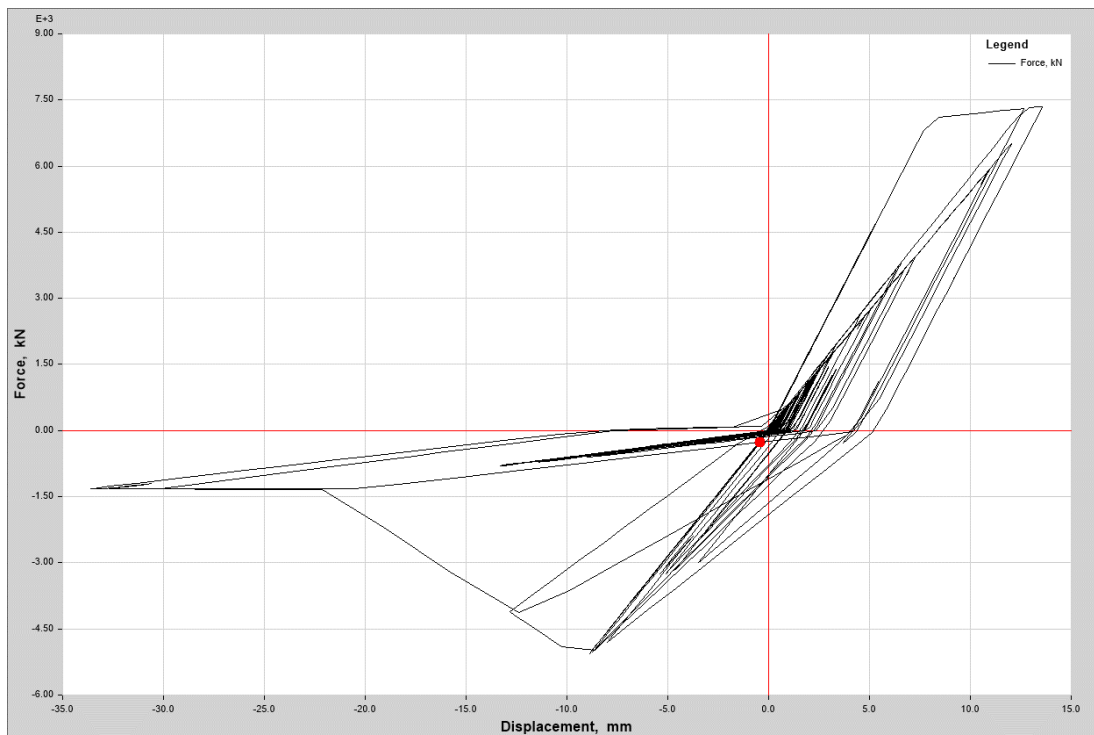


Figure 3-14 First storey left link force-displacement hysteresis for the VE_11x10.25 building model

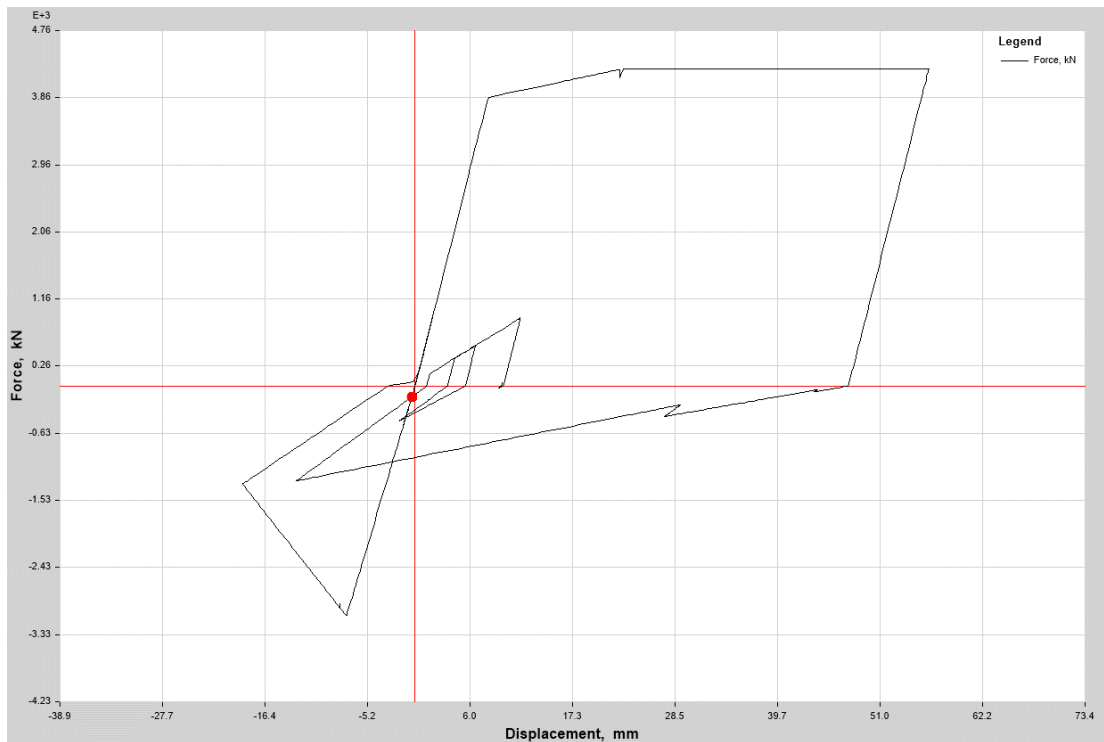


Figure 3-15 Third storey left link force-displacement hysteresis for the ME_13x11.75 building model

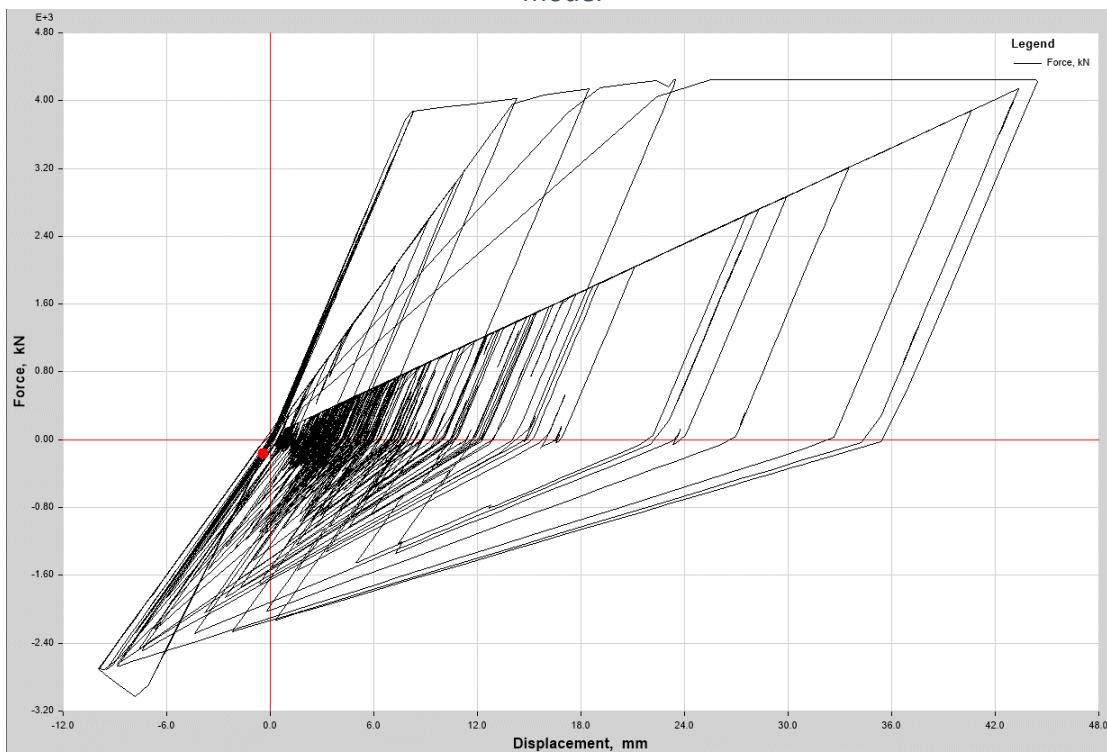


Figure 3-16 Third storey left link force-displacement hysteresis for the VC_13x11.75 building model

3.4.2. Loading protocol development

Following a review of common loading protocols as presented in Krawinkler (2009), the ATC-24 protocol (ATC, 1992) was found to be the most fitting for the cyclic testing of the specimens in this study. The amplitudes of this loading protocol are based on the deformation at yielding of the component being tested (Δ_y). According to Krawinkler, this protocol provides similar results as other protocols for steel specimens, such as the SAC protocol (Clark et al. 1997) and the FEMA 461 protocol (FEMA, 2007), because they possess similar energy dissipation demands. The ATC-24 protocol is based on structures located on site class D. Krawinkler comments in his paper that these protocols may therefore not be representative of the excitations experienced by structures on soil classes E and F. For this reason, the number of cycles and amplitudes of the loading protocol for this study needed to be modified based on a statistical review of results from the ETABS models as subjected to representative earthquakes for the geographical region and soil type. A symmetric (far-field) loading protocol was selected because it has been shown to cause more severe damage to the braces than the pulse or asymmetric (near-field) loading (Fell, 2008; Haddad, 2017). It was also shown that a dynamic loading rate had little impact on brace test results when compared to the typical quasi-static loading rate (Fell, 2008).

The development of the loading protocol is important for the laboratory testing of the brace specimens because it will affect the observed ductility, as shown in a study by Chen and Hu (2016). In their study, two sizes of HSS pipe specimens were tested under three loading protocols. The first loading protocol was developed by Krawinkler et al. (2000) for the testing of moment frame (MRF) SFRSs. The second loading protocol was proposed by Richards and Uang (2006) for the testing of eccentric braced frame (EBF) specimens. Lastly, the authors proposed a third loading protocol specifically developed for testing CBF specimens, which they had developed from the results of an OpenSees model of a chevron CBF subjected to 60 selected ground motions with probabilities of 50%, 10% and 2% exceedance in 50 years. The three loading protocols are shown in Figure 3-17. The noted parameters of the loading protocols are the total number of cycles (N_t), the number of plastic cycles (N_p), the sum of drift ratio range ($\Sigma\Delta\theta_i$), the maximum drift ratio range ($\Delta\theta_{max}$), and the maximum drift ratio (θ_{max}). The values of these parameters for each of the three loading protocols are provided in Table 3-9.

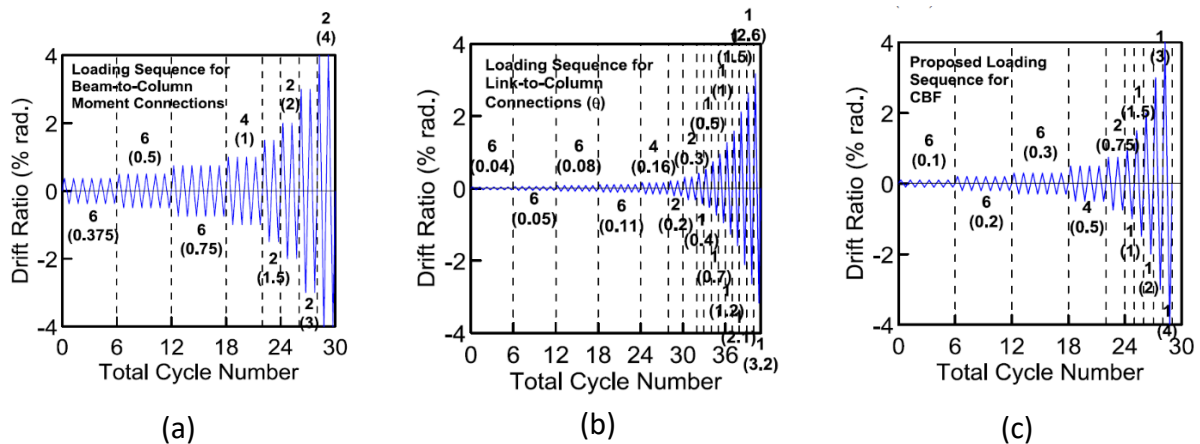


Figure 3-17 Loading protocols tested: (a) MRF (b) EBF (c) CBF (modified from Chen and Hu, 2016)

Table 3-9 Loading protocol parameters (modified from Chen and Hu, 2016)

Loading protocol	N_T	N_P	N_P/N_T (%)	$\Sigma\Delta\theta_i$ (RAD)	$\Delta\theta_{MAX}$ (RAD)	θ_{MAX} (RAD)
MRF	28	28	100	0.535	0.06	0.03
EBF	41	23	56	0.336	0.0635	0.0317
CBF	28	16	57	0.292	0.06	0.03

The tested specimens showed that the measured ductility was indeed influenced by the loading protocol. As suspected, the specimen subjected to the MRF loading protocol buckled globally within the first cycle. Ideally, tested specimens should undergo some elastic cycles prior to buckling as would occur in a real structure under seismic action. The ductility of the specimen tested with the MRF loading protocol was greatly reduced as compared to those tested with the EBF and CBF loading protocols. These specimens attained smaller maximum drift ratios than those tested with the other loading protocols (e.g. 0.005 rad for MRF versus 0.01 rad for CBF for the smaller section size). Conversely, it was found that the EBF loading protocol allowed the specimens to reach a higher ductility level than seen in the numerical model. However, the loading protocol selection seemed to have a lesser effect on the energy dissipation capacity of the specimens. It was concluded that the CBF loading protocol was the optimal testing method for CBF specimens under cyclic loading. Therefore, a specifically tailored loading protocol was also created for the test specimens in this study.

A statistical analysis of the displacement response histories for each of the three bolted connection types was conducted to create a meaningful loading protocol for the laboratory testing component of this study. The five building models, two brace sizes, three connection types, two sites, and ten or fifteen ground motions resulted in 715 displacement response histories. These response histories were then imported into Matlab (2016) for processing.

To create a loading protocol based on the available response histories, it was necessary to identify the axial elongations of the braces attained and to count number of cycles for each of these amplitudes for each ground motion such that statistics of these values could be established. The cycle counting methodology that was used was the simple rainflow counting algorithm. This is the first algorithm discussed in the paper by Downing and Socie (1982) which allows the counting of full cycles when the full response history is known. This method is used for creating loading protocols where fatigue due to number of cycles has an impact on the behaviour of the specimen being tested.

First, the data were reordered such that the response history began with the maximum or the minimum value within the response history, i.e. the response prior to this point is moved to the end of the response history. Then the algorithm, which counts cycles based on excursion amplitudes, was implemented. Subsequently, the amplitudes of each cycle were classed into predefined ranges such that they could be counted as discrete data points as opposed to continuous data. The amplitude ranges were based on the ranges selected in a previous study, in which a statistic analysis was conducted on response history data from building models with large steel brace sections (Bara, 2007). The ranges were based on the assumed yield displacement, δ_y , as is done in ATC-24 and other loading protocols. The δ_y was assumed to be 8.2 mm which was the average δ_y in the connection links as taken from Castonguay's test data. The ten ranges used were as follows: $[0.5\delta_y - 1.0\delta_y]$, $[1.0\delta_y - 1.5\delta_y]$, $[1.5\delta_y - 2.0\delta_y]$, $[2.0\delta_y - 2.5\delta_y]$, $[2.5\delta_y - 3.0\delta_y]$, $[3.0\delta_y - 3.5\delta_y]$, $[3.5\delta_y - 4.0\delta_y]$, $[4.0\delta_y - 4.5\delta_y]$, $[4.5\delta_y - 5.0\delta_y]$ and $[5.0\delta_y - \infty]$. Additionally, for information purposes, the range limits in brace axial displacements were converted to storey drifts ratios (SDR). SDRs were calculated from the geometry of the modeled braced frames, as

shown in Eq. 3-2 where δ is the axial displacement of the brace, L is the length of the brace (6667 mm), and θ is the initial angle of the brace to the storey below (34.3°).

$$SDR = \frac{\delta}{L \cos \theta \sin \theta} \quad (3-2)$$

A statistical analysis was conducted on the number of cycles per range for all 715 data sets. The average, 84th percentile, and maximum number of cycles per range are shown in Table 3-10.

Table 3-10 Statistical analysis results of displacement response histories

Original Intervals	[0.5 δ_y -1.0 δ_y]	[1.0 δ_y -1.5 δ_y]	[1.5 δ_y -2.0 δ_y]	[2.0 δ_y -2.5 δ_y]	[2.5 δ_y -3.0 δ_y]	[3.0 δ_y -3.5 δ_y]	[3.5 δ_y -4.0 δ_y]	[4.0 δ_y -4.5 δ_y]	[4.5 δ_y -5.0 δ_y]	5.0 δ_y +
Intervals in mm	4.1-8.2	8.2-12.3	12.3-16.4	16.4-20.5	20.5-24.6	24.6-28.7	28.7-32.8	32.8-36.9	36.9-41	41+
Intervals in SDR	0.0013-0.0026	0.0026-0.004	0.004-0.0053	0.0053-0.0066	0.0066-0.0079	0.0079-0.0093	0.0093-0.0106	0.0106-0.012	0.012-0.013	0.013+
Average	5	1	1	0	0	0	0	0	0	0
84%	12	4	2	1	1	1	0	0	0	0
Max	44	23	15	7	7	4	5	2	2	2

The number of elastic cycles (first displacement range only) is always significantly larger than the number of inelastic cycles. This is to be expected for a stiff CC-type building, which is design for larger loads when compared with an MD and LD design due to the smaller R_d factor of 1.5. Larger brace sections are therefore selected for CC-type design causing the overall building to be stiffer and attain small storey drifts when a ground motion is applied. For purposes of comparison, similar results for a four-storey structure taken from Bara's (2007) thesis are shown in Table 3-11. Bara's models included capacity design principles as used for MD- and LD-type structures. Nevertheless, Bara's results also show a concentration of elastic cycles followed by a steady decrease of the cycles in the inelastic ranges.

Table 3-11 Statistic analysis results of four-storey displacement response histories (from Bara, 2007)

Original Intervals	[0.5 δ_y -1.0 δ_y]	[1.0 δ_y -1.5 δ_y]	[1.5 δ_y -2.0 δ_y]	[2.0 δ_y -2.5 δ_y]	[2.5 δ_y -3.0 δ_y]	[3.0 δ_y -3.5 δ_y]	[3.5 δ_y -4.0 δ_y]	[4.0 δ_y -4.5 δ_y]	[4.5 δ_y -5.0 δ_y]	5.0 δ_y +
Average	19	8	3	1	0	1	0	0	0	0
84%	29	14	7	5	1	1	1	0	0	0
Max	48	18	13	7	3	4	3	1	1	9

For further comparison, the following lists summarize the loading protocol suggestions from the ATC-24 “Guidelines for Cyclic Seismic Testing of Components of Steel Structures for Buildings” (1992) and from FEMA 461 “Interim Protocols for Determining Seismic Performance Characteristics of Structural and Nonstructural Components through Laboratory Testing” (2007).

The ATC-24 guidelines suggest:

- Six or more cycles below δ_y
- Three or more cycles at δ_y
- Three or more cycles at $\delta_y + \Delta$
- Three or more cycles at $\delta_y + 2\Delta$
- Two or more cycles at $\delta_y + 3\Delta$ and every amplitude increase after that
- It is suggested that Δ be taken as δ_y

The FEMA 461 guidelines suggest:

- Two cycles at each amplitude except six cycles at the smallest amplitude below δ_y (a possible storey drift ratio is given as 0.0015)
- Steps increase incrementally by multiplying the previous amplitude by 1.4
- A possible maximum storey drift ratio is given as 0.03
- After the maximum expected drift (if failure of the specimen has not yet occurred), the loading is to be continued in increments of 0.3*(maximum expected drift)
- It is suggested that ten or more steps are used

The data in Table 3-9 show that there are fewer cycles in the inelastic displacement range for the CC braces than in the suggested loading protocols as detailed for the ATC-24 and FEMA 461 guidelines (one cycle at higher inelastic ranges as compared to two cycles).

The developed loading protocol for the laboratory testing component of this study, shown in Table 3-12 and Figure 3-18, was based on the 84th percentile data in Table 3-9, with influences from the ATC-24 and FEMA 461 loading protocols. The chosen loading rates were selected such that the tests would be quasi-static. The elastic cycles were separated into two steps: one at 30% of the expected buckling load (C_u) in load control and a second at 70% of C_u in displacement

control. These load levels are shown in Table 3-13. This was done so that the displacement at 70% of C_u could be calculated from the linear elastic slope observed in the first step. The loading protocol included six cycles at 30% of C_u (in load control at a rate of 60 kN/s) and four cycles at 70% of C_u (in displacement control at a rate of 0.5 mm/s) for a total of ten cycles in the elastic range (decreased from 12 cycles in Table 3-9 because the two extra elastic cycles were not expected to have a large influence on specimen behaviour). This was followed by four cycles at the yield load. However, since the yield load of the specimens could not be known in advance (due to multiple possible failure path and components), the first of these four cycles would be a slow monotonic-type loading (loading rate of 0.01 mm/s) until the slope would flatten to 10% of the calculated linear elastic slope. This load would then be used as δ_y for the remainder of the loading protocol. All following inelastic cycles were planned to run at a loading rate of 0.5 mm/sec. The next step was three cycles taken as the average between the ETABS model data results and the loading protocol of Chen and Hu at 0.5% SDR. The next step was two cycles at $\delta_y + 0.4\%$ SDR corresponding to 0.66% SDR with an assumed δ_y of 8.2 mm. These last two steps had extra cycles as compared to the number indicated in the statistical analysis of the data from the ETABS models to better observe behaviour at these force levels in testing; furthermore, two cycles are commonly used in other standard protocols. The subsequent large inelastic displacement cycles were reduced to one cycle typical of the response seen in the numerical modelling data. The loading protocol was adapted to suit the behaviours encountered during the testing of the first specimen. The loading protocol used for the remainder of the specimens will be discussed in Chapter 4.

Table 3-12 Amplitudes and number of cycles in the developed loading protocol

Amplitude	30% buckling load	70% buckling load	δ_y	$\delta_y +$ 0.2% SDR	$\delta_y +$ 0.4% SDR	$\delta_y +$ 0.7% SDR	$\delta_y +$ 1% SDR	$\delta_y +$ 1.5% SDR	$\delta_y +$ 2% SDR
No. of cycles	6	4	4	3	2	1	1	1	1
Control type	Load control			Displacement Control					
Loading rate	60 kN/s	0.5 mm/s	0.01 mm/s & 0.2 mm/s	0.5 mm/s					

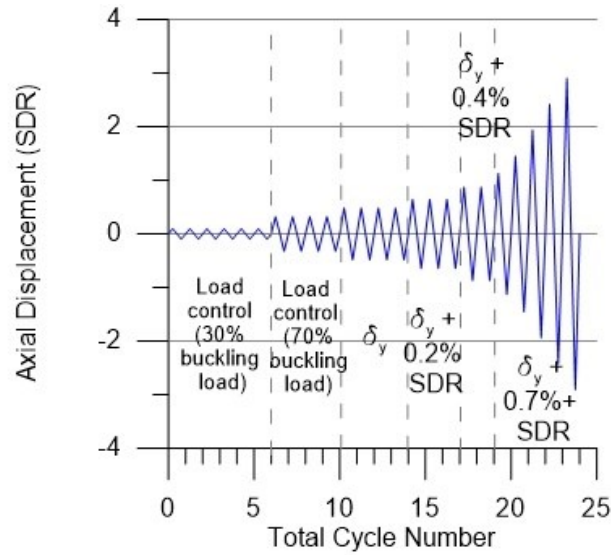


Figure 3-18 Loading protocol developed from numerical data

Table 3-13 Elastic load amplitudes used in loading protocol

Specimen No.	Expected buckling load (kN)	30% Expected buckling load (kN)	70% Expected buckling load (kN)	Location of buckling
1 & 2	5015	1505	3511	Gusset
3 & 4	5161	1548	3613	W-shape
5 & 6	3062	919	2143	W-shape
7 & 8	5161	1548	3613	W-shape

It should be acknowledged that when subjected to a seismic event, the demands on a brace and its connections will depend on the buckling modes, accumulation of damage, failure paths, nonlinear behaviour, and so on. However, in the interest of comparing the different specimens in this study, only one loading protocol was developed for all the specimens tested.

Chapter 4: Laboratory Testing of Full-scale CC-type Braces

4.1 Testing program

The laboratory component of this research on CC-type braces included the testing of six full-scale specimens. The objective of the laboratory testing was to design, build, and test braces with the two common bolted connection types, as described in Chapter 3, to observe and evaluate their behaviour and ductility, and to address the lack of previous experimental data of full-scale CC-type braces. Due to the complexity of these bolted connections with different failure modes expected in the webs and flanges, and expected failure capacities being within close range, theoretical predictions were based on assumptions. One assumption was that the capacity of the brace specimens is the sum of the expected capacities of the web and flanges, calculated based on their individual failure modes using unfactored design equations and probable material properties. The second assumption was that the forces in the brace were distributed between connecting plates relative to the areas of the flanges or the web to which they were connected. Predicting the ductility of these specimens was even more challenging due to displacements arising from different elements in the brace assemblies (e.g. deformations in bolts and plates, yielding, shearing, bearing, and tearing). In the design of CC-type braces however, the ductility capacity of these connections is required to determine whether the 1.5 penalty factor should be applied. These laboratory tests were therefore completed to address these questions for the common bolted brace connections used in the industry. The results of these laboratory tests could then be used to calibrate future numerical models and expand the pool of data available for engineers faced with designing CC-type braces.

Each specimen was tested in duplicate with the difference being the loading protocol. The first of two nominally identical specimens was tested with the loading protocol starting in tension, while the second specimen was tested with the loading protocol reversed to start in compression. The purpose was to evaluate the effect of the direction of the first loading excursion on these W-shape specimens with bolted end connections. The claw angle connection, unlike the jaw plate

connection, was only tested with the W360x134 brace. This was done to limit the number of specimens to a manageable number for the allotted testing period.

The specimens were labelled according to the connection type, section size, and direction of their first loading excursion. The first letter of each specimen label was either “J” for the jaw plate connections or “C” for the claw angle connections. The next three digits indicated the size of the W-shape brace with “310” for the W310x97 sections and “360” for the W360x134 sections. Finally, separated by a dash, the last letter indicated the direction of the first loading excursion, where “T” was used for tension loading first and “C” was used for compression loading first. The details, including nomenclature and testing order, are provided in Table 4-1.

Table 4-1 Testing parameters of the full-scale specimens

Connection type	Jaw plate	Jaw plate	Jaw plate	Jaw plate	Claw angle	Claw angle
Section Size	W310x97	W310x97	W360x134	W360x134	W360x134	W360x134
Direction of first loading excursion	Tension	Compression	Tension	Compression	Tension	Compression
Nomenclature	J310-T	J310-C	J360-T	J360-C	C360-T	C360-C
Testing order	1	2	3	4	5	6

The six specimens were tested in a 12 MN press at the Polytechnique de Montréal Structures Laboratory. The specimens were assembled in the press with a specially designed grip at each end, as shown in Figure 4-1. The grips were clamped on the T-stub ends of the gusset plates and were then bolted to the strong floor and the actuator piston’s platen with 50.8 mm (2”) bolts. The grips were designed for previous research projects to simulate the restraint conditions on a gusset when it is welded to the beam-column joint.

The specimens were designed to be 6.67m in length between the ends of the gusset plates, as shown in Figure 4-2. As a result, the lengths of the W-shape braces varied depending on the gusset and connection lengths. The length of the gussets was set to allow for a 25.4 mm clearance distance between the grips and the bottom edge of jaw plate or angle. This was done to allow for rotation in the gussets such as in the formation of a hinge without the grips interfering. However, the distance was not made long enough to comply with the $2t_g$ requirement of MD and LD design. Figure 4-3 shows the orthogonal views of the three types of end connections.

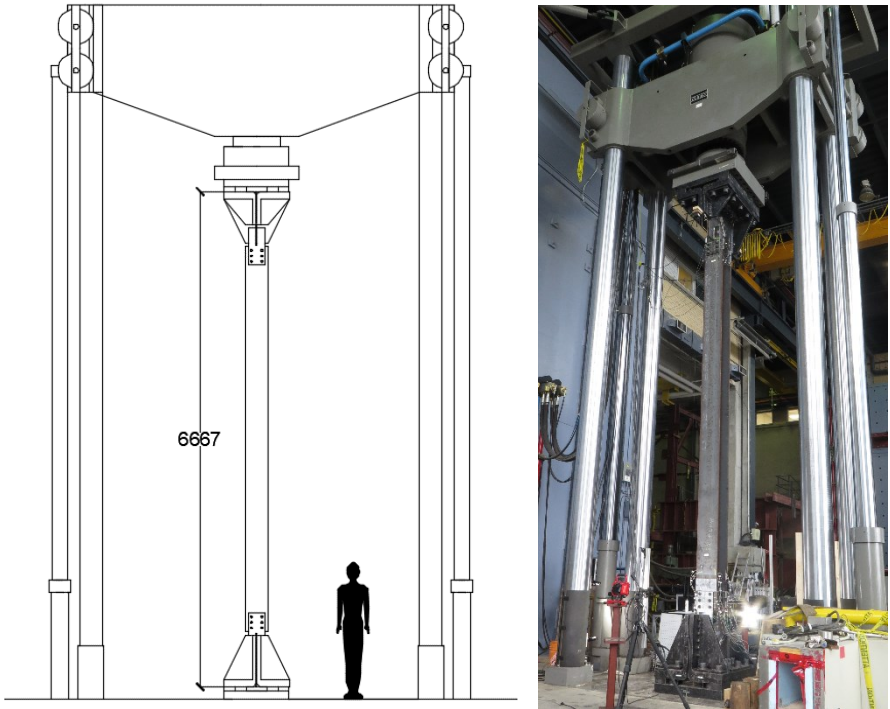


Figure 4-1 Diagram and photo of brace specimen assembly in the 12 MN press

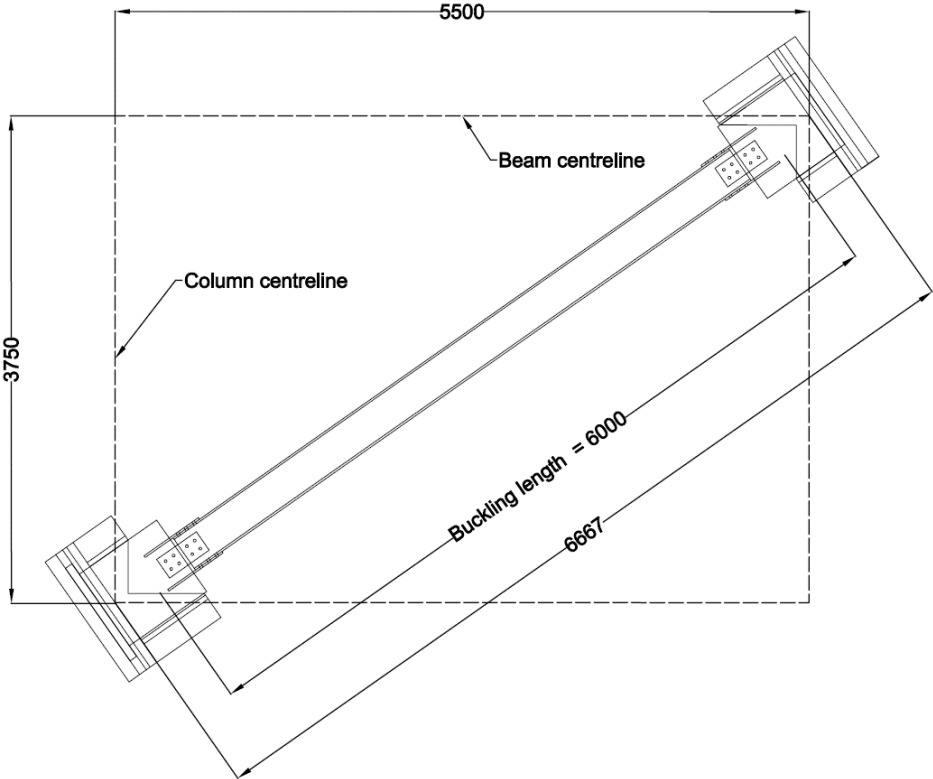


Figure 4-2 Brace length and buckling length (dimensions in mm)

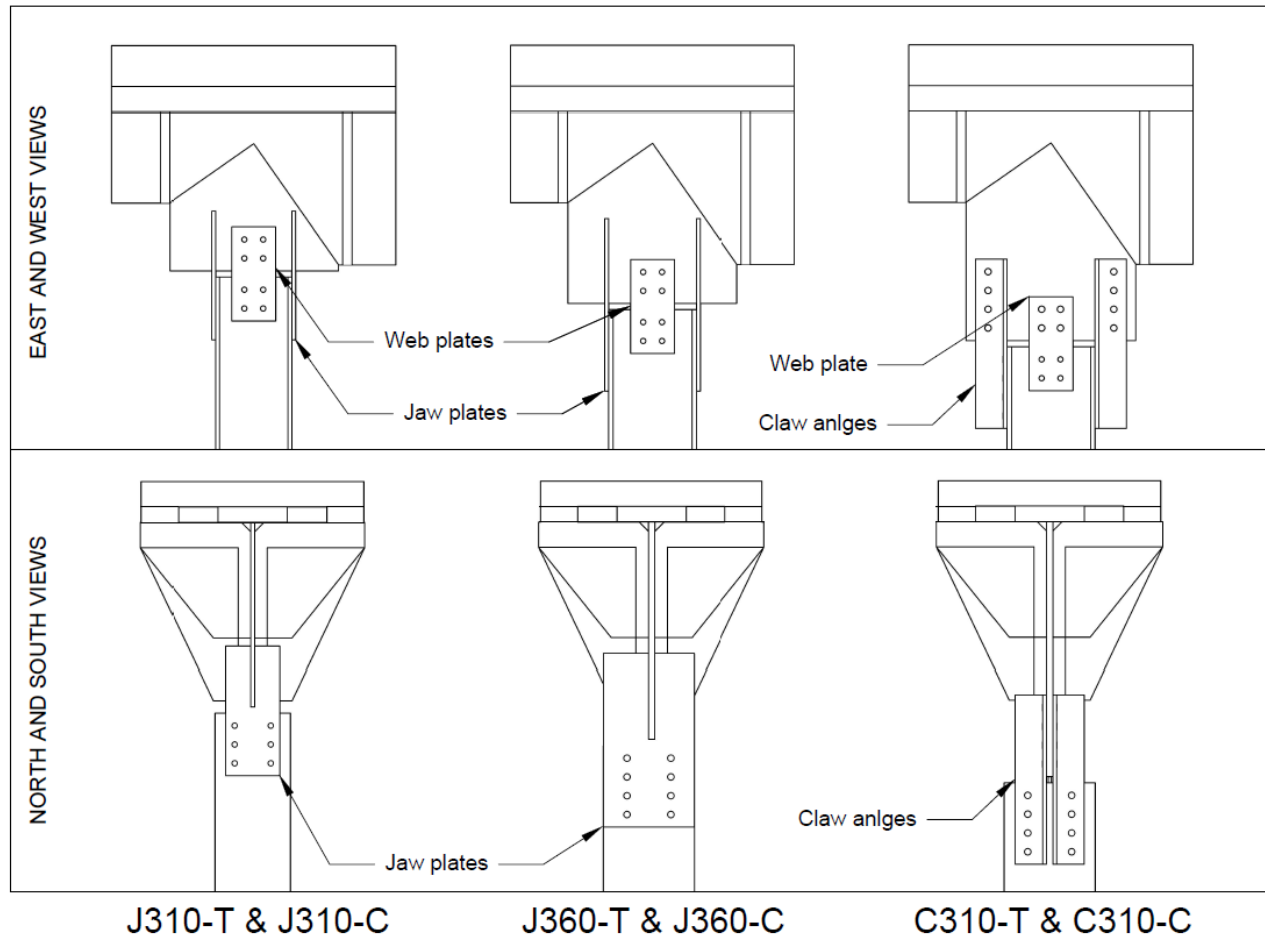


Figure 4-3 Drawings of brace specimens' end connections within testing grips

4.1.1. Material properties

The W-shape braces in this project were fabricated with ASTM A992 (2015) gr. 50 steel, the plates were fabricated with ASTM A572 (2018) gr. 50 steel, and the angles were fabricated with ASTM A6 (2017) gr. 44 steel. The nominal yield stress (F_y) for the braces and the plates was 345 MPa, while the nominal tensile stress (F_u) was 450 MPa. For the angles, the nominal F_y was 300 MPa and the nominal F_u was 450 MPa.

For the test predictions, these nominal values were multiplied by an R_y factor of 1.1. For the plates and braces, the probable material properties used were 380 MPa for F_y and 495 MPa for F_u (except the F_y of the braces which was taken as 385 MPa as per Clause 27.1.7 in the CSA S16-14 Standard (2014)). These values are reasonably close to the average values of $F_y = 379$ MPa and

$F_u = 494$ MPa obtained in 2007 tension tests of ASTM A992 flat-strap specimens (Bartlett et al., 2003). The standard deviations for these values were 21.4 and 25.5 MPa, respectively. For the angles, the expected material properties were taken as 330 MPa and 495 MPa.

However, for the analysis of the results and for future modelling of these braces, axial tension tests were performed on coupons taken from each heat of the brace sections and each parent plate and angle according to ASTM A370 (2017). For the brace sections, three coupons were taken from the webs of the sections (centered on the mid-depth of the web). A total of four coupons were taken from the flanges (two each) at the midpoints between the flange edge and the web. Three coupons were taken from each parent plate. Two coupons per leg (at the midpoints of each leg) were taken from the parent angle. The average results for each set of coupons are provided in Table 4-2. F_y was obtained from the stress-strain curves using the 2% offset method.

Table 4-2 Average material properties measured from coupon tests

Coupon origin		Average measured values					
Specimen(s)	Component	F_y (MPa)	F_u (MPa)	$\epsilon_y (\mu\epsilon)^1$	$\epsilon_u (10^5 \mu\epsilon)^2$	F_y/F_u	E (GPa) ³
J360-T, J360-C	W-shape (flanges)	357	493	1726	1.374	0.72	211
J360-T, J360-C	W-shape (web)	381	492	1875	1.425	0.77	207
C360-T, C360-C	W-shape (flanges)	359	494	1735	1.334	0.73	236
C360-T, C360-C	W-shape (web)	377	489	1912	1.340	0.77	229
J310-T, J310-C	W-shape (flanges)	342	438	1657	1.334	0.78	210
J310-T, J310-C	W-shape (web)	368	469	1688	1.487	0.78	207
J360-T, J360-C, J310-T, J310-C	Jaw plates	418	506	2093	0.9556	0.83	196
C360-T, C360-C	Angles	343	493	1647	1.378	0.70	206
J360-T, J360-C	Gusset plates	397	469	1778	1.271	0.85	216
C360-T, C360-C	Gusset plates	386	534	2289	1.100	0.72	195
J310-T, J310-C	Gusset plates	408	498	1989	1.048	0.82	197
ALL	Web plates	424	500	2135	1.177	0.85	203

1. ϵ_y was taken from extensometer readings as the strain for the corresponding F_y stress found using the 2% offset method

2. ϵ_u was taken from extensometer readings as the strain for the corresponding F_u stress (maximum stress obtained)

3. Based of strain measurements from strain gauges at the center of each face of the coupons (center of the neck area)

4.1.2. Calculation details

As mentioned in Section 3.1, the design load of the connections was based on the factored buckling capacities of the brace sections: 2209 kN for the W310x97 braces, and 3680 kN for the W360x134 braces. These were calculated using a distance of 6.67 m between beam-column joints and an assumed effective length factor, K , of 0.9. This total force was then divided between the flanges and the web proportionately to their respective areas. The flange and web design loads for both section sizes are provided in Table 4-3. The area of the web was assumed to be equal to the thickness of the web multiplied by the depth of the section minus two times the k distance, as shown in Figure 4-4.

Table 4-3 Design load components for W-shape flanges and web

		Area (mm ²)	Design load (kN)
W310x97	Flanges	9984	1793
	Web	2317	416
W360x134	Flanges	14284	3074
	Web	2816	606

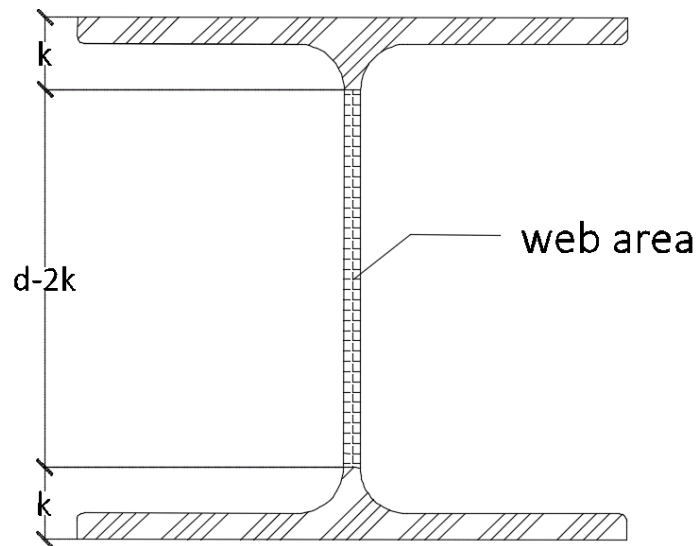


Figure 4-4 Definition of web area

Once the design load was known, bolt sizes and grades were selected; the number of bolts required to meet the design load was calculated based on their shear resistance. Bolt

configurations were kept symmetric to avoid eccentricities in the design. For specimens J310-T and J310-C, ASTM F3125 grade A325 bolts with a diameter of 7/8" (22.2 mm) were selected. For the remainder of the specimens with the W360x134 brace, ASTM F3125 grade A490 bolts with a 1" (25.4 mm) diameter were selected.

The jaw plates, claw angles, web plates, gusset plates, and welds were then designed based on the factored resistance as specified in the CSA S16-14 Standard with nominal material properties and nominal geometric properties. The main design parameters are shown in Table 4-4. Detailed design calculations and shop drawings of the specimens are provided in Appendices A and B, respectively.

Table 4-4 Summary of design parameters

Design element	Parameter	W310x97	W360x134
Bolts	Grade	A325	A490
	Size (inches)	7/8	1
	No. rows per flange	3	4
	No. rows in web	2	2
Bolt Spacing	End distance (mm)	32	38
	Spacing (mm)	76	76
	Gauge in flanges (mm)	146	152/178
	Gauge in web (mm)	76	76
Angles	Section	NA	L127x127x16
	Gauge 1 (mm)	NA	76
	Gauge 2 (mm)	NA	76
Web Plates	Width (mm)	140	156
	Thickness (mm)	9.5	9.5
Jaw Plates	Width (mm)	219	349
	Thickness (mm)	16	16
Welds	Height (mm)	8.0	11
	Length (mm)	4X241	4X343
Gusset Plate	Thickness (mm)	16	19/25

Clause 12.3.2 of the CSA S16-14 Standard (2014) requires that, in design calculations, 2 mm are to be added to the diameter of a bolt hole for bolt holes which are not drilled due to damage to the hole edges by the hole fabrication process. This requirement was waived for the web plates, jaw plates, and gusset plates. While these holes were punched (except for the holes in the gusset

plates for the claw angle connection specimens, which were drilled), a close inspection of the holes' edges showed little damage. Therefore, it was assumed that any damage caused by punching these holes would not significantly affect the tensile capacities of the connection. In contrast, the holes in the angles, showed more damage from the punching process. Consequently, 2 mm were added to the hole diameters for the calculations. The holes in the W-shape sections were drilled. Selected photos of the hole edges from the tested specimens are shown in Figure 4-5 for comparison.

Table 4-5 and Table 4-6 show both the design and expected capacities for the different failure modes as calculated with resistance equations from the CSA S16-14 and AISC 360-16 Standards, respectively. Expected bolt strengths were based on a database of bolt shear test results (Tide, 2010). Measured test capacities in this database were compared to unfactored bolt shear capacities using the bolt shear resistance equation as shown in Eq. 2-6 from the CSA S16-14 Standard, as well as Eq. 2-8 from the AISC 360-16 Standard. Only connections with a length of 762 mm (30 inches) or less were considered. The average factors ($P_{\text{test}}/P_{\text{predicted}}$) for grade A325 bolts were found to be 1.02 and 0.975 for the CSA S16-14 and AISC 360-16 Standards, respectively. For grade A490 bolts, the average factors were found to be 1.11 and 1.07 for the CSA S16-14 and AISC 360-16 Standards, respectively. These factors were used to obtain expected bolt shear strengths. The thickness of shims was also considered in the calculations of bolt shear capacities. Weld metal strengths were not increased for the expected calculations.

In Table 4-5 and Table 4-6, failure modes are separated by the component (i.e. brace, jaw plates, etc.) in which they occur. The lowest tensile capacity for each component is highlighted in yellow. If the lowest calculated capacity was gross section yielding, the second lowest capacity is also highlighted because the yielding of a section is not considered as an ultimate failure mode due to the ability of the steel to strain harden after yielding. Buckling capacities are highlighted in blue.

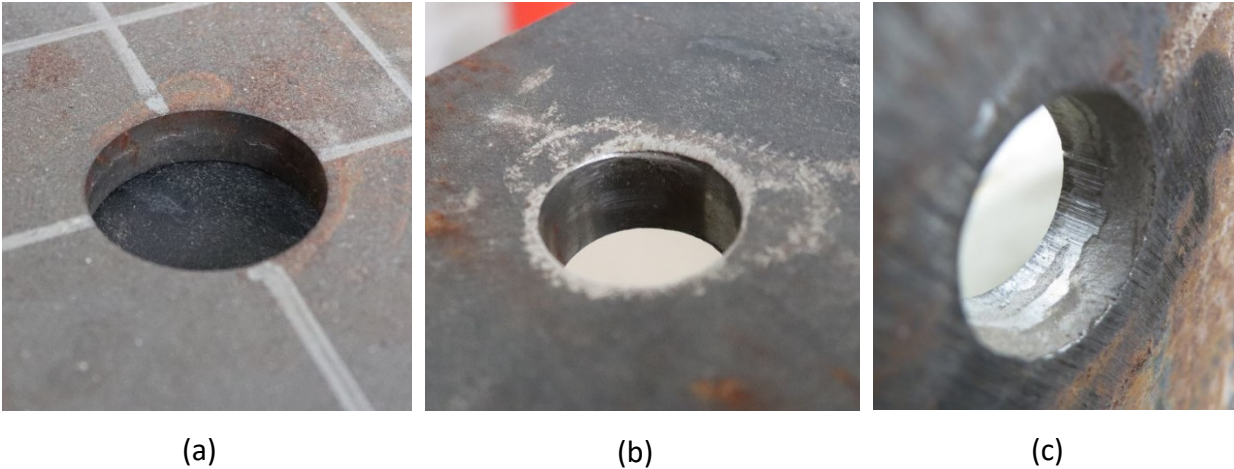


Figure 4-5 Hole edges of (a) punched holes in web plate (b) drilled holes in W-shape (c) punched holes in angle

Failure of the entire brace connection is considered to have occurred once there is failure, such as fracture or almost full loss of carrying capacity, in both the flanges and the web. Therefore, the capacity of a failure type in the W-shape flanges or in the jaw plates and angles must be combined with a failure type in the W-shape web or in the web plates to obtain the full capacity of the brace. If this combined capacity is smaller than that of the gusset and the full brace section, the connection capacity is considered to govern. For each specimen, the capacities of the governing failure modes are bolded and underlined in Table 4-5 and Table 4-6 for both tension and compression. If a gross section yielding capacity governs, the second least capacity is selected as the ultimate resistance. In all cases for tension, the failure capacities were combinations of a separate flange and web failure. A summary of the governing failure modes is provided in Table 4-7 and Table 4-8.

Table 4-5 Design and expected failure mode capacities based on CSA S16-14

Failure mode		J310-T & J310-C		J360-T & J360-C		C360-T & C360-C	
		Design	Expected	Design	Expected	Design	Expected
Whole W-shape	Buckling	2209	2582	3680	4364	3680	4364
	Gross yielding	3819	4736	5310	6584	5310	6584
	Net fracture	3656	5362	5115	7503	5115	7503
	T _u	4736	4736	6584	6584	6584	6584
	C _u	2945	2945	4906	4906	4906	4906
Flanges W-shape	Bolt shear	1844	2350	4028	5588	4028	5588
	Bolt bearing	4436	6099	7900	10863	7900	10863
	Block shear 1	4151	6113	6346	9348	6654	9801
	Block shear 2	3293	4849	5508	8110	5230	7703
	Block shear 3	3527	5178	5215	7658	5215	7658
	Plug shear	4058	5989	6870	10139	6870	10139
Web W-shape	Bolt shear	1229	1567	2014	2794	1811	2513
	Bolt bearing	951	1307	1207	1660	1207	1660
	Block shear	557	821	632	932	632	932
	Plug shear	765	1129	900	1328	900	1328
Web Plates	Gross yielding	826	1010	920	1125	920	1125
	Net fracture	592	868	653	958	653	958
	Bolt bearing	1829	2515	2090	2874	2090	2874
	Block shear 1	1073	1573	1095	1607	1095	1607
	Block shear 2	965	1416	1082	1587	1082	1587
	Plug shear	1471	2158	1558	2285	1558	2285
Jaw Plates / Angles	Gross yielding	2160	2640	3443	4208	4093	5003
	Net fracture (bolts)	1837	2695	3164	4641	3603	5285
	Net fracture (slot)	2145	3146	3506	5142	NA	NA
	Bolt bearing	4573	6287	6968	9581	6968	9581
	Block shear 1	3402	4989	4373	6414	3327	4880
	Block shear 2	2619	3841	4850	7113	NA	NA
	Welds	2402	3585	4266	6367	NA	NA
	Plug shear	4183	6136	6059	8886	5716	8383
Gusset	Buckling	2824	3418	3110	3689	4955	5989
	Gross yielding	3048	3725	4057	4958	5409	6611
	Net fracture	3313	4859	4409	6467	4954	7265
	Bolt bearing	NA	NA	NA	NA	8361	11497
	Block shear 1	3225	4730	4871	7144	6550	9607
	Block shear 2	NA	NA	NA	NA	5044	7398
	Plug shear	NA	NA	NA	NA	6924	10155

Table 4-6 Design and expected failure mode capacities based on AISC 360-16

Failure mode		J310-T & J310-C		J360-T & J360-C		C360-T & C360-C	
		Design	Expected	Design	Expected	Design	Expected
Whole W-shape	Buckling	2449	2885	3941	4721	3941	4721
	Gross yielding	3819	4736	5310	6584	5310	6584
	Net fracture	3656	5362	5115	7503	5115	7503
	T _u	4736	4736	6584	6584	6584	6584
	C _u	3264	3264	5330	5330	5330	5330
Flanges W-shape	Bolt shear	1638	2129	3521	5023	3521	5023
	Bolt bearing	4159	6099	7407	10863	7407	10863
	Block shear 1	3762	5518	5561	8156	5869	8608
	Block shear 2	2285	3370	3794	5597	3486	5144
	Block shear 3	3440	5058	5076	7464	5076	7464
	Plug shear	3109	4560	5023	7366	5023	7366
Web W-shape	Bolt shear	1092	1419	1760	2511	1751	2498
	Bolt bearing	891	1307	1132	1660	1132	1660
	Block shear	512	758	579	857	579	857
	Plug shear	579	850	658	965	658	965
Web Plates	Gross yielding	826	1010	920	1125	920	1125
	Net fracture	592	868	653	958	653	958
	Bolt bearing	1715	2515	1960	2874	1960	2874
	Block shear 1	894	1311	886	1299	886	1299
	Block shear 2	812	1192	906	1329	906	1329
	Plug shear	1277	1873	1347	1976	1347	1976
Jaw Plates / Angles	Gross yielding	2160	2640	3443	4208	4093	5003
	Net fracture (bolts)	1803	2645	3164	4641	3603	5285
	Net fracture (slot)	2145	3146	3506	5142	NA	NA
	Bolt bearing	4287	6287	6532	9581	7043	10329
	Block shear 1	2844	4172	3559	5219	2926	4291
	Block shear 2	2062	3024	4035	5918	NA	NA
	Welds	2402	3585	4266	6367	NA	NA
	Plug shear	3103	4551	4430	6497	7145	10479
Gusset	Buckling	2815	3414	3249	3883	4951	5998
	Gross yielding	3048	3725	4057	4958	5409	6611
	Net fracture	3313	4859	4409	6467	4954	7265
	Bolt bearing	NA	NA	NA	NA	7839	11497
	Block shear 1	3274	4802	5496	8061	5885	8632
	Block shear 2	NA	NA	NA	NA	5505	8074
	Plug shear	NA	NA	NA	NA	5062	7425

Table 4-7 Design and expected resistances of the specimens using CSA S16-14

		J310-T & J310-C		J360-T & J360-C		C360-T & C360-C	
		Tension	Compression	Tension	Compression	Tension	Compression
Design	Flange mode	Net section in jaw plates (at bolts)	Brace buckling	Net section in jaw plates (at bolts)	Gusset plate buckling	Block shear in angles	Brace buckling
	Web mode	Block shear in W		Block shear in W		Block shear in W	
	Flange capacity (kN)	1837	2209	3164	3110	3327	3680
	Web capacity (kN)	557		632		632	
	Total Capacity (kN)	2394		3796		3959	
Expected	Flange mode	Bolt shear	Brace Buckling	Net section in jaw plates (at bolts)	Gusset plate buckling	Block shear in angles	Brace buckling
	Web mode	Block shear in W		Block shear in W		Block shear in W	
	Flange capacity (kN)	2350	2582	4641	3689	4880	4364
	Web capacity (kN)	821		932		932	
	Total Capacity (kN)	3171		5573		5812	

Table 4-8 Design and expected resistances of the specimens using AISC 360-16

		J310-T & J310-C		J360-T & J360-C		C360-T & C360-C	
		Tension	Compression	Tension	Compression	Tension	Compression
Design	Flange mode	Bolt shear	Brace buckling	Net section in jaw plates (at bolts)	Gusset plate buckling	Block shear in angles	Brace buckling
	Web mode	Block shear in W		Block shear in W		Block shear in W	
	Flange capacity (kN)	1638	2449	3164	3249	2926	3941
	Web capacity (kN)	512		579		579	
	Total Capacity (kN)	2150		3743		3505	
Expected	Flange mode	Bolt shear	Brace Buckling	Net section in jaw plates (at bolts)	Gusset plate buckling	Block shear in angles	Brace buckling
	Web mode	Block shear in W		Block shear in W		Block shear in W	
	Flange capacity (kN)	2129	2885	4641	3883	4291	4721
	Web capacity (kN)	758		857		857	
	Total Capacity (kN)	2887		5498		5148	

The governing failure modes match for the calculations using the CSA S16-14 and AISC 360-16 Standards. The bolt shear and block shear equations are more conservative in the AISC 360-16 Standard (Eq. 2-8 and Eq. 2-31, respectively) than in the CSA S16-14 Standard (Eq. 2-6 and Eq. 2-25, respectively). The opposite is true for the buckling equations (shown in Eq. 2-2 and Eq. 4-1 for the CSA S16-14 and the AISC 360-16 Standards, respectively). The block shear resistance calculation is more conservative in the AISC 360-16 Standard (Eq. 2-31) because the net shear area is considered, as opposed to the gross shear area in the CSA S16-14 Standard (Eq. 2-25).

In the flanges, the expected tension failure modes were bolt shear for the W310x97 braces with the jaw plate connection, net section in the jaw plates for the W360x134 braces with the jaw plate connection, and block shear in the angles for the braces with the claw angle connection. In all cases, the expected failure in the web of the *W*-shapes was block shear. This is evident because the thickness of two splice web plates are greater than the thicknesses of the *W*-shape webs. The governing failure modes for the design and expected calculations match in all cases except one. For the W310x97 braces with the jaw plate connection, the governing failure mode in the flanges with the unfactored equations and nominal properties was net section fracture in the jaw plates at the bolt line, while the governing failure mode for the probable calculations is bolt shear in the flanges.

For the W360x134 braces with the jaw plate connection, the gusset was expected to buckle, while for the remaining specimens the brace was expected to buckle in compression. For consistency, the expected buckling capacities shown in the tables were unfactored, calculated with the design buckling equations and the expected material properties. The design buckling equation from the CSA S16-14 Standard is shown in Eq. 2-2. The corresponding buckling equation for the AISC 360-16 is shown in Eq. 4-1.

$$\phi_c P_n = F_{cr} A_g \quad (4-1)$$

Where ϕ_c is 0.9 and F_{cr} is calculated as shown in Eq. 4-2 if $F_y/F_e \leq 2.25$ or as shown in Eq. 4-3 if $F_y/F_e > 2.25$.

$$F_{cr} = \left[0.658^{\frac{F_y}{F_e}} \right] F_y \quad (4-2)$$

$$F_{cr} = 0.877F_e \quad (4-3)$$

And where F_e is calculated as shown in Eq. 4-4.

$$F_e = \frac{\pi^2 E}{\left(\frac{KL}{r} \right)^2} \quad (4-4)$$

However, it should be noted that, in the CSA S16-14 Standard, there exists a separate equation (shown in Eq. 2-3), C_u , used to calculate the expected compressive capacity of a brace in the context of seismic capacity based design. The C_u values are 2945 kN and 4906 kN for the W310x97 and the W360x134 braces, respectively. The AISC 341-16 Standard (2016) also has an equation that is used to calculate the expected buckling resistance of braces, as shown in Eq. 4-5.

$$\text{minimum}(R_y F_y A_g, 1.14 F_{cre} A_g) \quad (4-5)$$

Where F_{cre} was calculated as shown in Eq. 4-2 or Eq. 4-3 except all instances of F_y are replaced with $R_y F_y$, i.e. the probable material yield strength. The expected buckling values, calculated with Eq. 4-5, are 3264 kN and 5330 kN for the W310x97 and the W360x134 braces, respectively.

4.1.3. Specimen assembly details

The fabricated diameter of all bolt holes was specified to be approximately 2 mm (1/16") larger than the bolt diameter to allow for a certain tolerance in the assembly. Additionally, the space between the two welded jaw plates was specified to be 6.35 mm (1/4") greater than the depth of the beam. This was done to allow for a certain tolerance on the depths of the W-shape braces. Two shim plates of approximately 3.2 mm (1/8") were provided if this additional gap would not be required for the assembly of the connection. During the assembly of the connections, the use of shim plates varied for each specimen depending on the W-shape braces and the variance between the design and the actual brace depths. For specimen J310-T, all the shim plates were used, while for specimen J310-C, none of the shim plates could be installed between the W-shape flanges and the jaw plates. For the J360-T and J360-C specimens, the shim plates had to be

modified because the flanges of the W-shapes were found to be tilted, such that on one side of a flange additional shim plates were needed, while on the other, none fit. Shim plates were cut to fit on one side of the bolted connection and extra shim plates were added where they were required to close the gap for the snug tightening of the bolts, as shown in Figure 4-6. No shim plates were required between the flanges and angles of specimens C360-T and C360-C, because the fully bolted connections allowed for sufficient play in assembly. Shim plates were also used between the W-shape webs and the web plates to account for the difference in thickness between the gusset plates and the W-shape webs.



Figure 4-6 Modified shim plates (left) and shim plates in assembled connection (right)

The bolts in the connection assemblies were first tightened with a wrench to a snug tight level, which was followed by their pre-tensioning. While this is not a requirement for CC-type bolted connections, it is commonly done on-site during assembly. When possible, the bolts were tightened using the 1/3 turn of nut method. However, due to the extra shims and tilted flanges of the W-shapes, in some cases, it was preferable to tighten the bolts to a predetermined torque, which ranged between 1229 Nm and 1602 Nm.

The braces were installed such that their flanges faced the North and South directions of the laboratory, while the webs of the braces faced the East and West sides of the laboratory. As a result, the jaw plates and angles were on the North and South side, while the web plates were installed on the East and West sides of the W-shapes.

The assembly of the specimens followed the procedure described below once the grips were installed onto the platens of the press:

1. The bottom connection and bottom end of the W-shape were prepared and painted with a speckle pattern for the Digital Image Correlation (DIC) system (this will be further explained in Section 4.1.4.).
2. Brackets for the instrumentation were tack welded onto the W-shape and the gussets.
3. The top gusset was slid into the top grips and aligned with lasers in both plan directions.
4. The 2" (50.8 mm) bolts and threaded rods of the top grip were then tightened. If the T-stub was not completely level, shims were inserted into the grips to ensure contact.
5. Steps 3 and 4 were then repeated for the bottom grip and bottom gusset.
6. The W-shape brace end was then inserted into the top connection, and two bolts were inserted through the flanges and connecting plates or angles to serve as a pivot point (shim plates were added where possible).
7. The cross-head of the 12 MN press was then moved up, while the brace bottom was brought closer to the bottom grip to swing the W-shape into position.
8. The shim plates and web plates were added and the bolts were tightened with a wrench to the snug tight level.
9. The strain gauges were connected to the data acquisition system. This was done to capture the true zero of the strain gauges before any bolts were pre-tensioned.
10. The bolts were pre-tensioned either with the turn of nut method or to a pre-determined torque.

4.1.4. Instrumentation

The 12 MN MTS press captures displacement data with an internal LVDT and load data via a 12 MN load cell. MTS Series 793 software was used to control the press, while the MTS TestSuite

Multipurpose Elite software was used to implement the loading protocol. In addition to data recorded by the MTS software, three types of instrumentation were used to capture data during the tests: string potentiometers and linear potentiometers for axial and out-of-plane displacements, strain gauges for local strains, and the digital image correlation (DIC) system for the bottom connection. The measurement instruments (except the DIC system) were connected to Vishay Model 6100 scanners that were used to record data at ten scans per second using the Vishay System 6000 StrainSmart software. Figure 4-7 shows selected photos of the instrumented specimens in the set-up.

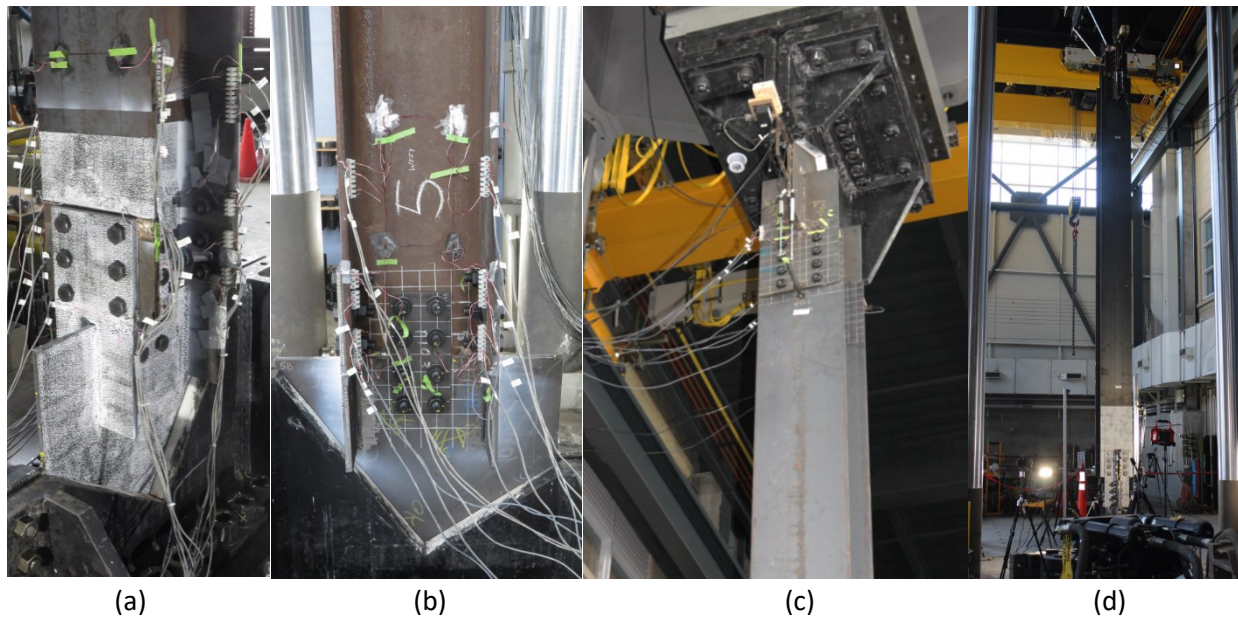


Figure 4-7 Instrumented specimens (a) Strain gauges on W-shape flanges, (b) strain gauges on W-shape web and web plate, (c) linear pots on top connection, and (d) overall set-up

The string potentiometers were used for the overall axial displacements and the out-of-plane displacements. The overall displacements were captured between points on the gusset plate outside the ends of the connections. These were installed on the North and South sides of the braces. The exact locations of the brackets onto which the string potentiometers were installed were determined based on the locations of the threaded rods in the grip that obstructed some points of access to the gusset plates. The measured initial lengths of the string potentiometers are shown in Table 4-9. The results for the overall displacements are shown as the average of the displacement captured on the North and South sides of the braces. The out-of-plane displacements were measured at the mid-point of the brace.

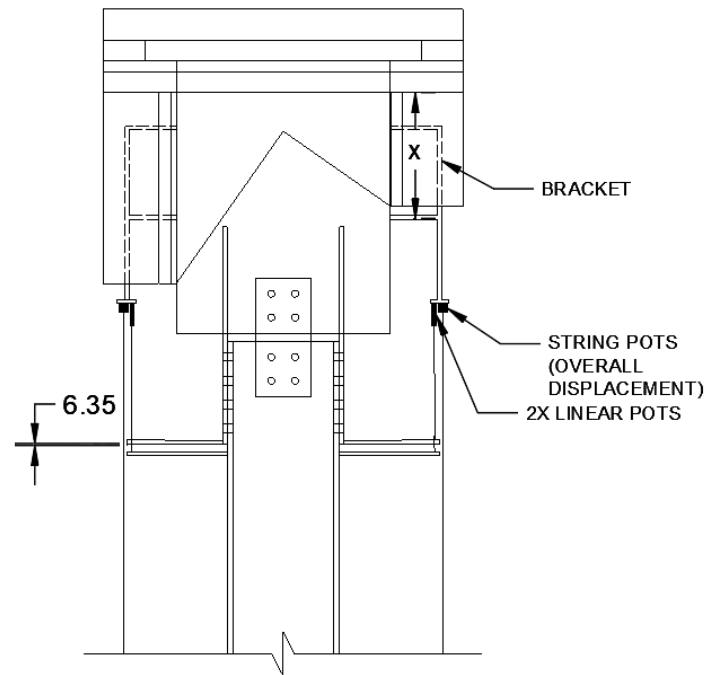
Table 4-9 Initial measured lengths of string potentiometers

	J310-T	J310-C	J360-T	J360-C	C360-T	C360-C
North	NA	NA	5795	6118	5568	5491
South	NA	NA	5795	6100	5542	5468
Average	5803*	5812*	5795	6109	5555	5479.5

*Estimated from other measurements

Two or four linear potentiometers per connection (one or two on the North and South sides) were used to record the axial displacements at the connections. Due to the digital image correlation recording information at the bottom connections, which recorded similar data, string potentiometers were only installed at the top connections. For the first two specimens, namely J310-T and J310-C, a single linear potentiometer recorded the axial displacements from a point on the gusset plate above the top edge of the connection plates to the top of the jaw plate on both the North and South sides. However, for this configuration, displacements between the jaw plates and the W-shape were not included because neither end of the string potentiometer was attached to the W-shape. For the remaining specimens, two additional linear potentiometers were added, which recorded the axial displacements between a point on the gusset plate just above the top edge of the connection and a point 25 mm below the ends of the jaw plates or angles on the W-shape flanges. Figure 4-8 shows the locations of the string and linear potentiometers for axial deformations.

However, due to strong shocks associated with the slip movements of the connections very early in the loading protocol procedure for specimens C360-T and C360-C, all linear potentiometers were lost (the glue used to attach the linear potentiometers, which was selected to protect the sensitive equipment from shocks, sheared during the tests). Axial displacements of the top connections for specimens C360-T and C360-C were therefore not recorded.



		Distance x in mm					
Specimen		J310-T	J310-C	J360-T	J360-C	C360-T	C360-C
Top connection	North	470	297	533	381	681	695
	South	476	475	533	381	710	700
Bottom connection	North	476	473	540	403	622	699
	South	481	473	537	387	622	702

Figure 4-8 String pot and linear pot locations

Strain gauges were used for two types of local strain measurements: the first measured strains in the connecting plates, while the second measured strains in two of the six W-shape sections to get a sense of how the forces distributed between the flanges and the web of the W-shapes.

The locations of the strain gauges in the connecting plates are shown in Figure 4-9. The strain gauges were placed in line with the lines of bolts to measure axial strains. Gauges were also placed on both the top and bottom connecting plates in the same locations. The strain gauges were labeled with a first letter indicating either the top (T) or bottom (B) connection, a second letter indicating the side of the brace the connecting plate was on (N, E, W, S), and third letter indicating the side of the connecting plate or angle the strain gauge was on (N, E, W, S). For angles, there was a fourth letter indicating if the strain gauge was on the leg connected to the W-shape (W) or on the leg connected to the gusset plate (G).

The strain gauges on the W-shapes were placed on specimens J310-T and J360-T, as illustrated in Figure 4-10. They were only placed at the bottoms of the brace sections. The first set of eight strain gauges was placed 25 mm from the top edges of the connecting jaw plates and a second set of eight was placed 305 mm away from the connection's edges. These strain gauges were labelled with a first letter indicating their height on the brace with "L" for the lowermost row and "H" for the row above, a second letter to indicate the side of the brace the strain gauge was on, and a last letter indicating side of the brace side.

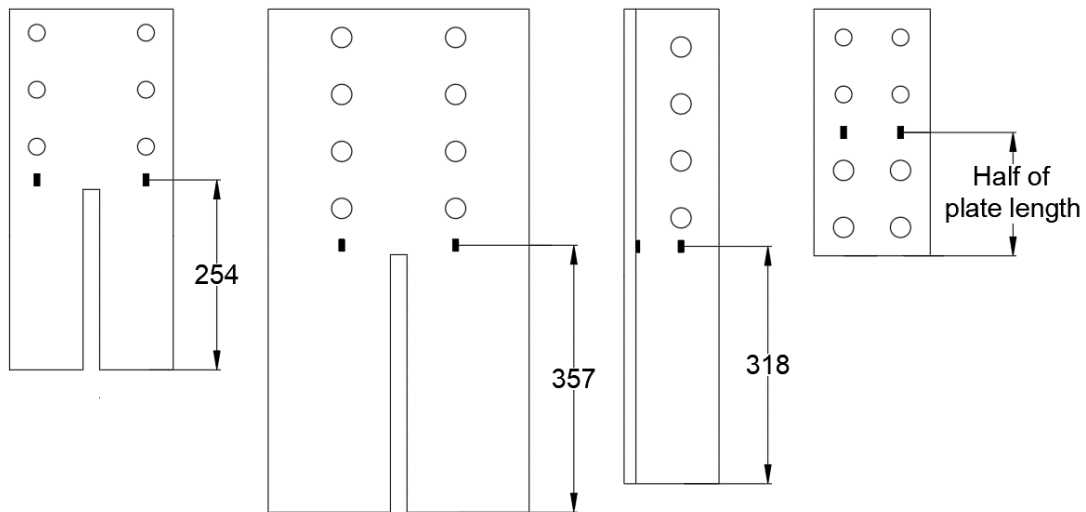


Figure 4-9 Locations of strain gauges in connecting plates (dimensions in mm)

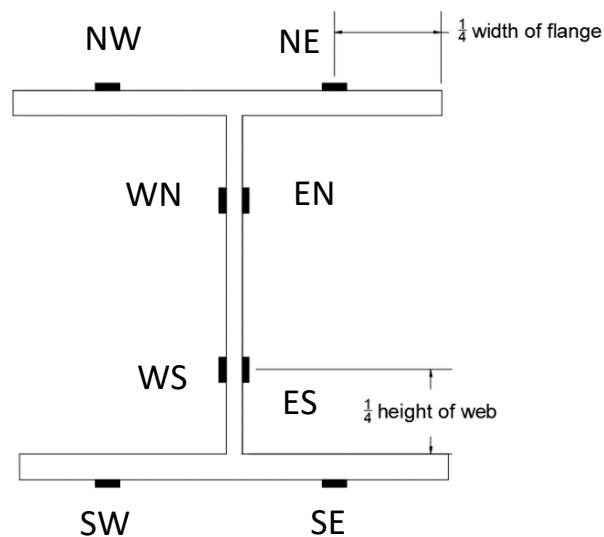


Figure 4-10 Locations of strain gauges on W-shape sections

At the bottom of the brace, three digital image correlation camera setups (Correlated Solutions Inc.) were used to capture the movements of a speckle pattern that was painted onto the visible portion of the gusset plate, the connecting plates, and the bottom of the brace on the North, South, and East sides (as shown in Figure 4-11). The VIC-Snap version 8 software was used for the image capture. These images were then processed in VIC3D version 8 to extract the displacements and strains at a precision of approximately $50\mu\epsilon$ (depending on the proximity of the set-up to the specimen). Each camera setup consisted of two Sony ICX625 cameras (type CCD 2/3" 5MP FireWire): one positioned at an angle above the connection and the other positioned at an angle below the connection, as shown in Figure 4-12. These cameras were positioned and calibrated prior to the beginning of the tests. Pre-test images were taken before torquing the bolts to capture stresses developed in the connections due to the torquing process (these images were lost for specimen J360-C and the East side of specimen C360-C because the cameras had to be recalibrated after the torquing process). Images were captured at a rate of one image per second during the test. In post-processing, after correlation of the images and identification of a plane of reference, it was possible to extract relative displacements and point strains from the painted regions. This system also allowed for the monitoring and adjusting for brightness of the captured images during the tests, as shown in Figure 4-13.

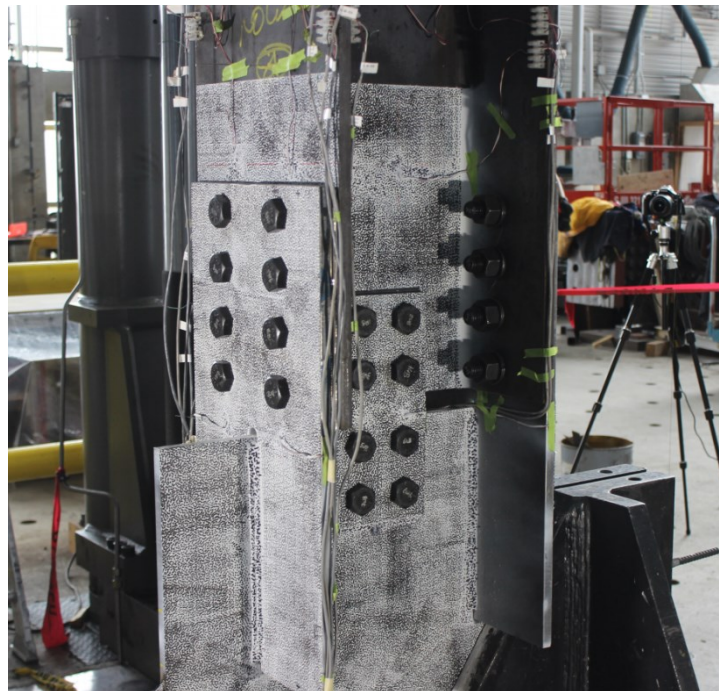


Figure 4-11 Speckle pattern on specimen J360-T



Figure 4-12 DIC camera set-up



Figure 4-13 DIC control setup showing views (on monitors) of the three camera angles

4.1.5. Loading protocol in testing

The development of the loading protocol was described in Section 3.4.2 of Chapter 3. The amplitudes in the inelastic ranges in the developed loading protocol relied on the displacement at yield, δ_y . As this displacement was not known beforehand, it was to be identified during testing.

The first specimen to be tested was J310-T. After the two sets of elastic cycles, the specimen was subjected to a slow tension excursion. Initially, it was planned to continue this excursion up to the point at which the slope of the load versus displacement curve reduced to 10% of the recorded linear elastic slope. However, because the force level approached the expected ultimate capacity of the specimen (3171 kN) before reaching the anticipated reduction in slope, the specimen was brought back to zero displacement to ensure that some additional cycles could be observed before failure. This loading protocol is shown in Figure 4-14. It was then decided that the approximate length of the slip plateau (7 mm) plus the average yield displacement found in Castonguay's (2010) connection tests (8.2 mm) would serve as the δ_y of 15.2 mm in the loading protocol for the remaining cycles and the following specimens. This yield displacement was expected to be composed of the sum of displacement in the different components of the brace systems. In comparison, the calculated yield displacement of the W310x97 brace is 7.5 mm and the corresponding value for the W360x134 brace is 11.6 mm (for yielding on the gross section of the brace). The following loading protocols therefore had the same displacement amplitudes, after the cycles under force control, as the loading protocol of specimen J310-T with the slow tension excursion being replaced with a fourth 15.2 mm displacement, as shown in Figure 4-15. The strain rate for this loading protocol was 0.5 mm/s.

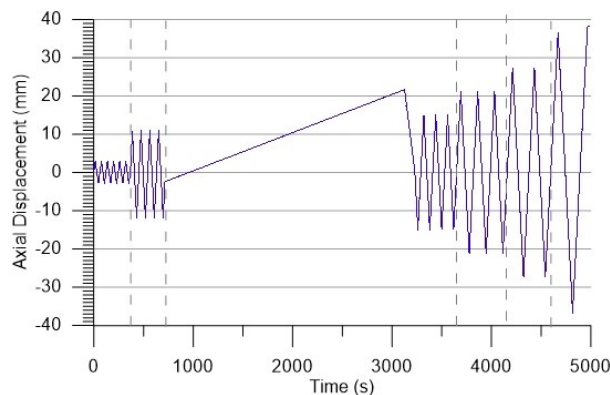


Figure 4-14 Loading protocol for specimen J310-T

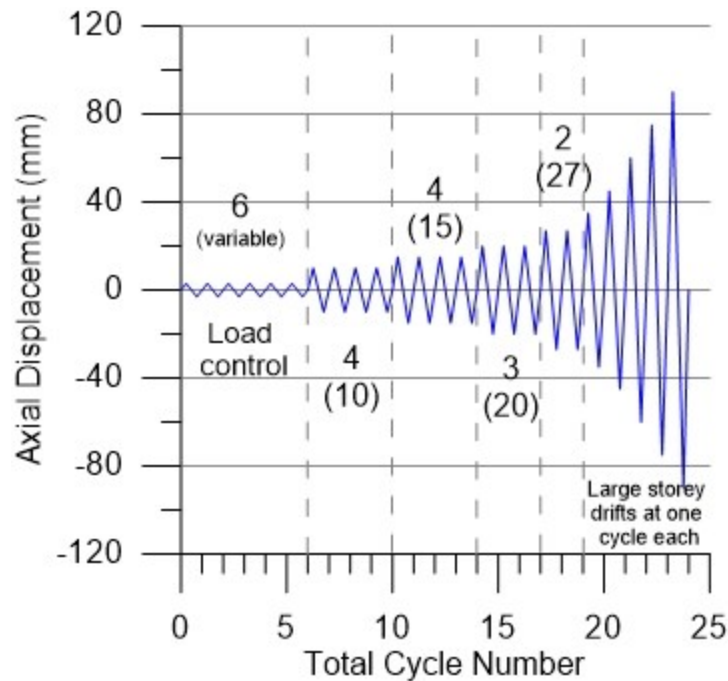


Figure 4-15 Loading protocol for remaining five specimens

4.2 Test Results

This section of the thesis contains a discussion of the results and observations from the testing of the six specimens. The results will be discussed in pairs of duplicate specimens, which had reversed loading protocols. Subsequently, some general aspects of the brace and connection behaviour will be discussed for all specimens.

4.2.1. J310-T and J310-C Results

Specimens J310-T and J310-C were composed of W310x97 sections and jaw plate connections. Matching predictions for specimen behaviour were made using the unfactored resistances with both probable and measured properties. For these tests, the W-shape brace was expected to buckle at mid-length in compression. In tension, the bolts in the flanges were expected to rupture in shear and the web of the W-shape was expected to experience block shear at failure.

4.2.1.1. Test observations

The observations made during the two tests are detailed in Table 4-10. The force-displacement hysteresses for specimens J310-T and J310-C are shown in Figure 4-16. The expected and design capacities are shown in Figure 4-16 for calculations following the CSA S16-14 Standard. Figure

4-17 shows images of the bottom connection (East side) of specimen J310-T at selected points throughout the test. These images show the relative displacement of the W-shape with respect to the web plate, the bending of the bolts, and the loss of the bolt heads in the flanges at the end of the test.

Table 4-10 Observations for specimens J310-T and J310-C

Step	Observations
6 load control cycles	<ul style="list-style-type: none"> • Linear elastic response to loading
4 load control cycles (with slow tension pull for J310-T)	<ul style="list-style-type: none"> • Crackling-like sounds were heard from slipping bolts • Amplitudes were not perfectly symmetric due to load control (+10.2 mm, -12.4 mm for J310-C)
4 cycles at 15 mm	<ul style="list-style-type: none"> • First cycle for J310-T is the slow tension excursion (identified in Figure 4-16(a)) • Slight buckling was perceptible to the eye at the second compression cycle for J310-C
3 cycles at 21.2 mm	<ul style="list-style-type: none"> • Buckling was significant with a 23% and 30% loss in compressive capacity for specimens J310-T and J310-C, respectively, in the first excursion in compression. Out-of-plane displacement at the midpoint was measured to be 89 mm and 170 mm at the second and last excursions in compression for specimen J310-C. • Figure 4-18(a) shows the overall buckled shape of J310-T • Yielding was observed in the force-displacement hysteresees
2 cycles at 27.4 mm	<ul style="list-style-type: none"> • Out-of-plane overall buckling continues
1 cycle at 36.7 mm	<ul style="list-style-type: none"> • Local buckling was observed in the W-shape for J310-C in compression (Figure 4-18(b)) • A first bolt sheared in the tension excursion for J310-T in the North flange in the bottom connection (bolt closest to the edge of the Jaw plate on the West side). A load noise was heard. Loading is continued.
1 cycle at 46 mm	<ul style="list-style-type: none"> • The remaining bolts sheared in the flanges of the bottom connection in the tension excursion for specimen J310-T. The piston was brought back to 0 mm. Figure 4-19 shows selected photos of specimen J310-T taken after the test completion.
1 cycle at 61.5 mm	<ul style="list-style-type: none"> • All bolts sheared in the flanges of the top connection in the tension excursion for J310-C. The piston was brought back to 0 mm. Figure 4-21 shows the sheared bolts. Figure 4-20 shows select photos specimen J310-T taken after the completion of the test.

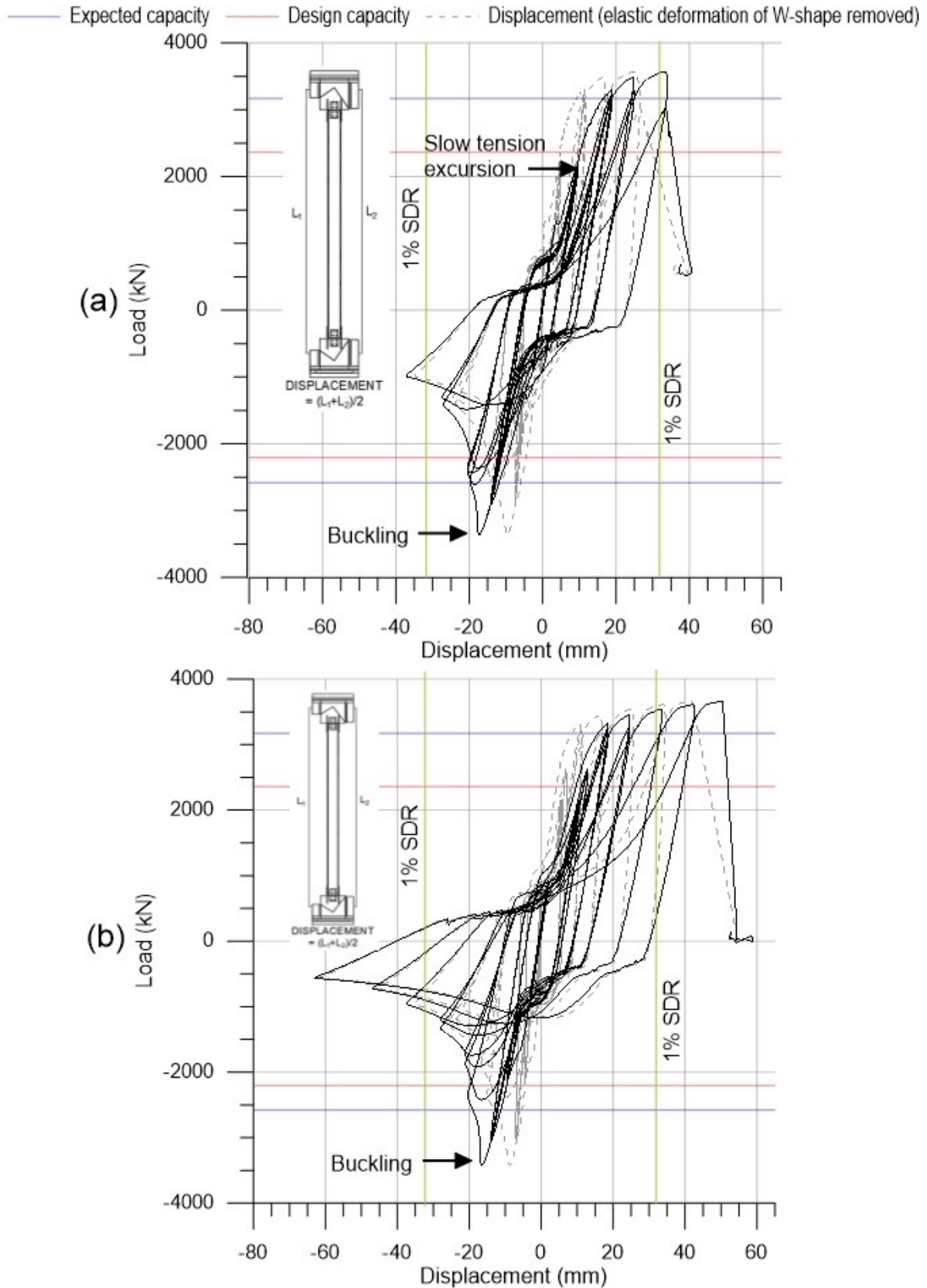


Figure 4-16 Force-displacement hysteretic curves of (a) J310-T and (b) J310-C

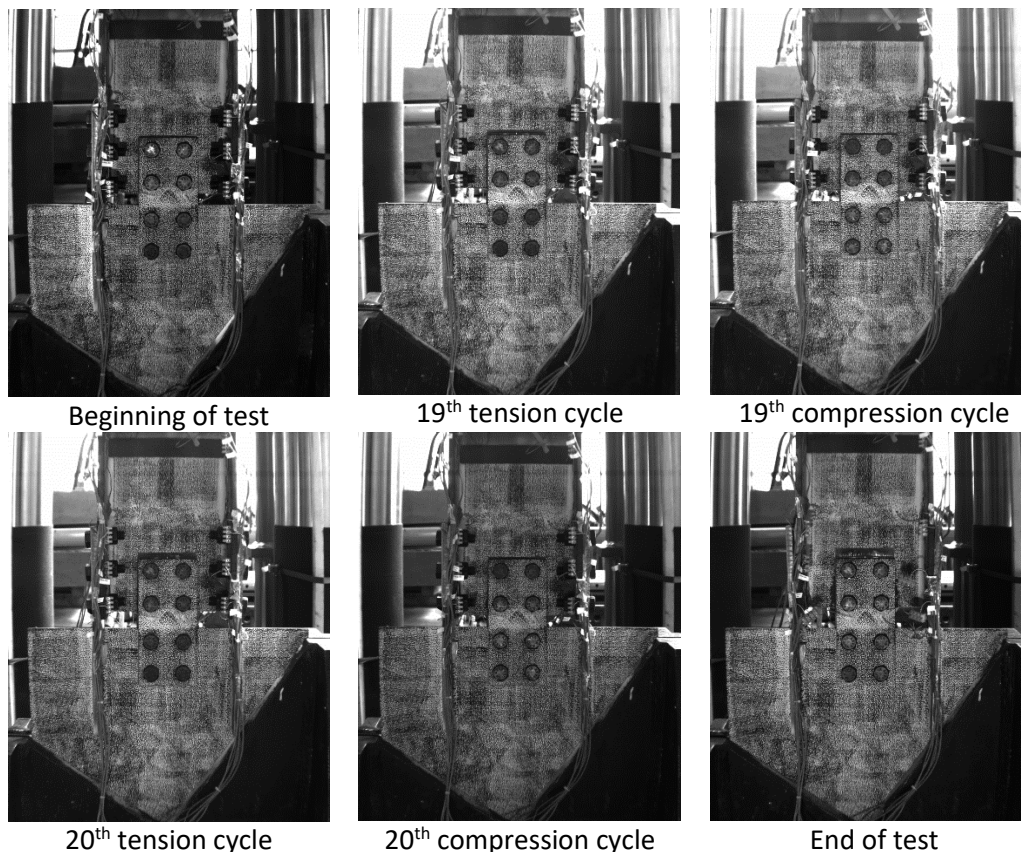


Figure 4-17 Images captured of the bottom connection of specimen J310-T taken at selected load peaks and valleys

Specimen J310-T failed in the bottom connection, while specimen J310-C failed in the top connection. Failure modes matched those expected. Photos of the bolts from the top and bottom flanges of J310-C are shown in Figure 4-20. From these photos, it can be observed that the bolts which did not fracture in shear (in the connection that did not fail) developed a visible shearing deformation. These deformations are most prominent in the bolts in the middle of the flange connections. Photos of the deformed webs of both specimens are shown in Figure 4-21. The brace end connection that failed showed considerably more deformation in the web compared with the web from the opposite end of the member. However, some of this web deformation took place after the shear rupture of the flange bolts since the force suddenly moved from the flanges to the web. The webs of specimen J310-C show greater deformations than those of specimen J310-T.

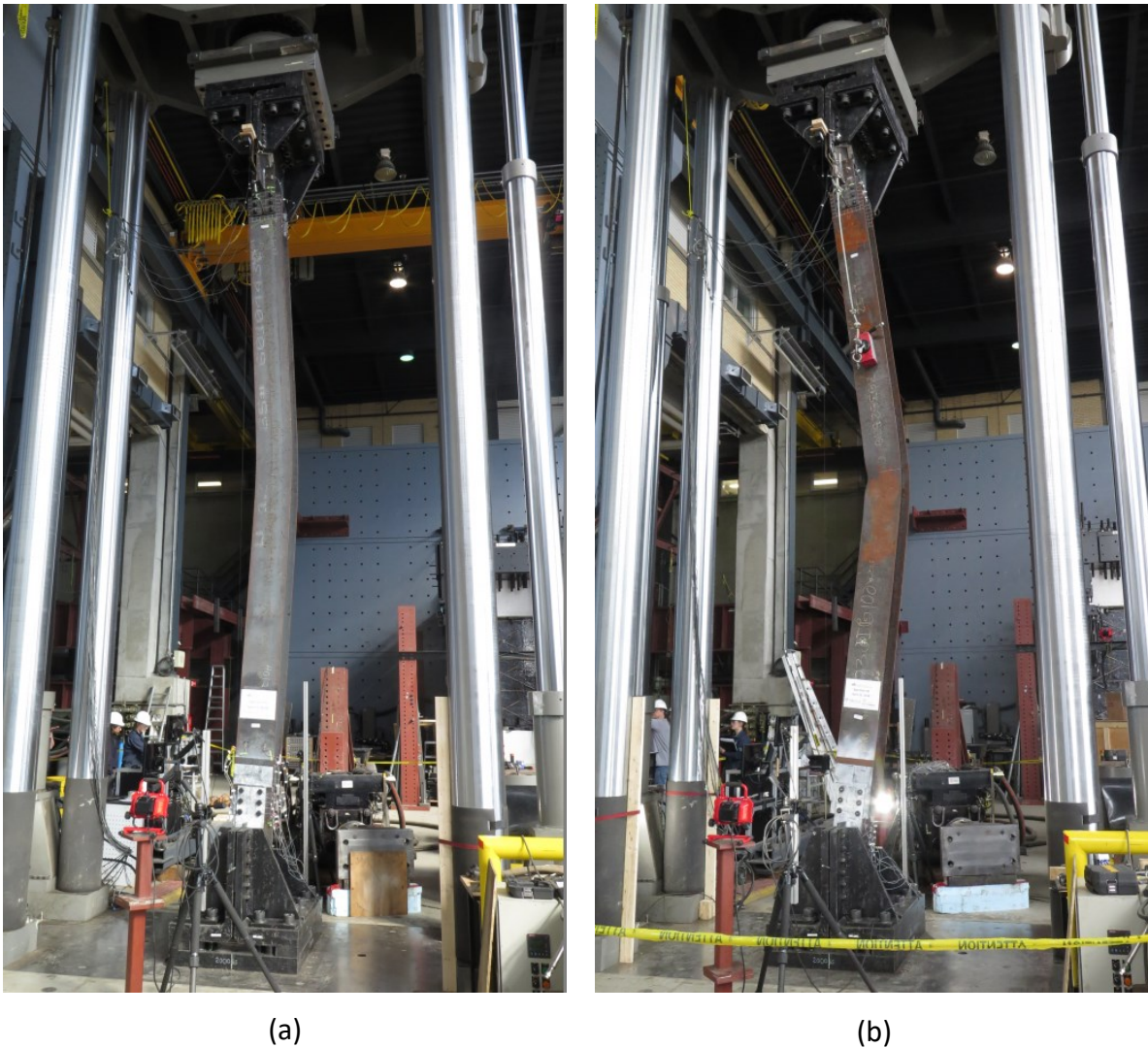


Figure 4-18 Buckling in specimens J310-T and J310-C (a) overall buckling in J310-T and (b) overall and local buckling in J310-C

Deformations were also observed in the elements that did not fail. Ovalization of the holes was observed in the gusset plate of the failed connection (no ovalization was visible to the eye in the holes of the opposite gusset plate). Some yielding and reduction of the area at the net sections of the jaw plates was observed. The net section at the jaw plates was the next possible failure mode from calculations; the calculated net section capacity was close to that of bolt shear at an expected capacity of 2645 kN (the design capacity was actually lower than the design capacity for bolt shear in the flanges). The web plates did not show significant signs of damage except for

indentations below the washers. Local buckling occurring in the flanges at the midpoint of the W-shape brace of specimen J310-C, as shown in Figure 4-23.

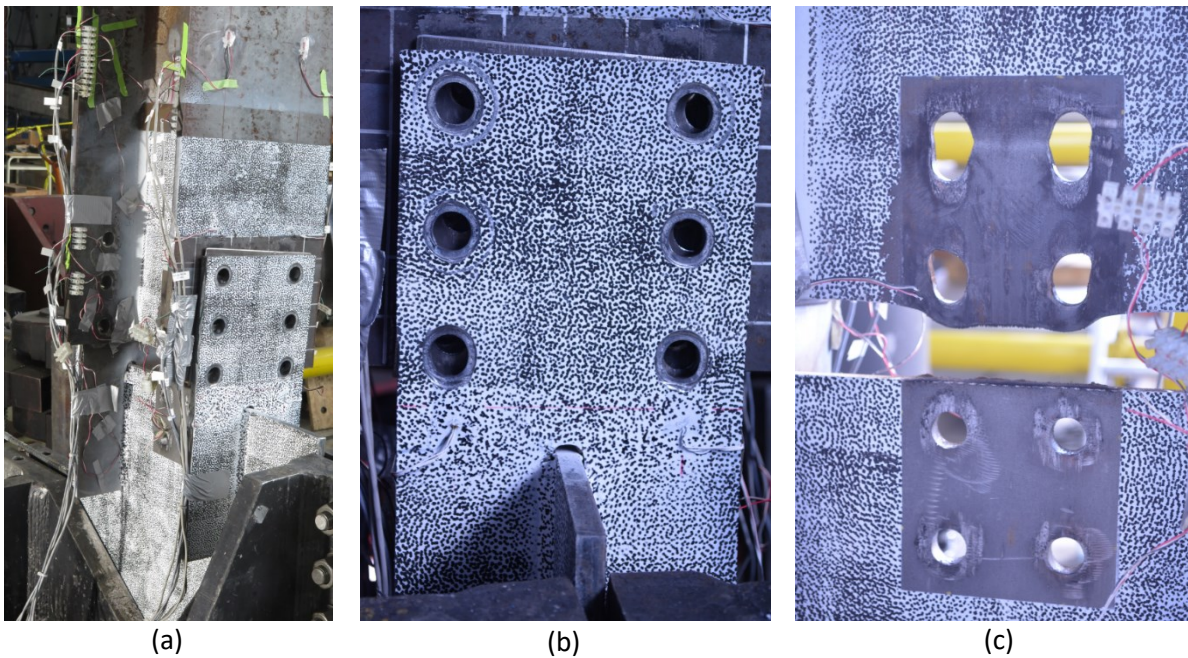


Figure 4-19 Post-test photos of bottom connection of specimen J310-T (a) North flange, (b) close-up of North flange, and (c) W-shape web and gusset plate with web plates removed

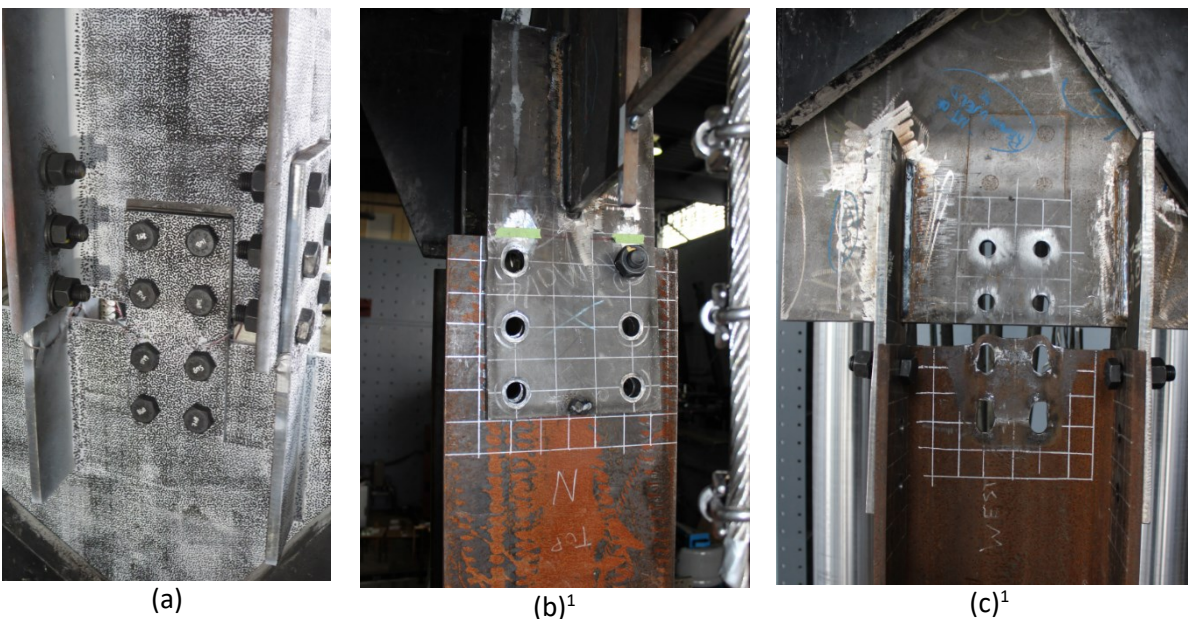


Figure 4-20 Post-test photos of specimen J310-C (a) bottom connection, (b) close-up of North flange, and (c) W-shape web and gusset plate with web plates removed from top connection
1. The bolts in the flanges shown in the photos were added after the test for safety reasons and for the removal of the specimen



Figure 4-21 Bolts from J310-C (a) bottom flange connection (b) top flange connection (sheared)



Figure 4-22 Deformed W-shape webs of J310-C on the left and J310-T on the right: (a) bottoms of W-shapes (b) tops of W-shapes



Figure 4-23 Local buckling in middle of W-shape of specimen J310-C

4.2.1.2. Test versus expected capacities

Design and expected (unfactored with probable material properties) capacities calculated with resistances as per the CSA S16-14 Standard, as well as the capacities calculated with the AISC 360-16 Standard and the capacities calculated with the measured geometric and strength properties of the specimens, are shown in Table 4-11. These are compared with the test values. In general, capacities using expected material properties and design geometry are fairly close to the capacities calculated using the measured material properties and the measured specimen geometry.

It should be noted that the compressive capacities in Table 4-11 were calculated with the design buckling equations (Eq. 2-2 and Eq. 4-1). The compressive capacity can also be predicted with the C_u equation (Eq. 2-3). The calculated C_u capacity for the W310x97 was 2945 kN according to CSA S16-14, whereas and the equivalent expected compression capacity based on AISC 341-16 (Eq. 4-5) resulted in a 3264 kN prediction. In a comparison with the average compressive capacities measured in the two tests, the expected capacity to average test compressive capacity ratio is 0.87 for the CSA S16-14 Standard equation and 0.96 for the AISC 341-16 Standard equation. Equations 2-3 and 4-5 were therefore significantly better than the buckling design equations, Equations 2-2 and 4-1, at predicting the compressive capacity of these braces. This may be due to the selection of the K factor in the design buckling equation (selected as 0.9 for these calculations). In general, the equations from the AISC 360-16 (Eq. 4-1) and AISC 341-16 Standards (Eq. 4-5) seem to allow closer predictions of the measured compressive capacities than the equations in the CSA S16-14 Standard (Eq. 2-2 and Eq. 2-3, respectively).

The tensile capacity predictions were conservative in all cases when compared to the test results. The CSA S16-14 Standard equations (Eq. 2-6 plus Eq. 2-25) predicted the tensile capacity within 19% and 12%, while the AISC 360-16 equations (Eq. 2-8 plus Eq. 2-31) predicted the tensile capacity within 17% and 24% for specimens J310-T and the J310-C, respectively.

Table 4-11 Comparison of predicted capacities to test results for J310-T and J310-C

		P_{exp1}	P_{exp2}	Design	Expected ²	Measured properties for J310- $T^{2,3,4}$	Measured properties for J310- $C^{2,3,4}$
CSA S16	Tension (kN)	3572	3653	2394	3171	3157	2876
	Compression (kN)	3369	3421	2209	2582	2518	2785
	Tension P/P_{exp}^1	1.00	1.00	0.66	0.88	0.88	0.81
	Compression P/P_{exp}^1	1.00	1.00	0.65	0.76	0.75	0.83
AISC 360	Tension (kN)	3572	3653	2150	2887	3045	2775
	Compression (kN)	3369	3421	2449	2885	2517	2783
	Tension P/P_{exp}^1	1.00	1.00	0.60	0.80	0.85	0.76
	Compression P/P_{exp}^1	1.00	1.00	0.72	0.85	0.74	0.81

1. Design and expected capacities were compared to an average of the two measured results
2. Expected capacities and capacities with measured properties for compression were calculated using the design buckling equations (Eq. 2-3 from the CSA S16-14 Standard and Eq. 4-1 from the AISC 360-16 Standard)
3. Design properties were used for the areas, radii of gyration, and moments of inertia of sections
4. Capacities with measured properties for the side which predicted the lowest capacity are shown even if this did not correspond to the side which failed in testing

It should also be noted that these tensile capacities depend heavily of the true shear strengths of the bolts. As stated in Section 4.1.2., the expected shear strengths of the bolts were obtained from the nominal properties modified with a factor calculated based on previous tests (Tide, 2010). In the case of the grade A325 bolts, the factors used were 1.02 for the CSA S16-14 calculation and 0.975 for the AISC 360-16 calculation. If this factor is changed to 1.2, for example, the expected tensile capacities become 3581 kN for the CSA S16-14 Standard equations (Eq. 2-6 plus Eq. 2-25) and 3378 kN for the AISC Standard equations (Eq. 2-8 plus Eq. 2-31). These calculated values divided by the average of the measured capacities become 1.00 for the CSA S16-14 Standard and 0.95 for the AISC 360-16 equations. These results are clearly closer to the test results. However, in the case of the CSA S16-14 calculations, if the shear strength modification factor were changed to 1.2, the expected bolt shear capacity of 2765 kN would exceed the expected net section capacity at the jaw plates of 2645 kN, and this would become the expected failure mode of the connection in the flanges. The ultimate net section fracture

capacity predictions therefore seem to have underestimated the laboratory net section capacity, though the jaw plates had yielded on their net sections during the tests.

4.2.1.3. Overall brace displacements

In terms of displacements, specimen J310-C achieved greater displacements in both tension and compression. Specimen J310-C was subjected to an extra cycle with an increased amplitude as compared to specimen J360-T. As such, the buckling of this specimen was more severe as can be observed in Figure 4-16 and Figure 4-24. The measured out-of-plane displacements were also significantly greater for specimen J310-C. Specimen J310-C was the only specimen of the two that displayed local buckling of the flanges at the midpoint of the W-shape brace. The significant difference in ductility between the two specimens may be attributed to the slow tension pull excursion applied to specimen J310-T in an attempt to identify the yield displacement. In this slow tension excursion, the specimen was pulled 21.7 mm in tension, at which point the axial load reached 3307 kN which was 93% of the ultimate tensile capacity. The remaining three cycles in that step of the loading protocol had a decreased amplitude of +/- 15 mm, however the first slow tension cycle may have already irreversibly damaged the specimen. Regardless of the loading protocol, both specimens were able to achieve at least a 1% storey drift ratio in both tension and compression.

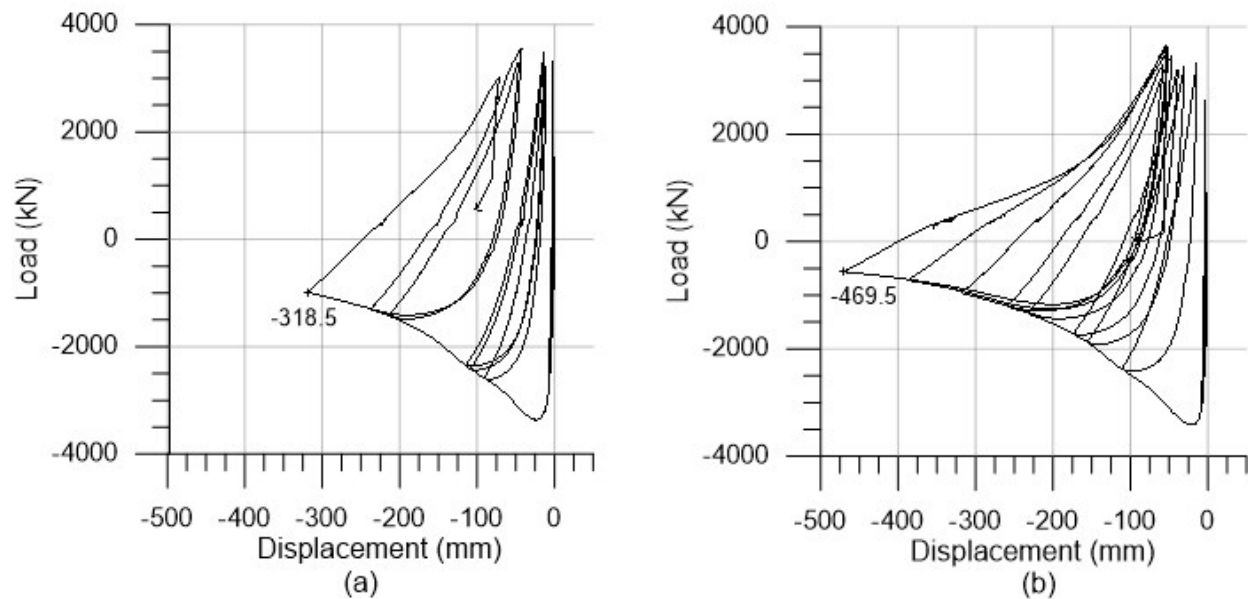


Figure 4-24 Out-of-plane displacements at midpoint of the brace for (a) J310-T and (b) J310-C

4.2.2. J360-T and J360-C Results

Specimens J360-T and J360-C were composed of W360x134 sections and jaw plate connections. Matching predictions for specimen behaviour were made using the unfactored resistances with both probable and measured properties. For these tests, the gusset plate was expected to buckle in compression. In tension, the jaw plates were expected to fracture at the net section and the web of the W-shape was expected to experience block shear at failure.

4.2.2.1. Test observations

The observations during the two tests are detailed in Table 4-12. The force-displacement hysteresses for specimens J360-T and J360-C are shown in Figure 4-25. The expected and design capacities are shown in Figure 4-25 for calculations following the CSA S16-14 Standard. Figure 4-26 show photos taken and certain points during the test of the bottom connection (East side) of specimen J360-C. These photos show the progressive bending of the gusset plate, buckling of the North W-shape flange in the compression cycles, and the growth of the tear in the gusset plate in the tension cycles.

Table 4-12 Observations for specimens J360-T and J360-C

Step	Observations
6 load control cycles	<ul style="list-style-type: none"> • Before the test the interlock safety was not turned off and a load was momentarily applied before the beginning of the J360-T test • For specimen J360-C, half a cycle was completed in compression, while two instruments were disconnected. The test was restarted. • The loading sequence was paused in the second cycle of J360-T to verify the if the data acquisition system was functioning properly • Linear elastic response to loading
4 load control cycles	<ul style="list-style-type: none"> • Slipping started in this set of cycles for both specimens • Loud bangs were heard during slipping at around 1500 kN
4 cycles at 15 mm	<ul style="list-style-type: none"> • Yielding is observed in several strain gauges of J360-T
3 cycles at 21.2 mm	<ul style="list-style-type: none"> • Bottom gussets bend at this amplitude for both specimens, as shown in Figure 4-27. • Bending of the gusset plates occurred on the South sides of the connections where the grip restraints are lower on the gusset plate
2 cycles at 27.4 mm	<ul style="list-style-type: none"> • Strain gauges in the bottom jaw plates were yielding for J360-T (those at the bottom connection more than those at the top connection)
1 cycle at 36.7 mm	<ul style="list-style-type: none"> • Local buckling was perceived at the North flange of the W-shape near the bottom connection of specimen J360-C (see Figure 4-31) • Tears were observed in the bottom gusset plate at the ends of the jaw plates and on the South edge of the gusset for specimen J360-C
1 cycle at 46 mm	<ul style="list-style-type: none"> • Significant rotation of the top platen is perceived for specimen J360-C, as shown in Figure 4-29. • Tearing increases at the South edge of the bottom gusset plate of specimen J360-C • Paint flakes off of the North flange of W-shape of specimen J360-C • Local buckling of the W-shape flanges of specimen J360-C continues and intensifies
1 cycle at 61.5 mm	<ul style="list-style-type: none"> • Approximately 50% of the tensile capacity is lost for specimen J360-T • The fracture in the bottom gusset plate of specimen J360-C continues to grow • Jaw plate fractures on the North side of the bottom connection of J360-T (Figure 4-28 shows the fracture of the North jaw plate)
1 cycle at 77 mm	<ul style="list-style-type: none"> • The test for specimen J360-T is ended in the tension excursion
1 cycle at 90 mm	<ul style="list-style-type: none"> • In compression excursion, the gusset plate continues to tear because of deformations. • The test for specimen J360-C is ended in the tension excursion

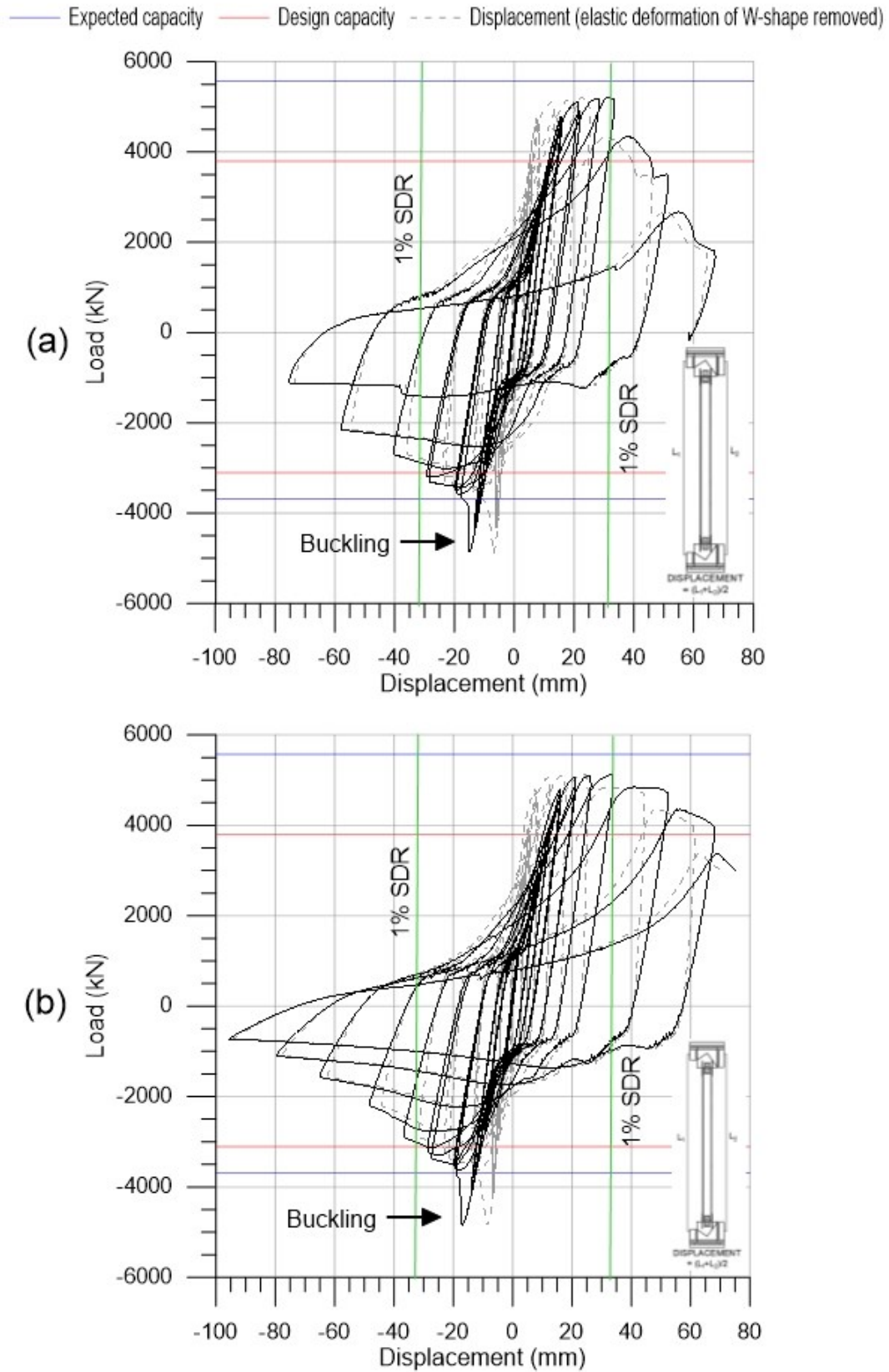


Figure 4-25 Force-displacement hysteretic curves of (a) J360-T and (b) J360-C

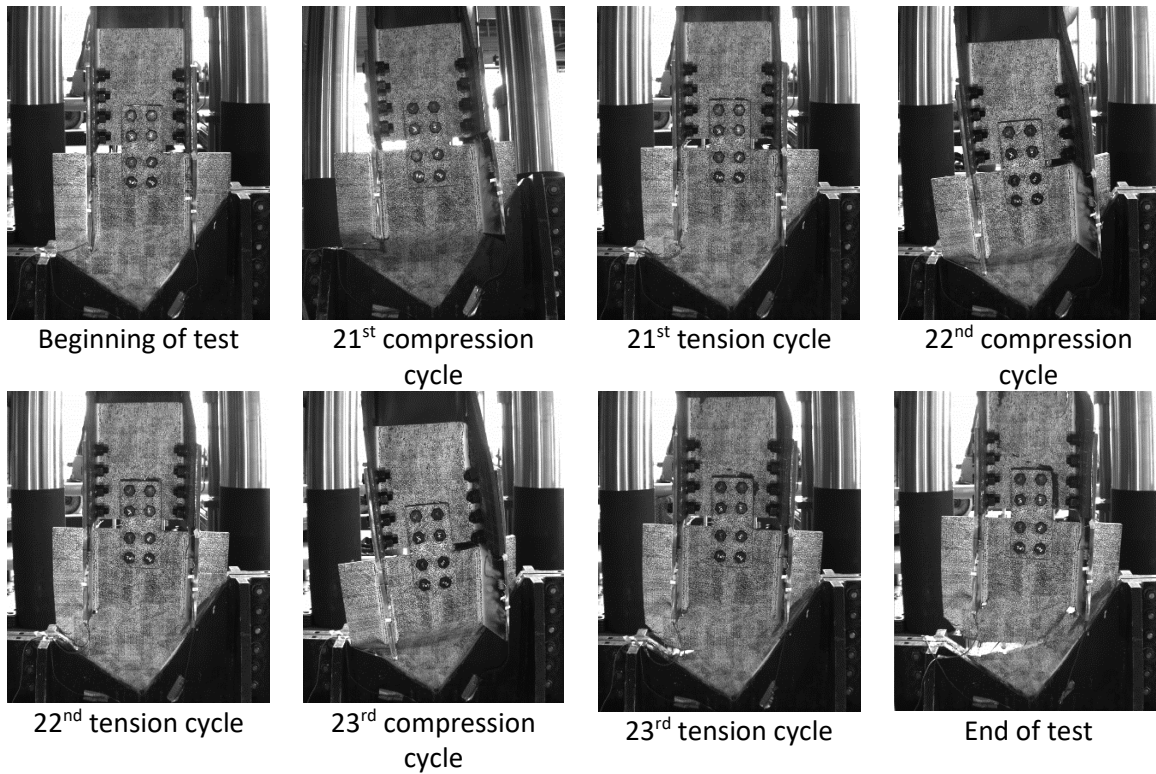


Figure 4-26 Images captured of the bottom connection of specimen J360-C taken at selected load peaks and valleys

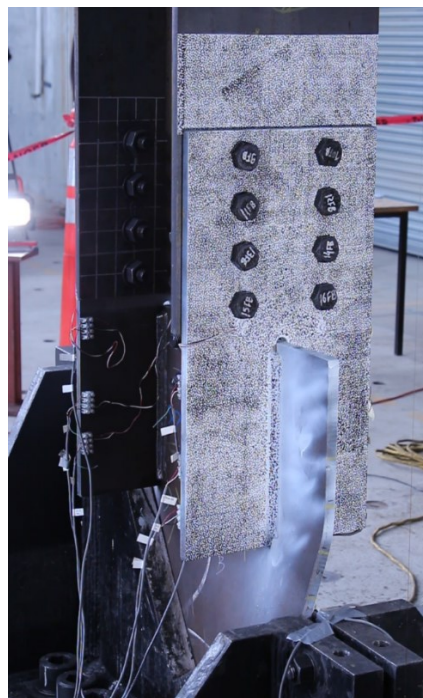


Figure 4-27 Bending of gusset plate in specimen J360-C

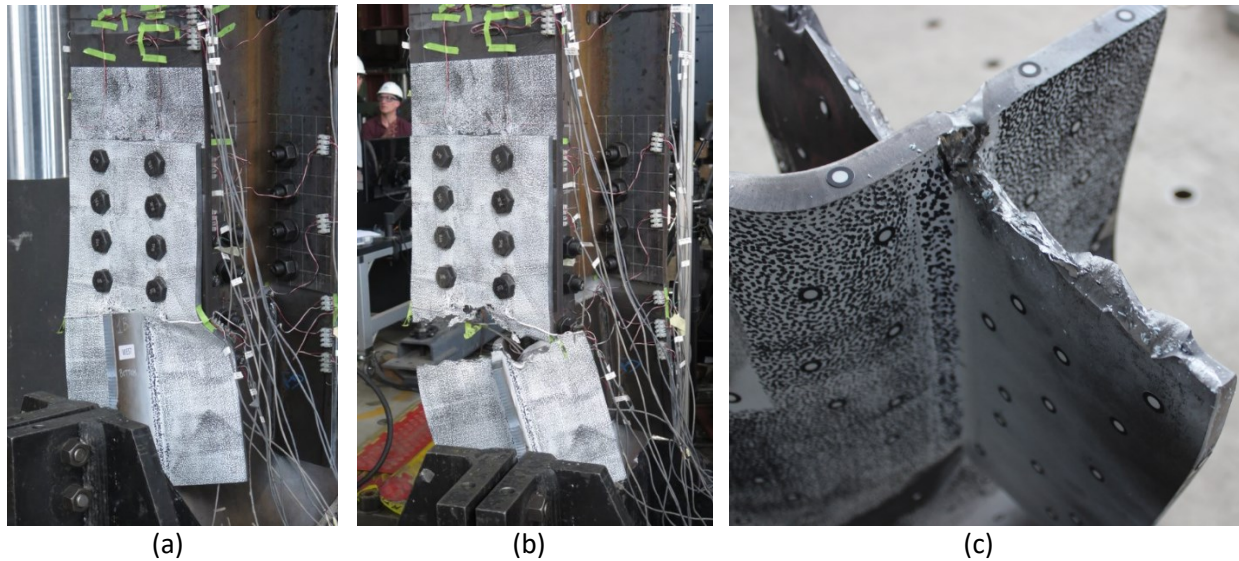


Figure 4-28 North jaw plate fracture in specimen J360-T (a) initial bending of plate, (b) complete fracture of plate, and (c) bottom fractured edge

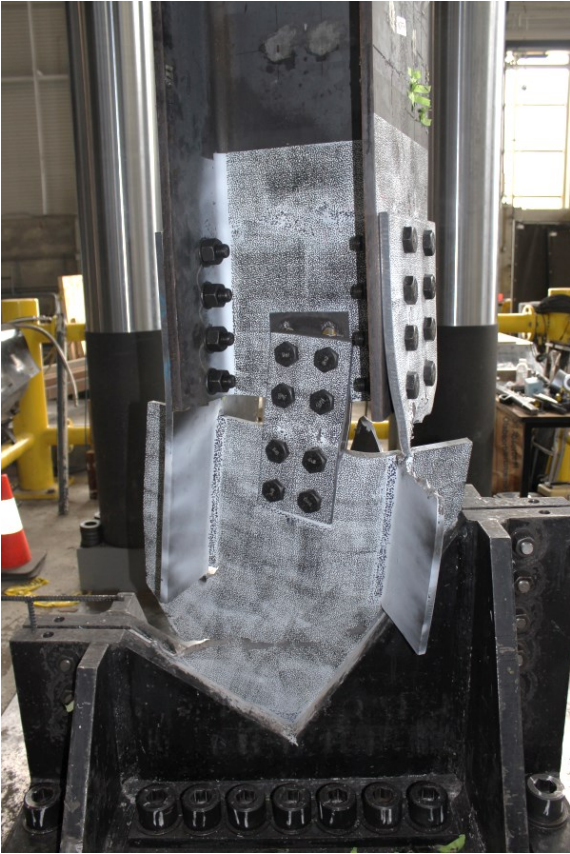
Both specimens failed at the bottom connections. This was a result of the end constraints in the press assembly. While the bottom grip was connected to the rigid strong floor creating a rotationally fixed connection (in the plane of the floor), the top grip was connected to the press's top platen that was allowed to rotate about the longitudinal axis of the brace, i.e. the actuator piston rotates freely within its housing. Figure 4-29 shows the extent of this rotation at the end of the test for specimen J360-T. The increased rigidity of the bottom connection caused the bottom gussets to bend before the top gussets. The bending of the gusset plates and the behaviour thereafter was strongly influenced by the restraint condition of the gusset plates. The asymmetric boundary condition of the grips (where one side of the gusset was more restrained than the other) caused the asymmetric bending of the gusset plates and, consequently, the rotation of the specimens as is visible from the photo in Figure 4-29. This additional moment in the asymmetric end connection is not accounted for in design. Additionally, the clearance distance between the end of the connection and the grips also has an impact on the bending of the gusset plates. For these tests, this distance was set to 25.4 mm. The distance was set to 25.4 mm because this was thought to be the minimum clearance distance that would allow rotation in the gusset plates, while not adhering to the $2t_g$ requirement imposed on MD- and LD-type CBFs. Future finite element modeling of these specimens may increase the understanding of this behaviour.

The possibility of an eccentricity in the assembly causing lateral torsional buckling in the two specimens was also investigated. The unfactored moment resistance was calculated for the brace sections (W360x134) with the probable yield stress giving 920 kNm of flexural resistance (the calculated M_y was greater than the M_r' for this brace length). This moment was then divided by the ultimate capacity of the brace specimens in compression to see what eccentricity would be required to cause the braces to buckle in the lateral torsional buckling mode. The eccentricity calculated was 185 mm. It would be unlikely that the eccentricity of the assembled specimen would have reached 185 mm in a single direction. Furthermore, the top of the specimens seemed to start rotating after reaching the ultimate capacity in compression at which point the axial load in compression would have decreased (thereby increasing the required eccentricity).

After the bending of the bottom gusset plates, the behaviours of the specimens diverged. This was due to localized strain concentrations caused by the bending of the gusset plates. Figure 4-30 shows the damage and state of the bottom connections at the end of each of the two tests. The first specimen, J360-T, failed when the gusset plate ruptured on the South side and the jaw plate on the North side ruptured at its net section at the end of the slot, as shown in Figure 4-28. The second specimen only ruptured in the gusset plate. Neither specimen failed exactly as was expected, with a net section fracture at the bolt line of the jaw plates. Additionally, the flanges of the W-shape of specimen J360-C buckled locally near the bottom connection and the web near the buckled flanges ruptured, as shown in Figure 4-31. The bending of the gusset plate may therefore make the prediction of the tension failure mode more challenging because the end restraints of the connection seem to have a strong effect on the overall behaviour.



Figure 4-29 Rotation at the top of the assembly at the end of the test for specimen J360-T



(a)



(b)

Figure 4-30 Bottom connections of specimens (a) J360-T and (b) J360-C at the end of the tests

The gussets of both specimens tore beneath the bottom of the slotted edges of the jaw plates. These tears were the first visible signs of damage in tension, which indicates that these areas seemed to attract high concentrations of strain. This may also have been due to imperfections in the material caused by the welds in these areas. In the case of specimen J360-T, the final failure crack went through this initial tear in the gusset plate. Figure 4-32 shows photos of these tears.

As expected, block shear failure took place in the web of the W-shape in the bottom connection of specimen J360-T. However, for specimen J360-C, the gusset plate tore on nearly its entire section, and the web in the W-shape did not fail in block shear. There was however the development of some ovalization of holes in the bottom web connection. Figure 4-33 shows the webs in the bottom ends of the W-shape braces for both specimens. Deformations in the W-shape web of specimen J360-T are significantly larger than those in the web of specimen J360-C.



Figure 4-31 Locally buckled flanges and torn web in specimen J360-C

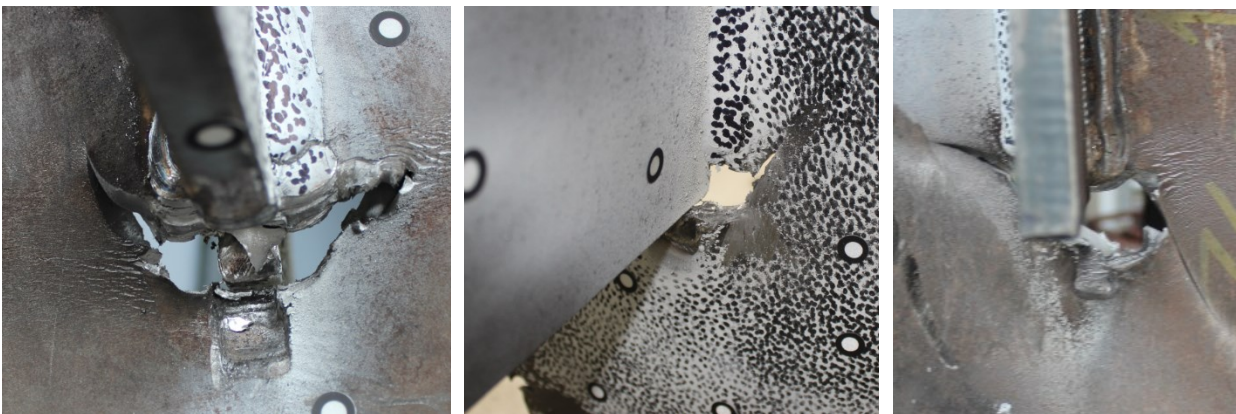


Figure 4-32 Torn gussets at the end of the welded jaw plates

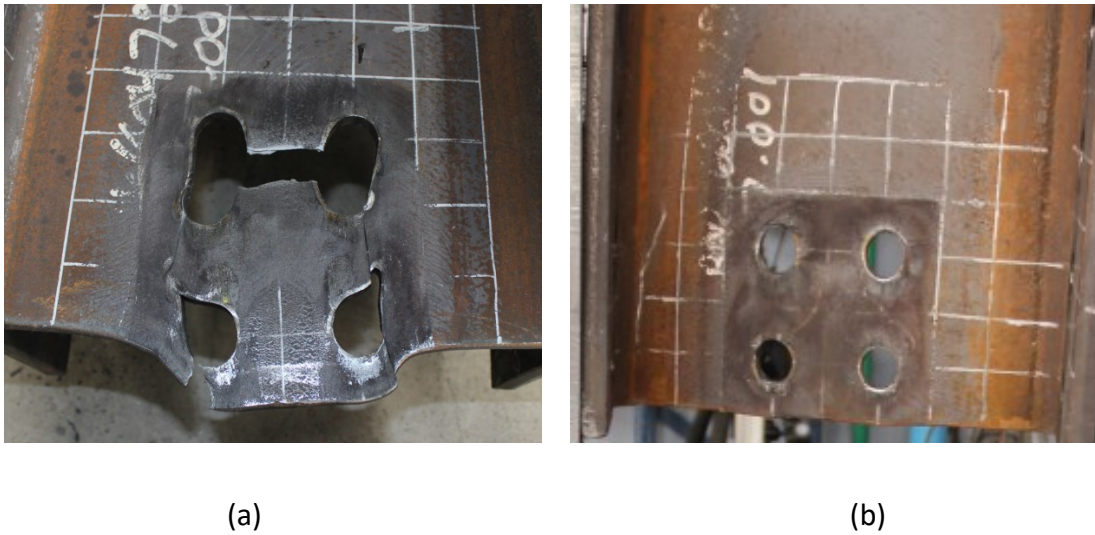


Figure 4-33 W-shape webs in the bottom connections of (a) J360-T and (b) J360-C

Other components of the brace assembly, for the most part, showed little permanent damage after the end of the tests. In the top connection, only slight ovalization of the holes in the W-shape was observed after the tests for the two specimens. The jaw plates at the bottom connection showed ovalization of the holes with the elongation of the holes increasing closer to the slotted edge of the jaw plates, i.e. the side that was welded to the gusset plate. The web plates at the bottom connections were bent and deformed due to the bending of the bottom gusset plates, as shown in Figure 4-34. As the braces did not buckle, they sustained little damage on the overall braces and damage was limited to hole ovalization and the previously mentioned damage in the area near or within the bottom connection.



Figure 4-34 Photos of deformed web plates

4.2.2.2. Test versus expected capacities

The measured capacities, as well as the predictions and the comparison of these values, are provided in Table 4-13. As for the previous two specimens, the compressive capacities in the table are calculated using buckling equations in the two design standards (Eq. 2-2 and Eq. 4-1). In this case, however, using the expected equation for C_u (Eq. 2-3) and the corresponding equation in the AISC 341-16 Standard (Eq. 4-5) was not relevant because these equations were developed specifically for buckling braces, which is not the case for these two specimens. The predicted compression capacity using Equations 2-2 and 4-1 underestimated the laboratory results by 24% for Eq. 2-2 in the CSA S16-14 Standard and by 20% for Eq. 4-1 in the AISC 360-16 Standard. Of course, the bending of the gusset plates observed in the laboratory tests does not correspond to the traditional buckling that is considered in these equations. The bending of the gusset plate depends heavily on the restraint conditions at its end. A simple equation, such as those used in design, does not seem to be adequate for predicting this behaviour; future finite

element modelling of this connection and test may better serve in predicting the compressive capacities and behaviours of these bending gusset plates.

Table 4-13 Comparison of predicted capacities to test results for J360-T and J360-C

		P_{exp1}	P_{exp2}	Design	Expected ²	Measured properties for J360-T ^{2,3}	Measured properties for J360-C ^{2,3}
CSA S16	Tension (kN)	5206	5112	3796	5573	5646	5532
	Compression (kN)	4880	4846	3110	3689	4095	4072
	Tension P/P_{exp}^1	1.00	1.00	0.74	1.08	1.08	1.06
	Compression P/P_{exp}^1	1.00	1.00	0.64	0.76	0.84	0.83
AISC 360	Tension (kN)	5206	5112	3743	5498	5568	5452
	Compression (kN)	4880	4846	3249	3883	4264	4242
	Tension P/P_{exp}^1	1.00	1.00	0.73	1.07	1.07	1.07
	Compression P/P_{exp}^1	1.00	1.00	0.67	0.80	0.88	0.88

1. Design and expected capacities were compared to an average of the two measured results
2. Expected capacities and capacities with measured properties for compression were calculated using the design buckling equation (Eq. 2-3 from the CSA S16-14 Standard and Eq. 4-1 from the AISC 360-16 Standard)
3. Design properties were used for the areas, radii of gyration, and moments of inertia of sections
4. Capacities with measured properties for the side which predicted the lowest capacity are shown even if this did not correspond to the side which failed in testing

The tension failures did not match those expected from either of the two standards. Predictions following both standards included an ultimate failure of net section rupture in the jaw plates at the bolt lines in combination with block shear in the web of the W-shape. The CSA S16-14 equations (Eq. 2-23 with Eq. 2-25) overestimated the measured tensile capacity by 8%, while the AISC 360-16 equations (Eq. 2-23 with Eq. 2-31), for which the net section resistance calculation does not vary, overestimated the measured tensile capacity by 7%.

The resistance prediction for gross section yielding in the gusset plates was actually lower than the predicted resistance of the jaw plate net section rupture in combination with block shear in the W-shape web. However, this was not considered an ultimate capacity and was therefore not reported as the expected failure mode. The calculated resistance prediction for the gross section yielding of the gusset plates was 4958 kN for both standards. This gross section yielding resistance underestimates the ultimate measured capacity by only 4%.

While the expected failure mode in tension was a combination of net section rupture in the jaw plates and block shear in the W-shape web, the observed failure mode in tension included fracture of the gusset plate (for specimen J360-T, one of two jaw plates fractured and for specimen J360-C, neither of the jaw plates fractured). The calculated net section fracture capacity for the gusset plates of these specimens was 6467 kN. This resistance overestimates the test results by 25%. However, the tearing in the gusset plates was influenced by the high strain deformations in the compression cycles which may have allowed the tearing to occur at a lower resistance. It should also be noted that the gusset plates fractured incrementally and not instantaneously i.e. the cracks in the gusset plates grew with each subsequent cycle. As a result, the section may not have attained the full level of strain hardening over the entire cross-section as would be expected for a coupon in axial tension. It could be suggested to therefore calculate the expected net section fracture with a fracture stress equivalent to the average of the yield stress and the ultimate stress of the material (397.5 MPa for this grade of steel). Using this stress, a net section fracture capacity of 5193 kN is obtained for these gusset plates. This value is equal to almost exactly the average of the two measured test results. However, the effects of the deformations in compression cannot be captured in a simple equation and should be investigated in future finite element studies.

4.2.2.3. Overall brace displacements

In terms of displacements, specimen J360-C, for which the loading protocol began with an excursion in compression, was once again able to undergo an additional cycle of loading before failure. Both specimens attained at least 1% storey drift in both tension and compression. The out-of-plane displacements, as measured at the midpoints of the W-shape braces and shown in Figure 4-35, were significantly smaller than the previous two specimens. This is to be expected because the braces themselves did not buckle for these two specimens. The bending of the gusset plates did cause some lateral displacement of the braces as recorded by the string potentiometer data. This recorded maximum lateral movement for specimen J360-C was double the maximum lateral movement of specimen J360-T.

It should be kept in mind that the measurements of the overall string potentiometers may have been affected by the bending of the gusset plates at the bottom connections because the potentiometer frames were tack welded directly onto the bottom gusset plates. The location of the string potentiometer on the bottom connection was moved down further into the grip for specimen J360-C to minimise this effect.

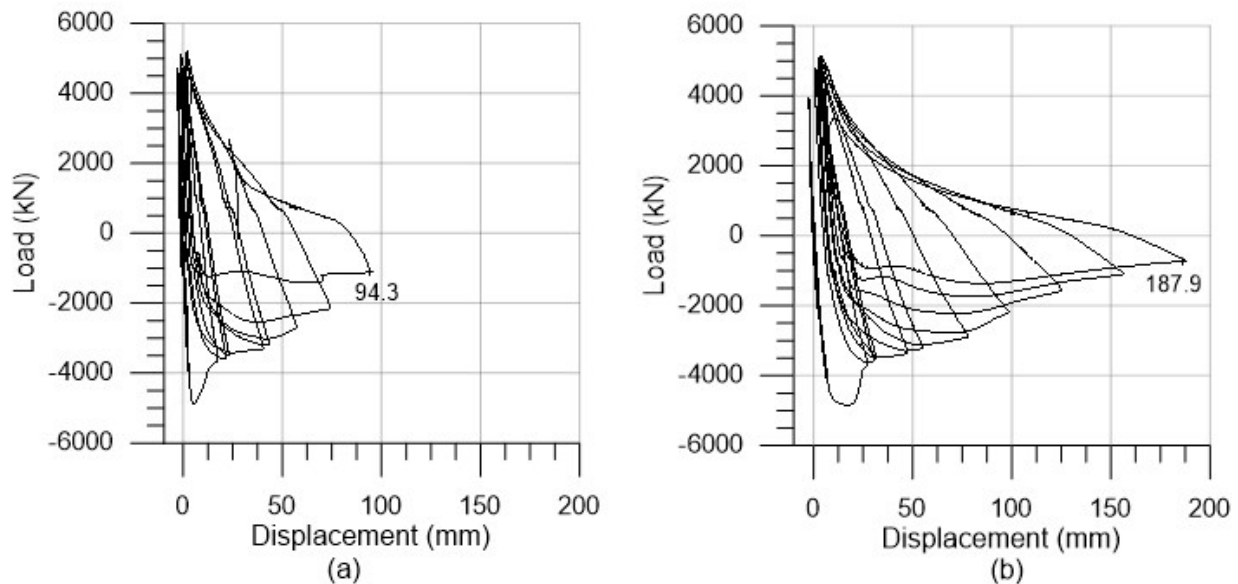


Figure 4-35 Out-of-plane displacements at the brace midpoint for (a) J360-T and (b) J360-C

4.2.3. C360-T and C360-C Results

Specimens C360-T and C360-C were composed of W360x134 sections and claw angle connections. Matching predictions for specimen behaviour were made using the unfactored resistances with both probable and measured properties. For these tests, the W-shape brace was expected to buckle at mid-length in compression, while the angles and the web of the W-shape were both expected fail in block shear in tension.

4.2.3.1. Test observations

The observations during the two tests are detailed in Table 4-14. The force-displacement hysteresses for specimens C360-T and C360-C are shown in Figure 4-36. The expected and design capacities are shown in Figure 4-36 for calculations following the CSA S16-14 Standard. Figure 4-38 shows the set-up for the specimens with the claw angle connections. Figure 4-37 shows

images taken of the bottom connection (East side) of specimen C360-C. The images show the relative displacements between the W-shape and the web plate, as well as the development of the block shear in both the web plate and the angles.

Table 4-14 Observations for specimens C360-T and C360-C

Step	Observations
6 load control cycles	<ul style="list-style-type: none"> • Linear elastic response to loading
4 load control cycles	<ul style="list-style-type: none"> • Sharp shocks perceived during slip. These cause the loss of the linear potentiometers at the top connection for C360-T. Large shocks during slips appeared as jumps in the force-displacement hystereses of C360-T (the hystereses were consequently more jagged than for other specimens). Slipping was very loud (louder than previous specimens). Sliding movements were very visible. • Shocks and loud bangs for specimen C360-C start in the third compression excursion.
4 cycles at 15 mm	<ul style="list-style-type: none"> • Slipping behaviour continues
3 cycles at 21.2 mm	<ul style="list-style-type: none"> • The beginning of yielding in tension was observed in the force-displacement hysteresis of specimen C360-T. • Overall buckling of the W-shape brace occurred for specimen C360-C. The hinge in the brace formed slightly lower than at the mid-point of the brace due to differences in rigidity between the press piston and the strong floor connection (see Figure 4-37).
2 cycles at 27.4 mm	<ul style="list-style-type: none"> • Bottom connection gusset bent on the south side in the first compression excursion for specimen C360-T (Figure 4-41 shows the final bent shape of the bottom gusset plate for specimen C360-T) • Paint started to flake off on the North flange of specimen C360-T. This was observed in conjunction with the local buckling of the North flange of the W-shape (see Figure 4-36).
1 cycle at 36.7 mm	<ul style="list-style-type: none"> • Buckling of W-shape continues.
1 cycle at 46 mm	<ul style="list-style-type: none"> • Local buckling was perceived in the W-shape of specimen J360-C on the West side (see Figure 4-37).
1 cycle at 61.5 mm	<ul style="list-style-type: none"> • Block shear was perceived in the Southwest and Northwest (on the side of the W-shape) and Southeast (on the gusset side) angles for specimen C360-T. This occurred at the same time as a significant loss in capacity in the tensile excursion. • For specimen C360-C, the Southwest angle in the bottom connection failed in block shear. Block shear deformations are visible in the web of the W-shape at the bottom connection.
1 cycle at 77 mm	<ul style="list-style-type: none"> • Failure in all angles was observed and the test was stopped for both specimens. Figure 4-38 shows select photos of angles failed in block shear.

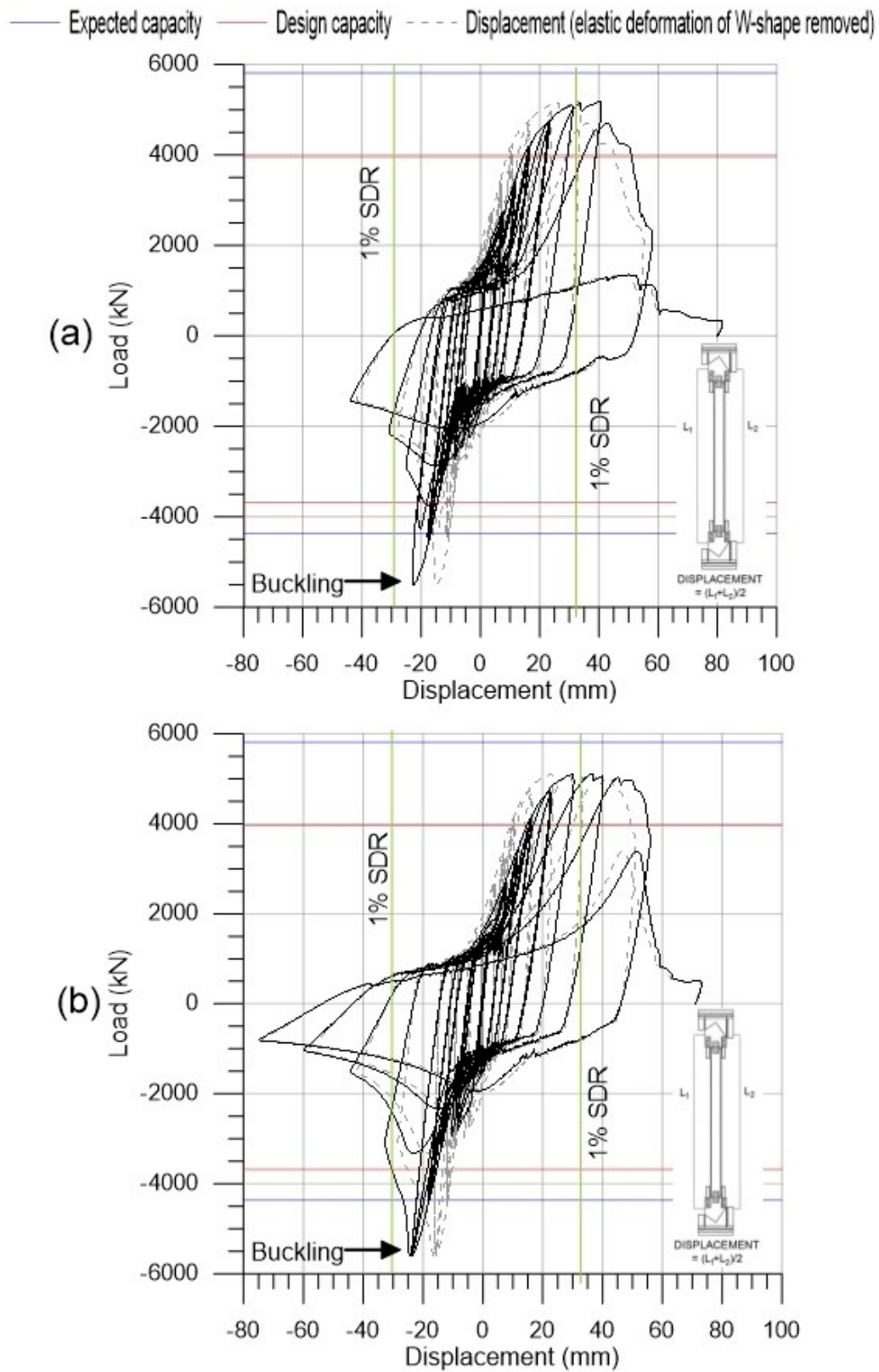


Figure 4-36 Force-displacement hysteretic curves of (a) C360-T and (b) C360-C

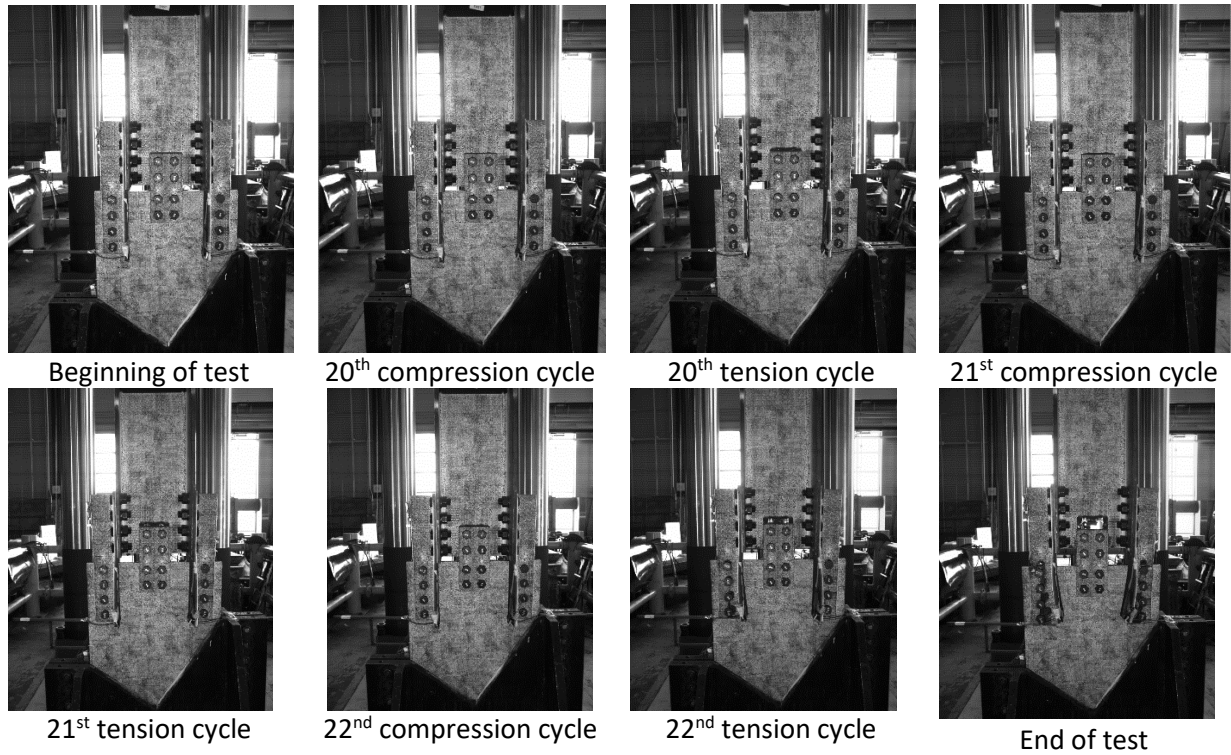


Figure 4-37 Images captured of the bottom connection of specimen C360-C taken at selected load peaks and valleys

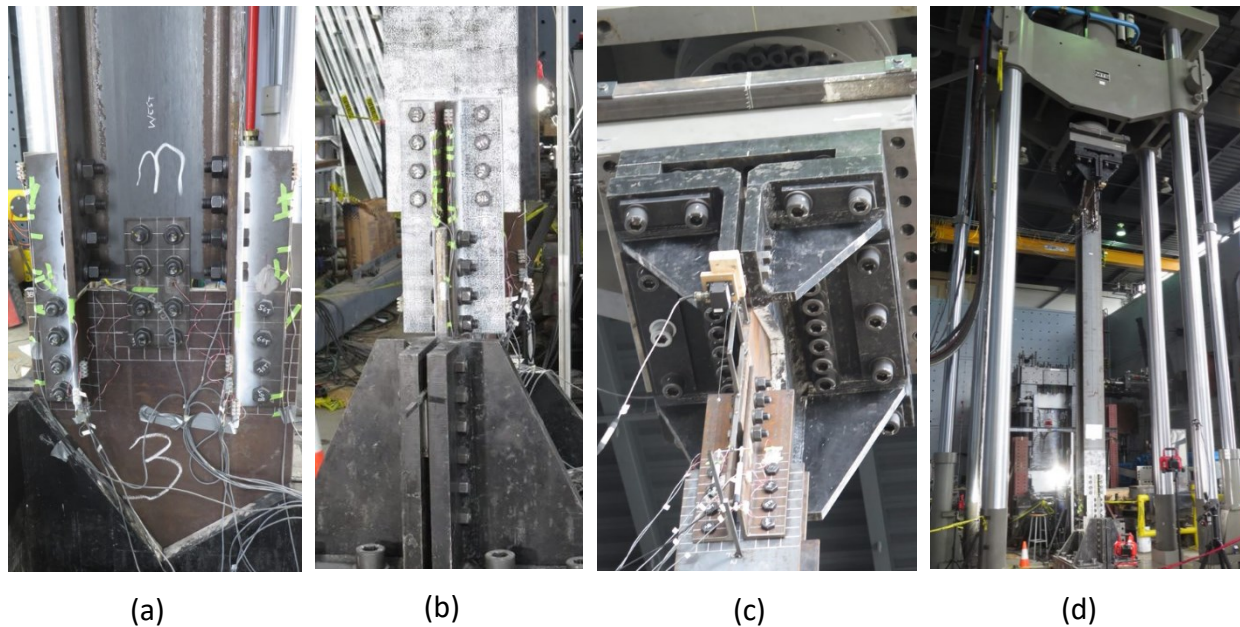


Figure 4-38 Set-up for specimens with claw angle connections (a) East of bottom connection, (b) North of bottom connection, (c) top connection, (d) overall brace assembly

The behaviour in compression varied between the two specimens. While the expected behaviour in compression was brace buckling, the bottom gusset of specimen C360-T bent out-of-plane

similarly to the J360 specimens. The bending in the gusset plate was also followed by local buckling in the W-shape flange just above the connection, as shown in Figure 4-39. It is suspected that this difference in behaviour was due to the misalignment of the parts in the brace assembly. While lasers were used to align the various components of these braces, due to the large scale of each of the components and tolerances in fabrication, it was very challenging to ensure precise alignment of the assemblies. Specimen C360-C buckled slightly below the midpoint of the brace due to the difference in rigidity of the two end constraints. The W-shape flanges had also buckled locally at this location. The globally and locally buckled shaped of specimen C360-C are shown in Figure 4-40.

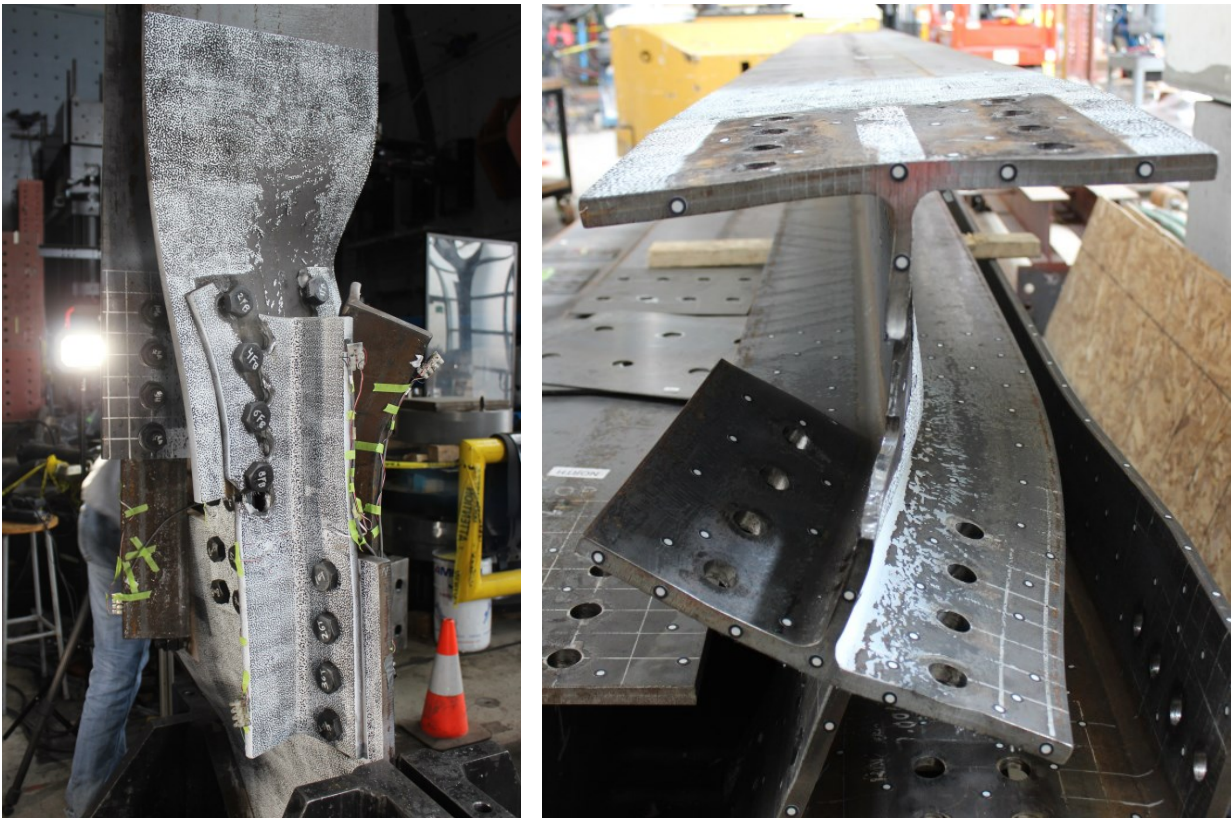


Figure 4-39 Buckled W-shape flange in specimen C360-T

Even though the behaviours of the two specimens were different in compression, the tensile failure modes matched those expected: block shear in both the angles and the webs of the W-shape braces. Block shear failure could have occurred in either of the two ends of an angle because the connections were designed to be the same on either side in different legs. Examples of the block shear failure in the angles are shown in Figure 4-41. Some of the angles in specimen

C360-T were much more warped due to the bending in the gusset plate, as shown in Figure 4-41(b). The block shear in the W-shape webs resulted in the complete removal of a block section of the W-shape web for both specimens, as shown in Figure 4-42.

Web plates showed no signs of significant damage except some ovalization of holes in one of the plates. The angles in the top connection only showed slight ovalization of holes. The holes in the flanges of the W-shape show significant ovalization in the bottom connection and very slight ovalization in the top connection. The W-shape webs in the top connections had deformations that were starting to resemble block shear: significantly elongated holes, thinning at the net section for specimen C360-T, and bulging of the steel at the edge of the W-shape web, as shown in Figure 4-43. In the bottom gussets, the holes for the angles were very elongated and the steel was bulging at the edge of the gusset plate. The bolts for these holes also showed increased shear deformations (the number of bolts on the side of the gusset plate is half the number on the W-shape because of the use of double shear planes in each bolt).



Figure 4-40 Global and local buckling of the W-shape brace of specimen C360-C



(a)



(b)

Figure 4-41 Block shear failure in angles of specimens: (a) C360-C and (b) C360-T



Figure 4-42 Block shear in the W-shape webs for specimens: (a) C360-T and (b) C360-C



Figure 4-43 Deformed W-shape web of top connection in specimen J360-T



Figure 4-44 Post-test bent bottom gusset plate from specimen C360-T

4.2.3.2. Test versus expected capacities

The measured test capacities, as well as the predictions and the comparison of these values, are provided in Table 4-15. As with specimens J310-T and J310-C, the C_u calculation from the CSA S16-14 Standard, Eq. 2-3, as well as the corresponding equation in the AISC 341-16 Standard, Eq. 4-5, were also performed for the W360x134 section giving 4906 kN and 5330 kN, respectively. Compared to the average of the two measured results, these compression capacity predictions

have a 12% and a 1% error. As seen with specimens J310-T and J310-C, these calculations give more accurate predictions than the unfactored design buckling equations (Eq. 2-2 and Eq. 4-1) with probable material properties. Additionally, Eq. 4-1 from the AISC 360-16 and Eq. 4-5 from the AISC 341-16 Standard give more accurate predictions than the corresponding Eq. 2-2 and Eq. 2-3 in the CSA S16-14 Standard.

The block shear equation (Eq. 2-31) is known to be more conservative in the AISC 360-16 Standard than in the CSA S16-14 Standard (Eq. 2-25). This is because the AISC 360-16 Standard uses the net shear area in the calculation of block shear as opposed the gross shear area used in the CSA S16-14 Standard. Experimental tests of the block shear failure (e.g. Cai and Driver, 2008) showed that the shear plane passes through a line just outside of the holes corresponding to a gross shear area. However, measured capacities of specimens C360-T and C360-C, which include a combination of block shear in four angles and block shear in the W-shape web, were closer to the AISC 360-16 Standard predictions. The unfactored equations with probable material properties gave predictions with 13% and 7% error for the CSA S16-14 Standard and the AISC 360-16 Standard, respectively. The result was further improved, achieving negligible error for the Eq. 2-31 from the AISC 360-16 Standard, when the measured specimen geometry and material properties were used. Figure 4-42 show that the shear area planes did indeed pass outside of the rows of holes in the web of the W-shape. This was however not the case for many of the angles as is shown in Figure 4-45. Furthermore, some of the overestimation may also be due to the fact that not all the angles failed at the same rate and some of these may not have attained the same levels of strain hardening.



Figure 4-45 Block shear through net shear area in angle

Table 4-15 Comparison of predicted capacities to test results for C360-T and C360-C

		P_{exp1}	P_{exp2}	Design	Expected ₂	Measured properties for C360-T ^{2,3}	Measured properties for C360-C ^{2,3}
CSA S16	Tension (kN)	5176	5115	3959	5812	5942	5932
	Compression (kN)	5515	5615	3680	4364	4474	4474
	Tension P/P_{exp}^1	1.00	1.00	0.77	1.13	1.15	1.15
	Compression P/P_{exp}^1	1.00	1.00	0.66	0.78	0.81	0.81
AISC 360	Tension (kN)	5176	5115	3743	5498	5197	5182
	Compression (kN)	5515	5615	3941	4721	4745	4745
	Tension P/P_{exp}^1	1.00	1.00	0.73	1.07	1.00	1.01
	Compression P/P_{exp}^1	1.00	1.00	0.71	0.85	0.85	0.85

1. Design and expected capacities were compared to an average of the two measured results
2. Expected capacities and capacities with measured properties for compression were calculated using the design buckling equation (Eq. 2-3 from the CSA S16-14 Standard and Eq. 4-1 from the AISC 360-16 Standard)
3. Design properties were used for the areas, radii of gyration, and moments of inertia of sections
4. Capacities with measured properties for the side which predicted the lowest capacity are shown even if this did not correspond to the side which failed in testing

4.2.3.3. Overall brace displacements

In terms of displacements, both specimens attained the same amplitude in the loading protocol before failure. The out-of-plane deformation of the C360-C brace significantly exceeded that of specimen C360-T because it exhibited global brace buckling in compression rather than the bending of the gusset plate. The out-of-plane displacements at the midpoint of the braces for these specimens are shown in Figure 4-46. The maximum out-of-plane displacement of C360-T was in the range of the maximums attained by specimens J360-T and J360-C (gusset bending in compression), while the maximum of out-of-plane displacement of specimen C360-C was in the range of the maximums attained by J310-T and J360-C (global brace buckling in compression).

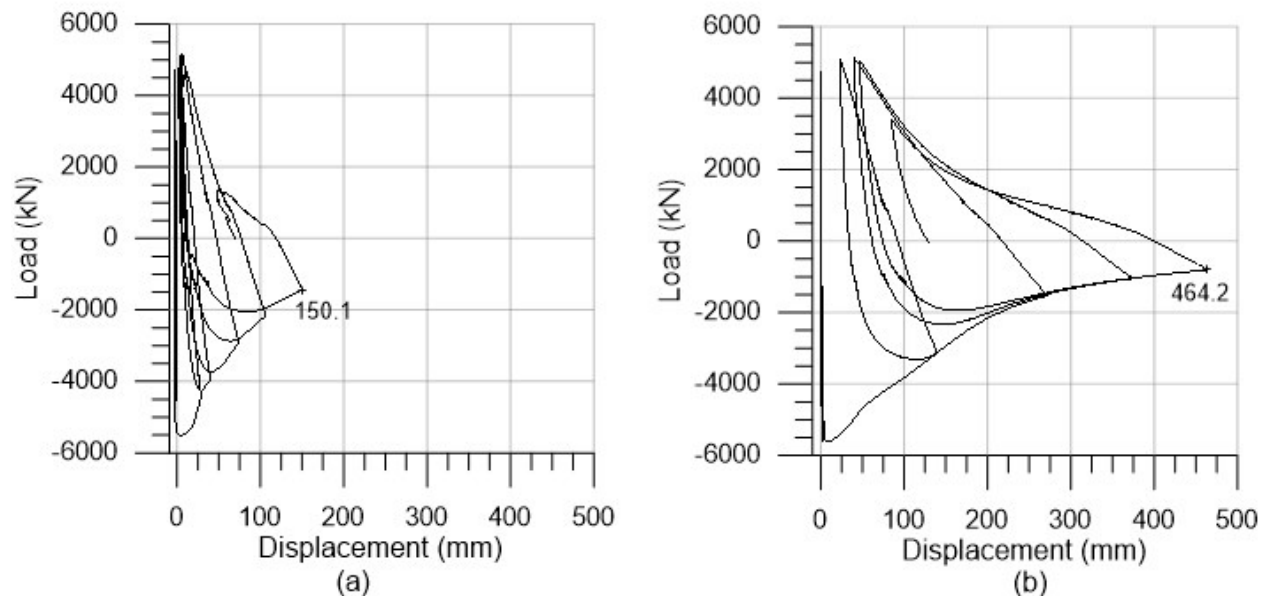


Figure 4-46 Out-of-plane displacements at the brace midpoint for (a) C360-T and (b) C360-C

4.2.4. Linear elastic slope

Due to the multiple components in the end connections, predicting the linear elastic slope of these specimens becomes more challenging than simply obtaining the elastic modulus of the W-shape brace itself. The test linear elastic slopes were taken from linear regressions of the slopes in the first six cycles of the loading protocols. The averages of these values are provided in Table 4-16. These calculated test values are compared to the elastic stiffness of the brace calculated with nominal properties of the brace sections and two lengths: (1) the design effective buckling length of the W-shape brace only, and (2) the corner-to-corner distance of the braced frame. For the four larger specimens, the test values lie within the two calculated values (closer to the lower calculated value). This is however not the case for specimens J310-T and J310-C whose elastic stiffness lies below the estimate with the corner-to-corner distance of the braced frame.

Table 4-16 Calculated and experimental elastic stiffness

	J310-T	J310-C	J360-T	J360-C	C360-T	C360-C
$K_{\text{elastic,exp}}$ (kN/mm)	348.4	342.9	533.6	513.2	594.4	610.6
$K_{\text{elastic,nominal1}}$¹ (kN/mm)	461.2		674.9		710.5	
$K_{\text{elastic,nominal2}}$² (kN/mm)	369.0		513.0		513.0	

1. Elastic stiffness of W-shape braces using nominal area and Young's modulus with the design effective buckling length of the W-shape brace

2. Elastic stiffness of W-shape braces using nominal area and Young's modulus with the corner-to-corner distance of the braced frame

4.2.5. Bolt slip

The slipping of bolts until bearing contact is made with the hole's edge is a fundamental part of the behaviour of bolted connections. This behaviour is dependent on the pretension in the bolts and the difference in diameters between the bolt and the bolthole. To a smaller degree, the presence and number of washers and the type and number of shim plates may affect bolt slip. While these bolted connections were designed for a bearing-type failure, the slip behaviour and slip resistance contribute to the dissipation of energy during a seismic event. Additionally, a complete understanding of the slip behaviour is integral to correctly modelling these connections in finite element models.

The holes in the tested specimens had diameters of 1.6 mm (1/16") larger than the specified bolt size. Assuming an equal amount of slip in all holes, this allowed for 3.2 mm (1/8") of slip for the jaw plate specimens (one bolted connection on both sides of the specimen and welded on the other side) and 6.35 mm (1/4") in the angles (the angles were bolted on either side of the two connections). Since the slip plateau is not a clear line parallel to the x-axis in the force-displacement hystereses obtained from the tests, the length of the slip plateaus and the slip resistances were estimated from the force-displacement hystereses. Only the second and third sets of cycles from the loading protocol were used for these observations because slip behaviour changes as the steel beneath the bolts yields and deforms. The slip of each bolt appears as a jump in the force-displacement hysteresis. Bolts in the connection slip and come into contact with the steel at different times because they are initially in different positions with respect to the center of the bolthole and they are pretensioned to different pressures. For this reason, it is

challenging to distinguish at what point all the bolts came into bearing. However, for all the specimens the slip plateaus seemed to be contained within approximately 5 mm in positive and negative directions. Table 4-17 shows the predicted slip resistance and the slip resistance as estimated from the force-displacement hysteresees. The slip resistance prediction was calculated according to the slip resistance design equation in the CSA S16-14 Standard as shown in Eq. 4-4 where c_1 is the coefficient for 5% probability of slip, k_s is the mean slip coefficient, n is the number of bolts, m is the number of faying surfaces, A_b is the cross-sectional area of the bolts, and F_u is the ultimate tension stress in the pretensioned bolts. The factors c_1 , k_s , and F_u are tabulated in the CSA S16-14 Standard.

Table 4-17 Predicted slip resistances compared to estimated slip resistances from tests

	J310-T	J310-C	J360-T	J360-C	C360-T	C360-C
P_{slip}¹ (kN)	918	918	1717	1717	1717	1717
P_{exp}² (kN)	808	920	1306	1280	1421	1552
P_{prob}/P_{exp}	0.88	1.00	0.76	0.75	0.83	0.90

1. Slip resistance as calculated from Eq. 4-4

2. Slip resistance estimated from test data

$$V_S = 0.53c_1k_s mnA_b F_u \quad (4-4)$$

It is possible to see that in most cases the prediction is an overestimate of the test results. However, due to challenges faced in assembly, the turn-of-nut method was not always implemented and multiple washers were used in certain cases for the assembly. Additionally, the CSA S16-14 Standard slip resistance does not take into account the presence of shim plates. The specimens with the greatest difference between the predicted and estimated test values are specimens J360-T and J360-C, which had more than one shim plate in certain locations (in the AISC 360-16 Standard, slip resistance is reduced by a factor of 0.85 if more than one shim plate is used). Lastly, the slip resistances were estimated from the seventh to the fourteenth cycle: the slip resistance tends to decrease incrementally with successive cycles so this may contribute to the lower slip resistances reported.

4.2.6. Effective buckling length

As mentioned in Sections 4.2.1. and 4.2.3., the unfactored buckling equations (Eq. 2-2 and Eq. 4-1) with probable material properties did not give very accurate predictions when compared to the measured capacities in compression. Both Eq. 2-2 from the CSA S16-14 Standard and Eq. 4-1 from the AISC 360-16 Standard, contain K , a factor to determine the effective buckling length of a member. The K factor used was 0.9 applied to the corner-to-corner distance of the braced frames. However, this may not be the correct factor to apply to these type of braces. To obtain the measured buckling capacities with Eq. 2-2 from the CSA S16-14 Standard, a K factor of 0.67 would need to be used for specimens J310-T and J310-C (to obtain the average measured value) and a K factor of 0.59 would need to be used for specimen C360-C. The K factors for specimens J360-T, J360-C, and C360-T were not recalculated because the bending of the gusset plates did not correspond to traditional buckling. The corresponding K factors for Eq. 4-1 from the AISC 360-16 Standard are 0.74 and 0.62, respectively. These K factors seem to be very low when observing the buckled shapes of the specimens in the tests as shown in Figure 4-40.

4.2.7. Energy dissipation

One of the objectives of SFRSs is to dissipate energy during seismic events. Braces with bolted end connections dissipate energy through friction in the slipping of the bolts, yielding and deformation of the steel, and buckling. The energy dissipated by a specimen under reverse cyclic loading can be measured from the area within the curves of the force-displacement hysteresis. A plot of the dissipated energy versus cumulative absolute displacement (energy was not plotted against time to remove the effect of the loading rate from the figure for better comparison) in Figure 4-47.

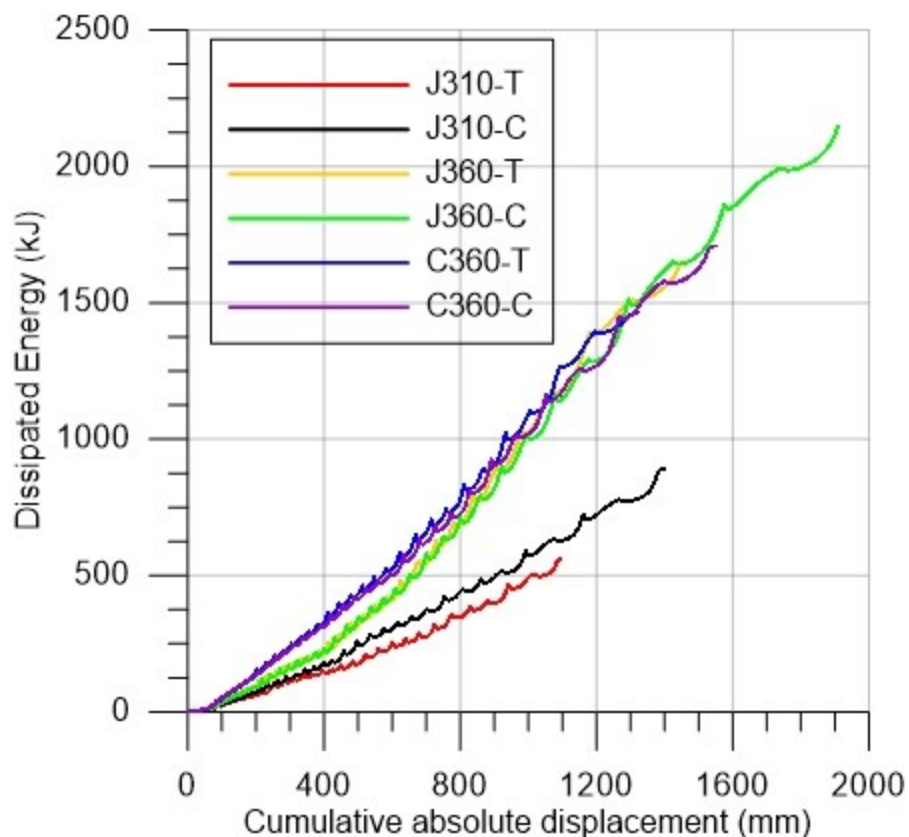


Figure 4-47 Dissipated energy of brace test specimens

Specimens J310-T and J310-C had the lowest rate of energy dissipation and, consequently, the lowest total dissipated energy when compared to the specimens with the W360-134 section size. The energy dissipation rate of the remaining four specimens was very similar between specimens. Specimens C360-T and C360-C started with a greater rate of energy dissipation when compared to specimens J360-T and J360-C, but the latter increased in energy dissipation rate by 800 mm of cumulative absolute displacement. Due to similar rates of energy dissipations, the specimens which underwent more cycles of loading before failure dissipated more energy overall. As a result, the specimens whose loading protocol started in compression dissipated more energy than the specimens whose loading protocol started in tension. Table 4-18 shows the total dissipated energy for each of the specimens.

Table 4-18 Total dissipated energy of brace test specimens

	J310-T	J310-C	J360-T	J360-C	C360-T	C360-C
Total dissipated energy (kJ)	559	887	1641	2147	1466	1708

4.2.8. Difference between capacities in tension and compression

One of the greatest drawbacks of the capacity based design principle is that the engineer must design the structural elements adjacent to the energy-dissipating element (e.g. a brace in a CBF) for the probable force in the dissipating element in the nonlinear range. For a brace, this means that the adjacent structural elements, such as the connections, must be designed for the probable tensile capacity of the brace, while the brace itself is selected based on its factored design capacity in compression. Due to a large difference in the probable tensile capacity of the brace and its design capacity in compression, the connections must be designed for a relatively large force. Table 4-19 shows these capacities for the W310x97 and W360x134 braces with an assumed effective buckling length of 6 m and an end connection design such as in the tested specimens (based on Equations 2-2 and 2-3 from the CSA S16-14 Standard for C_r and C_u , respectively). In comparing the probable capacities for tension and compression, the tension capacity divided by the capacity in compression is 1.61 for W310x97 and 1.34 for W360x134.

Table 4-19 Factored and probable capacities of W310x97 and W360x134 braces

	W310x97		W360x134	
	Tension ¹	Compression ²	Tension ¹	Compression ²
Factored design capacity (kN)	3656	2209	5115	3680
Probable capacity (kN)	4736	2945	6584	4906

1. Based on net section fracture at the end connection with six holes through the net section for design factored capacity and T_u for the probable capacity

2. Based on a 6 m effective buckling length. Eq. 2-2 for design capacity and Eq. 2-3 for probable capacity

In CC-type seismic design, the connections are designed for the same design load as the brace itself. For this reason, the capacities in tension and compression of the brace assembly are relatively close as seen in the tests. Table 4-20 shows the ultimate capacities of the tested specimens in tension and compression. It is clear that these capacities are much closer to each other than the tension and compression capacities of Table 4-19. For specimens C360-T and C360-C, the capacity in tension was actually smaller than the capacity in compression.

Table 4-20 Measured capacities in tension and compression

	J310-T	J310-C	J360-T	J360-C	C360-T	C360-C
P_{tension} (kN)	3572	3653	5206	5112	5176	5115
P_{compression} (kN)	3369	3421	4880	4846	5515	5615
P_{tension}/P_{compression}	1.06	1.07	1.07	1.05	0.94	0.91

4.2.9 Force distribution between the flanges and the web of the W-shape

The design of bolted connections in W-shape where both the flanges and the web of the W-shape are connected requires an assumption of the distribution of axial force between the flanges and the web of the W-shape. For this project, it was assumed that the forces in the W-shape distributed in proportion to the areas of the flanges and the web. During the tests, two of the specimens, specifically J310-T and J360-T, were instrumented with strain gauges on the flanges and web of the W-shape to observe the distributions of strains for the two section sizes. The strains were compared before yielding occurred in the specimens (i.e. within the first ten cycles of the loading protocol). This was done for two reasons. The first reason was that after yielding, the strains in the strain gauges are affected by the location of the yielding. Secondly, in the elastic range, strains are proportionate to stresses. A relative comparison of the strains is therefore analogous to a relative comparison of stresses. Therefore, higher stresses in one part of the W-shape means that the force levels per unit of area are greater in that part of the W-shape relative to other parts. If the assumption that forces distribute according to the area were true, the strains would need to be relatively uniform in all locations of the W-shape in the elastic range.

Two sets of strain gauges were installed on the bottom side of the W-shapes: one set 25 mm from the uppermost edge of the bottom connection (labelled “L” for low) and the other set 305 mm from the uppermost edge (labelled “H” for high). Each set included two strain gauges on each side of the web and two strain gauges on each flange, as shown in Figure 4-10.

For each of the sets of recorded data, the values of strain at the peaks and valleys were compared between the strain gauges. Strain gauge data was grouped by specimen, height on the W-shape, and position on the flanges or the web to be compared. In each group, the strain values at the peaks and valleys were normalized by the maximum strain value in the group. Average and

minimum normalized values for each group are reported in Table 4-21 for the first six cycles, the next four cycles, and for all ten elastic cycles.

Table 4-21 Average and minimum normalized strain values of W-shape strain gauges

Specimen		J360-T				J310-T			
		Low		High		Low		High	
Height		Flanges	Web	Flanges	Web	Flanges	Web	Flanges	Web
Position		Flanges	Web	Flanges	Web	Flanges	Web	Flanges	Web
First six cycles	Average	0.941	0.922	0.931	0.986	0.928	0.834	0.945	0.944
	Minimum	0.820	0.839	0.898	0.968	0.820	0.779	0.809	0.917
Next four cycles	Average	0.800	0.787	0.853	0.906	0.944	0.798	0.948	0.961
	Minimum	0.561	0.606	0.689	0.862	0.839	0.676	0.869	0.909
All elastic cycles	Average	0.885	0.868	0.900	0.954	0.934	0.820	0.946	0.951
	Minimum	0.561	0.606	0.689	0.862	0.820	0.676	0.809	0.909

For specimen J310-T, 305 mm from the edge of the connection, the minimum values of strains were further from the maximum value in the flanges than in the web. In general, the strains were fairly uniform over the entire section. However, closer to the connection, strains in the web were further away from the maximum strain. Strains were 11.4% further away from the maximum strain value in the web in the first ten cycles than they were in the flanges. This seems to indicate that there was more force per area in the flanges than there was in the web. In general, the strains were less uniform across the entire section closer to the connection.

For specimen J360-T, similar observations were made about the strains as in specimen J310-T. Minimum strains in the flanges were even further from the maximum strain values than in specimen J310-T. Closer to the connection, again, the strains were less uniform than further from the connection. However, there was not a significant difference between the ranges found in the flange and the web.

Another observation was made regarding the strains in the W-shape during the slow tension excursion in the loading protocol of specimen J310-T. Figure 4-48 shows the strains in different locations on the W-shape of specimen J310-T during the slow tension excursion. The nomenclature of the strain gauges is the same as the one shown in Figure 4-10.

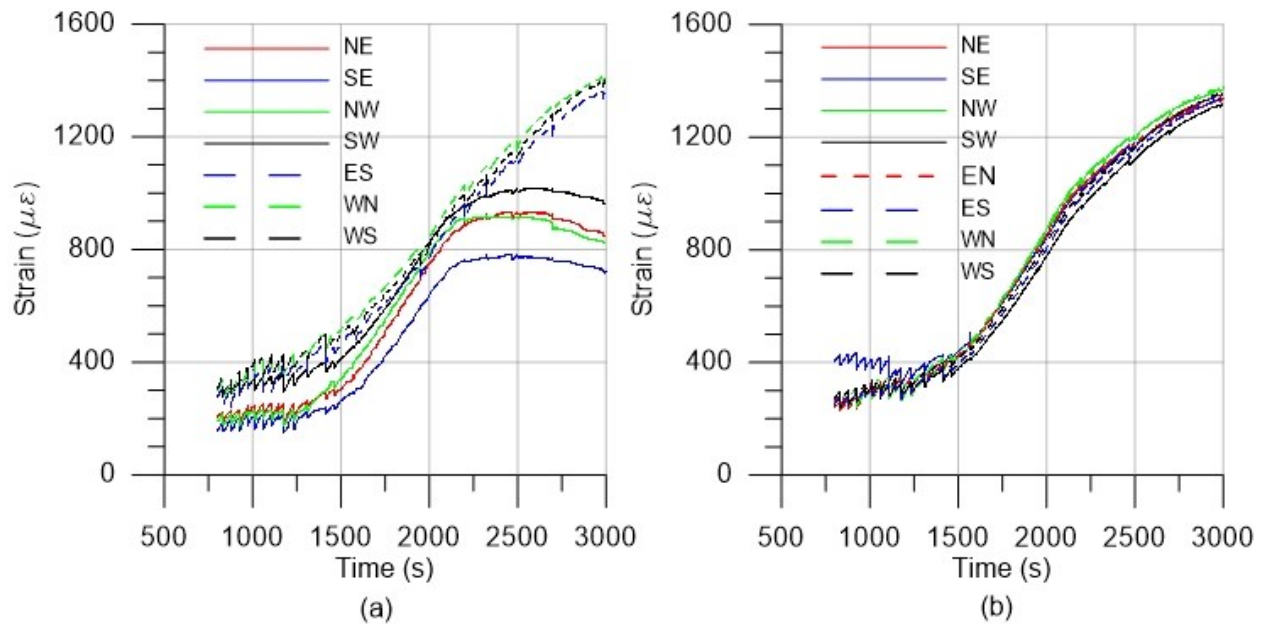


Figure 4-48 Strains in the J310-T W-shape during the slow tension excursion at (a) 25 mm from the uppermost edge of the connection and (b) 305 mm above the uppermost edge of the connection

In Figure 4-48(a), beyond 2000 s, the strains in the flanges of the W-shape diverge from the strains in the web of the W-shape. The strains in the flanges start to decrease after about 2500 s into the test, while the strains in the web continue to increase. Further up in the connection, as shown in Figure 4-48(b), the strains remain relatively uniform in the W-shape cross-section throughout the entire slow tension excursion. This may be explained through the relative stiffness's of the connecting components (i.e. the jaw plates and the web plates). The web plates were stiffer than the web of the W-shape (larger cross-section area), while the jaw plates were less stiff than the flanges of the W-shape (smaller cross-section area). At this point in the loading protocol, the jaw plates had yielded (as verified from strain data from strain gauges on the jaw plates). The yielded jaw plates were then allowing for the elongation on the North and South sides of the W-shape and the flanges were not further strained.

4.2.10. Ductility

One of the objectives of this study was to record data to provide insight on the ductility of these specimens. The overall elongation of the specimens in tension at yield, ultimate load (P_u), 80% of ultimate load, and 50% of ultimate load are shown in Table 4-22. Some of these values are

dependant on the loading protocol experienced by the specimen. The elongations are also shown in terms of storey drift ratios as based on the geometry of the braced frame from the building design. Additionally, the elastic elongation of the W-shape was calculated at each of these points and subtracted from the total elongation. This allowed to separate out most of the inelastic elongations of the specimens (because the remaining elastic components of the connections would be relatively small).

The ductility at yield was taken from the force-displacement hysteresees at the point where the slope of the curve was below 10% of the initial linear elastic slope. The elongations at yield are very similar between specimens (between 17.9 mm and 20.0 mm), with specimens J310-T and J310-C yielding slightly earlier (between 17.9 and 18.5 mm) than the specimens with the larger W-shape section did.

In general, the displacements at $0.8P_u$ and $0.5P_u$ are very similar with two exceptions. Specimens J310-C, J360-T, C60-T, and C360-C had elongations between 42.0 and 55.0 mm at $0.8 P_u$ and between 52.5 and 55.3 mm at $0.5 P_u$. This shows that even if some specimens were subjected to more cycles before near complete rupture, at the same level of reduction in capacity, these specimens had similar levels of elongation. However, specimen J310-T showed lower levels of elongation at the specified load levels (36.9 mm at $0.5P_u$). This may have been due to the slow tension excursion during which the specimen was elongated further than the other specimens were. Specimen J360-C, in contrast, showed higher levels of elongation at these force levels (75.2 mm at $0.5P_u$). The two specimens with W310x97 W-shape braces, J310-T and J310-C, had a sharper decline in capacity after reaching the ultimate load as shown by the closeness of the elongation values at P_u , $0.8P_u$, $0.5P_u$ as compared to that of the other specimens. This complies with what was expected because bolt shear is known to be a rather brittle failure mode.

Table 4-22 Elongations in tension at P_y , P_u , $0.8P_u$, and $0.5P_u$

	Load	J310-T	J310-C	J360-T	J360-C	C360-T	C360-C
Elongation (mm)	P_y	17.9	18.5	19.7	19.7	20.0	19.4
	P_u	33.3	49.9	31.2	33.0	40.6	36.6
	$0.8P_u$	34.1	51.4	42.0	65.6	50.5	55.0
	$0.5P_u^1$	36.9	52.6	52.5	75.2	55.3	54.4
Storey drift ratio (%)	P_y	0.58	0.60	0.63	0.64	0.64	0.63
	P_u	1.07	1.61	1.01	1.06	1.31	1.18
	$0.8P_u$	1.10	1.66	1.36	2.12	1.63	1.77
	$0.5P_u^1$	1.19	1.70	1.69	2.43	1.78	1.76
Elastic component ² (mm)	P_y	7.5	7.7	8.3	8.7	6.4	6.2
	P_u	8.2	8.5	8.7	9.0	7.4	7.3
	$0.8P_u$	6.6	7.0	15.0	7.3	5.9	5.8
	$0.5P_u^1$	4.1	4.2	4.3	5.3	0.6	3.7
Inelastic component ³ (mm)	P_y	10.4	10.8	11.4	11.0	13.6	13.2
	P_u	25.1	41.4	22.5	24.0	33.2	29.3
	$0.8P_u$	27.5	44.4	27.0	58.3	44.6	49.2
	$0.5P_u^1$	32.8	48.4	48.2	69.9	54.7	50.7

1. $0.5P_u$ or the last recorded elongation value if $0.5P_u$ was not attained during the test

2. The elastic component is simplified as the elastic elongation of the W-shape only

3. The inelastic component is the difference between the full elongation and the elastic elongation of the W-shape

All of the specimens attained at least 1% storey drift at their ultimate capacity and only one specimen, J360-C, exceeded 2% storey drift. From the nonlinear numerical modelling (see Chapter 3), the ductility requirement was 34.7 mm for the W360x97 brace and 10.2 mm for the W360-134 brace. All specimens achieved these elongations by $0.5P_u$. The W360x134 specimens exceeded the 10.2 mm requirement of axial elongation before yielding occurred. Specimen J310-T was the only specimen that did not quite reach the 34.7 mm requirement by $0.8P_u$. Ductility levels, defined as the displacement at the ultimate capacity divided by the displacement at the yield capacity (δ_u/δ_y), are shown in Table 4-23. These ductility levels range between 1.59 and 2.70.

Table 4-23 Calculated specimen ductility

	J310-T	J310-C	J360-T	J360-C	C360-T	C360-C
δ_u/δ_y	1.86	2.70	1.59	1.67	2.03	1.88

The total inelastic ductility for these specimens comes from the damage incurred by the components of the assemblies. Some observations and measurements were taken of the specimens and their components after the test to attempt to quantify these contributions.

For specimens J310-T and J310-C, it should be noted that some deformations in the W-shape webs may have occurred at the very end of the test after the sudden loss of resistance in the flanges due to the shear fracture of the bolts in the flanges. This would cause measurements of deformations after the tests to be greater than their actual contributions to ductility during loading. In an attempt to obtain the magnitude of this additional deformation, the displacements between the top of the web plate and the point on the W-shape web that was originally just above the web plate were extracted from the DIC data before and after the shearing of the bolts in the flanges. The difference in displacements was found to be only 1.3 mm.

The different inelastic components of ductility include bolt deformations, bolthole ovalization, deformation of the steel at the edge, and the yielding, shearing, and tearing of the connected plates and sections. The yielding, shearing and tearing of the connecting plates and sections are more challenging to quantify precisely than the other ductility components because measurements would include other deformations.

Bolt deformations (as shown in Figure 4-21(a)) do not account for much of the total inelastic deformations. These deformations were most prominent (greater than 1 mm on average) in the flanges of specimens J310-T and J310-C (where bolt shear was expected to occur) and in the bolts going through the angles and the gusset plate in specimens C360-T and C360-C (these bolts were in double shear). In these bolts, which showed relatively large deformations, the average deformation was 1.3 mm. The maximum deformation measured was 3.28 mm. Average and maximum measured bolt deformations are shown in Table 4-24.

Bolthole diameters in the axial direction were measured from 3D models of scans from the post-test specimens and compared to the pre-test measurements. Only holes in the bottom jaw plates and angles were measured because failures happened in the bottom connections (except J310-C, which failed in bolt shear in the flanges so little hole ovalization was observed). Additionally, holes were not measured in the web plates and the jaw plates of specimens J310-T and J310-C because these showed very little damage to the holes. Table 4-25 shows the measured bolthole elongations. The level of ovalization varied with the position of the bolthole relative to the edge. Generally, the rows of bolts at the centre of the connection were less elongated than those nearest and furthest from the edge. The largest hole elongations were observed in the holes of the W-shape webs where the connection failed. These webs failed in block shear. The holes furthest from the web's edge had the largest elongations.

Table 4-24 Average and maximum measured bolt deformations

			J310-T	J310-C	J360-T	J360-C	C360-T	C360-C
Top connection	Flanges	Average (mm)	1.74	FRACTURED		0	NG	NG
		Maximum (mm)	2.95	FRACTURED		0	1.06	1.28
	Web	Average (mm)	NG	0		NG	NG	NG
		Maximum (mm)	NG	0		0.53	0.98	0.8
	Gusset	Average (mm)	NA	NA		NA	1.32	0.65
		Maximum (mm)	NA	NA		NA	3.35	1.23
Bottom connection	Flanges	Average (mm)	FRACTURED	1.58	Data unavailable	NG	NG	NG
		Maximum (mm)	FRACTURED	3.28		1.31	3.11	1.21
	Web	Average (mm)	NG	NG		NG	0.50	NG
		Maximum (mm)	0.68	0.65		0.93	1.66	0.8
	Gusset	Average (mm)	NA	NA		NA	1.08	1.51
		Maximum (mm)	NA	NA		NA	2.81	3.19

NG – Negligible

NA - Not Applicable

Table 4-25 Measured bolthole elongations

	Elongations											
	J310-T		J310-C		J360-T		J360-C		C360-T		C360-C	
	(mm)	(%)	(mm)	(%)	(mm)	(%)	(mm)	(%)	(mm)	(%)	(mm)	(%)
Brace bottom flanges¹	4.2	17.7	3.9	16.5	3.0	11.2	3.5	13.1	5.0	18.7	4.9	18.3
Row 1	5.3	22.4	6.1	25.7	2.3	8.6	3.8	14.2	7.6	28.4	7.1	26.5
Row 2	3.5	14.8	2.9	12.3	3.3	12.3	3.1	11.6	4.3	16.0	6.3	23.5
Row 3	3.7	15.6	2.9	12.3	2.9	10.8	2.4	9.0	3.0	11.2	1.4	5.2
Row 4	NA	NA	NA	NA	3.7	13.8	4.6	17.2	5.1	19.0	5.0	18.7
Brace bottom web¹	15.8	66.7	6.9	29.1	29.8	111.2	4.9	18.4	FR	FR	FR	FR
Row 1	11.5	48.5	4.4	18.6	7.2	26.8	3.3	12.4	FR	FR	FR	FR
Row 2	20.0	84.4	9.3	39.2	40.8	152.8	6.6	24.7	FR	FR	FR	FR
Brace top flanges¹	3.0	12.7	4.3	18.2	2.5	9.3	ND	ND	1.6	6.0	3.3	12.3
Row 1	3.3	13.9	5.8	24.5	2.8	10.4	ND	ND	1.9	7.1	4.8	17.9
Row 2	2.9	12.2	2.7	11.4	2.3	8.6	ND	ND	1.2	4.5	2.0	7.5
Row 3	2.7	11.4	4.3	18.2	2.5	9.3	ND	ND	0.3	1.1	3.3	12.4
Row 4	NA	NA	NA	NA	ND	ND	ND	ND	2.0	7.5	3.0	11.2
Brace top web¹	5.1	21.5	18.8	79.3	1.8	6.7	4.2	15.7	11.9	44.4	9.7	36.3
Row 1	5.3	22.4	15.3	64.6	1.2	4.5	3.1	11.6	10.2	38.1	6.6	24.7
Row 2	4.9	20.7	22.3	94.1	2.4	9.0	5.2	19.5	13.6	50.7	12.9	48.1
Bottom jaw plates / angles¹	ND	ND	ND	ND	3.0	11.1	2.7	10.0	4.2	15.6	3.6	13.3
Row 1	ND	ND	ND	ND	5.4	19.9	3.3	12.3	4.0	14.9	4.3	15.9
Row 2	ND	ND	ND	ND	1.4	5.1	1.4	5.2	3.7	13.8	2.3	8.6
Row 3	ND	ND	ND	ND	1.5	5.5	1.9	7.1	3.7	13.8	2.6	9.6
Row 4	NA	NA	NA	NA	4.1	15.1	3.9	14.4	5.8	21.6	4.9	18.1
Bottom gusset web¹	ND	ND	ND	ND	7.6	28.6	8.6	32.3	1.4	5.3	0.9	3.4
Row 1	ND	ND	ND	ND	4.8	18.0	8.2	30.8	1.2	4.5	0.8	3.0
Row 2	ND	ND	ND	ND	10.4	39.2	9.2	34.7	1.4	5.3	0.9	3.4
Bottom gusset flanges¹	NA	NA	NA	NA	NA	NA	NA	NA	4.7	17.7	6.1	23.0
Row 1	NA	NA	NA	NA	NA	NA	NA	NA	6.1	23.0	10.4	39.0
Row 2	NA	NA	NA	NA	NA	NA	NA	NA	4.3	16.3	6.2	23.4
Row 3	NA	NA	NA	NA	NA	NA	NA	NA	3.3	12.5	4.3	16.3
Row 4	NA	NA	NA	NA	NA	NA	NA	NA	5.1	19.2	3.6	13.6

1. These are the average values for the rows below

NA - Not Applicable

ND - No Data

FR - Complete fracture of part of the steel

Bolthole elongations on the North and South sides of the braces (W-shape flanges, jaw plates, angles, and sides of gussets) averaged 3.7 mm and ranged between 0.3 mm and 7.6 mm. Bolthole elongations in the webs of the braces averaged 10.89 mm and ranged between 1.2 mm and 40.8 mm. Finally, elongations in the holes at the centre of the bottom gusset plates averaged 4.6 mm and ranged between 0.8 mm and 10.4 mm. Figure 4-49 shows an example of elongated hole in the bottom gusset plate of specimen C360-T.



Figure 4-49 Deformation beyond the edge of the bottom gusset plate of specimen C360-C

Lastly, deformations at the edges of the connected plates and sections (beyond the original edge) were measured for some of the plates and sections. These measurements included some of the deformations from bolthole ovalization, bearing of the bolts on the steel, and yielding and tearing of the steel. As before, the largest deformations were seen for the block shear in the webs of the braces where failure occurred (see Figure 4-50). Table 4-26 shows these measured deformations.

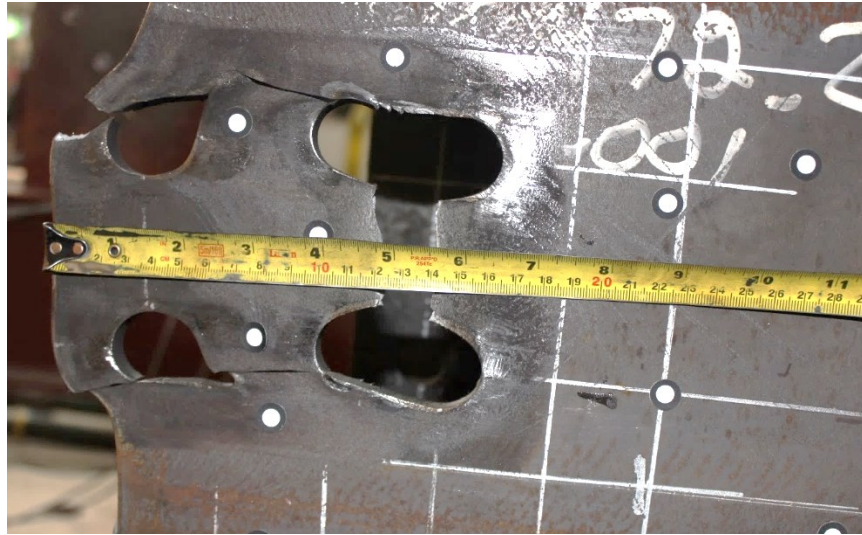


Figure 4-50 Block shear deformations in the bottom W-shape web of specimen J360-T

Table 4-26 Measured deformations beyond the original edge of the steel

	Deformations (mm)					
	J360-T	J360-C	C360-T	C360-C	J310-T	J310-C
Brace bottom flanges	NG	NG	2.7	NG	4.7	2.8
Brace bottom web	31.0	5.1	18.3	11.95	16.3	7.9
Brace top flanges	NG	ND	NG	NG	1.8	3.1
Brace top web	NG	ND	11.3	10.3	4.6	19.4
Jaw plates / Angles	2.7	NG	FR	FR	ND	ND
Bottom gusset sides	NA	NA	6.2	8.1	NA	NA
Bottom gusset centre	2.9	5.0	NG	NG	ND	ND

NA - Not Applicable

ND - No Data

NG – Negligible

FR - Complete fracture of part of the steel

Chapter 5: Summary and Recommendations

The main objective of this study was to observe the behaviour and ductility of seismic conventional construction (type CC) W-shape braces with bolted end connections under reversed cyclic loading to address the gap in research knowledge for these types of members. This objective was achieved through the two phases of this study. There was first a preliminary numerical modelling phase, in which estimates of the connection displacement requirements were obtained and a tailored loading protocol was developed from statistical analysis of data gathered from the numerical models. This phase was followed by the laboratory testing of six full-scale specimens with two common bolted connections under reversed cycle loading. A summary of the concluding remarks, as well as some recommendations for future studies, are provided in this chapter.

5.1 Numerical modelling observations

Five two-dimensional braced frame simplifications of buildings were modelled in ETABS v. 17.0.1 to perform nonlinear, dynamic analysis and assess the performance of the CC-type braces. Nonlinear links were used to model the brace behaviour in tension and compression. The following points summarize the findings from these numerical models.

1. Various models using nonlinear link elements (hinge, gap, and multilinear elements) in parallel and in series to superpose the linear elastic, slip, and nonlinear behaviours of the connection and brace in tension and compression were found to be unsuccessful. These models were either unable to converge or did not correspond to the expected behaviour when subjected to ground motions.
2. These connections were therefore modelled with one multilinear element to characterise the nonlinear behaviour of the braces and a connection (assuming that the nonlinear behaviour of only one connection would drive the response) and two frame elements. The backbone curves of these multilinear elements were based on data from two studies: Castongay's thesis (2010) and Brunet's thesis (2018).

3. Numerical models were run with the Fast Nonlinear Analysis, the Ritz vector modal analysis, and constant 3% modal damping. The P-Delta automation method specified was iterative based on the gravity loads. These options allowed for fast analysis times, while accounting for P-Delta effects in the nonlinear range.
4. Drifts in the upper two storeys of the four-storey building were found to be significantly greater than the drifts in the lower two storeys.
5. Displacement demands were found to be 10.2 mm (0.3% SDR) for the W360x134 braces and 34.7 mm (1.1% SDR) for the W310x97 braces from the axial elongations of the multilinear link elements in tension in the numerical models.
6. Storey drifts in the response histories of the numerical models corresponded largely to elongations within the elastic ranges of the braces. Large inelastic elongations were relatively unlikely. This is to be expected as CC-type braces are designed for larger loads when compared to MD and LD-type braces; their sections must be larger and the buildings are therefore stiffer.

5.2 Laboratory testing observations

Even though the six specimens were design for the CC category, every specimen displayed some amount of inelastic behaviour and ductility. Preliminary findings show that these specimens have enough ductility to achieve the displacement demand estimates extracted for the numerical models. The following points summarize the results of the laboratory testing phase.

1. Specimens J310-T and J310-C failed just as expected: bolt shear in the flanges and block shear in the web of the W-shapes. In compression, both of the braces buckled.
2. Capacity predictions of combined bolt shear in the flanges and block shear in the web of the W-shapes were slightly conservative for both the CSA S16-14 Standard and the AISC 360-16 Standard. However, this may be due to the estimation of the probable bolt shear strength.
3. The out-of-plane deformations of both specimens J360-T and J360-C occurred in the gusset plates just as expected. The progression and development of these deformations were dependant on the end restraints.

4. After gusset plate bending, in specimens J360-T and J360-C, the tensile failures did not occur as expected. While the expected failure modes in tension were net section through the bolt holes in the jaw plates and block shear in the web of the W-shapes, tearing occurred in the gusset plates and the North jaw plate of specimen J360-T fractured at the net section at the end of the slot. The gusset plate bending may have caused stress concentrations in the gussets and gusset plate tearing at a lower capacity than that which was predicted. Tensile capacity predictions for these specimens overestimated the laboratory results.
5. In compression, the braces of both specimens C360-T and C360-C were expected to buckle. However, for specimen C360-T, the gusset plate bent similarly to the gussets of specimens J30-T and J360-C. It was suspected that this difference in behaviour was due to the misalignment of the parts in the brace assembly.
6. In tension, the failure modes in specimens C360-T and C360-C matched those expected; block shear in both the angles and the webs of the W-shapes. Capacity predictions overestimated the laboratory results. The capacity attained may be lower than in calculations because the angles do not rupture simultaneously. The shear planes in the webs of the W-shapes seemed to pass outside the bolt holes (gross section area), while the shear planes in the angles passed through the bolt holes (net section area).
7. For the prediction of buckling capacities, Eq. 4-1 from the AISC 360-16 Standard and Eq. 4-5 from the AISC 341-16 Standard resulted in closer predictions to the measured test results than the corresponding Equations 2-2 and 2-3 in the CSA S16-14 Standard. The C_u probable brace buckling capacity, Eq. 2-3, from the CSA S16-14 Standard and the corresponding Eq. 4-5 in the AISC 341-16 both resulted in better predictions than the design buckling equations (Equations 2-2 and 4-1), which were more conservative. This may be due to the selection of an appropriate effective length factor, K .
8. Out-of-plane displacements measured at the midpoint of the braces, were larger for the specimens whose braces buckled than those whose gusset bent out-of-plane. Between duplicate specimens, the maximum recorded out-of-place displacements were always

greater for the specimens whose loading protocol started with an excursion in compression.

9. The linear elastic slopes observed in the test force-displacement hystereses for specimens J310-T and J310-C were lower than the estimated linear elastic slope calculated as the elastic stiffness of W-shape brace using nominal cross-section area and Young's modulus with the corner-to-corner length of the braced frame from the design of the braces. For the remaining specimens, the linear elastic slopes observed in the test force-displacement hystereses were between the elastic stiffness of W-shape braces calculated with the corner-to-corner distance of the braced frame and the elastic stiffness calculated with the W-shape brace length only.
10. Calculated bolt slip capacities had slightly overestimated laboratory results, but this may be because the bolt slip capacities will tend to decrease with subsequent cycles (the test bolt slip capacities were estimated from seven force-displacement hysteresis loops).
11. Energy dissipation rates are vary with the size of the W-shape section. For the same W-shape section, energy dissipation rates are similar. As a result, specimens that underwent more loading cycles before failure dissipated the most energy overall.
12. Since the connections were designed for the design buckling load of the W-shape braces (assumed to be equivalent or close to the design load), the difference between the tension and compression capacities of these specimens was very small (between 5% and 9%) as compared to the difference between the probable buckling and probable gross section tension capacities of the braces (between 34% and 61%).
13. In the elastic range, strains, and consequently stresses, were more evenly distributed between the flanges and the web of specimen J360-T than specimen J310-T (where the flanges were more strained than the web).
14. The elongations of the specimens at yield are very similar between specimens (between 17.9 mm and 20.0 mm). Specimens J310-T and J310-C yielded slightly earlier (between 17.9 and 18.5 mm) than the specimens with the larger W-shape section did.
15. Elongations at the ultimate capacity (P_u) of the specimens varied between 31.2 mm and 49.9 mm.

16. At 50% of P_u (or at the last recorded value if 50% of P_u was never recorded), the elongations in tension of the specimens except specimens J310-T and J360-C were between 52.5 mm and 55.3 mm.
17. The elongations in tension at 50% of P_u of specimens J310-T and J360-C were 36.9 mm and 75.2 mm, respectively. It was suspected that the axial elongations of specimen J310-T were reduced due to the slow tension excursion that surpassed the amplitude of following excursions and may have damaged the specimen.
18. All specimens achieved at least a 1% SDR but only specimen J360-C exceeded 2% SDR by 50% of P_u .
19. The specimens attained the required ductility demands as determined from the response histories of the numerical models (10.2 mm or 0.3% SDR for the W360x134 braces and 34.7 mm or 1.1% SDR for the W310x97 braces). The specimens with the W360x134 braces attained the ductility demand of 10.2 mm within the elastic range.
20. Ductility ratios, calculated as the axial elongation at P_u divided by the axial elongation at P_y , ranged between 1.59 and 2.70.
21. Inelastic deformations were observed in the form of bolt shear deformations, hole ovalization, bulging of the steel beyond the edges of the plates and sections, and yielding, shearing and tearing of the steel plates and sections.

5.3 Recommendations

Additional research on CC-type braces with bolted end connections will need to be carried out before conclusions can be made and before the findings could be incorporated into the CSA S16 Standard. Further numerical analysis, in particular, will allow for a better understanding of the results found in this study. Recommendations for future work are presented in this section.

1. More fibre-based numerical models of the buildings described in Chapter 3 should be created to validate the results obtained.
 - a. Phenomenological behaviour applied to elements in the models can be based on the force-displacement hysteresis data created in this study. These models can also be calibrated with these results.

- b. These building models should be used to validate the accuracy of the ductility demands reported in this study and re-compare to the axial elongations achieved by the specimens in laboratory testing to make a recommendation regarding the ductility of these connections with regards to Clause 27.11.1 of the CSA S16-14 (2014).
 - c. Additional building models should be created to test the effects of different brace geometries, building heights, and brace sizes and locations.
 2. Robust continuum-based finite element models of the tested specimens should be built and calibrated using the test results.
 - a. These models can be used to conduct parametric studies to evaluate the effects of the many parameters in the design of these connections.
 - b. These models can also be used to evaluate the sensitivity of the specimens to proper alignment of the assembly and to end restraint conditions.
 - c. These models should include the initial strains in the connections of the specimens induced by the assembly process, which were recorded as the initial values in the strain gauges and by the DIC system.
 3. The data collected from the DIC system can be used to further investigate the behaviours of these specimens and to calibrate finite element models by comparing strain distributions in the different elements of the connections.
 4. The proposed modified bearing connection, as described in Section 3.1, should be tested to verify if this connection design has improved ductility due to the forced bearing in the bearing plate. Shop drawings for these specimens are included in Appendix C.

BIBLIOGRAPHY

- Abdelfattah, F. A., and Soliman, M. S. "Shear Lag in Bolted Tension Members at Elastic and Yielding Loading Conditions." *Alexandria Engineering Journal* 42.4 (2003): 463-74.
- AISC. "Load and Resistance Factor Design Specification for Structural Steel Buildings" *American Institute of Steel Construction, Chicago, IL* (1986).
- AISC. "Load and Resistance Factor Design Specification for Structural Steel Buildings" *American Institute of Steel Construction, Chicago, IL* (1993).
- AISC. "Load and Resistance Factor Design Specification for Structural Steel Buildings" *American Institute of Steel Construction, Chicago, IL* (1999).
- AISC. "Seismic Provisions for Structural Steel Buildings, ANSI/AISC 341-16." *American Institute of Steel Construction, Chicago, IL* (2016).
- AISC. "Specification for Structural Steel Buildings, ANSI/AISC 360-05." *American Institute of Steel Construction, Chicago-Illinois* (2005).
- AISC. "Specification for Structural Steel Buildings, ANSI/AISC 360-10." *American Institute of Steel Construction, Chicago-Illinois* (2010).
- AISC. "Specification for Structural Steel Buildings, ANSI/AISC 360-16." *American Institute of Steel Construction, Chicago-Illinois* (2016).
- Alipour, M., and Aghakouchak, A. A. "Numerical Analysis of the Nonlinear Performance of Concentrically Braced Frames under Cyclic Loading." *International Journal of Steel Structures* 13.3 (2013): 401-19.
- Arasaratnam, P. L. "Effects of Flange Holes on Flexural Behavior of Steel Beams." McMaster University, Hamilton, Ontario, Canada, 2008.
- ASTM. "Standard Specification for General Requirements for Rolled Structural Steel Bars, Plates, Shapes, and Sheet Piling, ASTM A6 / A6M - 17a." *ASTM International, West Conshohocken, PA* (2017).
- ASTM. "Standard Specification for High-Strength Low-Alloy Columbium-Vanadium Structural Steel, A572 / A572M-18." *ASTM International, West Conshohocken, PA* (2018).
- ASTM. "Standard Specification for Structural Steel Shapes, A992 / A992M-11." *ASTM International, West Conshohocken, PA* (2015).

- ASTM. "Standard Test Methods and Definitions for Mechanical Testing of Steel Products, A370 – 17a." *ASTM International, West Conshohocken, PA* (2017).
- Atkinson, G. M. "Earthquake Time Histories Compatible with the 2005 National Building Code of Canada Uniform Hazard Spectrum" *Canadian Journal of Civil Engineering* 36.6 (2009): 991-1000.
- ATC. "Guidelines for Cyclic Seismic Testing of Components of Steel Structures for Buildings." *Report No. ATC-24, Applied Technology Council, Redwood City, CA, USA, 1992.*
- Ballio, G., and Castiglioni, C. A. "Seismic Behaviour of Steel Sections." *Journal of Constructional Steel Research* 29.1 (1994): 21-54.
- Bara, C. I. "The Seismic Behaviour of Steel Braces with Large Sections." Diss. École Polytechnique de Montréal, 2007.
- Bartlett, F. M., Dexter, R. J., Graeser, M. D., Jelinek, J. J., Schmidt, B. J., and Galambos, T. V. "Updating Standard Shape Material Properties Database for Design and Reliability." *Engineering Journal – American Institute of Steel Construction* 40.1 (2003): 2-24.
- Black, R. G., Wenger, W. A., and Popov, E. P. "Inelastic Buckling of Steel Struts under Cyclic Load Reversals." University of California, 1980.
- Brunet, F. "Conception parasismique des contreventements concentriques pour les structures industrielles lourdes en acier." Polytechnique Montréal, 2018.
- Cai, Q., and Driver, R. G. "End Tear-out Failures of Bolted Tension Members." University of Alberta, 2008.
- Castonguay, P. X. "Seismic Performance of Concentrically Braced Steel Frames of the Conventional Construction Category." Diss. École Polytechnique de Montréal, 2010.
- Chong, K. P, and Matlock, R.B. "Light-Gage Steel Bolted Connections without Washers." *Journal of the Structural Division* 101.7 (1975): 1381-91.
- CISC. "Handbook of Steel Construction." *Canadian Institute of Steel Construction*. Markham, Ontario, Canada (2016).
- Clark, K. A. "Experimental Performance of Multi-Story X-Braced SCBF Systems." Diss. University of Washington, 2009.

- Clark, P., Frank, K., Krawinkler, H., and Shaw, R. "Protocol for Fabrication, Inspection, Testing, and Documentation of Beam-Column Connection Tets and Other Experimental Specimens." *Report No. SAC/BD-97/02, SAC Steel Project Background Document*, 1997.
- CEN. "Eurocode 3: Design of Steel Structures, EN 1993." *European Committee for Standardization, Brussels, Belgium* (1993).
- CSA. "Design of Steel Structures, CAN/CSA-S16-09" *Canadian Standards Association, Mississauga, Ontario, Canada* (2009).
- CSA. "Design of Steel Structures, CAN/CSA-S16-14" *Canadian Standards Association, Mississauga, Ontario, Canada* (2014).
- CSA. "Limit States Design of Steel Structures, CAN/CSA-S16-01". *Canadian Standards Association, Mississauga, Ontario, Canada* (2001).
- CSA. "Supplement 1 to CAN/CSA-S16-01, Limit States Design of Steel Structures, CSA S16s1-05." *Canadian Standards Association, Mississauga, Ontario, Canada* (2005).
- Cunningham, T. J., Orbison, J. G., and Ziemian, R. D. "Assessment of American Block Shear Load Capacity Predictions." *Journal of Constructional Steel Research* 35.3 (1995): 323-38.
- D'Aniello, M., Ambrosino, G. L. M., Portioli, F., and Landolfo, R. "Modelling Aspects of the Seismic Response of Steel Concentric Braced Frames." *Steel and Composite Structures, an International Journal* 15.5 (2013): 539-66.
- Dexter, R. J., and Altstadt, S. A. "Strength and Ductility of Tension Flanges in Girders." *Recent Developments in Bridge Engineering. Ed. Mahmoud, K. M. Leiden: A A Balkema Publishers, 2003.*
- Dexter, R. J., Altstadt, S. A., and Gardner, C. A. "Strength and Ductility of HPS70W Tension Members and Tension Flanges with Holes". University of Minnesota, 2002.
- Dicleli, M., and Calik, E. E. "Physical Theory Hysteretic Model for Steel Braces." *Journal of Structural Engineering* 134.7 (2008): 1215-28.
- Dowell, R. K., Seible, F., and Wilson, E. L. "Pivot Hysteresis Model for Reinforced Concrete Members". *ACI Structural Journal* 95.5 (1998): 607-617.
- Downing, S. D., and Socie, D. F. "Simple Rainflow Counting Algorithms." *International Journal of Fatigue* 4.1 (1982): 31-40.

- Driver, R. G., Grondin, G. Y., and Kulak, G. L. "Unified Block Shear Equation for Achieving Consistent Reliability." *Journal of Constructional Steel Research* 62.3 (2006): 210-22.
- Egloff, O. "Développement D'un Fusible Ductile Pour Les Diagonales De Contreventement Faites De Profilés W Pour La Conception Parasismique De Charpentes Lourdes En Acier." Diss. École Polytechnique de Montréal, 2013.
- Egloff, O., Tremblay, R., Vincent, R., and Dussault, S. "Finite Element Analysis of Ductile Fuses for W-Shape Steel Bracing Members." 15th World conference of earthquake engineering, Lisboa. 2012.
- Epstein, H. I. "Block Shear of Structural Tees in Tension-Alternate Paths." *Engineering Journal - American Institute of Steel Construction* 33.4 (1996a): 147-52.
- Epstein H. I. "Effects of the Latest LRFD Block Shear Code Change." *Engineering Journal - American Institute Of Steel Construction* 33 (1996b): 30-33.
- Epstein, H. I., and D'Aiuto, C. L. "Using Moment and Axial Interaction Equations to Account for Moment and Shear Lag Effects in Tension Members." *Engineering Journal* 39.2 (2002): 91-99.
- Epstein, H. I., and Stamberg, H. "Block Shear and Net Section Capacities of Structural Tees in Tension: Test Results and Code Implications." *Engineering Journal* 39.4 (2002): 228-239.
- ETABS. 2018. *ETABS Ultimate v. 17.0.1*. Computers and Structures, Inc. Walnut Creek, CA, USA.
- Fell, B. V. "Large-Scale Testing and Simulation of Earthquake-Induced Ultra Low Cycle Fatigue in Bracing Members Subjected to Cyclic Inelastic Buckling." Diss. University of California, 2008.
- Fell, B. V., and Kanvinde, A. M. "Tensile Forces for Seismic Design of Braced Frame Connections—Experimental Results." *Journal of Constructional Steel Research* 66.4 (2010): 496-503.
- Fell, B.V., Kanvinde, A. M., Deierlein, G. G., and Meyers, A.T. "Experimental Investigation of Inelastic Cyclic Buckling and Fracture of Steel Braces." *Journal of Structural Engineering* 135.1 (2009): 19-32.

- FEMA. "Interim Protocols for Determining Seismic Performance Characteristics of Structural and Nonstructural Components Through Laboratory Testing." *FEMA 461 Draft document, Federal Emergency Management Agency, 2007.*
- Franchuk, C. R., Driver, R. G., and Grondin, G. Y. *Block Shear Behaviour of Coped Steel Beams:* Department of Civil Engineering, University of Alberta, Edmonton, 2002.
- Geschwindner, Louis F. "Notes on the Impact of Hole Reduction on the Flexural Strength of Rolled Beams." *Engineering Journal* 47.1 (2010): 37.
- Gilchrist, R. T, and Chong, K. P. "Thin Light-Gage Bolted Connections without Washers." *Journal of the Structural Division* 105.1 (1979): 175-83.
- Grondin, G. Y. "Discussion: Using Moment and Axial Interaction Equations to Account for Moment and Shear Lag Effects in Tension Members." *Engineering Journal* 42.1 (2005): 45-50.
- Gugerli, H. and Goel, S. C. "Large Scale Tests for the Hysteresis Behavior of Inclined Bracing Members." Proceedings of the 7th World Conference on Earthquake Engineering. 1980. Turk Natl Comm on Earthquake Eng, Ankara.
- Haddad, M. "Cyclic Behavior and Finite Element Modeling of Wide Flange Steel Bracing Members." *Thin-Walled Structures* 111 (2017): 65-79.
- Hsiao, P. C., Lehman, D. E., Berman, J. W., Roeder, C. W., and Powell, J. "Seismic Vulnerability of Older Braced Frames." *Journal of Performance of Constructed Facilities* 28.1 (2014): 108-20.
- Hsiao, P. C., Lehman, D. E., and Roeder C. W. "Improved Analytical Model for Special Concentrically Braced Frames." *Journal of Constructional Steel Research* 73 (2012): 80-94.
- Huns, B. B. S., Grondin, G. Y. and Driver, R. G. "Block Shear Behaviour of Bolted Gusset Plates." Department of Civil Engineering, University of Alberta, Edmonton, 2002.
- Ikeda, K., and Mahin, S. A. "A Refined Physical Theory Model for Predicting the Seismic Behaviour of Braced Steel Frames." *Report No. UCB/EERC-84/12, Earthquake Engineering Research Center, 1984.*

- Ikedda, K., Mahin, S. A., and Dermitzakis, S. N. "Phenomenological Modeling of Steel Braces under Cyclic Loading." *Report No. UCB/EERC-84/09, Earthquake Engineering Research Center*, 1984.
- Karamanci, E. "Collapse Assessment and Performance-Based Evaluation Techniques for Concentrically Braced Frames Designed in Seismic Regions." Diss. McGill University, 2013.
- Karamanci, E., and Lignos, D. G. "Computational Approach for Collapse Assessment of Concentrically Braced Frames in Seismic Regions." *Journal of Structural Engineering* 140.8 (2014): A4014019.
- Kim, H. J., and Yura, J. A. "The Effect of Ultimate-to-Yield Ratio on the Bearing Strength of Bolted Connections." *Journal of Constructional Steel Research* 49.3 (1999): 255-69.
- Krawinkler, H. "Loading Histories for Cyclic Tests in Support of Performance Assessment of Structural Components." *The 3rd international conference on advances in experimental structural engineering, San Francisco*, 2009.
- Kulak, G. L., Fisher, J.W., and Struik, J. H. *Guide to Design Criteria for Bolted and Riveted Joints*. New York: Wiley, 1987.
- Kulak, G. L., and Wu, E. Y. "Shear Lag in Bolted Angle Tension Members." *Journal of Structural Engineering New York, N.Y.* 123.9 (1997): 1144-52.
- Lai, J. W. "Experimental and Analytical Studies on the Seismic Behavior of Conventional and Hybrid Braced Frames." Diss. University of California, Berkeley, 2012.
- Lee, K., and Bruneau, M. "Energy Dissipation Demand of Compression Members in Concentrically Braced Frames." *Steel and Composite Structures* 5.5 (2005): 345-58.
- Lehman, D. E., Roeder, C. W., Herman, D., Johnson, S., and Kotulka, B. "Improved Seismic Performance of Gusset Plate Connections." *Journal of Structural Engineering* 134.6 (2008): 890-901.
- Leowardi, L. S., and Walpole, W. R. "Performance of Steel Brace Members." Department of Civil Engineering, University of Canterbury, 1996.

- Lewis, B. E., and Zwerneman, F. J. "Edge Distance, Spacing, and Bearing in Bolted Connections." *School of Civil and Environmental Engineering, Oklahoma State University, Oklahoma, OK* (1996).
- Lignos, D. G., Karamanci, E., and Martin, G. "A Steel Database for Modeling Post-Buckling Behavior and Fracture of Concentrically Braced Frames under Earthquakes." *Proceedings of the 15th World Conference of Earthquake Engineering (15WCEE), Lisbon, Portugal.* 2012.
- Lignos, D. G., and Karamanci, E. "Drift-based and Dual-parameter Fragility Curves for Concentrically Braced Frames in Seismic Regions." *Journal of Constructional Steel Research* 90 (2013): 209-220.
- Lilly, S. B., and Carpenter, S. T. "Effective Moment of Inertia of a Riveted Plate Girder." *Proceedings of the American Society of Civil Engineers, ASCE, 1939.*
- Lumpkin, E. J. "Enhanced Seismic Performance of Multi-Story Special Concentrically Brace Frames Using a Balanced Design Procedure." *University of Washington, 2009.*
- Lumpkin, E. J., Hsiao, P. C., Roeder, C. W., Lehman, D. E., Tsai, C. Y., Wu, A. C., Wei, C. Y., and Tsai, K.C. "Investigation of the Seismic Response of Three-Story Special Concentrically Braced Frames." *Journal of Constructional Steel Research* 77 (2012): 131-44.
- Mahmoud, H., and Wen, H. "Fracture Characteristic of Bolted Connections under Block Shear." (2016).
- Matlab. 2016. *Matlab R2016b*. The MathWorks Inc. Massachusetts, USA.
- Menegotto, M., and Pinto, P. E. (1973). "Method of analysis for cyclically loaded R.C. plane frames including changes in geometry and non-elastic behaviour of elements under combined normal force and bending", *Proceedings of the IABSE Symposium on Resistance and Ultimate Deformability of Structures Acted on by Well Defined Repeated Loads: Final Report*, 15-22.
- Mitchell, D., Tremblay, R., Karacebeyli, E., Paultre, P., Saatcioglu, M., and Anderson, D.L. "Seismic force modification factors for the proposed 2005 edition of the National Building Code of Canada". *Canadian Journal of Civil Engineering*, 30 (2) (2003): 308– 327.

- Može, P., and Beg, D. "A Complete Study of Bearing Stress in Single Bolt Connections." *Journal of Constructional Steel Research* 95 (2014): 126-140.
- Munse, W. H. "The Effect of Bearing Pressure on the Static Strength of Riveted Connections" University of Illinois at Urbana Champaign, College of Engineering. Engineering Experiment Station, 1959.
- Nakashima, M., Roeder, C. W., and Maruoka, Y. "Steel Moment Frames for Earthquakes in United States and Japan." *Journal of Structural Engineering* 126.8 (2000): 861-868.
- NRCC. *National Building Code of Canada*. Ottawa: Associate Committee on the National Building Code, National Research Council, 2016.
- Osgood, W. R., Morris, C. T., Leffler, B. R., Lane, E. N. W., Moore, L. E., Grinter, L. E., Spofford, C. M., Mirabelli, E., Godfrey, E., Weiskopf, W. H., Williams, C. D., Auerbach, A. B., Jones, J., Moore, R. L., Garrelts, J. M., Witmer, F.P., Fischer, A. W., Shank, J. R., Hussey, H. D., Kring, C. U., Shedd, T. C., Lilly, S. B., and Carpenter, S. T. "Discussion of Effective Moment of Inertia of a Riveted Plate Girder by Scott B. Lilly and Samuel T. Carpenter." *Transactions of the American Society of Civil Engineers* 195.1 (1940): 1477-1514.
- Perry, W. C. "The Bearing Strength of Bolted Connections." Diss. 1981.
- Powell, J. A. "Evaluation of Special Concentrically Braced Frames for Improved Seismic Performance and Constructability." Diss. University of Washington, 2010.
- Rabinovitch, J. S., and Cheng, J. J. R. "Cyclic Behavior of Steel Gusset Plate Connections." Department of Civil and Environmental Engineering, University of Alberta, Edmonton, Alta." *Structural Engineering Report* 191 (1993).
- Rex, C. O, and Easterling, W. S. "Behavior and Modeling of a Bolt Bearing on a Single Plate." *Journal of Structural Engineering* 129.6 (2003): 792-800.
- Richard, J. "Étude Du Comportement Sismique De Bâtiments Industriels Avec Systèmes De Contreventement En Acier De Faible Ductilité." Diss. École Polytechnique de Montréal, 2009.
- Richards, P. W. and Uang, C. M. "Testing Protocol for Short Links in Eccentrically Braced Frames." *Journal of Structural Engineering* 132.8 (2006): 1183-1190.

- Roeder, C. W., Lehman, D. E., Christopolus, A., Gunnarson, I., Johnson, S., and Yoo, J. H. "Seismic Design of Braced Frame Gusset Plate Connections." *WIT Transactions on The Built Environment* 81 (2005).
- Roeder, C. W., Lehman, D. E., and Clark, K. "Influence of Gusset Plate Connections and Braces on the Seismic Performance of X-Braced Frames." *Earthquake Engineering & Structural Dynamics* 40.4 (2011a): 355-74.
- Roeder, C. W., Lumpkin, E. J. and Lehman, D. E. "A Balanced Design Procedure for Special Concentrically Braced Frame Connections." *Journal of Constructional Steel Research* 67.11 (2011b): 1760-72.
- SAP 2000. 2018. *SAP 2000 v. 20.1.0*. Computers and Structures, Inc. Walnut Creek, CA, USA.
- Sheikh-Ibrahim, F. I. "Design Method for the Bolts in Bearing-Type Connections with Fillers." *Engineering Journal* 39.4 (2002): 189-95.
- Simpson B. G., and Mahin S. A. "Experimental and Numerical Investigation of Strongback Braced Frame System to Mitigate Weak Story Behavior." *Journal of Structural Engineering* 144.2 (2018): 04017211.
- Sivakumaran, K. S., Arasaratnam, P. and Tait, M. "Strength and Ductility of Steel Beams with Flange Holes." *Stability and Ductility of Steel Structures*. Ed. Batista, E. D., P. Vellasco and L. De Limas: 2010.
- Tanaka, A., and Enomoto, N. "Strength of High Strength Bolted Wide Flange Connections Subjected to Tensile Load." *Taisei Technical Research Report* 18.193 (1986): 195-204.
- Tanaka, A., and Enomoto, N. "Statical Characteristics of High Strength Bolted Connections of Wide Flange Steel Braces." *Journal of Structural Engineering, AII*, 404 (1989): 51-63.
- Tide, R. H. R. "Bolt Shear Design Considerations." *Engineering Journal* 47.1 (2010): 47-63.
- Topkaya, C. "A Finite Element Parametric Study on Block Shear Failure of Steel Tension Members." *Journal of Constructional Steel Research* 60.11 (2004): 1615-35.
- Tremblay, R. "Inelastic Seismic Response of Steel Bracing Members." *Journal of Constructional Steel Research* 58.5-8 (2002): 665-701.

- Tremblay, R. "Influence of Brace Slenderness on the Seismic Response of Concentrically Braced Steel Frames." *Behaviour of Steel Structures in Seismic Areas*. Eds. Mazzolani, F. M. and R. Tremblay. Leiden: *A A Balkema Publishers*, 2000.
- Tremblay, R., Archambault, M.-H., and Filiatrault, A. "Seismic Response of Concentrically Braced Steel Frames Made with Rectangular Hollow Bracing Members." *Journal of Structural Engineering* 129.12 (2003): 1626-1636.
- Tremblay, R., Filiatrault, A., Bruneau, M., Nakashima, M., Prion, H. G., and DeVall, R. "Seismic Design of Steel Buildings: Lessons from the 1995 Hyogo-Ken Nanbu Earthquake." *Canadian Journal of Civil Engineering* 23.3 (1996): 727-56.
- Tremblay, R., Filiatrault, A., Timler, P., and Bruneau, M. "Performance of Steel Structures during the 1994 Northridge Earthquake." *Canadian Journal of Civil Engineering* 22.2 (1995): 338-60.
- Tremblay, R., Haddad, M., Martinez, G. Richard, J., and Moffatt, K.. "Inelastic Cyclic Testing of Large Size Steel Bracing Members." The 14th WCEE, Beijing, China (2008).
- Tsai, C. Y., Tsai, K. C., Lin, C. H., Wei, C. Y., Wang, K. G., Yu, Y. J., and Wu, A. C. "Cyclic Responses of Three 2-Story Seismic Concentrically Braced Frames." *Frontiers of Architecture and Civil Engineering in China* 4.3 (2010): 287-301.
- Udagawa, K., Yamada, T., and Yuhara, Y. "Ultimate Strength of H-Shaped Tension Members Jointed with High-Strength Bolts." *Kou kouzou rombunshuu* 5.18 (1998): 113-25.
- Uriz, P., Filippou, F. C., and Mahin, S. A. "Model for Cyclic Inelastic Buckling of Steel Braces." *Journal of Structural Engineering* 134.4 (2008): 619-628.
- Wakabayashi, M., Nakamura, T., and Yoshida, N. "Experimental Studies on the Elastic-Plastic Behavior of Braced Frames under Repeated Horizontal Loading. Part 1 Experiments of Braces with an H-Shaped Cross Section in a Frame." (1977).
- Wakabayashi, M., Nakamura, T., and Yoshida, N. "Experimental Studies on the Elastic-Plastic Behavior of Braced Frames under Repeated Horizontal Loading. Part 2 Experiments of Braces Composed of Steel Circular Tubes, Angle-Shapes, Flat Bars or Round Bars." (1980).

- Walbridge, S. S., Grondin, G. Y. and Cheng, J. J. R. "Gusset Plate Connections under Monotonic and Cyclic Loading." *Canadian Journal of Civil Engineering* 32.5 (2005): 981-95.
- Winter, G. "Tests on Bolted Connections in Light Gage Steel." *Journal of the Structural Division* 82.2 (1956): 1-25.
- Yoo, J., Roeder, C. W., and Lehman, D. E. "Analytical Performance Simulation of Special Concentrically Braced Frames." *Journal of Structural Engineering* 134.6 (2008): 881-89.
- Yuan, Q. "Investigation of Hole Making Practices in the Fabrication of Structural Steel." Diss. University of Cincinnati, 2005.
- Yura, J. A., Hansen, M. A. and Frank, K. H. "Bolted Splice Connections with Undeveloped Fillers." *Journal of the Structural Division* 108.12 (1982): 2837-49.
- Zhang, W., Huang, M., Zhang, Y., and Sun, Y. "Cyclic Behavior Studies on I-Section Inverted V-Braces and Their Gusset Plate Connections." *Journal of Constructional Steel Research* 67.3 (2011): 407-20.

APPENDICES

APPENDIX A: DETAILED DESIGN CALCULATIONS

1 **Connection design for specimens J310-T and J310-C (based on S16-14)**

2
3 **Factors (CSI S16-14)**

4 ϕ 0.90 ϕ_{bi} 0.80 Probable:
5 ϕ_u 0.75 ϕ_{oe} 0.75 ϕ 1.00
6 ϕ_b 0.80 ϕ_{br} 0.80 R_y 1.1

Steel properties of W-shape brace

Nominal (MPa) Probable (MPa)
 F_y 345 F_u 450 F_y 385 F_u 495
E 2E+05 Mpa G 77000 Mpa
 μ 0.3

7
8 **Bolt properties**

9 Bolt grade A325 Size 7/8 in
10 V_{bolt} (kN) 154 (CSA Table 3-4)
11 d_{bolt} (mm) 22 d_{hole} 25

12 *Threads excluded

13
14 **Section Properties**

15 **W310x97**

Area	I_x	S_x	r_x	Z_x	I_y	S_y	r_y	Z_y	J
(mm ²)	(mm ⁴)	(mm ³)	(mm)	(mm ³)	(mm ⁴)	(mm ³)	(mm)	(mm ³)	(mm ⁴)
12300	2.2E+08	1440000	134	1590000	7.3E+07	478000	77	725000	912000

C_w	N. Mass	d	b	t	w	T	k	k_1	d-2t	Imperial Designation	Web class:	Flange class:
(mm ⁶)	(kg/m)	(mm)	(mm)		1	3						
1.6E+12	97	308	305	15.4	9.9	234	37	25	277	W12x65		

23
24 $A_w = 2316.6 \text{ mm}^2$ $A_f = 4991.7 \text{ mm}^2$

25
26 **Axial compression***

27 Length of the member and connections, L= 6.7 m OR 6667 mm
28 K= 0.9

29 $\frac{KL}{r_x} =$

45 < 200

OK

31 $\frac{KL}{r_y} =$

78 < 200

OK

33 $\lambda_x = \frac{KL}{r_x} \sqrt{\frac{F_y}{\pi^2 E}} =$

0.592

Probable:

0.625

35 $\lambda_y = \frac{KL}{r_y} \sqrt{\frac{F_y}{\pi^2 E}} =$

1.03 GOVERNS

1.09 GOVERNS

39
40 n = 1.34 (W-shape)

41 *Connection design based on factored axial compression capacity for CC design.

42

43 **Compressive resistance:**

44 Design: $C_{ry} = \phi A F_y (1 + \lambda_y^{2n})^{-1/n} =$ 2206 kN

45 Probable: $C_{ry} = (A_w F_{yw} + A_f F_{yF})$
 46 $(1 + \lambda_y^{2n})^{-1/n} =$ 2578 kN

47	Web and flange force deviation by area:	Design	Probable
48	Flanges:	1790 kN	2092 kN
49	Web:	415 kN	486 kN

50

51 **Bolt design** (bolt design for shear failure - no oversized holes)

52 Number of bolts required in flanges: $C_{ry} / V_{bolt} =$ 11.63 bolts round up: 12 bolts

53 Number of bolts required in web: $C_{ry} / V_{bolt} =$ 1.35 bolts round up: 4 bolts

54 Therefore use 6 bolts per flange and 4 bolts on the web (in double shear - plug shear on web governs)

55 Minimum centre-to-centre spacing: $2.7d_b$ 60 mm Choose: 76 mm (3")

56 Minimum edge distance (gas cut edge): (Table 6 S16-14) 38 mm Choose: 32 mm (1.25")

57 Maximum edge distance: 150 mm OR $12t =$ 185 mm

58 Connection length: $L = 2spacing =$ 152 mm < 760 mm **OK**

59 Minimum edge distance (rolled edge) (S16-14 Table 6): 28 mm

60 Gauge distance (to accommodate gusset plate of 38mm): 146 mm (5 3/4") 76 mm (web)

61 Check bearing of W-shape: $B_{r1} = 3\phi_{br} t d_b n F_u$ 4437 kN (flanges)

62 $B_{r2} = 3\phi_{br} t d_b n F_u$ 951 kN (web)

63 $B_{rtotal} = B_{r1} + B_{r2}$ 5387 kN Ratio: 0.4 **OK**

64 Probable: $B_{r1exp} = 3t d_b n F_{uexp}$ 6101 kN (flanges)

65 $B_{r2exp} = 3\phi_{br} t d_b n F_u$ 1307 kN (web)

66 $B_{rtotal} = B_{r1} + B_{r2}$ 7408 kN

67 Check bolt shear:

68 A325 bolts F_u (S16-14 Table 3-3) = 825 MPa Flanges Web

69 Design: $V_r = 0.60\phi_b n m A_b F_u =$ 1844 kN 1230 kN

70 Unfactored: $V_r = 0.60 n m A_b F_u =$ 2305 kN 1537 kN

71

72 The next calculations are carried out for the purposes of predicting the failure mode at ultimate loading

73 **Gross section yielding and probable and post-buckling compression capacity**

74 Design (tension): $T_r = \phi A_g F_y =$ 3819 kN (S16-14 clause 27.5.3.4)

75 Probable (tension): $T_u = R_y A_g F_y =$ 4736 kN

76 Probable (compression): $C_u = \frac{1.2 C_r}{\phi} =$ 3093 kN **GOVERNS**

77 $C_u' = 0.2 A_g R_y F_y =$ 947 kN **GOVERNS**

78 Post-buckling: $C_u' = C_r / \phi =$ 2578 kN

79

80

81 **Net section fracture** (checked at the last row of bolts)

82 $A_n: A_n = A_g - 4 \times d_{hole} \times t_f =$ 10735 mm²

83 No shear lag factor because web & flanges are connected

84 Design: $T_r = \phi_u A_n F_u =$ 3623 kN

85 Probable: $T_{rexp} = A_n F_{uexp} =$ 5314 kN

86

87 **Check failure mode in flanges**

88 **Block shear path 1 (flanges)**

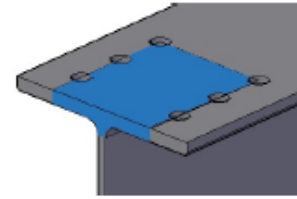
89 Net area in tension: A_n
 90 $= (A - Tw)/2$
 91 $= (b - d_{gauge} + d_{hole})t = 2177 \text{ mm}^2$

92 Gross area in shear (in flange):

93 $A_{gv1} = (d_{edge} + 2pitch) \times (2t_f) = 5672 \text{ mm}^2$

94 $A_{gv2} = (d_{edge} + 2pitch) \times (w) = 1823 \text{ mm}^2$

95 Resistance: $T_r = 2\phi_u \left(U_t A_n F_u + 0.6 A_{gv} \frac{(F_y + F_u)}{2} \right) = 4151 \text{ kN}$
 96
 97 Probable: 6113 kN



Block shear path 1

99 **Block shear path 2 (flanges)**

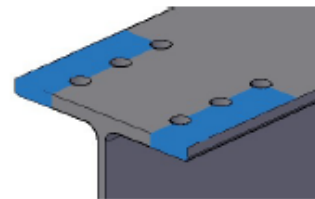
100 Net area in tension: $A_n = (b - d_{gauge} - d_{hole})t = 2081 \text{ mm}^2$

101 Gross area in shear (in flange):

102 $A_{gv} = (d_{edge} + 2pitch) \times (2t_f) = 5672 \text{ mm}^2$

103 Resistance:

104 $T_r = 2\phi_u \left(U_t A_n F_u + 0.6 A_{gv} \frac{(F_y + F_u)}{2} \right) = 3293 \text{ kN}$
 105
 106 Probable: 4849 kN



Block shear path 2

108 **Block shear path 3 (flanges)**

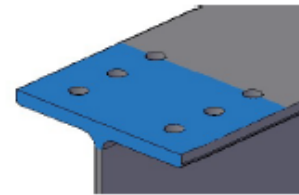
109 Net area in tension: $A_n = \frac{(A - Tw - 4d_{hole}t)}{2} = 4258 \text{ mm}^2$

110 Gross area in shear (in flange):

111 $A_{gv} = (d_{edge} + 2pitch) \times (w) = 1823 \text{ mm}^2$

112 Resistance:

113 $T_r = 2\phi_u \left(U_t A_n F_u + 0.6 A_{gv} \frac{(F_y + F_u)}{2} \right) = 3527 \text{ kN}$
 114
 115 Probable: 5178 kN



Block shear path 3

117 **Plug shear in flanges**

118 $A_{gv} = (d_{edge} + 2pitch) \times (4t_f) = 11344 \text{ mm}^2$

119 $T_r = 2\phi_u \left(0.6 A_{gv} \frac{(F_y + F_u)}{2} \right) = 4058 \text{ kN}$
 120
 121 Probable: 5989 kN

122 **Flange failure mode: Block shear 2**

3293 kN Probable: 4849 kN

124 **Check failure mode in web**

125 **Block shear path 1 (web)**

126 Net area in tension: $A_n = (d_{gauge} - d_{hole})w = 519 \text{ mm}^2$

127 Gross area in shear (in flange):

128 $A_{gv} = (d_{edge} + pitch) \times (2w) = 2137 \text{ mm}^2$
 129

130	Resistance:				
131	$T_r = \varphi_u \left(U_t A_n F_u + 0.6 A_{gv} \frac{(F_y + F_u)}{2} \right) =$	552	kN		
132					
133	Probable:	813	kN		
134					
135	Plug shear in web				
136	$A_{gv} = (d_{edge} + pitch) \times (4w) =$	4275	mm ²		
137	$T_r = \varphi_u \left(0.6 A_{gv} \frac{(F_y + F_u)}{2} \right) =$	765	kN		
138					
139	Probable:	1129	kN		
140					Probable:
141	Web failure mode: Block shear path 1	552	kN	813	kN
142					
143	Therefore total connection capacity = Block shear 2 + Block shear 1=				
144		3831	kN	Ratio:	0.58 OK
145	Probable:	5640	kN	Ratio:	0.46 OK
146					
147	JAW PLATES				
148					
149	Jaw plate design				
150	A572-50 Grade steel:	$F_y = 345$ MPa	$F_u = 450$ MPa		
151		$F_{yprob} = 380$ MPa	$F_{uprob} = 495$ MPa		
152	Force in one plate:	895	kN		
153	Choose thickness:	16	mm		
154	Choose width of plate:	219	mm	Edge distance:	32 mm
155	Gross section yielding				
156	$T_r = \varphi A_g F_y =$	1080	kN		
157	Probable:	1320	kN		
158					
159	Net section fracture				
160					
161	At bolts				
162	$T_r = \varphi_u A_n F_u =$	902	kN		
163	Probable:	1322	kN		
164					
165	At slot				
166	$T_r = \varphi_u A_n F_u =$	1073	kN		
167	Probable:	1573	kN		
168					
169	Bearing:				
170	Design:	$B_r = 3\varphi_{br} t d_b n F_u =$	2287	kN	
171	Probable:	$B_r = 3 t d_b n F_u =$	3144	kN	
172					

173 **Plug shear:**

174 $A_{gv} = (d_{edge} + 2pitch) \times (4t) =$ 11694 mm²

175 $T_r = \phi_u \left(0.6A_{gv} \frac{(F_y + F_u)}{2} \right) =$ 2092 kN

176 Probable: 3068 kN

178

179 **Block shear**

180 **Block shear path 1**

181 Net area in tension: $A_n = (d_{gauge} - d_{hole})t =$ 1941 mm²

182 Gross area in shear (in flange):

183 $A_{gv1} = (d_{edge} + 2pitch) \times (2t) =$ 5847 mm²

184 Resistance: $T_r = \phi_u \left(U_t A_n F_u + 0.6A_{gv} \frac{(F_y + F_u)}{2} \right) =$ 1701 kN

185 Probable: 2494 kN

187

188 **Block shear path 2**

189 Net area in tension: $A_n = (b - d_{gauge} - d_{hole})t =$ 781 mm²

190 Gross area in shear: $A_{gv} = (d_{edge} + 2pitch) \times (2t) =$ 5847 mm²

192 Resistance:

193 $T_r = \phi_u \left(U_t A_n F_u + 0.6A_{gv} \frac{(F_y + F_u)}{2} \right) =$ 1310 kN

194 Probable: 1921 kN

196

197 **Weld design**

198 E49 Electrode $F_u =$ 490 MPa

199 Maximum weld size: $t_{gusset} =$ 16 mm $D_{max} =$ 14 mm

200 Minimum weld size: $t_{plate} =$ 16 mm $D_{min} =$ 8 mm

201 Choose D= 8 mm

202 Length must be > 4D = 32 mm Choose 483 mm (19")

203 Or use 9.5" welds on both sides of the jaw plate

204 **Eccentric loading**

205 e= 51 mm

206 Elastic bending shear flow:

207 $q_1 = 3Ve/L^2$ 1.171 kN/mm $D_1 \geq q_1/(1.5 * 0.156) =$ 5.01 mm

208 $q_{y2} = V/L$ 0.927 kN/mm $D_2 \geq q_2/0.156 =$ 5.94 mm

209 $q_{max} = \sqrt{q_x^2 + q_y^2} =$ 1.494 kN/mm $D \geq \sqrt{D_1^2 + D_2^2} =$ 7.77 mm OK

211

212 **Weld metal fracture**

213 $V_r = 0.67 \phi_w A_w X_u (1.00 + 0.5 \sin^{1.5} \theta) M_w =$ 600 kN For 2 welds: 1201 kN

214

215

216 **WEB PLATE**

217 A572-50 Grade steel: $F_y = 345 \text{ MPa}$ $F_u = 450 \text{ MPa}$ Edge: 32 mm

218 $F_{yprob} = 380 \text{ MPa}$ $F_{uprob} = 495 \text{ MPa}$

219 Force in each web plate: 207.72 kN

220 Width of plate: 140 mm (5.5")

221 Required area: $A_{ne} = T_r / F_u \phi_u =$ 615 mm^2 *minimum plate thickness

222 Calculate thickness: $A_{ne} = (w_{pl} - 2d_{hoie})t =$ 6.92 mm Choose 9.5 mm plate

223 $T_r = \phi_u A_{ne} F_u =$ 286 kN Exp: 419 kN

224

225 **Gross section yielding**

226 Design: $T_r = \phi A_g F_y =$ 413 kN

227 Probable: 505 kN

228

229 **Bearing:**

230 Design: $B_r = 3\phi_b r t d_b n F_u =$ 915 kN

231 Probable: $B_r = 3t d_b n F_u =$ 1258 kN

232

233 **Plug shear:**

234 $A_{gv} = (d_{edge} + pitch) \times (4t) =$ 4113 mm^2

235 $T_r = \phi_u \left(0.6 A_{gv} \frac{(F_y + F_u)}{2} \right) =$ 736 kN

237 Probable: 1079 kN

238

239 **Block shear**

240 **Block shear path 1**

241 $A_n = (d_{gauge} - d_{hoie})t =$ 484 mm^2

242 $A_{gv} = (d_{edge} + pitch) \times (2t) =$ 2056 mm^2

243 $T_r = \phi_u \left(U_t A_n F_u + 0.6 A_{gv} \frac{(F_y + F_u)}{2} \right) =$ 493 kN

245 Probable: 779 kN

246

247 **Block shear path 2**

248 Net area in tension: $A_n = (b - d_{gauge} - d_{hoie})t =$ 363 mm^2

249 Gross area in shear: $A_{gv} = (d_{edge} + pitch) \times (2t) =$

250 2056 mm^2

251 Resistance:

252 $T_r = \phi_u \left(U_t A_n F_u + 0.6 A_{gv} \frac{(F_y + F_u)}{2} \right) =$ 478 kN

254 Probable: 701 kN

255

256

257

258

259 **GUSSET PLATE**

260 A572-50 Grade steel: $F_y = 345$ MPa $F_u = 450$ MPa
 261 $F_{yprob} = 380$ MPa $F_{uprob} = 495$ MPa
 262 Design force: 2205.69 kN Probable force: 2577.87 kN

263 Calculate Whitmore width:

264 $w = 2 \times L_{weld} \times \tan 30^\circ + 2t_{plate} + d_{beam} =$
 265 618 mm
 266 max: 688 mm

268 Choose thickness: 16 mm
 269 (5/8" plate)

270 **Compression resistance:**

271
 272 Buckling length: 151 mm
 273 Radius of Gyration: 4.6 mm
 274 K (conservative) 1
 275 $KL/r = 33$

276 $\lambda_y = \frac{KL}{r_y} \sqrt{\frac{F_y}{\pi^2 E}} = 0.435$

278
 279 $\lambda_{exp} = \frac{KL}{r_y} \sqrt{\frac{F_{yprob}}{\pi^2 E}} = 0.456$

281 Design: $C_{ry} = \phi A F_y (1 + \lambda_y^{2n})^{-1/n} = 2825$ kN

283 Probable:
 284 $C_{ry} = (A F_y) (1 + \lambda_y^{2n})^{-1/n} = 3419$ kN
 285

287 **Gross section yielding**

288 Design: $T_r = \phi A_g F_y = 3048$ kN
 289 Probable: $T_r = A_g F_y = 3725$ kN

291 **Net section**

292 Design: $T_r = \phi_u A_{ne} F_u = 3686$ kN
 293 Probable: $T_r = A_{ne} F_u = 5406$ kN

295 **Block shear**

296 $A_n = 2 \times t_{jaw} \times t = 504$ mm²
 297 $A_{gv} = 4 \times L_{weld} \times t = 15323$ mm²
 298 $T_r = \phi_u \left(U_t A_n F_u + 0.6 A_{gv} \frac{(F_y + F_u)}{2} \right) =$
 299 2911 kN
 300
 301 Probable: 4269 kN

1 **Connection design for specimens J360-T and J360-C (based on S16-14)**

3 **Factors (CSI S16-14)**

4 ϕ 0.90 ϕ_{bi} 0.80 Unfactored:
 5 ϕ_u 0.75 ϕ_{be} 0.75 ϕ 1.00
 6 ϕ_b 0.80 ϕ_{br} 0.80 R_y 1.1

Steel properties of W-shape brace

Nominal (MPa) Probable (MPa)
 F_y 345 F_u 450 F_y 385 F_u 495
 E 2E+05 Mpa G 77000 Mpa
 μ 0.3

8 **Bolt properties**

9 Bolt grade A490 Size 1
 10 V_{bolt} (kN) 252 (CSA Table 3-4)
 11 d_{bolt} (mm) 25 d_{hole} 27 *No 2 mm penalty following inspection of holes
 12 *Threads excluded

14 **Section Properties**

15 **W360x134**

Area	I_x	S_x	r_x	Z_x	I_y	S_y	r_y	Z_y	J
(mm ²)	(mm ⁴)	(mm ³)	(mm)	(mm ³)	(mm ⁴)	(mm ³)	(mm)	(mm ³)	(mm ⁴)
17100	4.2E+08	2330000	156	2560000	1.5E+08	817000	94	1240000	1680000

C_w	N. Mass	d	b	t	w	T	k	k_1	d-2t	Imperial Designation	Web class:	
(mm ⁶)	(kg/m)	(mm)	(mm)		Flange class:							
4.3E+12	134	356	369	18	11	256	50	36	320	W14x90		1
												3

24 $A_w = 2816 \text{ mm}^2$ $A_f = 7142 \text{ mm}^2$

26 **Axial compression***

27 Length of the member and connections, L= 6.7 m OR 6667 mm
 28 K= 0.9

29 $\frac{KL}{r_x} = 38 < 200$ OK

31 $\frac{KL}{r_y} = 64 < 200$ OK

33 $\lambda_x = \frac{KL}{r_x} \sqrt{\frac{F_y}{\pi^2 E}} = 0.509$ Probable: 0.537

35 $\lambda_y = \frac{KL}{r_y} \sqrt{\frac{F_y}{\pi^2 E}} = 0.84$ GOVERNS 0.89 GOVERNS

37 $n = 1.34$ (W-shape)

40 *Connection design based on factored axial compression capacity for CC design.

41
 42

43 **Compressive resistance:**

44 Design: $C_{ry} = \phi A F_y (1 + \lambda_y^{2n})^{-1/n} =$ 3680 kN

45 Probable: $C_{ry} = (A_w F_{yw} + A_f F_{yF})$
 46 $(1 + \lambda_y^{2n})^{-1/n} =$ 4364 kN

47	Web and flange force deviation by area:	Design	Probable
48	Flanges:	3074 kN	3645 kN
49	Web:	606 kN	719 kN

50

51 **Bolt design** (bolt design for shear failure - no oversized holes)

52 Number of bolts required in flanges: $C_{ry} / V_{bolt} =$ 12.20 bolts round up: 16 bolts

53 Number of bolts required in web: $C_{ry} / V_{bolt} =$ 1.20 bolts round up: 4 bolts

54 Therefore use 8 bolts per flange and 4 bolts on the web (in double shear - bearing governs)

55 Minimum centre-to-centre spacing: $2.7d_b$ 69 mm Choose: 76 mm (3")

56 Minimum edge distance (sheared edge): (Table 6 S16-14) 44 mm Choose: 38 mm (1.5")

57 Maximum edge distance: 150 mm OR $12t =$ 216 mm

58 Connection length: $L = 3spacing =$ 229 mm < 760 mm **OK**

59 Minimum edge distance (rolled edge) (S16-14 Table 6): 32 mm

60 Gauge distance (to accommodate gusset plate of 38mm): 152 mm (6") 76 mm (web)

61 Check bearing of W-shape: $B_{r1} = 3\phi_b t d_b n F_u$ 7900 kN (flanges)

62 $B_{r2} = 3\phi_b t d_b n F_u$ 1207 kN (web)

63 $B_{rtotal} = B_{r1} + B_{r2}$ 9107 kN Ratio: 0.4 **OK**

64 Probable: $B_{r1exp} = 3t d_b n F_{uexp}$ 10863 kN (flanges)

65 $B_{r2exp} = 3\phi_b t d_b n F_u$ 1660 kN (web)

66 $B_{rtotal} = B_{r1} + B_{r2}$ 12523 kN

67 Check bolt shear: Factor accounting for shims: $R_v =$ 1.000

68 A490 bolts F_u (S16-14 Table 3-3) = 1035 MPa Flanges Web

69 Design: $V_r = 0.60\phi_b n m A_b F_u =$ 4028 kN 2014 kN

70 Unfactored: $V_r = 1.11 \times 0.60 n m A_b F_u =$ 5588 kN 2794 kN

71

72 The next calculations are carried out for the purposes of predicting the failure mode at ultimate loading

73 **Gross section yielding and probable and post-buckling compression capacity**

74 Design (tension): $T_r = \phi A_g F_y =$ 5310 kN (S16-14 clause 27.5.3.4)

75 Probable (tension): $T_u = R_y A_g F_y =$ 6584 kN

76 Probable (compression): $C_u = \frac{1.2 C_r}{\phi} =$ 4906 kN GOVERNS

78 Post-buckling: $C_u' = 0.2 A_g R_y F_y =$ 1317 kN GOVERNS

79 $C_u' = C_r / \phi =$ 4364 kN

80

81 **Net section fracture** (checked at the last row of bolts)

82 $A_n: A_n = A_g - 4 \times d_{hole} \times t_f =$ 15157 mm²

83 No shear lag factor because web & flanges are connected

84 Design: $T_r = \phi_u A_{ne} F_u =$ 5115 kN

85 Probable: $T_{rexp} = A_{ne} F_{uexp} =$ 7503 kN

86

87 **Check failure mode in flanges**

88 **Block shear path 1 (flanges)**

89 Net area in tension: $A_n = (A - Tw)/2 - (b - d_{gauge} + d_{hole})t = 2757 \text{ mm}^2$

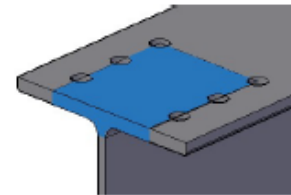
92 Gross area in shear (in flange):

93 $A_{gv1} = (d_{edge} + 3pitch) \times (2t_f) = 9601 \text{ mm}^2$

94 $A_{gv2} = (d_{edge} + 3pitch) \times (w) = 2934 \text{ mm}^2$

95 Resistance: $T_r = 2\phi_u \left(U_t A_n F_u + 0.6 A_{gv} \frac{(F_y + F_u)}{2} \right) = 6346 \text{ kN}$

96 Probable: 9348 kN



Block shear path 1

99 **Block shear path 2 (flanges)**

100 Net area in tension: $A_n = (b - d_{gauge} - d_{hole})t = 3413 \text{ mm}^2$

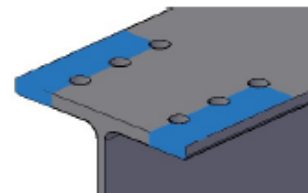
101 Gross area in shear (in flange):

102 $A_{gv} = (d_{edge} + 3pitch) \times (2t_f) = 9601 \text{ mm}^2$

103 Resistance:

104 $T_r = 2\phi_u \left(U_t A_n F_u + 0.6 A_{gv} \frac{(F_y + F_u)}{2} \right) = 5508 \text{ kN}$

105 Probable: 8110 kN



Block shear path 2

108 **Block shear path 3 (flanges)**

109 Net area in tension: $A_n = \frac{(A - Tw - 4d_{hole}t)}{2} = 6170 \text{ mm}^2$

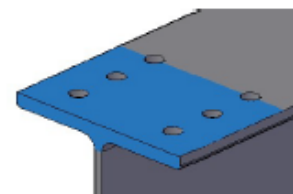
110 Gross area in shear (in flange):

111 $A_{gv} = (d_{edge} + 3pitch) \times (w) = 2934 \text{ mm}^2$

112 Resistance:

113 $T_r = 2\phi_u \left(U_t A_n F_u + 0.6 A_{gv} \frac{(F_y + F_u)}{2} \right) = 5215 \text{ kN}$

114 Probable: 7658 kN



Block shear path 3

117 **Plug shear in flanges**

118 $A_{gv} = (d_{edge} + 3pitch) \times (4t_f) = 19202 \text{ mm}^2$

119 $T_r = 2\phi_u \left(0.6 A_{gv} \frac{(F_y + F_u)}{2} \right) = 6870 \text{ kN}$

120 Probable: 10139 kN

122 **Flange failure mode: Block shear path 3** 5215 kN

Probable: 7658 kN

124 **Check failure mode in web**

125 **Block shear path 1 (web)**

126 Net area in tension: $A_n = (d_{gauge} - d_{hole})w = 541 \text{ mm}^2$

127 Gross area in shear (in flange):

128 $A_{gv} = (d_{edge} + pitch) \times (2w) = 2515 \text{ mm}^2$

129

130	Resistance:				
131	$T_r = \varphi_u \left(U_t A_n F_u + 0.6 A_{gv} \frac{(F_y + F_u)}{2} \right) =$	632	kN		
132					
133	Probable:	932	kN		
134					
135	Plug shear in web				
136	$A_{gv} = (d_{edge} + pitch) \times (4w) =$	5029	mm ²		
137	$T_r = \varphi_u \left(0.6 A_{gv} \frac{(F_y + F_u)}{2} \right) =$	900	kN		
138					
139	Probable:	1328	kN		
140				Probable:	
141	Web failure mode: Block Shear Path 1	632	kN	932	kN
142					
143	Therefore total connection capacity = Flange block shear 3 + Web block shear 1 =				
144		5847	kN	Ratio: 0.63	OK
145	Probable:	8590	kN	Ratio: 0.51	OK
146					
147	JAW PLATES				
148					
149	Jaw plate design				
150	A572-50 Grade steel:	$F_y = 345$ MPa	$F_u = 450$ MPa		
151		$F_{yprob} = 380$ MPa	$F_{uprob} = 495$ MPa		
152	Force in one plate:	1537	kN		
153	Choose thickness:	16	mm		
154	Choose width:	349	mm	End: 38	mm
155	Gross section yielding				
156	$T_r = \varphi A_g F_y =$	1722	kN		
157	Probable:	2104	kN		
158					
159	Net section fracture				
160	At bolts				
161	$T_r = \varphi_u A_{ne} F_u =$	1582	kN		
162	Probable:	2320	kN		
163					
164	At slot				
165	$T_r = \varphi_u A_{ne} F_u =$	1753	kN		
166	Probable:	2571	kN		
167					
168	Bearing:				
169	Design: $B_r = 3\varphi_{br} t d_b n F_u =$	3484	kN		
170	Probable: $B_r = 3t d_b n F_u =$	4790	kN		
171					
172					

173 **Plug shear:**

174 $A_{gv} = (d_{edge} + 3pitch) \times (4t) =$ 16935 mm²

175 $T_r = \phi_u \left(0.6A_{gv} \frac{(F_y + F_u)}{2} \right) =$ 3029 kN

176 Probable: 4443 kN

178

179 **Block shear**

180 **Block shear path 1**

181 Net area in tension: $A_n = (d_{gauge} - d_{hole})t =$ 1991 mm²

182 Gross area in shear (in flange):

183 $A_{gv1} = (d_{edge} + 3pitch) \times (2t) =$ 8468 mm²

184 Resistance: $T_r = \phi_u \left(U_t A_n F_u + 0.6A_{gv} \frac{(F_y + F_u)}{2} \right) =$ 2187 kN

185 Probable: 3207 kN

187

188 **Block shear path 2**

189 Net area in tension: $A_n = (b - d_{gauge} - d_{hole})t =$ 2697 mm²

190 Gross area in shear: $A_{gv} = (d_{edge} + 3pitch) \times (2t) =$ 8468 mm²

192 Resistance:

193 $T_r = \phi_u \left(U_t A_n F_u + 0.6A_{gv} \frac{(F_y + F_u)}{2} \right) =$ 2425 kN

194 Probable: 3556 kN

196

197 **Weld design**

198 E49 Electrode $F_u =$ 490 MPa

199 Maximum weld size: $t_{gusset} =$ 19 mm $D_{max} =$ 17 mm

200 Minimum weld size: $t_{plate} =$ 16 mm $D_{min} =$ 8 mm

201 Choose D = 10 mm

202 Length must be $> 4D =$ 40 mm Choose 686 mm (27")

203 Or use 13.5" weld on both sides of the jaw plate

204 **Eccentric loading**

205 $e =$ 83 mm

206 Elastic bending shear flow:

207 $q_1 = 3Ve/L^2$ 1.618 kN/mm $D_1 \geq q_1/(1.5 * 0.156) =$ 6.92 mm

208 $q_{y2} = V/L =$ 1.120 kN/mm $D_2 \geq q_2/0.156 =$ 7.18 mm

209 $q_{max} = \sqrt{q_x^2 + q_y^2} =$ 1.968 kN/mm $D \geq \sqrt{D_1^2 + D_2^2} =$ 9.97 mm OK

211

212 **Weld metal fracture**

213 $V_r = 0.67\phi_w A_w X_u (1.00 + 0.5\sin^{1.5}\theta) M_w =$ 1067 kN For 2 welds: 2133 kN

214

215

216 **WEB PLATES**

217	A572-50 Grade steel:	$F_y = 345$ MPa	$F_u = 450$ MPa
218		$F_{yprob} = 380$ MPa	$F_{uprob} = 495$ MPa
219	Force in each of the web plate:	303	kN
220	Width of plate:	156 mm	(6.125") End: 38 mm
221	Required area: $A_{ne} = T_r / F_u \phi_u =$	898	mm ² *minimum plate thickness
222	Calculate thickness: $A_{ne} = (w_{pl} - 2d_{hole})t =$	8.836	mm Choose 9.5 mm plate
223	$T_r = \phi_u A_{ne} F_u =$	327	kN Exp: 479 kN

225 **Gross section yielding**

226	Design: $T_r = \phi A_g F_y =$	460	kN
227	Probable:	562	kN

229 **Bearing:**

230	Design: $B_r = 3\phi_{br} t d_b n F_u =$	1045	kN
231	Probable: $B_r = 3t d_b n F_u =$	1437	kN

233 **Plug shear:**

234	$A_{gv} = (d_{edge} + pitch) \times (4t) =$	4355	mm ²
235			
236	$T_r = \phi_u \left(0.6 A_{gv} \frac{(F_y + F_u)}{2} \right) =$	779	kN
237	Probable:	1142	kN

239 **Block shear**

240 **Block shear path 1**

241	$A_n = (d_{gauge} - d_{hole})t =$	469	mm ²
242	$A_{gv} = (d_{edge} + pitch) \times (2t) =$	2177	mm ²
243	$T_r = \phi_u \left(U_t A_n F_u + 0.6 A_{gv} \frac{(F_y + F_u)}{2} \right) =$	548	kN
244			
245	Probable:	803	kN

247 **Block shear path 2**

248	Net area in tension: $A_n = (b - d_{gauge} - d_{hole})t =$	499	mm ²
249	Gross area in shear: $A_{gv} = (d_{edge} + pitch) \times (2t) =$		
250		2177	mm ²
251	Resistance:		
252	$T_r = \phi_u \left(U_t A_n F_u + 0.6 A_{gv} \frac{(F_y + F_u)}{2} \right) =$	541	kN
253			
254	Probable:	794	kN

255
256
257
258

259 **GUSSET PLATES**

260 A572-50 Grade steel: $F_y = 345$ MPa $F_u = 450$ MPa
 261 $F_{yprob} = 380$ MPa $F_{uprob} = 495$ MPa
 262 Design force: 3679.66 kN Probable force: 4363.87 kN

263 Calculate Whitmore width:

264 $w = 2 \times L_{weld} \times \tan 30^\circ + 2t_{plate} + d_{beam} =$
 265 784 mm
 266 max: 686 mm

268 Choose thickness: 19 mm
 269 (3/4" plate)

270 **Compression resistance:**

271
 272 Buckling length: 303 mm
 273 Radius of Gyration: 5.50 mm
 274 K(conservative) 1
 275 $KL/r = 55$

276 $\lambda_y = \frac{KL}{r_y} \sqrt{\frac{F_y}{\pi^2 E}} =$
 277 0.728

278 $\lambda_{exp} = \frac{KL}{r_y} \sqrt{\frac{F_{yexp}}{\pi^2 E}} =$
 279 0.764

281 Design: $C_{ry} = \phi A F_y (1 + \lambda_y^{2n})^{-1/n} =$
 282 3110 kN

283 Probable:
 284 $C_{ry} = (A F_y) (1 + \lambda_y^{2n})^{-1/n} =$
 285 3689 kN

287 **Gross section yielding**

288 Design: $T_r = \phi A_g F_y = 4057$ kN
 289 Probable: $T_r = A_g F_y = 4958$ kN

291 **Net section**

292 Design: $T_r = \phi_u A_{ne} F_u = 4409$ kN
 293 Probable: $T_r = A_{ne} F_u = 6467$ kN

294 **Block shear**

295 $A_n = (d + t_{shims} + 2 \times t_{jaw}) \times t = 7508$ mm²

297 $A_{gv} = 4 \times L_{weld} \times t = 13064$ mm²

298 $T_r = \phi_u \left(U_t A_n F_u + 0.6 A_{gv} \frac{(F_y + F_u)}{2} \right) = 4871$ kN
 300 Probable: 7144 kN

1 **Connection design for specimens C360-T and C360-C (based on S16-14)**

3 **Factors (CSI S16-14)**

4 ϕ 0.90 ϕ_{bi} 0.80 Unfactored:
 5 ϕ_u 0.75 ϕ_{be} 0.75 ϕ 1.00
 6 ϕ_b 0.80 ϕ_{br} 0.80 R_y 1.1

Steel properties of W-shape brace

Nominal (MPa) **Probable (MPa)**
 F_y 345 F_u 450 F_y 385 F_u 495
 E 2E+05 Mpa G 77000 Mpa
 μ 0.3

8 **Bolt properties**

9 Bolt grade A490 Size 1 in
 10 V_{bolt} (kN) 252 (CSA Table 3-4)
 11 d_{bolt} (mm) 25 d_{hole} 27 *No 2 mm penalty following inspection of holes
 12 *Threads excluded

14 **Section Properties**

15 **W360x134**

Area	I_x	S_x	r_x	Z_x	I_y	S_y	r_y	Z_y	J
(mm ²)	(mm ⁴)	(mm ³)	(mm)	(mm ³)	(mm ⁴)	(mm ³)	(mm)	(mm ³)	(mm ⁴)
17100	4.2E+08	2330000	156	2560000	1.5E+08	817000	94	1240000	1680000

C_w	N. Mass	d	b	t	w	T	k	k_1	d-2t	Imperial Designation	Web class:	1
(mm ⁶)	(kg/m)	(mm)	(mm)		Flange class:	3						
4.3E+12	134	356	369	18	11	256	50	36	320	W14x90		

24 $A_w = 2816 \text{ mm}^2$ $A_f = 7142 \text{ mm}^2$

26 **Axial compression***

27 Length of the member and connections, L= 6.7 m OR 6667 mm
 28 K= 0.9

29 $\frac{KL}{r_x} = 38 < 200$ OK

31 $\frac{KL}{r_y} = 64 < 200$ OK

33 $\lambda_x = \frac{KL}{r_x} \sqrt{\frac{F_y}{\pi^2 E}} = 0.509$ Probable: 0.537

35 $\lambda_y = \frac{KL}{r_y} \sqrt{\frac{F_y}{\pi^2 E}} = 0.84$ GOVERNS 0.89 GOVERNS

40 n = 1.34 (W-shape)

41 *Connection design based on factored axial compression capacity for CC design.

43 **Compressive resistance:**

44 Design: $C_{ry} = \phi A F_y (1 + \lambda_y^{2n})^{-1/n} =$ 3680 kN

45 Probable: $C_{ry} = \frac{(A_w F_{yw} + A_f F_{yf})}{(1 + \lambda_y^{2n})^{-1/n}} =$ 4364 kN

47 Web and flange force deviation by area:

	Design	Probable
48 Flanges:	3074 kN	3645 kN
49 Web:	606 kN	719 kN

50

51 **Bolt design** (bolt design for shear failure - no oversized holes)

52 Number of bolts required in flanges: $C_{ry} / V_{bolt} =$ 12.20 bolts round up: 16 bolts

53 Number of bolts required in web: $C_{ry} / V_{bolt} =$ 1.20 bolts round up: 4 bolts

54 Therefore use 8 bolts per flange and 4 bolts on the web (in double shear - bearing governs)

55 Minimum centre-to-centre spacing: $2.7d_b$ 69 mm Choose: 76 mm (3")

56 Minimum edge distance (sheared edge): (Table 6 S16-14) 44 mm Choose: 38 mm (2")

57 Maximum edge distance: 150 mm OR $12t =$ 216 mm

58 Connection length: $L = 3spacing =$ 229 mm < 760 mm **OK**

59 Minimum edge distance (rolled edge) (S16-14 Table 6): 32 mm

60 Gauge distance (to accommodate gusset plate of 25.4 mm): 178 mm (7") 76 mm (web)

61 Check bearing of W-shape: $B_{r1} = 3\phi_b r t d_b n F_u$ 7900 kN (flanges)

62 $B_{r2} = 3\phi_b r t d_b n F_u$ 1207 kN (web)

63 $B_{rtotal} = B_{r1} + B_{r2}$ 9107 kN Ratio: 0.4 **OK**

64 Probable: $B_{r1exp} = 3t d_b n F_{uexp}$ 10863 kN (flanges)

65 $B_{r2exp} = 3\phi_b r t d_b n F_u$ 1660 kN (web)

66 $B_{rtotal} = B_{r1} + B_{r2}$ 12523 kN

67 Check bolt shear: Factor accounting for shims: $R_y =$ 0.899

68 A490 bolts F_u (S16-14 Table 3-3) = 1035 MPa Flanges Web

69 Design: $V_r = 0.60\phi_b n m A_b F_u =$ 4028 kN 1811 kN

70 Unfactored: $V_r = 1.11 \times 0.60 n m A_b F_u =$ 5588 kN 2513 kN

71

72 The next calculations are carried out for the purposes of predicting the failure mode at ultimate loading

73 **Gross section yielding and probable and post-buckling compression capacity**

74 Design (tension): $T_r = \phi A_g F_y =$ 5310 kN (S16-14 clause 27.5.3.4)

75 Probable (tension): $T_u = R_y A_g F_y =$ 6584 kN

76 Probable (compression): $C_u = \frac{1.2 C_r}{\phi} =$ 4906 kN **GOVERNS**

78 Post-buckling: $C_u' = 0.2 R_y F_y A_g =$ 1317 **GOVERNS**

79 $C_u' = C_r / \phi =$ 4364 kN

80

81 **Net section fracture** (checked at the last row of bolts)

82 $A_n: A_n = A_g - 4 \times d_{hole} \times t_f =$ 15157 mm²

83 No shear lag factor because web & flanges are connected

84 Design: $T_r = \phi_u A_{ne} F_u =$ 5115 kN

85 Probable: $T_{rexp} = A_{ne} F_{uexp} =$ 7503 kN

86

87 **Check failure mode in flanges**

88 **Block shear path 1 (flanges)**

89 Net area in tension: $A_n = (A - Tw)/2$
 90 $= (b - d_{gauge} + d_{hole})t = 3215 \text{ mm}^2$

92 Gross area in shear (in flange):

93 $A_{gv1} = (d_{edge} + 3pitch) \times (2t_f) = 9601 \text{ mm}^2$

94 $A_{gv2} = (d_{edge} + 3pitch) \times (w) = 2934 \text{ mm}^2$

95 Resistance: $T_r = 2\phi_u \left(U_t A_n F_u + 0.6 A_{gv} \frac{(F_y + F_u)}{2} \right) = 6654 \text{ kN}$

96 Probable: 9801 kN

98

99 **Block shear path 2 (flanges)**

100 Net area in tension: $A_n = (b - d_{gauge} - d_{hole})t = 2956 \text{ mm}^2$

101 Gross area in shear (in flange):

102 $A_{gv} = (d_{edge} + 3pitch) \times (2t_f) = 9601 \text{ mm}^2$

103 Resistance:

104 $T_r = 2\phi_u \left(U_t A_n F_u + 0.6 A_{gv} \frac{(F_y + F_u)}{2} \right) = 5230 \text{ kN}$

105 Probable: 7703 kN

107

108 **Block shear path 3 (flanges)**

109 Net area in tension: $A_n = \frac{(A - Tw - 4d_{hole}t)}{2} = 6170 \text{ mm}^2$

110 Gross area in shear (in flange):

111 $A_{gv} = (d_{edge} + 3pitch) \times (w) = 2934 \text{ mm}^2$

112 Resistance:

113 $T_r = 2\phi_u \left(U_t A_n F_u + 0.6 A_{gv} \frac{(F_y + F_u)}{2} \right) = 5215 \text{ kN}$

114 Probable: 7658 kN

116

117 **Plug shear in flanges**

118 $A_{gv} = (d_{edge} + 3pitch) \times (4t_f) = 19202 \text{ mm}^2$

119 $T_r = 2\phi_u \left(0.6 A_{gv} \frac{(F_y + F_u)}{2} \right) = 6870 \text{ kN}$

120 Probable: 10139 kN

121 **Flange failure mode: Block shear path 2** 5215 kN

123

124 **Check failure mode in web**

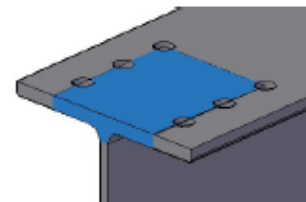
125 **Block shear path 1 (web)**

126 Net area in tension: $A_n = (d_{gauge} - d_{hole})w = 539 \text{ mm}^2$

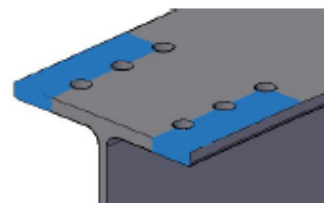
127 Gross area in shear (in flange):

128 $A_{gv} = (d_{edge} + pitch) \times (2w) = 2515 \text{ mm}^2$

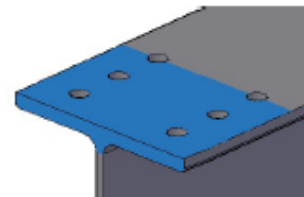
129



Block shear path 1



Block shear path 2



Block shear path 3

Probable:
7658 kN

130 Resistance:

131 $T_r = \phi_u \left(U_t A_n F_u + 0.6 A_{gv} \frac{(F_y + F_u)}{2} \right) =$ 632 kN

132 Probable: 931 kN

134

135 **Plug shear in web**

136 $A_{gv} = (d_{edge} + pitch) \times (4w) =$ 5029 mm²

137 $T_r = \phi_u \left(0.6 A_{gv} \frac{(F_y + F_u)}{2} \right) =$ 900 kN

138 Probable: 1328 kN

139

Probable:

141 **Web failure mode: Block Shear Path 1** 632 kN 931 kN

142

143 **Therefore total connection capacity = Flange block shear 3 + Web block shear 1 =**

144 5846 kN Ratio: 0.63 **OK**

145 Probable: 8588 kN Ratio: 0.51 **OK**

151

152 **CLAW ANGLE**

153 **Angle design**

154 A572-50 Grade steel: $F_y = 300$ MPa $F_u = 450$ MPa

155 $F_{yprob} = 330$ MPa $F_{uprob} = 495$ MPa

156 Force required in one angle: 768 kN

157 Bolt hole size: 29 *Because the edge of the punched hole were much more damaged

158 **L127x127x16**

Area	I_x	S_x	r_x	I_y	S_y	r_y	J	C_w
(mm ²)	(mm ⁴)	(mm ³)	(mm)	(mm ⁴)	(mm ³)	(mm)	(mm ⁴)	(mm ⁶)
3790	5660000	63300	38.7	5660000	63300	39	319000	3.8E+08

162

N. Mass	d	b	t	Imperial Designation
(kg/m)	(mm)	(mm)	(mm)	
29.7	127	127	16	L5x5x0.625

Gauge: 76 mm (3")
Vertical leg gauge: 76 mm (3")

166

167 **Gross section yielding**

168 Design: $T_r = \phi A_g F_y =$ 1023 kN

169 Probable: $T_r = A_g F_y =$ 1251 kN

170

171 **Net section fracture**

172 $U_t = 0.8$ (S-16 Cl. 12.3.3.2(b)(i))

173 $A_n: A_n = A_g - d_{hole} \times t =$ 3336 mm²

174 Design: $T_r = \phi_u A_n F_u =$ 901 kN

175 Probable: $T_r = A_n F_u =$ 1321 kN

176

178 **Bearing:**

179 Design: $B_r = 3\phi_{br}t d_b n F_u =$ 1742 kN

180 Probable: $B_r = 3t d_b n F_u =$ 2395 kN

181

182 **Plug shear:**

183 $A_{gv} = (d_{edge} + 3pitch) \times (2t) =$ 8468 mm²

184 $T_r = \phi_u \left(0.6A_{gv} \frac{(F_y + F_u)}{2} \right) =$ 1429 kN

186 Probable: 2096 kN

187

188 **Block shear**

189 $A_n = (b - d_{gauge(angles)} - d_{hole}/2) \times t =$ 580 mm²

190 $A_{gv} = (d_{edge} + 3pitch) \times (t) =$ 4234 mm²

191 $T_r = \phi_u \left(U_t A_n F_u + 0.6A_{gv} \frac{(F_y + F_u)}{2} \right) =$ 832 kN

193 Probable: 1220 kN

194

195 **WEB PLATE**

196 A572-50 Grade steel: $F_y = 345$ MPa $F_u = 450$ MPa

197 $F_{yprob} = 380$ MPa $F_{uprob} = 495$ MPa

198 Force in each of the web plate: 302.98 kN

199 Width of plate: 156 mm (6.125") Edge: 38 mm

200 Required area: $A_{ne} = T_r / F_u \phi_u =$ 898 mm² *minimum plate thickness

201 Calculate thickness: $A_{ne} = (w_{pl} - 2d_{hole})t =$ 8.836 mm Choose 9.5 mm plate

202 $T_r = \phi_u A_{ne} F_u =$ 327 kN Exp: 479 kN

203

204 **Gross section yielding**

205 Design: $T_r = \phi A_g F_y =$ 460 kN

206 Probable: 562 kN

207

208 **Bearing:**

209 Design: $B_r = 3\phi_{br}t d_b n F_u =$ 1045 kN

210 Probable: $B_r = 3t d_b n F_u =$ 1437 kN

211

212 **Plug shear:**

213 $A_{gv} = (d_{edge} + pitch) \times (4t) =$ 4355 mm²

214 $T_r = \phi_u \left(0.6A_{gv} \frac{(F_y + F_u)}{2} \right) =$ 779 kN

216 Probable: 1142 kN

217

218

219

220

221 **Block shear**

222 **Block shear path 1**

223 $A_n = (d_{gauge} - d_{hole})t =$ 467 mm²

224 $A_{gv} = (d_{end} + pitch) \times (2t) =$ 2177 mm²

225 $T_r = \phi_u \left(U_t A_n F_u + 0.6 A_{gv} \frac{(F_y + F_u)}{2} \right) =$

226 510 kN

227 Probable: 802

228

229 **Block shear path 2**

230 Net area in tension: $A_n = (b - d_{gauge} - d_{hole})t =$ 501 mm²

231 Gross area in shear: $A_{gv} = (d_{edge} + pitch) \times (2t) =$

232 2177 mm²

233 Resistance:

234 $T_r = \phi_u \left(U_t A_n F_u + 0.6 A_{gv} \frac{(F_y + F_u)}{2} \right) =$

235 542 kN

236 Probable: 794 kN

237

238 **GUSSET PLATE**

239 A572-50 Grade steel:	$F_y =$ 345 MPa	$F_u =$ 450 MPa
240	$F_{yprob} =$ 380 MPa	$F_{uprob} =$ 495 MPa
241 Design force:	3680 kN	Probable force: 4364 kN

242

243 Calculate Whitmore width:

244 w

245 $= 2(3spacing) \times \tan 30^\circ$

246 $+ 2gauge_{angle} + d_{beam} =$ 772 mm

247 max: 686 mm

248 Choose thickness: 25 mm

249 (1" plate)

250 **Compression resistance**

251

252 Buckling length: 255 mm

253 Radius of Gyration: 7.3 mm

254 k (conservative) 1

255 $KL/r =$ 35

256 $\lambda_y = \frac{KL}{r_y} \sqrt{\frac{F_y}{\pi^2 E}} =$ 0.460

258 $\lambda_{exp} = \frac{KL}{r_y} \sqrt{\frac{F_{yexp}}{\pi^2 E}} =$ 0.482

261 Design: C_{ry}

262 $= \phi A F_y (1 + \lambda_y^{2n})^{-1/n} =$ 4953 kN

263

264 Probable:

265 $C_{ry} = (AF_y)$

266 $(1 + \lambda_y^{2n})^{-1/n} = 5987 \text{ kN}$

267

268 **Bearing:** N. Bolts angles: 8 web: 4

269 $B_{r1} = 3\phi_{br}t d_b n F_u = 8361 \text{ kN}$

270 $B_{r1exp} = 3 \times 11497 \text{ kN}$

271 $t d_b n F_u$

272 **Gross section yielding**

273 Design: $T_r = \phi A_g F_y = 5407 \text{ kN}$

274 Probable: $T_r = A_g F_y = 6609 \text{ kN}$

275

276 **Net section**

277 Design: $T_r = \phi_u A_n F_u = 4952 \text{ kN}$

278 Probable: $T_r = A_n F_u = 7263 \text{ kN}$

279

280 **Block shear**

281 $A_n = (d_{beam} + 2gauge_{angle} - d_{hole}) \times t = 12228 \text{ mm}^2$

282 $A_{gv} = (d_{edge} + 3pitch) \times (2t) = 13548 \text{ mm}^2$

283 $T_r = \phi_u \left(U_t A_n F_u + 0.6 A_{gv} \frac{(F_y + F_u)}{2} \right) = 6550 \text{ kN}$

284 Probable: 9607 kN

285

286

287 **Block shear path 2**

288 $A_n = (w_g - (d_{beam} + 2gauge_{angle} + d_{hole})) \times t = 3815 \text{ mm}^2$

289 $A_{gv} = (d_{edge} + 3pitch) \times (2t) = 13548 \text{ mm}^2$

290 $T_r = \phi_u \left(U_t A_n F_u + 0.6 A_{gv} \frac{(F_y + F_u)}{2} \right) = 3582 \text{ kN}$

291 Probable: 5254 kN

292

293 **With web block shear:**

294 $A_n = (d_{gauge} - d_{hole})t = 1245 \text{ mm}^2$

295 $A_{gv} = (d_{edge} + pitch) \times (2t) = 5806 \text{ mm}^2$

296 $T_r = \phi_u \left(U_t A_n F_u + 0.6 A_{gv} \frac{(F_y + F_u)}{2} \right) = 1459 \text{ kN}$

297 Probable: 2140 kN

298

299 Totals:

300 Design: 5041 kN

301 Probable: 7394 kN

302

303 **Plug shear**

304 $A_{gv} = (2d_{edge} + 4pitch) \times (4w) = 38710 \text{ mm}^2$

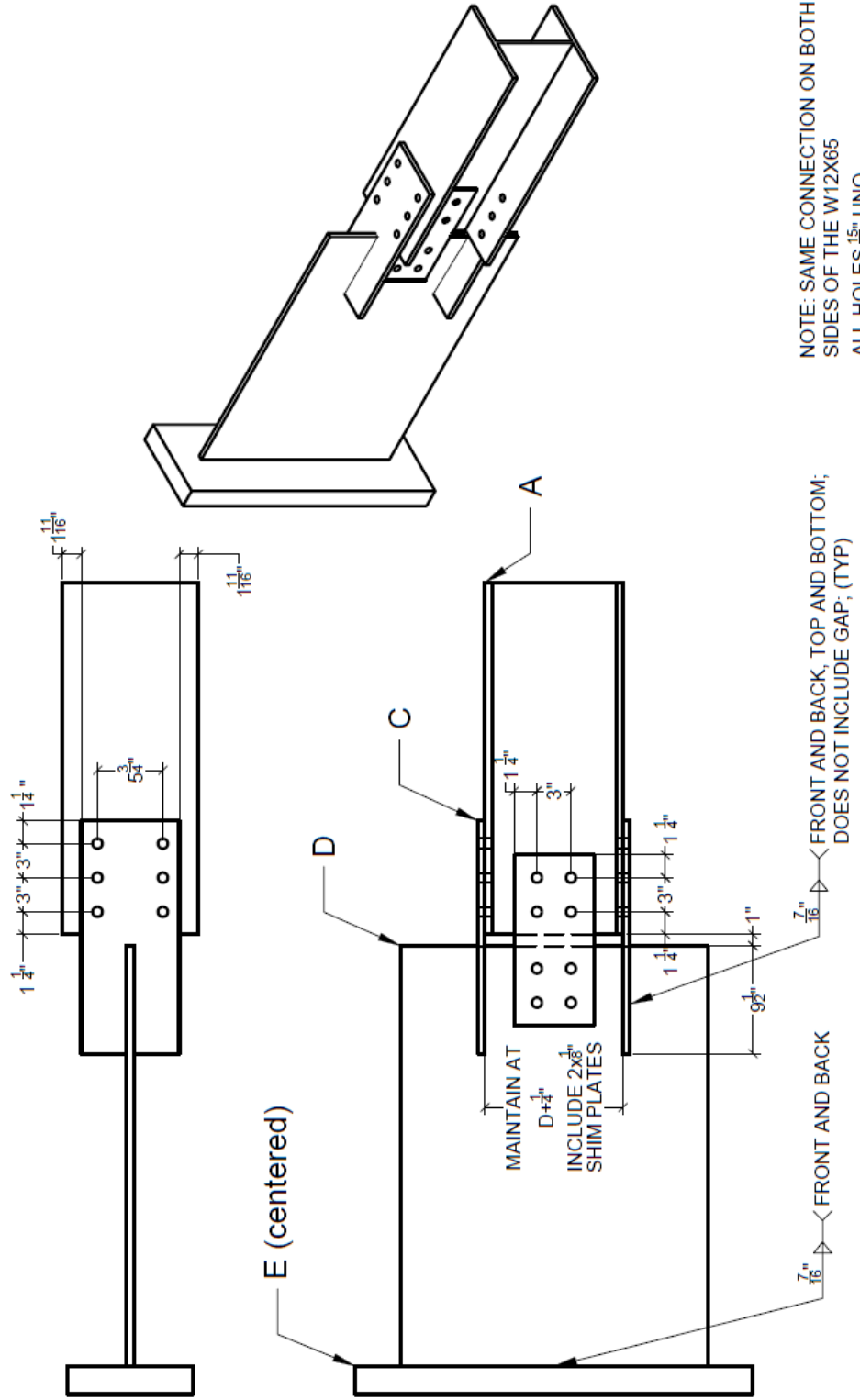
305 $T_r = \phi_u \left(0.6 A_{gv} \frac{(F_y + F_u)}{2} \right) = 6924 \text{ kN}$

306 Probable: 10155 kN

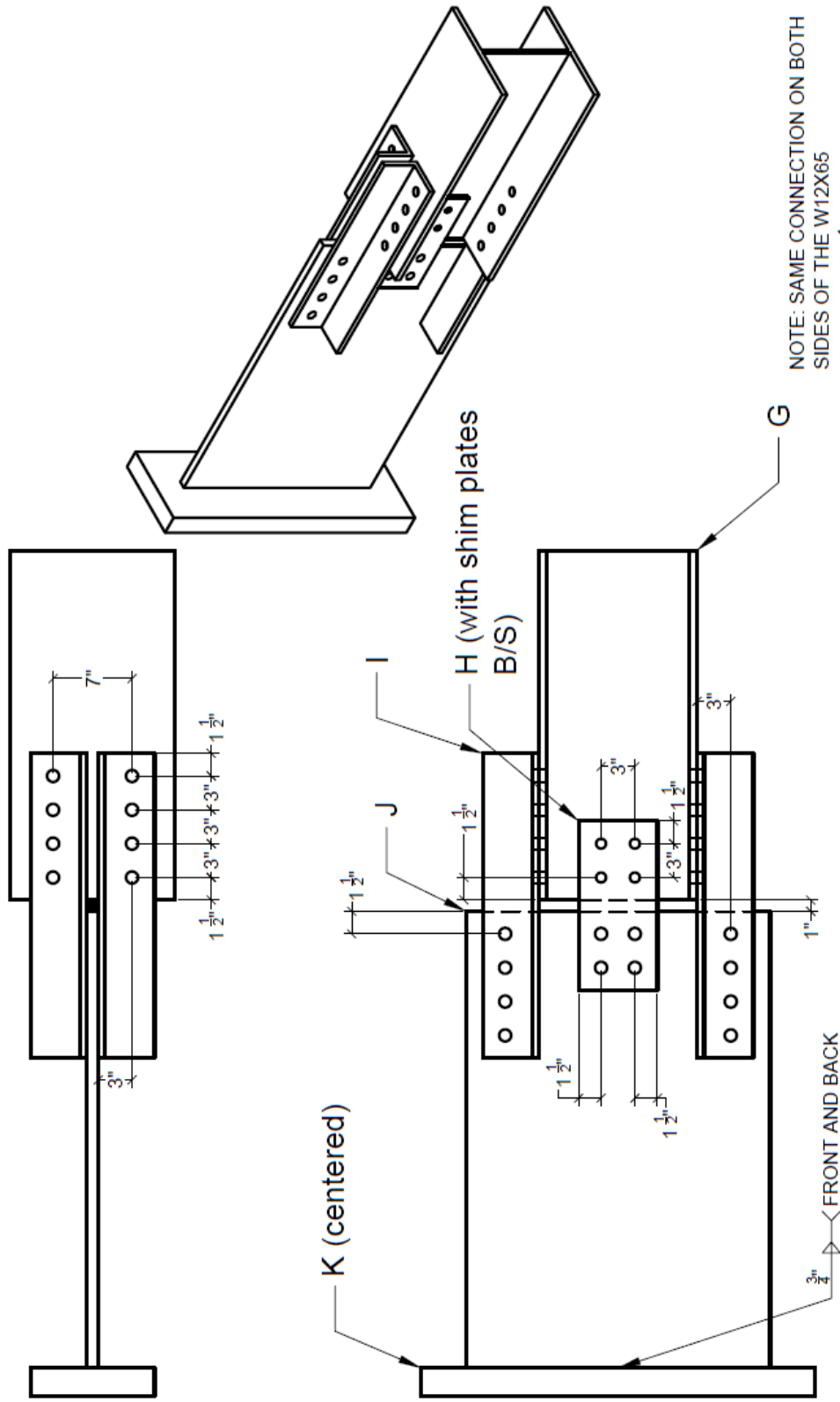
307

APPENDIX B: SPECIMEN SHOP DRAWINGS

LIST OF PARTS - SPECIMENS J310-T AND J310-C				
LABEL	TYPE	QTY	GRADE	DETAILS
A	W12x65	2	A992-50	LENGTH: 17'-6"
B	PL 12x5.5x0.375	8	A572-50	WEB PLATES
C	PL 19x8.625x0.625	8	A572-50	JAW PLATES
D	PL 29.25x27x0.625	4	A572-50	GUSSET PLATES
E	PL 35x11x2.5	4	A572-50	
NA	7/8" BOLT ASSEMBLIES	96	A325	VARIED LENGTHS



LIST OF PARTS - SPECIMENS C360-T AND C360-C					
LABEL	TYPE	QTY	GRADE	DETAILS	
G	W14x90	2	A992-50	LENGTH: 15' 9 1/2"	
H	PL 13x6.125x0.375	8	A992-44	WEB PLATES	
I	L5x5x0.625	16	A572-50	ANGLES, LENGTH: 27"	
J	PL 40.5x27x1	4	A572-50	GUSSET PLATES	
K	PL 35x11x2.5	4	A572-50		
NA	1" BOLT ASSEMBLIES	164	A490	VARIED LENGTHS	



NOTE: SAME CONNECTION ON BOTH SIDES OF THE W12X65 ALL HOLES 1 1/16" UNO

APPENDIX C: TABLES OF CALCULATED CAPACITIES

Table C-1 Calculated capacities of J310-T and J310-C (CSA S16-14)

Failure mode		J310-T				J310-C			
		Design ¹	Probable ²	Top ³	Bottom ³	Design ¹	Probable ²	Top ³	Bottom ³
Whole W-shape	Cr	2209	2582	2518	2518	2209	2582	2517	
	Tr (gross)	3819	4736	4273	4273	3819	4736	4268	4268
	Tr (net)	3656	5362	4842	4852	3656	5362	4825	4815
	Tu	4736	4736	4736	4736	4736	4736	4736	4736
	Cu	2945	2945	2945	2945	2945	2945	2945	2945
	Cu'	947	947	947	947	947	947	947	947
Flanges W-shape	Vr	1844	2350	2350	2350	1844	2350	2350	2350
	Br	4436	6099	5201	5118	4436	6099	5310	5377
	BS1	4151	6113	5425	5432	4151	6113	5440	5247
	BS2	3293	4849	4098	4041	3293	4849	4190	4083
	BS3	3527	5178	4595	4612	3527	5178	4598	4548
	PS	4058	5989	5100	5031	4058	5989	5209	4961
Web W-shape	Vr	1229	1567	1567	1567	1229	1567	1567	1567
	Br	951	1307	1201	1204	951	1307	1114	1114
	BS	557	821	807	810	557	821	746	695
	PS	765	1129	1112	1117	765	1129	1029	923
Web Plates	Tr (gross)	826	1010	1151	1161	826	1010	1148	1104
	Tr (net)	592	868	897	906	592	868	894	858
	Br	1829	2515	2574	2596	1829	2515	2568	2481
	BS1	1073	1573	1646	1653	1073	1573	1633	1581
	BS2	965	1416	1491	1497	965	1416	1479	1426
	PS	1471	2158	2280	2284	1471	2158	2256	2186
Jaw Plates	Tr (gross)	2160	2640	2889	2893	2160	2640	2876	2869
	Tr (net bolts)	1837	2695	2743	2748	1837	2695	2731	2718
	Tr (net slot)	2145	3146	3197	3199	2145	3146	3181	3171
	Br	4573	6287	6390	6389	4573	6287	6376	6363
	BS1	3402	4989	5200	4821	3402	4989	5195	5206
	BS2	2619	3841	4022	4400	2619	3841	4009	4025
	Welds	2402	3585	5904	5989	2402	3585	6804	6186
	PS	4183	6136	6479	6473	4183	6136	6473	6513
Gusset	Cr	2824	3418	3463	3469	2824	3418	3471	3519
	Tr (gross)	3048	3725	3802	3806	3048	3725	3815	3848
	Tr (net)	3313	4859	4641	4646	3313	4859	4657	4697
	BS	3225	4730	4584	4590	2911	4269	3960	3986
	PS	3318	4866	5057	5097	3318	4866	5047	5091

Compression failure mode Lowest failure mode capacity in component

If the lowest capacity is gross section yielding, the second lowest capacity becomes the failure mode

BOLD The tension failure modes for the specimen are bolded

1. Factored capacities with design equations, design geometry, and nominal properties
2. Unfactored capacities with design equations, design geometry, and probable properties
3. Unfactored capacities with design equations and measured geometry and material properties from the top or bottom connections of the specimen

Table C-3 Calculated capacities of C360-T and C360-C (CSA S16-14)

Failure mode		C360-T				C360-C			
		Design ¹	Probable ²	Top ³	Bottom ³	Design ¹	Probable ²	Top ³	Bottom ³
Whole W-shape	Cr	3680	4364	4474	4474	3680	4364	4474	4474
	Tr (gross)	5310	6584	6199	6198	5310	6584	6200	6199
	Tr (net)	5115	7503	7480	7473	5115	7503	7477	7473
	Tu	6584	6584	6584	6584	6584	6584	6584	6584
	Cu	4906	4906	4906	4906	4906	4906	4906	4906
	Cu'	1317	1317	1317	1317	1317	1317	1317	1317
Flanges W-shape	Vr	4028	5588	5588	5588	4028	5588	5588	5588
	Br	7900	10863	10217	10286	7900	10863	10254	10274
	BS1	6654	9801	9390	9336	6654	9801	9373	9320
	BS2	5230	7703	7185	7198	5230	7703	7226	7194
	BS3	5215	7658	7432	7402	5215	7658	7416	7389
	PS	6870	10139	9418	9409	6870	10139	9460	9402
Web W-shape	Vr	1811	2513	2521	2522	1811	2513	2519	2520
	Br	1207	1660	1678	1659	1207	1660	1702	1652
	BS	632	932	960	932	632	932	981	932
	PS	900	1328	1386	1342	900	1328	1415	1344
Web Plates	Tr (gross)	920	1125	1268	1261	920	1125	1257	1258
	Tr (net)	653	958	987	978	653	958	975	975
	Br	2090	2874	2922	2922	2090	2874	2917	2918
	BS1	1095	1607	1672	1673	1095	1607	1674	1667
	BS2	1082	1587	1652	1644	1082	1587	1644	1639
	PS	1558	2285	2388	2388	1558	2285	2393	2380
Angles	Tr (gross)	4093	5003	5288	5246	4093	5003	5275	5235
	Tr (net)	3603	5285	5355	5312	3603	5285	5340	5298
	Br	6968	9581	9703	9628	6968	9581	9692	9602
	BS	3327	4880	5032	5010	3327	4880	5016	5000
	PS	5716	8383	8673	8633	5716	8383	8660	8621
Gusset	Cr	4955	5989	6060	6199	4955	5989	6153	6049
	Tr (gross)	5409	6611	6697	6825	5409	6611	6780	6712
	Tr (net)	4954	7265	7817	7985	4954	7265	7920	7847
	Br	8361	11497	12362	12573	8361	11497	12487	12394
	BS1	6550	9607	10342	10472	6550	9607	10427	10283
	BS2	5044	7398	7829	7962	5044	7398	7907	7729
	PS	6924	10155	10761	10859	6924	10155	10823	10558

Compression failure mode Lowest failure mode capacity in component

If the lowest capacity is gross section yielding, the second lowest capacity becomes the failure mode

BOLD The tension failure modes for the specimen are bolded

1. Factored capacities with design equations, design geometry, and nominal properties
2. Unfactored capacities with design equations, design geometry, and probable properties or bottom connections of the specimen

Table C-4 Calculated capacities of J310-T and J310-C (AISC 360-16)

Failure mode		J310-T				J310-C			
		Design ¹	Probable ²	Top ³	Bottom ³	Design ¹	Probable ²	Top ³	Bottom ³
Whole W-shape	Cr	2449	2885	2785	2785	2449	2885	2783	2783
	Tr (gross)	3819	4736	4273	4273	3819	4736	4268	4268
	Tr (net)	3656	5362	4842	4852	3656	5362	4825	4815
	Tu	4736	4736	4736	4736	4736	4736	4736	4736
	Cu	3264	3264	3264	3264	3264	3264	3264	3264
Flanges W-shape	Vr	1638	2129	2129	2129	1638	2129	2129	2129
	Br	4159	6099	5201	5118	4159	6099	5310	5377
	BS1	3762	5518	4930	4948	3762	5518	4925	4698
	BS2	2285	3370	2838	2798	2285	3370	2904	2868
	BS3	3440	5058	4481	4497	3440	5058	4492	4448
	PS	3109	4560	3881	3832	3109	4560	3967	3663
Web W-shape	Vr	1092	1419	1419	1419	1092	1419	1419	1419
	Br	891	1307	1286	1289	891	1307	1193	1193
	BS	512	758	747	749	512	758	690	646
	PS	579	850	836	840	579	850	772	653
Web Plates	Tr (gross)	826	1010	1151	1161	826	1010	1148	1104
	Tr (net)	592	868	897	906	592	868	894	858
	Br	1715	2515	2574	2596	1715	2515	2568	2481
	BS1	894	1311	1326	1330	894	1311	1312	1272
	BS2	812	1192	1210	1214	812	1192	1197	1154
	PS	1277	1873	1915	1916	1277	1873	1891	1833
Jaw Plates	Tr (gross)	2160	2640	2889	2893	2160	2640	2876	2869
	Tr (net bolts)	1803	2645	2743	2748	1803	2645	2731	2718
	Tr (net slot)	2145	3146	3197	3199	2145	3146	3181	3171
	Br	4287	6287	6390	6389	4287	6287	6376	6363
	BS1	2844	4172	4378	3998	2844	4172	4378	4383
	BS2	2062	3024	3200	3577	2062	3024	3192	3203
	PS	3103	4551	4835	4827	3103	4551	4839	4868
Gusset	Cr	2815	3414	3464	3470	2815	3414	3473	3517
	Tr (gross)	3048	3725	3802	3806	3048	3725	3815	3848
	Tr (net)	3313	4859	4641	4646	3313	4859	4657	4697
	BS	3274	4802	4334	4311	3274	4802	4330	4359
Compression failure mode				Lowest failure mode capacity in component					
If the lowest capacity is gross section yielding, the second lowest capacity becomes the failure mode									

BOLD The tension failure modes for the specimen are bolded

1. Factored capacities with design equations, design geometry, and nominal properties
2. Unfactored capacities with design equations, design geometry, and probable properties
3. Unfactored capacities with design equations and measured geometry and material properties from the top or bottom connections of the specimen

Table C-5 Calculated capacities of J360-T and J360-C (AISC 360-16)

Failure mode		J360-T				J360-C			
		Design ¹	Probable ²	Top ³	Bottom ³	Design ¹	Probable ²	Top ³	Bottom ³
Whole W-shape	Cr	3941	4721	4594	4595	3941	4721	4595	4596
	Tr (gross)	5310	6584	6183	6185	5310	6584	6184	6186
	Tr (net)	5115	7503	7516	7500	5115	7503	7524	7521
	Tu	6584	6584	6584	6584	6584	6584	6584	6584
	Cu	5330	5330	5330	5330	5330	5330	5330	5330
Flanges W-shape	Vr	3521	5023	4996	4996	3521	5023	4996	4996
	Br	7407	10863	10350	10513	7407	10863	10301	10337
	BS1	5561	8156	8044	7979	5561	8156	8017	7972
	BS2	3794	5597	5186	5253	3794	5597	5189	5194
	BS3	5076	7464	7277	7239	5076	7464	7263	7241
	PS	5023	7366	7140	7177	5023	7366	7149	7103
Web W-shape	Vr	1760	2511	2511	2511	1760	2511	2511	2511
	Br	1132	1660	1660	1687	1132	1660	1649	1703
	BS	579	857	873	877	579	857	864	888
	PS	658	965	1005	994	658	965	1011	1016
Web Plates	Tr (gross)	920	1125	1268	1239	920	1125	1264	1258
	Tr (net)	653	958	984	965	653	958	982	976
	Br	1960	2874	2938	2861	1960	2874	2924	2916
	BS1	886	1299	1326	1280	886	1299	1321	1313
	BS2	906	1329	1347	1304	906	1329	1340	1333
	PS	1347	1976	1995	1918	1347	1976	1983	1975
Jaw Plates	Tr (gross)	3443	4208	4607	4588	3443	4208	4598	4459
	Tr (net bolts)	3164	4641	4725	4691	3164	4641	4715	4564
	Tr (net slot)	3506	5142	5220	5196	3506	5142	5211	5052
	Br	6532	9581	9739	9702	6532	9581	9718	9436
	BS1	3559	5219	5350	5320	3559	5219	5331	5193
	BS2	4035	5918	6044	6014	4035	5918	6026	5878
	BP Welds	NA	NA	NA	NA	NA	NA	NA	NA
	PS	4430	6497	6668	6642	4430	6497	6643	6507
Gusset	Cr	3249	3883	4264	4303	3249	3883	4242	4255
	Tr (gross)	4057	4958	5275	5315	4057	4958	5256	5268
	Tr (net)	4409	6467	6231	6279	4409	6467	6209	6223
	BS	5496	8061	7092	6900	5496	8061	7124	6883

Compression failure mode
 If the lowest capacity is gross section yielding, the second lowest capacity becomes the failure mode

BOLD The tension failure modes for the specimen are bolded

1. Factored capacities with design equations, design geometry, and nominal properties
2. Unfactored capacities with design equations, design geometry, and probable properties
3. Unfactored capacities with design equations and measured geometry and material properties from the top or bottom connections of the specimen

Table C-6 Calculated capacities of C360-T and C360-C (AISC 360-16)

Failure mode		C360-T				C360-C			
		Design ¹	Probable ²	Top ³	Bottom ³	Design ¹	Probable ²	Top ³	Bottom ³
Whole W-shape	Cr	3941	4721	4745	4745	3941	4721	4746	4745
	Tr (gross)	5310	6584	6199	6198	5310	6584	6200	6199
	Tr (net)	5115	7503	7480	7473	5115	7503	7477	7473
	Tu	6584	6584	6584	6584	6584	6584	6584	6584
	Cu	5330	5330	5330	5330	5330	5330	5330	5330
Flanges W-shape	Vr	3521	5023	5023	5023	3521	5023	5023	5023
	Br	7407	10863	10217	10286	7407	10863	10254	10274
	BS1	5869	8608	8442	8369	5869	8608	8424	8353
	BS2	3486	5144	4744	4762	3486	5144	4776	4760
	BS3	5076	7464	7218	7192	5076	7464	7199	7180
	PS	5023	7366	7095	7056	5023	7366	7129	7049
Web W-shape	Vr	1751	2498	2501	2502	1751	2498	2501	2501
	Br	1132	1660	1695	1676	1132	1660	1720	1669
	BS	579	857	874	850	579	857	894	850
	PS	658	965	1037	992	658	965	1062	997
Web Plates	Tr (gross)	920	1125	1268	1261	920	1125	1257	1258
	Tr (net)	653	958	987	978	653	958	975	975
	Br	1960	2874	2922	2922	1960	2874	2917	2918
	BS1	886	1299	1313	1314	886	1299	1316	1307
	BS2	906	1329	1343	1335	906	1329	1336	1329
	PS	1347	1976	1974	1975	1347	1976	1981	1966
Angles	Tr (gross)	4093	5003	5288	5246	4093	5003	5275	5235
	Tr (net)	3603	5285	5355	5312	3603	5285	5340	5298
	Br	7043	10329	10463	10392	7043	10329	10440	10368
	BS	2926	4291	4369	4347	2926	4291	4337	4332
	PS	7145	10479	10693	10650	7145	10479	10642	10625
Gusset	Cr	4951	5998	6071	6205	4951	5998	6160	6065
	Tr (gross)	5409	6611	6697	6825	5409	6611	6780	6712
	Tr (net)	4954	7265	7817	7985	4954	7265	7920	7847
	Br	7839	11497	12362	12573	7839	11497	12487	12394
	BS1	5885	8632	9406	9527	5885	8632	9480	9340
	BS2	5505	8074	8645	8851	5505	8074	8756	8541
	PS	5062	7425	8125	8219	5062	7425	8168	7966

Compression failure mode Lowest failure mode capacity in component
 If the lowest capacity is gross section yielding, the second lowest capacity becomes the failure mode

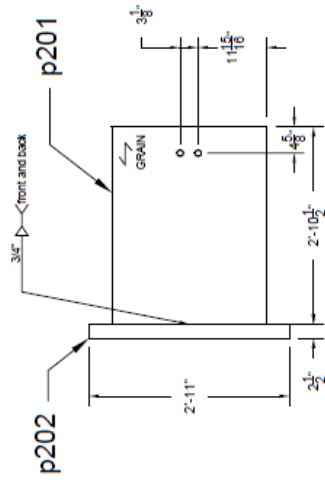
BOLD The tension failure modes for the specimen are bolded

1. Factored capacities with design equations, design geometry, and nominal properties
2. Unfactored capacities with design equations, design geometry, and probable properties
3. Unfactored capacities with design equations and measured geometry and material properties from the top or bottom connections of the specimen

**APPENDIX D: SHOP DRAWINGS OF MODIFIED BEARING PLATE
SPECIMENS**

GUSSET ASSEMBLY

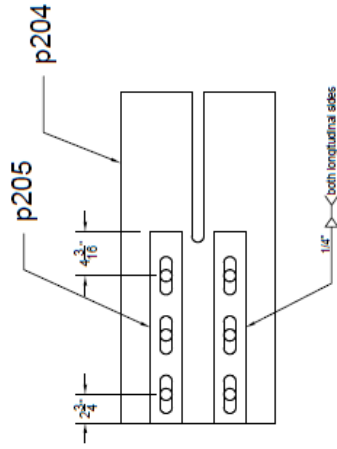
p203



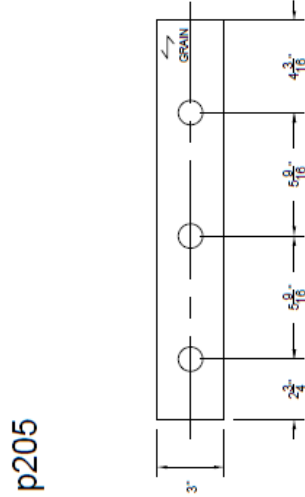
SPECIMEN P2J14X90

LABEL QTY	DESCRIPTION	LENGTH	GRADE
p201	PL1X27	2'-10 1/2"	A572 GR.50
p202	PL2 1/2X11	2'-11"	A572 GR.50
p203	PL3/8X6 7/8	1'-4 1/4"	A572 GR.50
p204	PL5/8X14	2'-7 1/16"	A572 GR.50
p205	PL3/8X3	1'-6"	A572 GR.50
B21	W14X90	16'-7 5/8"	A992 GR.50
NA	36 1 1/8" BOLT ASSEMBLIES	4"	A490

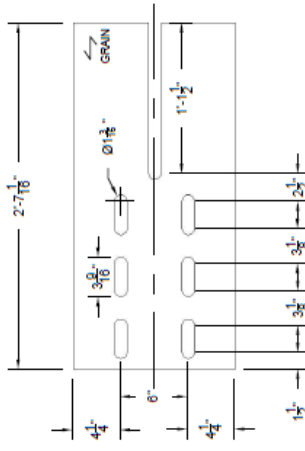
FUSE PLATE ASSEMBLY



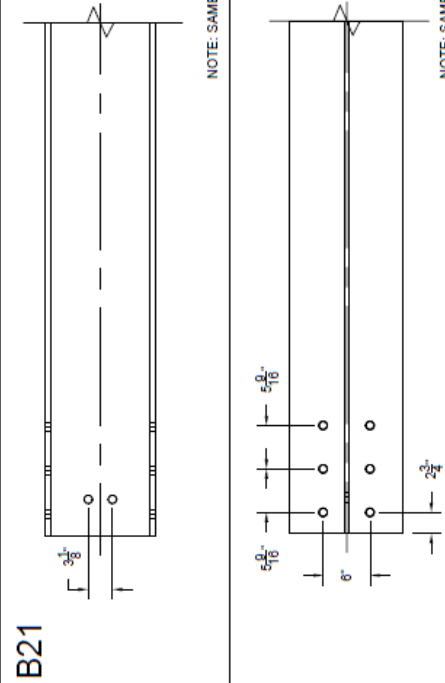
p205



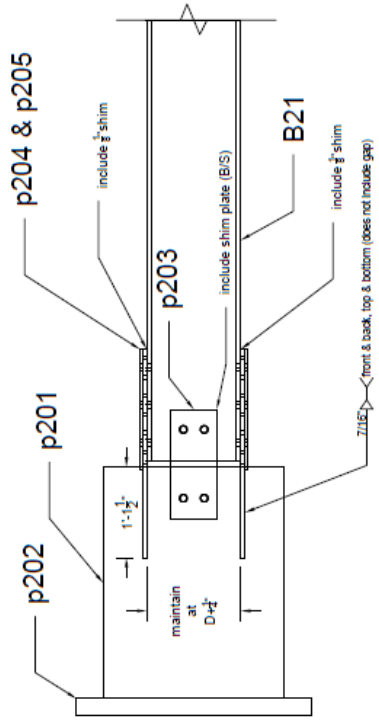
p204



B21



CONNECTION ASSEMBLY

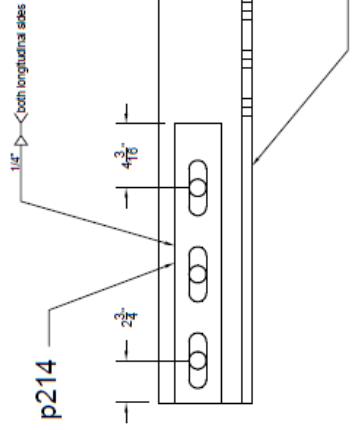


SPECIMEN P2A14X90

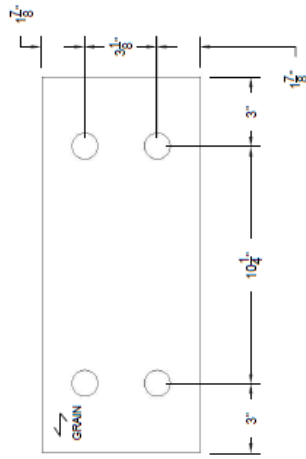
LABEL	QTY	DESCRIPTION	LENGTH	GRADE
p211	2	PL1 1/4X27	3'- 5 5/8"	A572 GR.50
p212	2	PL2 1/2X11	2'-11"	A572 GR.50
p213	4	PL3/8X6 7/8	1'-4 1/4"	A572 GR.50
a211	8	L6X6X5/8	2'-6 9/16"	A572 GR.44
p214	8	PL3/8X3	1'-6"	A572 GR.50
B22	1	W14X90	15'-5 5/16"	A992 GR.50
NA	54	1 1/8" BOLT ASSEMBLIES	44X4", 10X4 1/4"	A490

1 3/16" Ø HOLES UNO

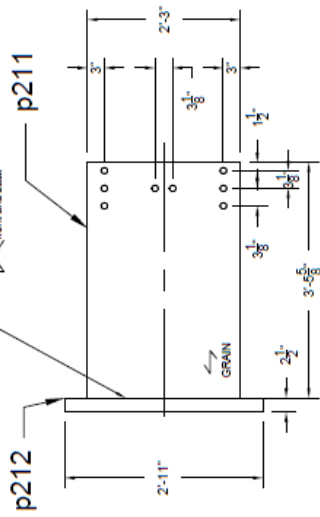
FUSE PLATE ASSEMBLY



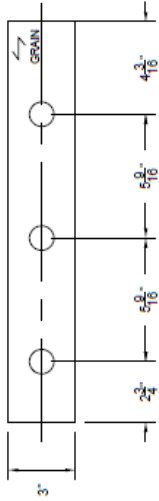
p213



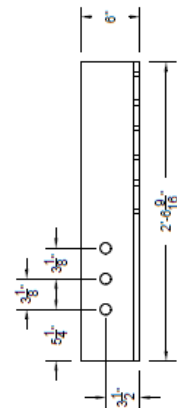
GUSSET ASSEMBLY



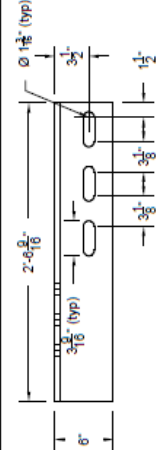
p215



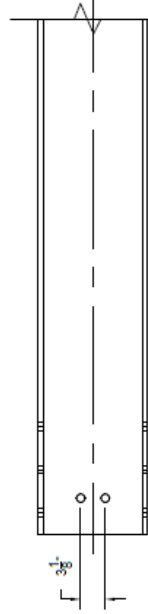
a211



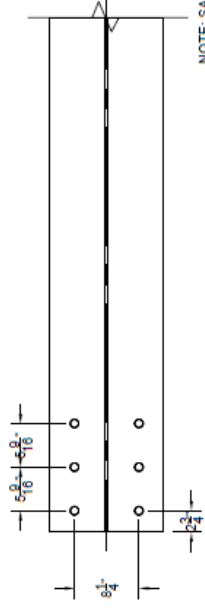
a211



B22

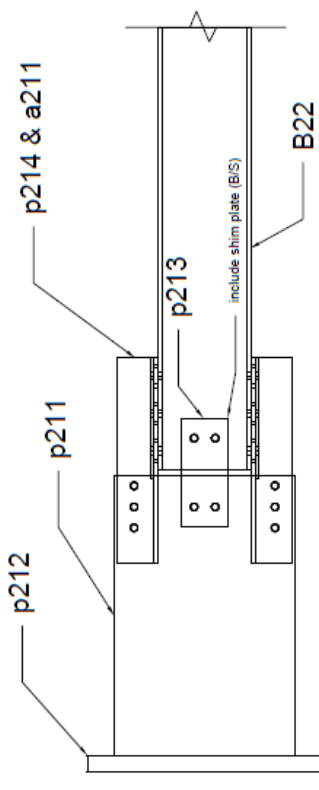


NOTE: SAME AT BOTH ENDS

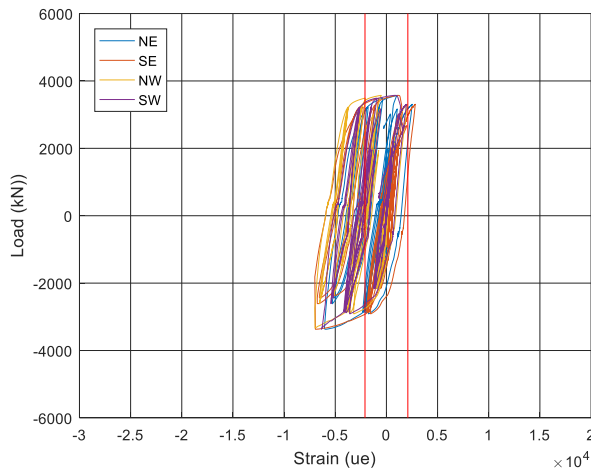


NOTE: SAME AT BOTH ENDS

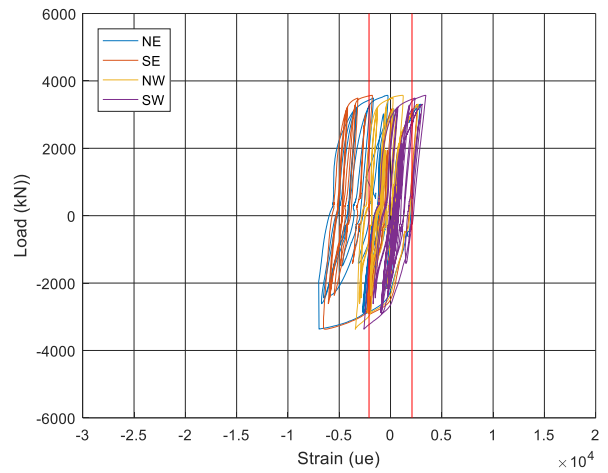
CONNECTION ASSEMBLY



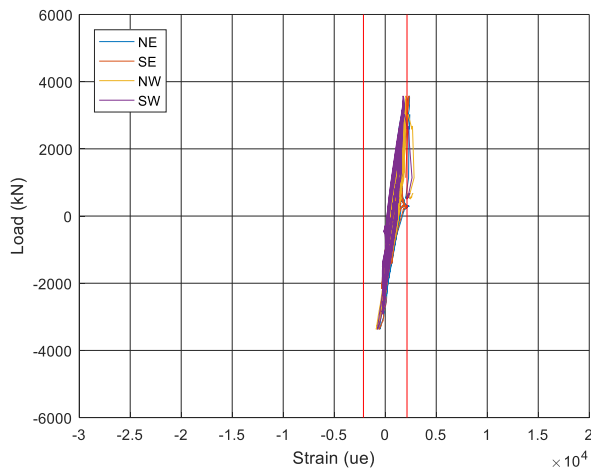
**APPENDIX E: FORCE-STRAIN HYSTERESIS OF STRAIN GAUGES IN
CONNECTIONS**



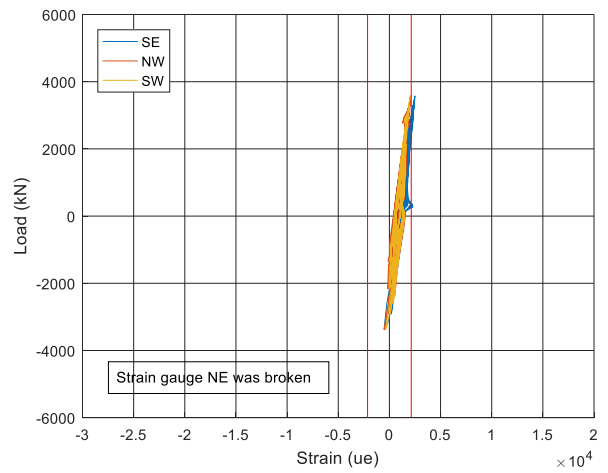
(a)



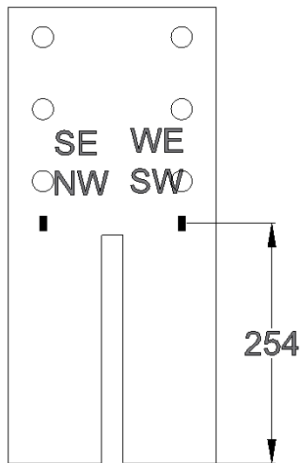
(b)



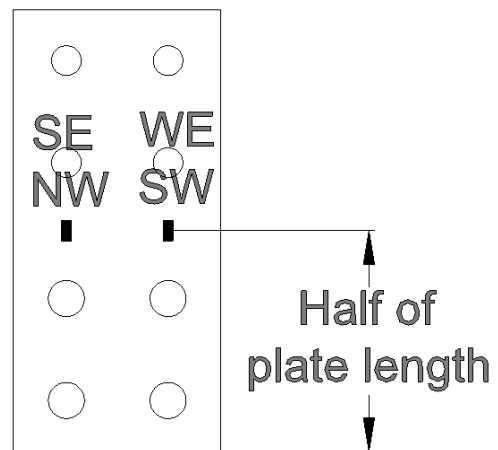
(c)



(d)

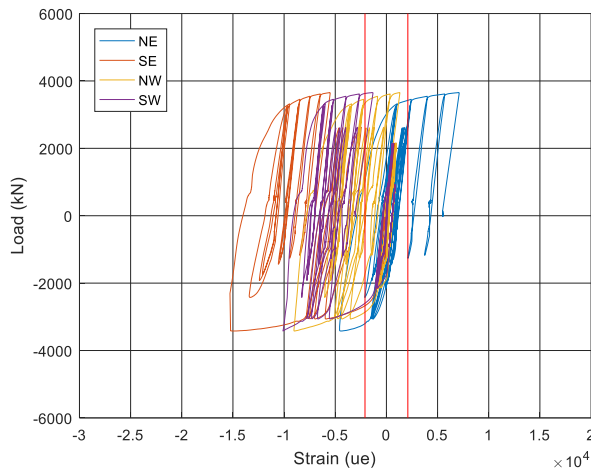


(e)

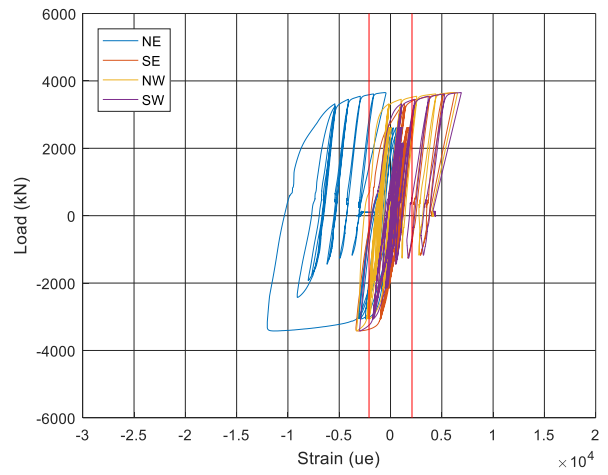


(f)

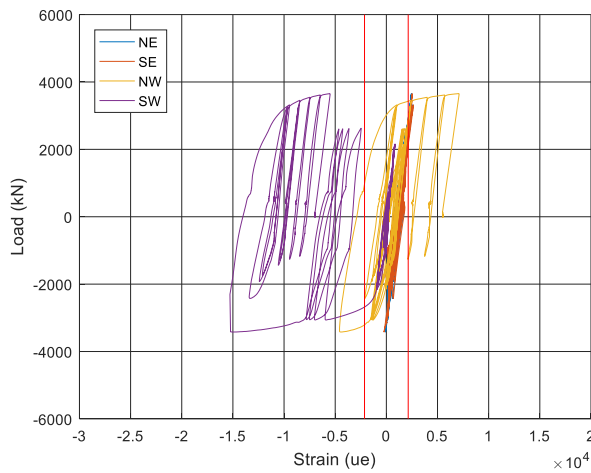
Figure E-1 Force-displacement hysteresses for strain gauges in connections of specimen J310-T (a) Bottom jaw plates (b) Top jaw plates (c) Bottom web plates (d) Top web plates (e) Location of strain gauges on jaw plates (dimension in mm) (f) Location of strain gauges on web plates



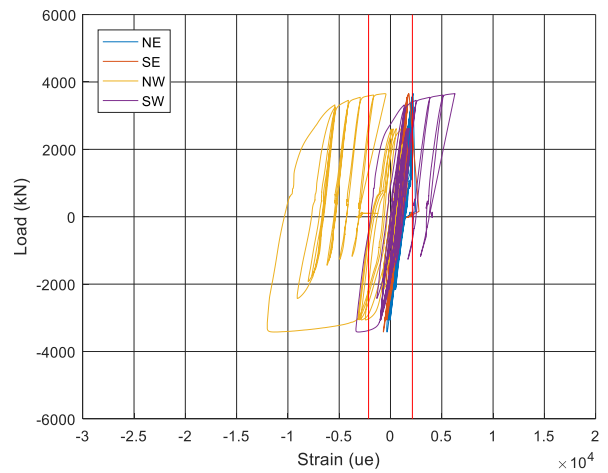
(a)



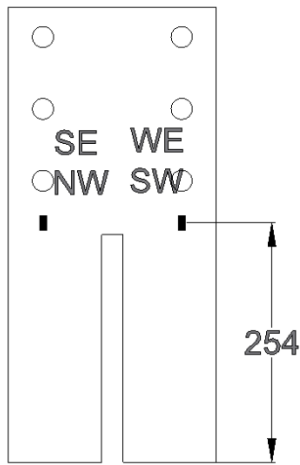
(b)



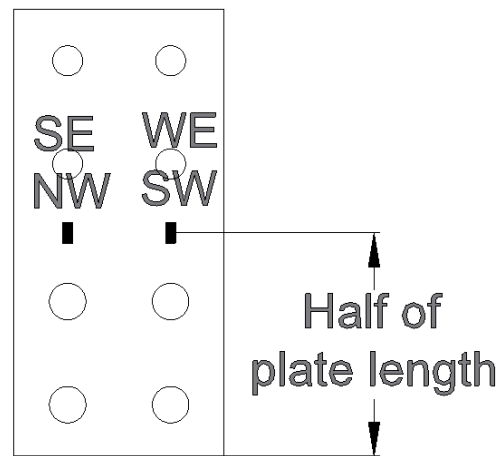
(c)



(d)

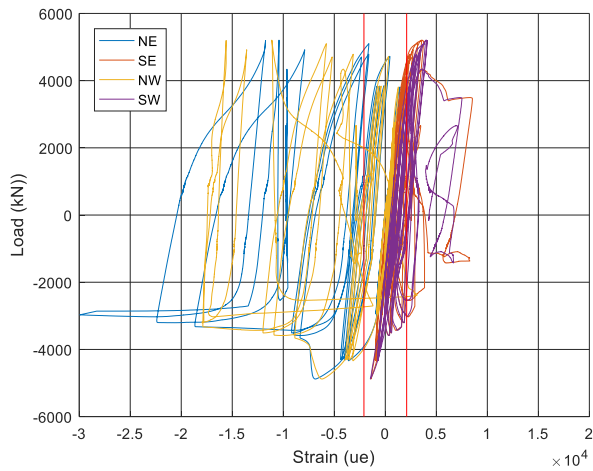


(e)

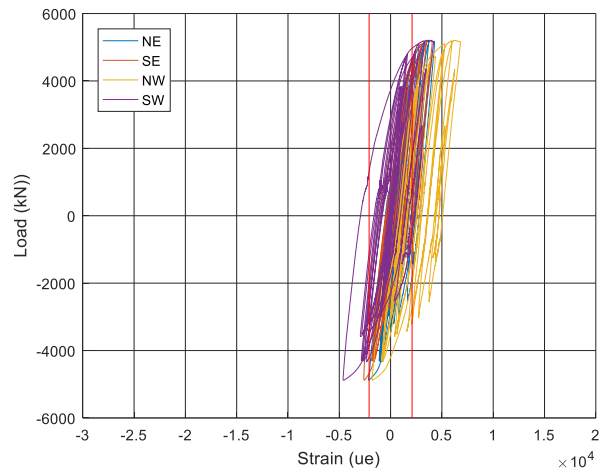


(f)

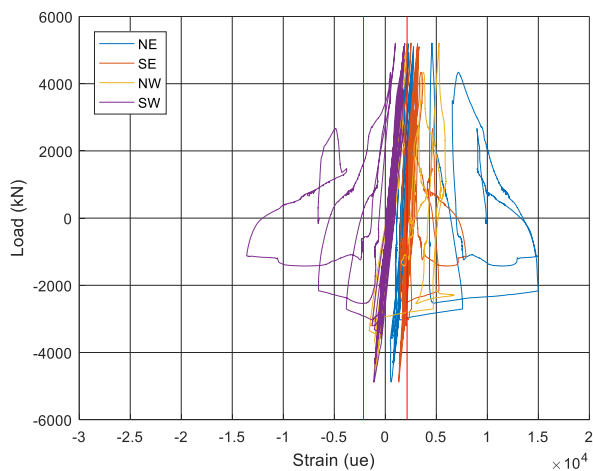
Figure E-2 Force-displacement hysteresees for strain gauges in connections of specimen J310-C
 (a) Bottom jaw plates (b) Top jaw plates (c) Bottom web plates (d) Top web plates (e) Location of strain gauges on jaw plates (dimension in mm) (f) Location of strain gauges on web plates



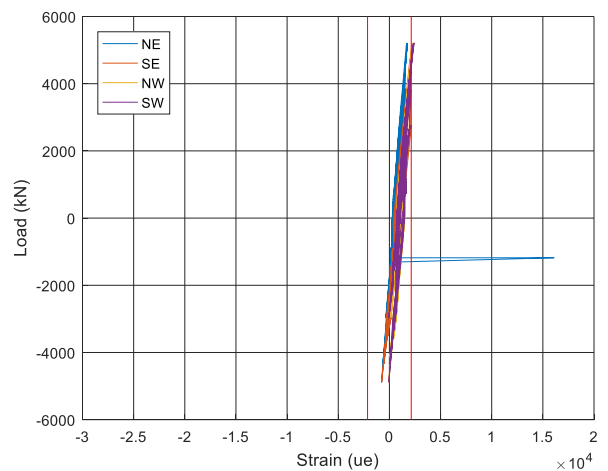
(a)



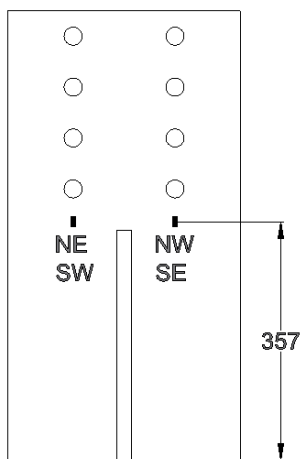
(b)



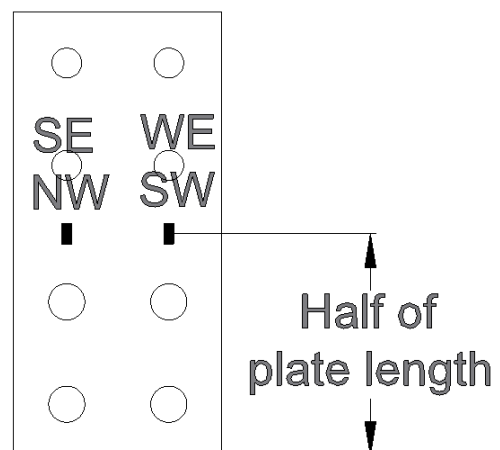
(c)



(d)



(e)



(f)

Figure E-3 Force-displacement hysteresses for strain gauges in connections of specimen J360-T (a) Bottom jaw plates (b) Top jaw plates (c) Bottom web plates (d) Top web plates (e) Location of strain gauges on jaw plates (dimension in mm) (f) Location of strain gauges on web plates

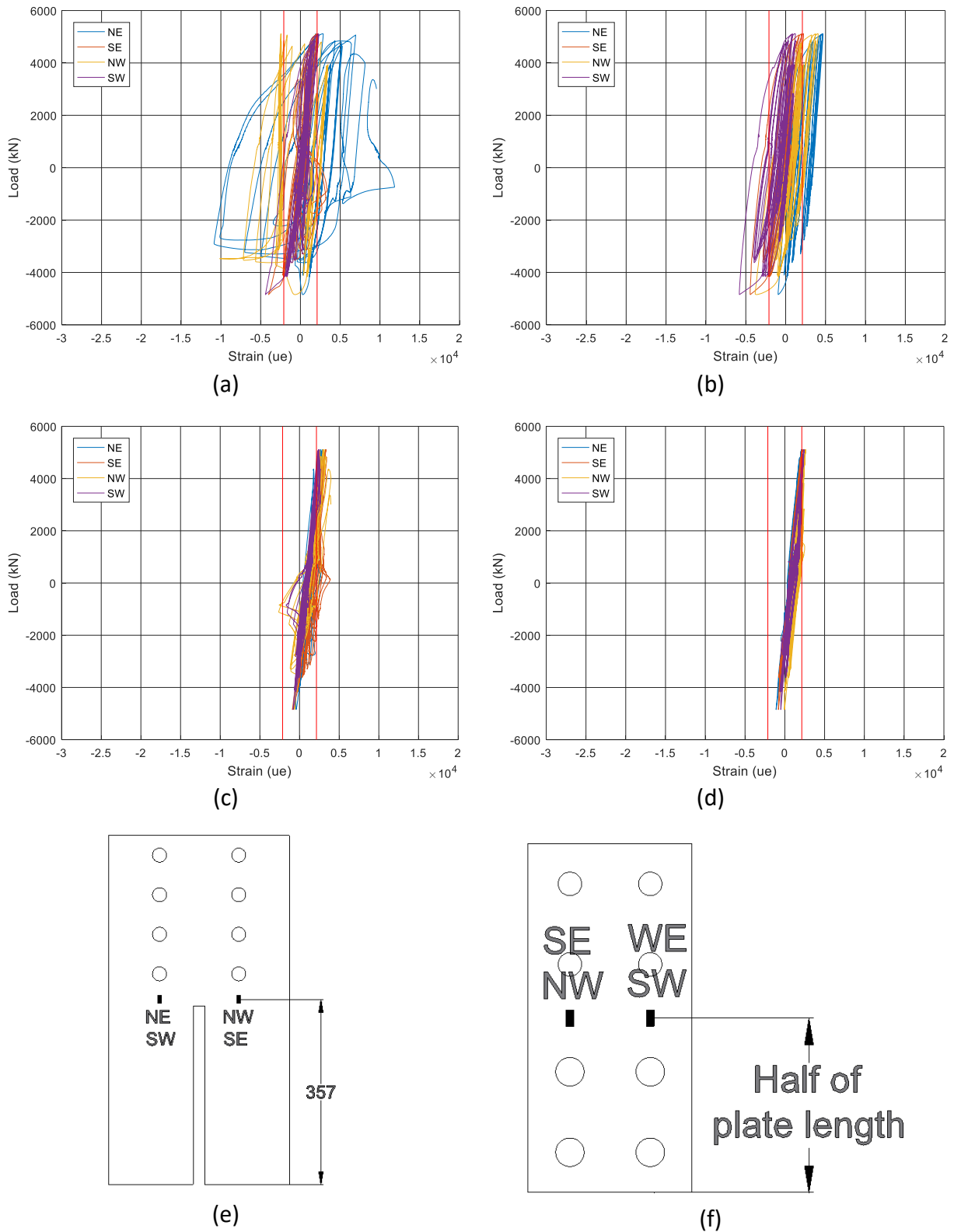
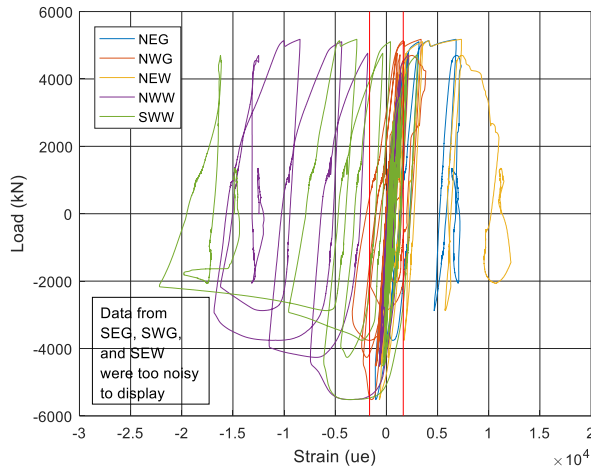
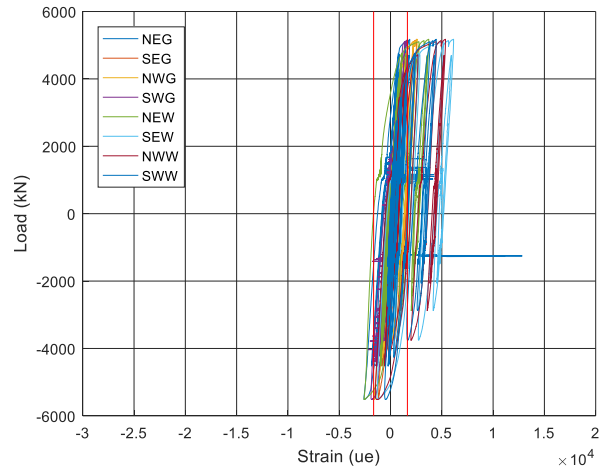


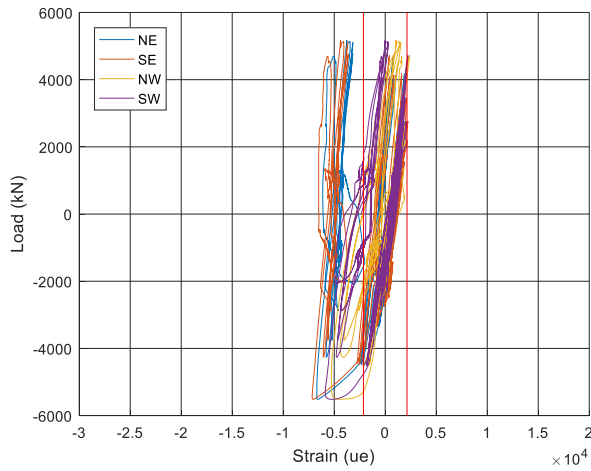
Figure E-4 Force-displacement hysteresses for strain gauges in connections of specimen J360-C
 (a) Bottom jaw plates (b) Top jaw plates (c) Bottom web plates (d) Top web plates (e) Location of strain gauges on jaw plates (dimension in mm) (f) Location of strain gauges on web plates



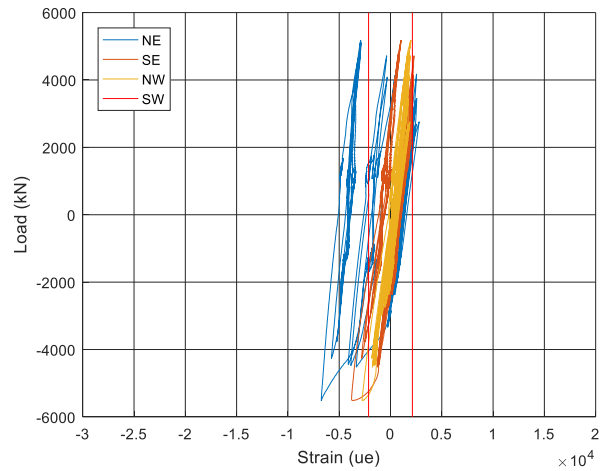
(a)



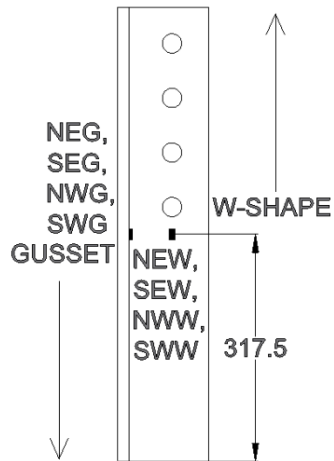
(b)



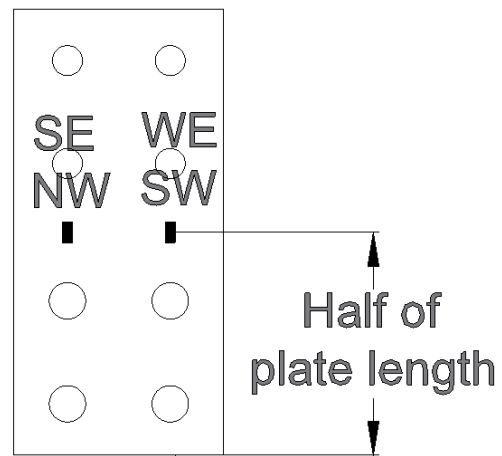
(c)



(d)

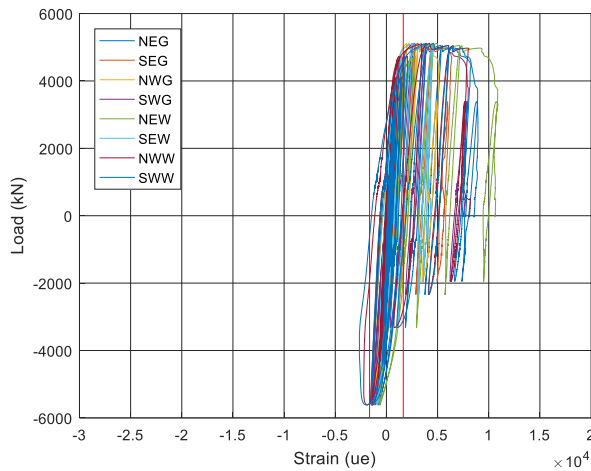


(e)

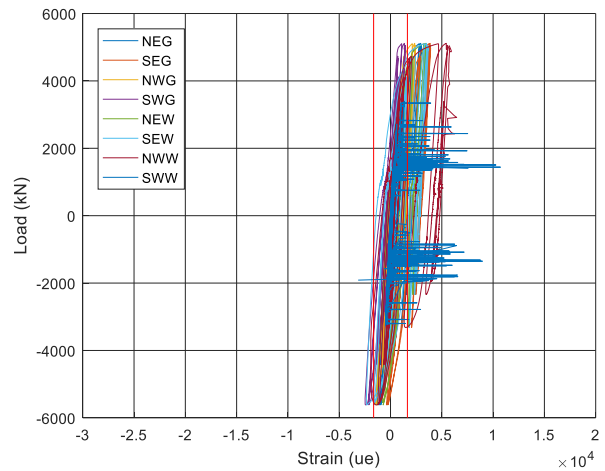


(f)

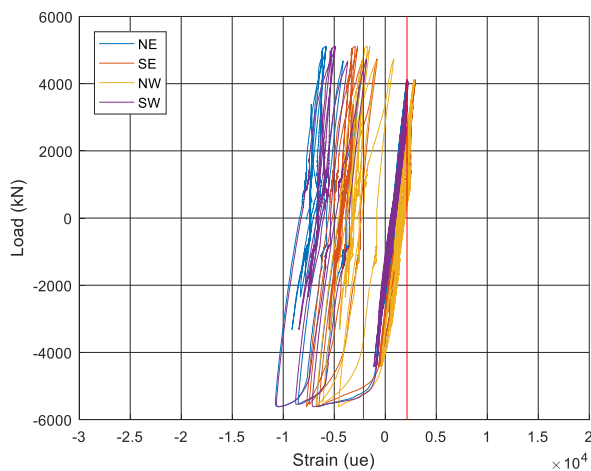
Figure E-5 Force-displacement hysteresees for strain gauges in connections of specimen C360-T
 (a) Bottom angles (b) Top angles (c) Bottom web plates (d) Top web plates (e) Location of strain gauges on angles (dimension in mm) (f) Location of strain gauges on web plates



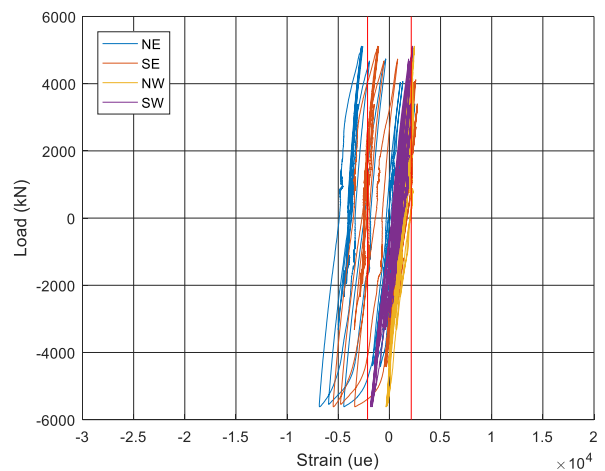
(a)



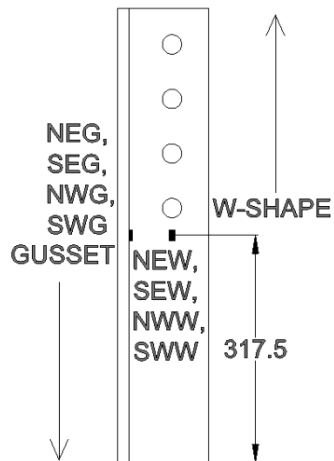
(b)



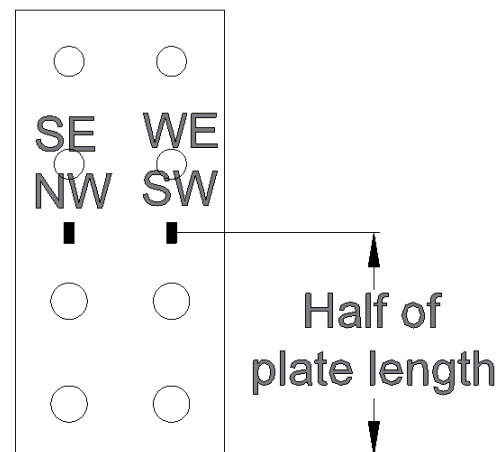
(c)



(d)



(e)



(f)

Figure E-6 Force-displacement hysteresses for strain gauges in connections of specimen C360-C (a) Bottom jaw plates (b) Top jaw plates (c) Bottom web plates (d) Top web plates (e) Location of strain gauges on jaw plates (dimension in mm) (f) Location of strain gauges on web plates